frontiers | Research Topics

Miniaturized high-power solid-state laser and applications

Edited by
Zhi-Han Zhu, Zhenxu Bai, Baitao Zhang, Liyuan Chen and Mingjun Xia

Published in
Frontiers in Physics

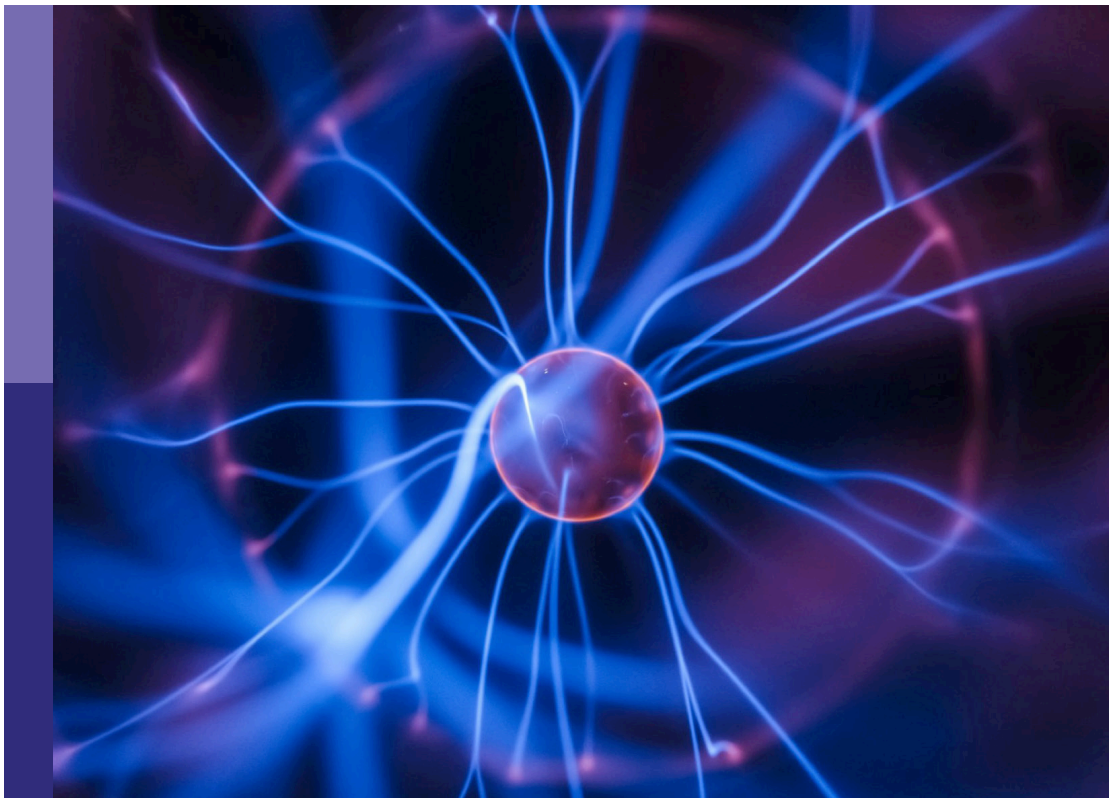

ISSN 1664-8714
ISBN 978-2-8325-2554-8
DOI 10.3389/978-2-8325-2554-8

About Frontiers

Frontiers is more than just an open access publisher of scholarly articles: it is a pioneering approach to the world of academia, radically improving the way scholarly research is managed. The grand vision of Frontiers is a world where all people have an equal opportunity to seek, share and generate knowledge. Frontiers provides immediate and permanent online open access to all its publications, but this alone is not enough to realize our grand goals.

Frontiers journal series

The Frontiers journal series is a multi-tier and interdisciplinary set of open-access, online journals, promising a paradigm shift from the current review, selection and dissemination processes in academic publishing. All Frontiers journals are driven by researchers for researchers; therefore, they constitute a service to the scholarly community. At the same time, the *Frontiers journal series* operates on a revolutionary invention, the tiered publishing system, initially addressing specific communities of scholars, and gradually climbing up to broader public understanding, thus serving the interests of the lay society, too.

Dedication to quality

Each Frontiers article is a landmark of the highest quality, thanks to genuinely collaborative interactions between authors and review editors, who include some of the world's best academicians. Research must be certified by peers before entering a stream of knowledge that may eventually reach the public - and shape society; therefore, Frontiers only applies the most rigorous and unbiased reviews. Frontiers revolutionizes research publishing by freely delivering the most outstanding research, evaluated with no bias from both the academic and social point of view. By applying the most advanced information technologies, Frontiers is catapulting scholarly publishing into a new generation.

What are Frontiers Research Topics?

Frontiers Research Topics are very popular trademarks of the *Frontiers journals series*: they are collections of at least ten articles, all centered on a particular subject. With their unique mix of varied contributions from Original Research to Review Articles, Frontiers Research Topics unify the most influential researchers, the latest key findings and historical advances in a hot research area.

Find out more on how to host your own Frontiers Research Topic or contribute to one as an author by contacting the Frontiers editorial office: frontiersin.org/about/contact

Miniaturized high-power solid-state laser and applications

Topic editors

Zhi-Han Zhu — Harbin University of Science and Technology, China
Zhenxu Bai — Hebei University of Technology, China
Baitao Zhang — Shandong University, China
Liyuan Chen — Hilase Center, Czechia
Mingjun Xia — Technical Institute of Physics and Chemistry, Chinese Academy of Sciences (CAS), China

Citation

Zhu, Z.-H., Bai, Z., Zhang, B., Chen, L., Xia, M., eds. (2023). *Miniaturized high-power solid-state laser and applications*. Lausanne: Frontiers Media SA. doi: 10.3389/978-2-8325-2554-8

Table of contents

frontiers | Frontiers in Physics

TYPE Original Research
PUBLISHED 19 August 2022
DOI 10.3389/fphy.2022.982232

OPEN ACCESS

EDITED BY
Liyuan Chen,
Hilase Center, Czechia

REVIEWED BY
Dario Vangi,
University of Florence, Italy
Yulai She,
Guilin University of Electronic Technology, China
Pengbai Xu,
Guangdong University of Technology, China

*CORRESPONDENCE
Yudong Lian,
ydlian@hebut.edu.cn

SPECIALTY SECTION
This article was submitted to Optics and Photonics, a section of the journal Frontiers in Physics

RECEIVED 30 June 2022
ACCEPTED 25 July 2022
PUBLISHED 19 August 2022

CITATION
Han S, Lian Y, Xie L, Hu Q, Ding J, Wang Y and Lu Z (2022), Numerical simulation of angled surface crack detection based on laser ultrasound.
Front. Phys. 10:982232.
doi: 10.3389/fphy.2022.982232

Numerical simulation of angled surface crack detection based on laser ultrasound

Shiwei Han[1,2], Yudong Lian[1,2,3]*, Luyang Xie[1,2], Qi Hu[1,2], Jie Ding[1,2,3], Yulei Wang[1,2,3] and Zhiwei Lu[1,2,3]

[1]Center for Advanced Laser Technology, Hebei University of Technology, Tianjin, China, [2]Hebei Key Laboratory of Advanced Laser Technology and Equipment, Tianjin, China, [3]Tianjin Key Laboratory of Electronic Materials and Devices, Tianjin, China

As an important branch of non-destructive testing, laser ultrasonic testing has attracted increasing attention in the field of material testing because of its instantaneity, non-contact and wide adaptability. Based on the finite element method, the process of laser-excited ultrasonic signal is numerically simulated, and the influence of angled cracks on the ultrasonic signal is analyzed. In this paper, the effects of the time function, pulse width, and spot radius of a Gaussian light source are analyzed through the transient field. The different modes of the ultrasonic signal are used to fit the crack's angle, depth, and width to complete the characteristic analysis of the surface angled crack. The results show that the displacement peak-valley difference of the direct Rayleigh wave is negatively correlated with the crack angle. The displacement extremes of the transmitted Rayleigh wave boundary are negatively correlated with crack depth and width, while the transmitted Rayleigh wave is positively correlated. This paper presents a method for the quantitative analysis of surface-angled cracks and provides a theoretical basis for further experimental verification.

KEYWORDS

laser ultrasound, nondestructive testing, angled crack, Rayleigh wave, stress displacement

1 Introduction

Nondestructive testing has been widely employed in engineering applications as an important tool for evaluating the safety of materials [1–4]. With the development of laser technology, laser ultrasonic testing has become an important nondestructive testing technology [5–8]. This technology has a bright future because of its non-contact [9], wide-band [10], instantaneous [11, 12], and high-sensitivity characteristics [13]. It is not only suitable for remote detection in severe environments [14, 15] but also for real-time online analysis of micro-cracks [16, 17]. In the transmission process of ultrasonic signals, transmission waves, reflection waves and mode conversion waves will appear due to the influence of cracks. We can judge the defect information of the sample by analyzing the reflection or transmission waveform of the crack.

Early researchers analyzed laser ultrasonic detection based on the thermoelastic mechanism through numerical simulation. I. Arias presented a two-dimensional

theoretical model for solving the thermoelastic problem and analyzed the effects of the spot radius and pulse width in generating ultrasonic signals [18]. Xu analyzed the thickness detection of an aluminum plate by laser ultrasound in terms of temperature and displacement [19]. Wang analyzed the effects of thermal diffusion and finite spatial and temporal shape pulses of lasers on the generation of elastic waves in non-metallic materials [20]. Guan studied the relationship between the half-width of a pulsed line source laser and the displacement signal characteristics of Rayleigh and Lamb waves [21]. S. Rajagopal studied the effect of the optical attenuation coefficient and laser pulse duration on acoustic pulses [22]. However, the analysis between laser parameters and the excitation ultrasound signals is limited to the displacement field, which should also include the transient temperature field and stress field.

In recent years, laser ultrasonic testing has been widely used for detecting defects. A. Cavuto built a complete axle-wheel detection model that considered the propagation of ultrasound waves into both the solid and air domains [23]. L. Bustamante proposed a hybrid laser and air-coupled ultrasonic method and achieved an error tolerance of 13.6%–17.6% [24]. Before experimental validation, mathematical analysis utilizing the finite element method is an important aspect of the procedure to better understand the physical process of laser ultrasonic detection. There are many studies on laser ultrasonic numerical simulation of angled surface cracks [25, 26]. Based on the finite element method, B. Dutton verified that the transmission and reflection coefficients are related to the Angle and length of the defect [25]. Zeng observed the changes in the amplitude and spectrum of Rayleigh waves to determine the angle of surface cracks [27]. Zhou used the method of fitting the transmission coefficient and reflection coefficient of the Rayleigh wave to quantitatively identify surface-breaking cracks [28]. Wang proved that the peak-to-valley difference of the Rayleigh echo and the crack depth can be linearly fitted [29]. Most of the research only focuses on a specific defect characteristic, which requires systematic quantitative research.

In this paper, a two-dimensional cross-sectional model of aluminum material is established for crack detection. First, the effects of the time function, pulse width, and spot radius on laser ultrasonic detection are verified through transient fields. Second, the quantitative detection of inclined cracks is carried out. The angle, depth, and width of the surface crack are obtained by numerical fitting of different modes of Rayleigh waves. The larger the difference between the peak and valley of the Y displacement of the direct Rayleigh wave (RW), the smaller the crack inclination angle. The displacement extreme value of the transmitted Rayleigh wave boundary (TRW-B) increases as the crack depth or width increases, while the transmitted Rayleigh wave (TRW) decreases. The simulation results show that the maximum error of fitting data of different modes is 4.7%.

2 Theory and numerical models

2.1 Theoretical basis

The ultrasonic signal produced by the pulse light source can be classified as an ablation or thermoelastic mechanism. Ablation occurs when the laser power density exceeds the material damage threshold, evaporating a small amount of plasma and damaging the material in the process. When the laser power density is lower than the material damage threshold, a thermoelastic phenomenon will occur. This thermoelastic mechanism is suitable for nondestructive testing. It can generate ultrasonic waves such as shear-wave (SW), longitudinal-wave (LW), and RW to meet the detection of different defects. Under this mechanism, the material's surface absorbs light energy rapidly and produces a heating source. The heat energy is continuously conducted to the far-field region and forms an irregular temperature field. The thermoelastic stress generated by temperature-induced thermal expansion becomes the source of excitation for ultrasound.

Since the spatial distribution of the laser beam irradiated on the isotropic sample material is axisymmetric, the physical model can be simplified to solve the two-dimensional plane problem. While ignoring the influence of thermal convection and radiation between the material and environment on the temperature variation, the heat conduction formula can be expressed as [30, 31]:

$$\rho c\frac{\partial T(r,z,t)}{\partial t}=\frac{1}{r}\frac{\partial}{\partial x}\left(rk\frac{\partial T(r,z,t)}{\partial r}\right)+\frac{\partial}{\partial z}\left(k\frac{\partial T(r,z,t)}{\partial z}\right) \tag{1}$$

where ρ is the material density, c is the specific heat capacity of the material, $T(r,z,t)$ is the temperature distribution at time t, k is the thermal conductivity coefficient, and $\rho c\partial T/\partial t$ represents the heat required for the differential body to heat up per unit time. The boundary conditions of thermoelastic theory can be described as:

$$-k\frac{\partial T(r,z,t)}{\partial z}|z=0=I_0 f(x)g(t) \tag{2}$$

where I_0 is the laser peak power density, and the space function $f(x)$ and time function $g(t)$ can be expressed as [32–34]:

$$f(x)=exp\left(\frac{(x-x_0)^2}{r_0^2}\right) \tag{3}$$

$$g_1(t)=\frac{t}{t_0}exp\left(-\frac{t}{t_0}\right) \tag{4}$$

$$g_2(t)=\frac{t}{t_0}exp\left(-\frac{t^2}{t_0^2}\right) \tag{5}$$

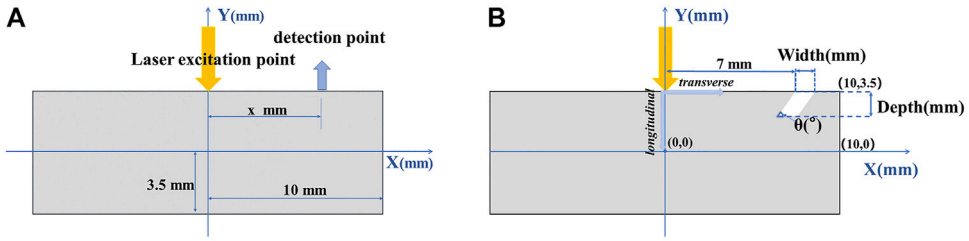

FIGURE 1
Laser ultrasonic detection model: **(A)** without crack; **(B)** with angled crack.

where x_0 is the abscissa of the pulse action point, r_0 is the laser spot radius, and t_0 is the rise time of the pulsed laser.

The transient displacement field excited by thermoelastic expansion is expressed as [30, 31]:

$$\mu\nabla^2\boldsymbol{U}(r,z,t) + (\lambda+2\mu)\nabla(\nabla\boldsymbol{U}(r,z,t)) - \alpha(3\lambda+2\mu)\nabla\boldsymbol{T}(r,z,t) = \rho\frac{\partial^2\boldsymbol{U}(r,z,t)}{\partial t^2} \tag{6}$$

where $U(r, z, t)$ is the transient displacement vector of the ultrasonic wave. $\alpha(3\lambda + 2\mu)\nabla T$ represents the transient force source generated by the temperature gradient. α is the thermal expansion coefficient, and λ and μ are lame constants.

The laser thermoelectricity equation is solved by the finite element method. Eq. 7 is expressed as the laser heat conduction finite element equation under the thermoelastic regime:

$$[\boldsymbol{K}]\{\boldsymbol{T}\} + [\boldsymbol{C}]\{\dot{\boldsymbol{T}}\} = \{\boldsymbol{R}_q\} + \{\boldsymbol{R}_Q\} \tag{7}$$

where $[K]$ is the conduction matrix, $[C]$ is the heat capacity matrix, $\{T\}$ is the temperature vector, and $\{\dot{T}\}$ is the rate of change of temperature with time. $\{R_q\}$ is the heat flow vector of the material. $\{R_Q\}$ is the heat source vector of the material.

For the propagation of ultrasonic waves, under the condition of ignoring the damping effect, the finite element equation under the linear thermoelastic mechanism is

$$[\boldsymbol{M}]\{\ddot{\boldsymbol{U}}\} + [\boldsymbol{K}][\boldsymbol{U}] = \{\boldsymbol{R}_{ext}\} \tag{8}$$

where $[M]$ is the mass matrix of the material, $\{\ddot{U}\}$ is the vector acceleration, $[K]$ is the stiffness matrix, and $[U]$ is the vector displacement. $\{R_{ext}\}$ is the thermal stress vector.

2.2 Numerical model

Since the overall structure is symmetrical, the process can be converted from three-dimensional to two-dimensional analysis, and the laser can be converted from a line source to a point source. In this paper, the two-dimensional interface of an aluminum plate is used as the numerical model to simulate the process of laser-excited ultrasound and crack detection. The detection model of laser ultrasound is shown in Figure 1. The whole model is axisymmetric, the length is 20 mm and the width is 7 mm. The origin of the coordinate system was at the center of the aluminum material. The excitation point was set at (0, 3.5), the detection points were set on the surface at (x, 3.5). The vertex of the defect with angle θ is at (7, 3.5).

In this model, Gaussian time functions, pulse width and spot radius are studied employing control variables. The influence of these characteristic properties on the excitation process is studied through the transient temperature field, stress field, and resulting displacement. The parameters of the excitation pulse light as well as the physical properties of the aluminum material used in the model are shown in Tables 1, 2. The equations should be inserted in editable format from the equation editor.

3 Simulation results and analysis

The laser excited ultrasound simulation process has two parts: physical thermal and structural mechanics. The pulsed laser is loaded on the aluminum material's surface and generates a quick heat source. Transient temperature fields are formed due to the rapid accumulation of heat. The heat energy is imparted to the aluminum through thermal expansion, resulting in a transient stress field. The efficiency of excitation can be reflected in the form of stress displacement in the stress field. Therefore, the transient temperature field, stress field, and stress displacement can be used to determine the efficiency of laser excitation ultrasonic signals.

3.1 Laser ultrasonic signal generation

3.1.1 Effect of time function

It is one of the critical parts of the simulation to select reasonably the time function of the Gaussian pulse. Therefore, Gaussian pulse light sources of g_1 and g_2 with the same energy are analyzed, whose pulse peak power density is P_1 and P_2, as shown

TABLE 1 Parameters of pulsed laser.

Monopulse-energy (mJ)	Pulse width (ns)	Spot radius (μm)	Peak power-density
0.7	10	400	$1.3926 \times 10^{11} W/m^2$

in Figure 2. The pulse power spectrum density of the laser is considerably varied under the same space function as well as different time functions with the same upper and lower limit parameters. Figure 2A has pulse durations of approximately 60 ns, while (B) has a pulse duration of approximately 20 ns However, the maximum value of P_1 is less than that of P_2. It can be seen that the laser's power density increases as the time function narrows. As a result, selecting a time function should be based on personal experiment.

Different time functions induce changes in the temperature field, as seen in Figures 2C,D. The maximum temperature of the g_1 function is greater than that of the g_2 function at all detection points. The narrower the time function is, the less time there is for light energy to be converted into heat energy. This results in a lower temperature for the laser with a narrow time function at the same energy. Heat conduction causes a decrease in temperature away from the laser radiation point, which leads to differences in temperature at different detection points. The temperature field flattens out within 0.3 μs, which suggests that the temperature gradient is instantaneous. The time function g_1 was employed in this simulation because of the higher temperature with a low power density.

3.1.2 Effect of pulse width

After a pulse energy of 0.7 mJ, and a spot radius of 0.4 mm, the pulse width of the laser was adjusted from 1 to 100 ns to evaluate the impact on the laser excitation ultrasound waves. The temperatures of different positions detected by the probe in the transverse and longitudinal directions are shown in Figure 3. Different probes are spaced 2 μm apart in both directions. 533, 483, 456, 423, 403, 389, 378, and 351 K are the maximum temperatures produced by pulse lengths of 1–100 ns at (0, 3.5). The farther away from the (0, 3.5) point, as shown in Figure 3, the lower the temperatures are both transverse and longitudinal. We consider that the difference of the pulse width causes the peak power density to change, resulting in a different temperature acting instantaneously on the sample surface, leading to a change in the transient temperature field.

TABLE 2 Physical properties of aluminum materials.

Characteristic	Aluminum
Coefficient of thermal expansion	$23.4 \times 10^{-6} K^{-1}$
Constant pressure heat capacity	900 J/(kg*K)
Density	2,700 kg/m^3
Thermal Conductivity	201 W/(m*K)
Young's modulus	69×10^9 Pa
Poisson's ratio	0.33
Relative permeability	1

The displacements of pulse widths detected by the probe in different directions are shown in Figures 3C,D. Figure 3C indicates that a pulse width of 1 ns reduces the displacement from 22.6 nm at point (0, 3.5) to 16.8 nm at point (0.01, 3.5), while a pulse width of 100 ns reduces the displacement from 10.25 to 8.33 nm. This shift is more noticeable in the longitudinal direction; the displacement created by the laser with a pulse of 1 ns grows from 6.25 to 22.6 nm, whereas the displacement produced by the pulse of 100 ns increases from 1.05 to 4.15 nm, as shown in Figure 3D. The temperature field determines the stress field in the laser radiation region, and a larger temperature gradient results from a faster shift in the longitudinal temperature field; hence, longitudinal stress displacement is more variable. Due to the causal relationship between temperature and stress displacement, the overall trends of temperature and thermal stress wave displacements are similar. That is, the total displacement will decay away from the laser irradiation point. Therefore, it can be seen that the narrower the pulse width of the laser is, the higher efficiency of exciting the ultrasound.

3.1.3 Effect of spot radius

Figure 4 shows the temperature field of the domain probe with varied spot radii after setting a pulse energy of 0.7 mJ and a pulse width of 10 ns The power density of the laser is directly affected by the size of the spot radius. The smaller the spot is, the higher the power density, which causes the temperature to increase. This trend is more noticeable in the smaller radius. In the case of lower than the damage threshold of the sample, the laser with a small spot radius should be selected as much as possible for exciting the ultrasound.

The displacement caused by thermal stress can intuitively reflect the ultrasonic wave's amplitude. The laser's incident point was detected to obtain displacement, the X component of which is illustrated in Figure 5A and the Y component in Figure 5B. The thermal expansion force generated by thermal energy interacts with the impeding force in the normal temperature area, resulting in a relatively complex value of the X displacement component. In Figure 5A, the X

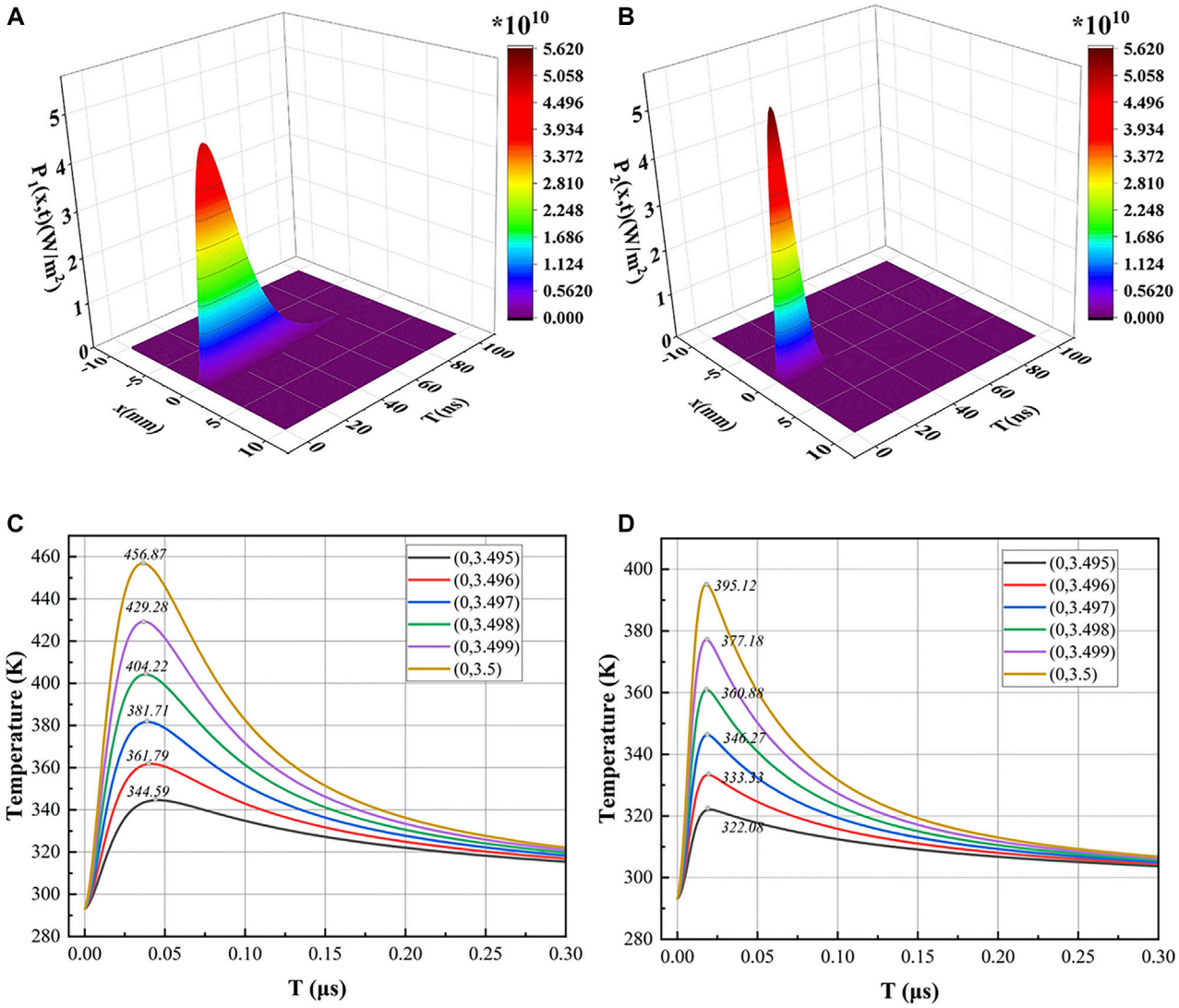

FIGURE 2
Gaussian pulse and temperature field of different time functions: **(A)** Gaussian pulse of time function g_1; **(B)** Gaussian pulse of time function g_2; **(C)**Temperature field of time function g_1; **(D)** Temperature field of time function g_2.

displacement after 1 μs is expanded, while the 0.05 mm displacement is masked for clarity. As heat energy is transmitted within the material, the X displacement becomes more noticeable. The spot radius is shown to be inversely linked with the X displacement. The longer the X displacement component exists, the smaller the radius is. In Figure 5B, the Y displacement corresponding to the spot radius of 0.3–1.0 mm is magnified for easy observation. The maximum Y displacements from 0.05 to 1.0 mm are 343.2, 142.4, 53.4, 28.4, 17.6, 11.9, 8.6, and 3.3 nm, showing a negative correlation. The smaller the spot is, the more energy is accumulated and the higher the power density. This will result in greater stress displacement in two directions. Usually, the data required in the actual detection is the Y displacement because it can be visualized to reflect the ultrasonic wave.

The wide spectrum and high amplitude of ultrasonic is one of the reasons why it is used to detect information. The influence of light spot radius on spectrum under the condition of same energy and same energy density is analyzed here. Figure 6A demonstrates that when the laser loading energy is constant, the smaller the spot, the greater the amplitude of the ultrasonic spectrum, and the information it can contain is easier to be extracted. Figure 6B shows that the spectrum amplitude of the ultrasonic wave will increase with increasing spot radius while the energy density of the laser remains constant. This is because

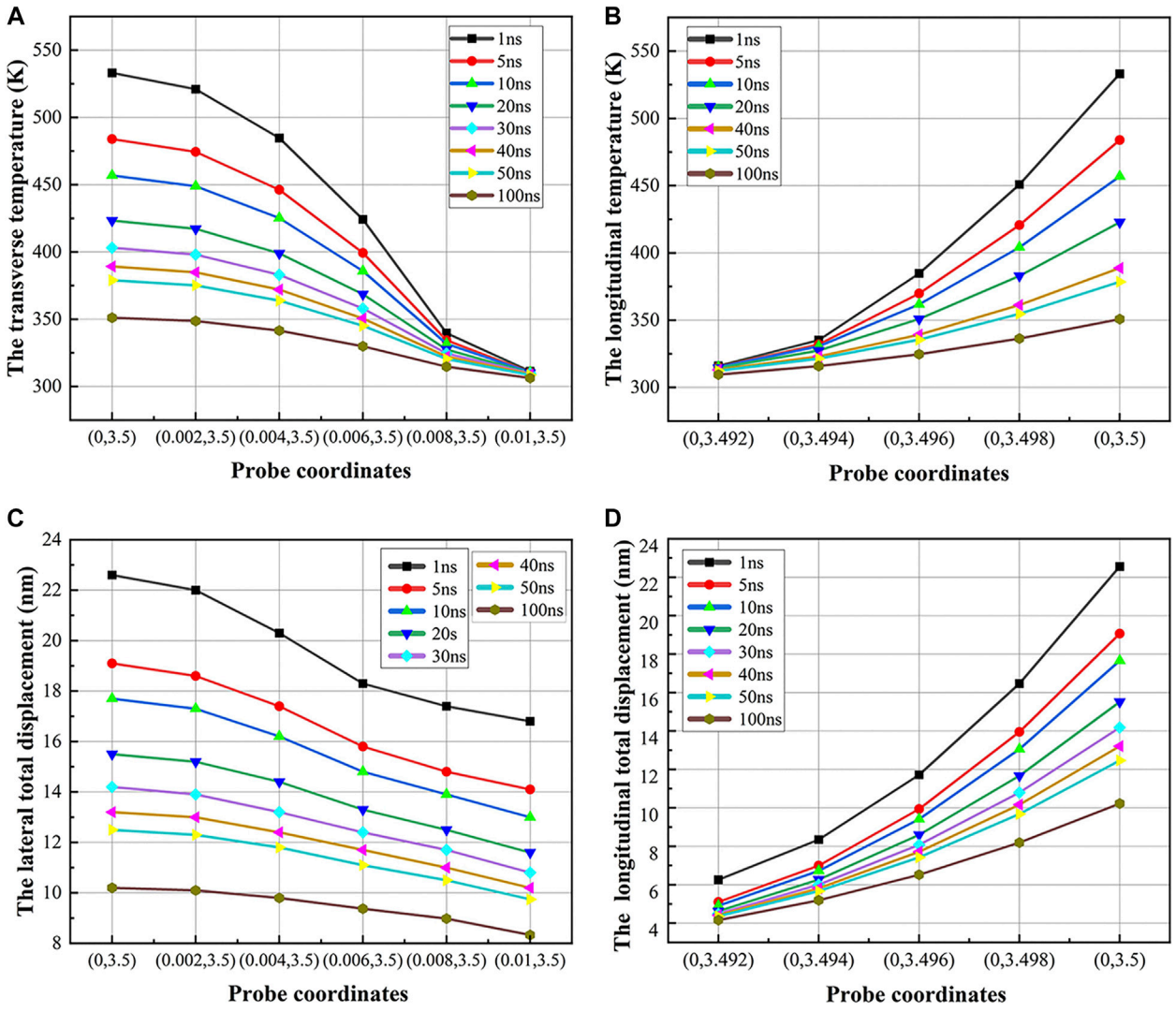

FIGURE 3
Temperature field and displacement field: **(A)** Temperatures in Transverse; **(B)** Temperatures in Longitudinal; **(C)** Total displacement in Transverse; **(D)** Total displacement in Longitudinal.

the spatial function of the Gaussian pulse is inversely proportional to the square of the radius of the laser spot, and the size of the radius of the laser spot radiates with the same energy density without attenuation.

3.2 Angled surface crack detection

Angled surface cracks are common surface defects with random angles, widths, and depths, which makes quantitative detection difficult. The surface wave excited by the laser has a good function in detecting defects that is very suitable for the quantitative detection of surface angled cracks. The ratio of the depth of the defect to the ultrasonic center wavelength (D/λ) is used to reflect the detection in various cases to increase rigor [25].

3.2.1 Angle detection

The propagation of ultrasonic waves and the mode transition that occurs following ultrasonic contact with the fracture are illustrated using a 70° crack model. Figure 7A shows different ultrasonic signals after laser irradiation for 2.0 μs The surface wave that directly reaches the crack is defined as the Rayleigh wave (RW), whose waveform is relatively apparent. At 3.1 μs, the ultrasonic waves reach the crack in Figure 7B, where the mode transition occurs. Some waves penetrate the edge of the crack and create a TRW, while other waves are reflected by it. A tiny percentage of waves are changed into mode transition shear or

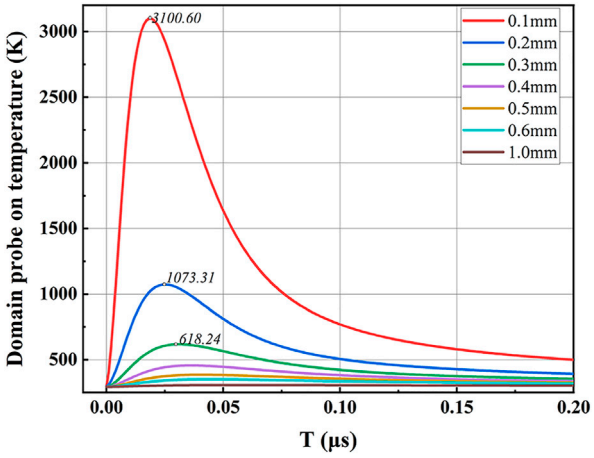

FIGURE 4
Transient temperature field with different spot radii.

longitudinal waves after reflection; however, the vast majority of waves form crack-reflected Rayleigh wave (CRW). In Figure 7C, when the time reaches 3.75 μs, the TRW on the right side of the crack is reflected by the boundary, and its propagation direction reverses. After reflection, this waveform is called TRW-B. Figure 7D shows that the right-propagating reflection wave will also reflect through the right boundary.

If no special circumstances are specified, the default feature of the crack is that the angle is 70°, the depth is 0.3 mm, the width is 0.3 mm and Rayleigh waves have a wavelength of 890 μm. Different detection points are set to determine the angle of the crack. The Y displacement components obtained from these detection points are shown in Figure 8A. The Y displacement of these detection points from (2, 3.5) to (6, 3.5) is approximately −0.18 to 0.1 nm, while the Y displacement of the detection point (7, 3.5) is a maximum of 4.12 nm and a minimum of −4.7 nm, making it the largest of the detection locations. This phenomenon occurred at both acute and obtuse angles, with acute being the most noticeable. The tilt angle of the surface cracks in the numerical simulation is changed from 20° to 160° for different angle detection. The position (7, 3.5) was chosen as the detecting point to better examine the Y displacement components.

The Y displacements at different angles are shown in Figures 8B,C, which mainly reflects the variation in the RW waveform during this period of time. From 20° to 90°, there is a time delay in RW whose amplitude of Y displacement changes significantly as well. Part of the ultrasonic energy is blocked by the angled crack and continuously accumulates at the left end of the crack, which leads to the amplitude change as well as time delays of the RW. If the angle is greater than the right angle, the energy of the RW will no longer accumulate but will directly pass which is only reflected in the amplitude of the ultrasonic Y displacement. Therefore, the main change of the RW is in the displacement amplitude with angle changing from 90° to 160°.

It is a great method to fit correlation curves to solve the problem. The relationship between the angles and RW is obtained by fitting the difference between the peak and valley of RW. The relevant result is shown in Figure 8D. The curve from 20° to 80° is steeper, and the Y displacement difference between the peak and the valley drops from 0.714 to 0.0701 nm, as seen in the figure. The curve from 80° to 160° is flatter, whose Y displacement decreases from 0.714 to 0.0250 nm. The nonlinear curve fitting's mean square error value (MSE) is 1.771810^{-9}. The fitting regression coefficient R^2 reaches 99.947%. The expression of the fitted curve is:

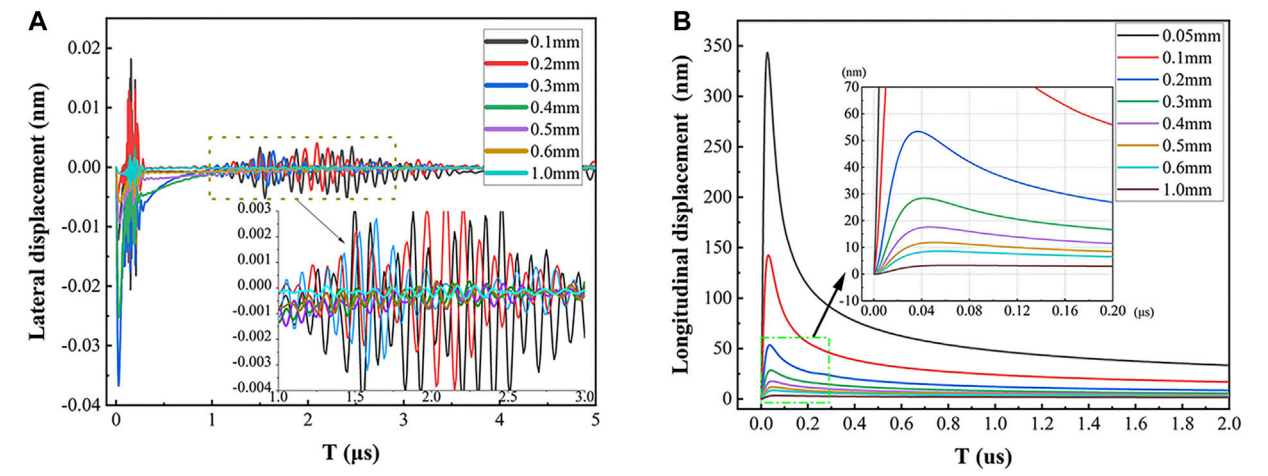

FIGURE 5
Stress displacement: **(A)** X displacement in the lateral direction; **(B)** Y displacement in the longitudinal direction.

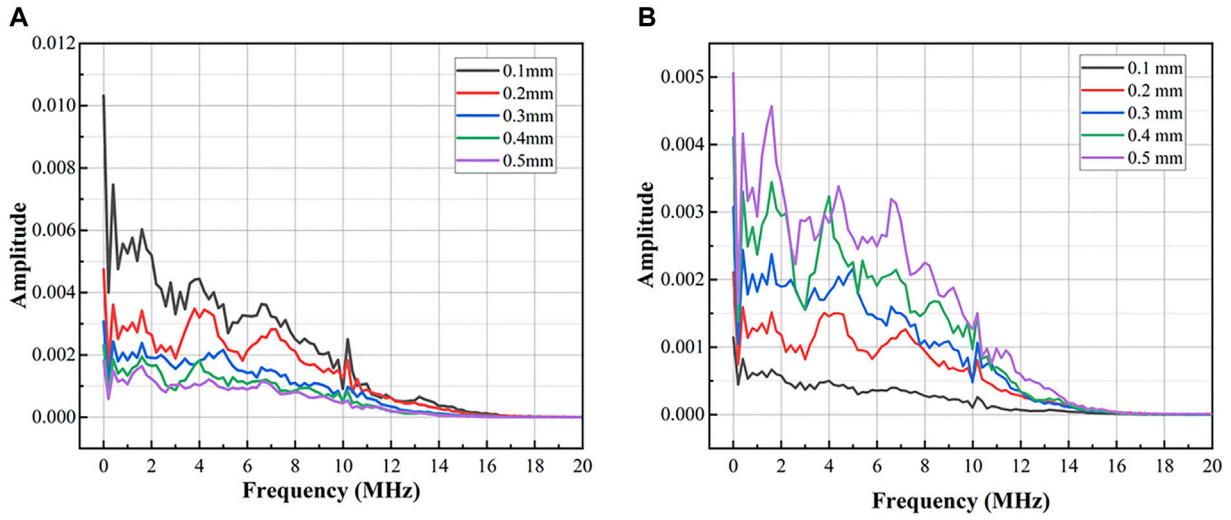

FIGURE 6
Spectrum of different spot radii: **(A)** Same impulse energy; **(B)** Same energy density.

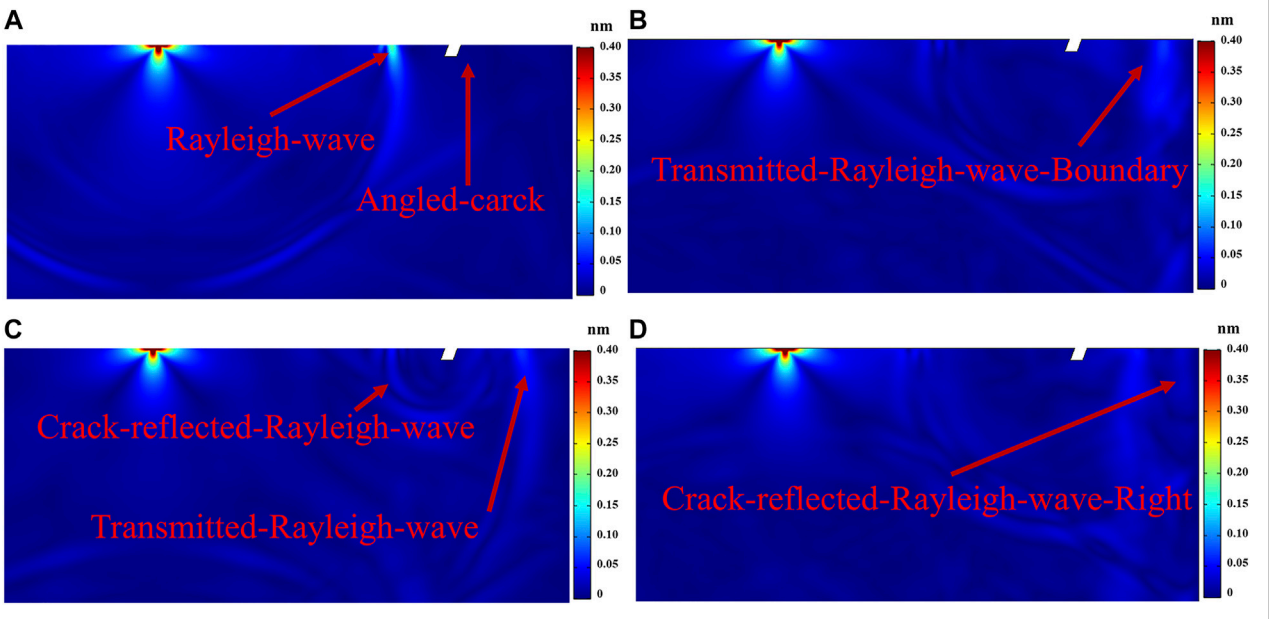

FIGURE 7
Rayleigh waves at different times: **(A)** 2.0 μs; **(B)** 3.1 μs; **(C)** 3.75 μs **(D)** 4.0 μs

$$\Delta Y = 0.0248836 + 10.68 \times exp\left(\frac{\theta}{-24.68562}\right) + 58462092 \times exp\left(\frac{\theta}{-1.02959}\right) \quad (9)$$

where ΔY is the peak-to-valley displacement difference of the RW and θ is the degree of surface crack. It can be concluded that the higher the peak-valley difference of Rayleigh waves is, the smaller the surface tilt angle. Table 3 shows the data of some defect tilt angles and peak-to-peak values of direct Rayleigh waves under different crack depth/wavelength (D/λ) ratios. The trend is consistent in the case where the ratio of D/λ is less than 1.11. If the depth-wavelength ratio changes, then the peak-to-peak and Angle fitting expressions need to change as well. The quantitative

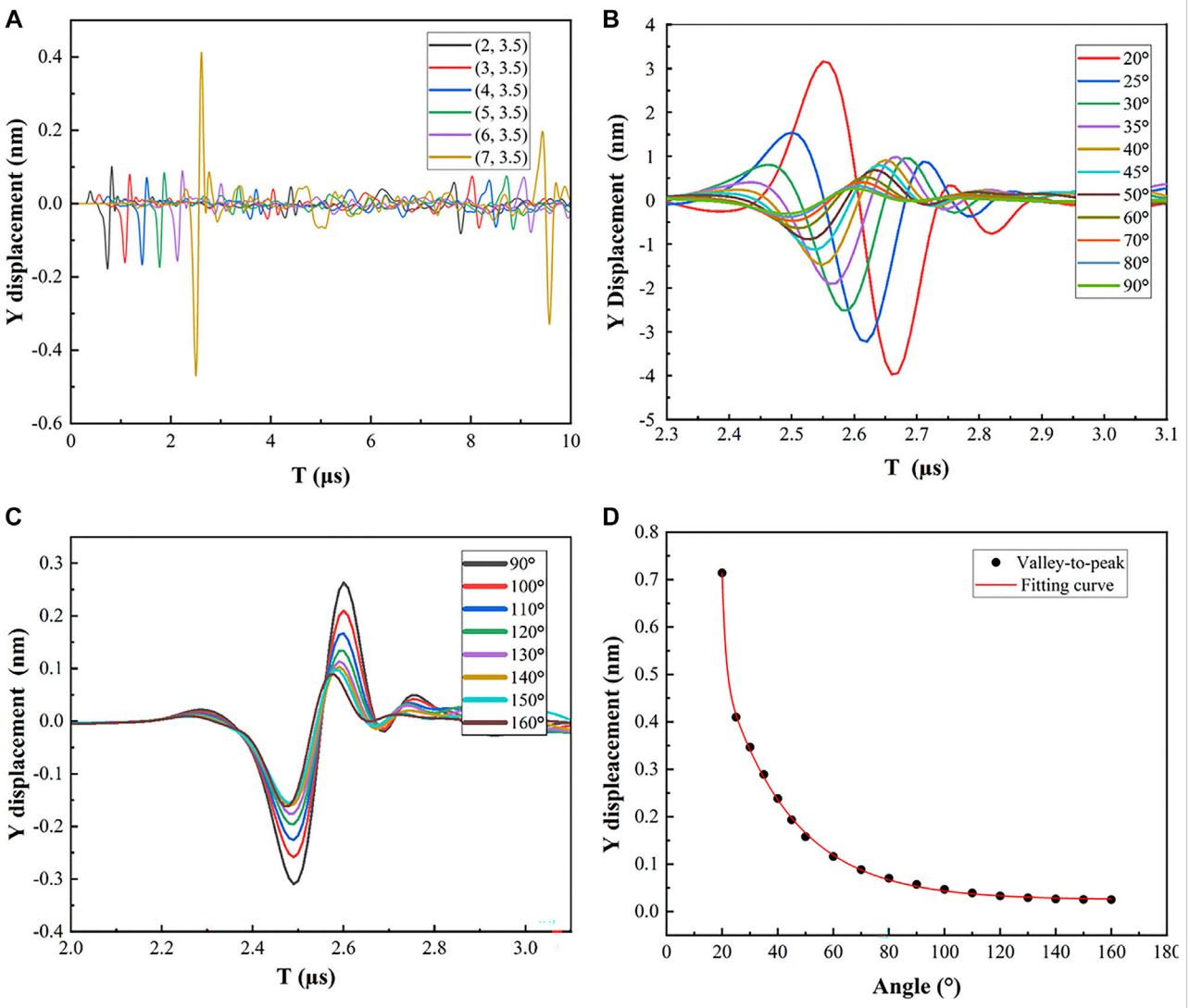

FIGURE 8
Y displacement and Fitting curve: **(A)** Y displacement components detected by different detection points at 70°; **(B)** Displacement of cracks with inclination angles from 20° to 90°; **(C)** Displacement of cracks with inclination angles from 90° to 160°; **(D)** Peak-valley displacement difference.

TABLE 3 Peak-peak vlaue of different ratios.

Angle	Peak-peak-displacement (nm)					
	D/λ = 0.11	D/λ = 0.34	D/λ = 0.56	D/λ = 0.79	D/λ = 1.01	D/λ = 1.11
30°	2.60	3.47	3.91	4.16	4.16	4.22
45°	1.44	1.93	1.97	1.87	1.77	1.78
60°	0.82	1.16	1.13	1.07	0.99	0.97
90°	0.44	0.57	0.56	0.57	0.59	0.58
120°	0.32	0.33	0.32	0.33	0.33	0.33
150°	0.26	0.25	0.26	0.26	0.26	0.26

correlation between the surface angle crack and Y displacement is obtained by fitting the curve, proving that it is a feasible analysis method.

3.2.2 Depth detection

By fixing the angle and width of the crack, the depth of the crack was increased from 0.1 to 0.6 mm. The identification of crack depth was discussed in the case that the detection point and excitation point are on the same side and opposite side. The change of crack depth will cause the change of D/λ ratio, so the depth detection will include a variety of ratios.

The detection point and the excitation point were (7, 3.5) and (0, 3.5), which constituted the excitation detection on the same side of the crack. The Y displacement component based on the detection point is shown in Figure 9A. The portion of the displacement from 2.40 to 2.58 μs was RW. The Y displacement from 4.5 to 5.5 μs indicates TRW-B. When TRW-B returns to the detection site, there is a time delay, and the Y displacement gradually decreases. It can be concluded that the deeper the depth is, the longer the propagation path along the crack. Most Rayleigh waves change into body waves, resulting in a decrease in the amplitude of TRW-B, which is more obvious with the increase of crack depth.

The maximum Y displacement of TRW-B and the peak-peak displacement of RW were fit to estimate the crack depth. The fitting result was shown in Figure 9B. The RW does not exhibit a monotonous change with increasing depth: it increases and then decreases slightly. The Y displacement decreases from −0.903 to −5.571 nm for TRW-B as the crack depth increases from 0.1 to 0.6 mm, which shows a negative correlation between displacement and crack depth. The expression of the TRW-B and RW fitting curve is:

$$Y_1 = -0.063264 + 0.185148 \times exp\left(\frac{-D}{0.51517}\right) \quad (10-1)$$

$$Y_2 = 0.1373 + 7.02 \times D - 24.09 \times D^2 + 35.7 \times D^3 - 19.7 \times D^4 \quad (10-2)$$

where Y_1 is the maximum Y displacement of TRW-B, Y_2 is the peak-peak displacement of RW, D is the depth of crack. The MSE of the fitting curves are 1.392×10^{-12} (Y_1) and 1.221×10^{-11} (Y_2), the fitting regression coefficient R^2 is 99.853% and 99.889%. The maximum error of TRW-B's fitting data is 2.42% and that of RW is 0.38%. Therefore, TRW-B and RW is suitable for defect depth identification. And the higher the fitting correlation coefficient, the more accurate the fitting result.

To place the excitation and detection sites on both sides of the crack, point (8, 3.5) was chosen as the detection point. As the RW goes through the crack, the depth feature information will be included in the waveform. Detecting the Y displacement of TRW or TRW-B on the right side of the crack can provide the necessary information. Figure 10A shows the Y displacement components of the detection points at different times. TRW is the figure from 0.25 to 0.32 μs, and TRW-B is the figure from 0.39 to 0.45 μs TRW and TRW-B are two waveforms of transmitted waves that occur at distinct times. When stress propagates to the right boundary, the propagation direction is reversed, and the original negative stress becomes positive. The stress-related Y displacement is changed from a negative to a positive value, revealing a difference in displacement between the two waveforms.

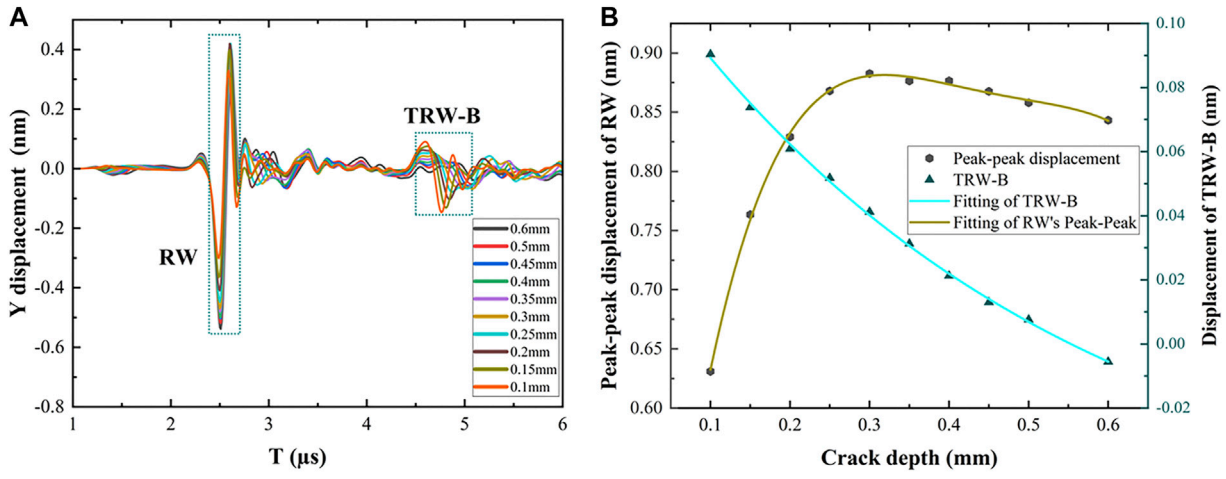

FIGURE 9
Y displacement and Fitting curves: **(A)** Y displacement of different depths on the same side; **(B)** Fitting curves of TRW-B (bule) and RW's Peak-peak (brown).

These two waveforms were fitted into the same graph, as shown in Figure 10B. TRW's displacement value increases from −0.1128 to −0.0328 nm when the crack grows from 0.1 to 0.6 mm, while TRW-B's displacement value drops from 0.0826 to 0.0333 nm. The trend of these two waves is symmetrical, but there is a tiny difference in displacement because the stress is somewhat lost due to the resistance during propagation. Here are the two fitting expression:

$$Y_3 = 0.0319678 + 0.0922522 \times 0.00267^D \quad (11-1)$$

$$Y_4 = -0.0340272 - 0.178835 \times 0.000317^D \quad (11-2)$$

where Y_3 is the extreme value of the Y displacement of TRW-B, and Y_4 is Y displacement of TRW. The fitting curves were convergent, TRW-B with better fitting effect was introduced. Its MSE is 1.03764×10^{-12}, and the fitting regression coefficient R^2 is 99.591%. The maximum fitting error is 2.7% at a depth of 0.3 mm. TRW-B's displacement is negatively associated with depth as it increases. The measured Y displacement and fitting the expression can yield the specific defect depth, demonstrating that the depth can be quantitatively detected by fitting the curve. TRW-B is therefore convenient for determining the quantitative depth of cracks on either the same or the opposite side. At the same time, it is also suitable for the D/λ range of 0.11 to 0.67 (depth of 0.1 to 0.6 mm).

3.2.3 Width detection

The angle and depth of the crack were fixed, and the width was increased from 0.1 to 0.6 mm. The identification analysis of the width is still in the same and opposite cases. The ratio of defect depth to Rayleigh wavelength remained 0.34.

Point (6, 3.5) was taken as the detection point to keep the excitation and detection points on the crack's left side. If the angle and depth of the crack remain unchanged, the structure impeding the propagation of RW will remain unchanged. With the increase in the crack width, the component of the RW converted to transmitted waves will be larger than the component converted to CRW. The Y displacement components at different times are shown in Figure 11A. The waveform at 3 μs is a direct CRW. The waveform at 5 μs is the right CRW, which is reflected by the boundary. To distinguish these two waveforms, they were called CRW-L and CRW-R, respectively. The Y displacement figure from 4.8 to 5.1 μs was magnified to make the relationship between CRW-R and width easier to see. Since the CRW-R wave will pass through the crack twice, the maximum Y displacement of the wave is selected for fitting, whose fitting result is shown in Figure 11B. The expression of the fitting straight line is:

$$Y_5 = 0.0237416 - 0.0198169 \times W \quad (12)$$

where Y_5 is the Y displacement corresponding to CRW-R and W is the crack width. The fitting regression coefficient R^2 is 99.149%. The residual sum of squares is 5.0562×10^{-13}. When the crack width is 0.2 mm, the simulated value is 1.93936×10^{-2} nm, and the fitted value is 1.977822×10^{-2} nm, which is the farthest point from the fitted straight line with an error of 1.98%. CRW-R is linearly and negatively linked with crack width, according to the fit results. This negative correlation also exists at other inspection points on the left side of the defect.

The detection point was (8, 3.5) to keep excitation and detection points on both sides of the crack. The Y displacement components of (8, 3.5) at different times are shown in Figure 12A. The waveform of 2.5–3.0 μs in the figure corresponds to TRW, and the waveform of 4.0–4.5 μs corresponds to TRW-B.

The extreme displacement values of TRW and TRW-B are still selected for fitting, as shown in Figure 12B. The displacement of TRW increases

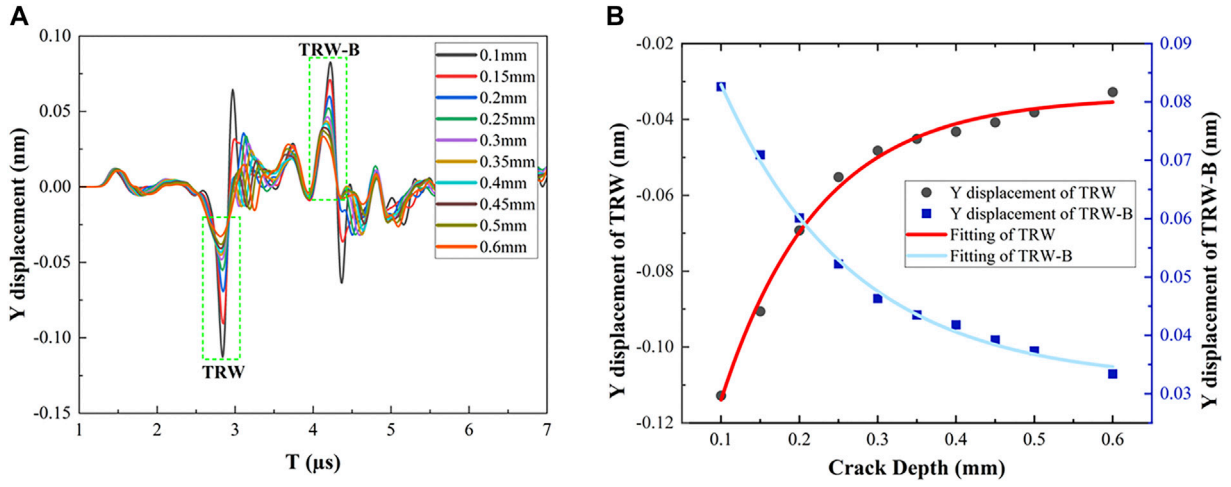

FIGURE 10
Y displacement and Fitting curves: **(A)** Different depths on the opposite side; **(B)** Fitting curves for TRW (red) and TRW-B (blue).

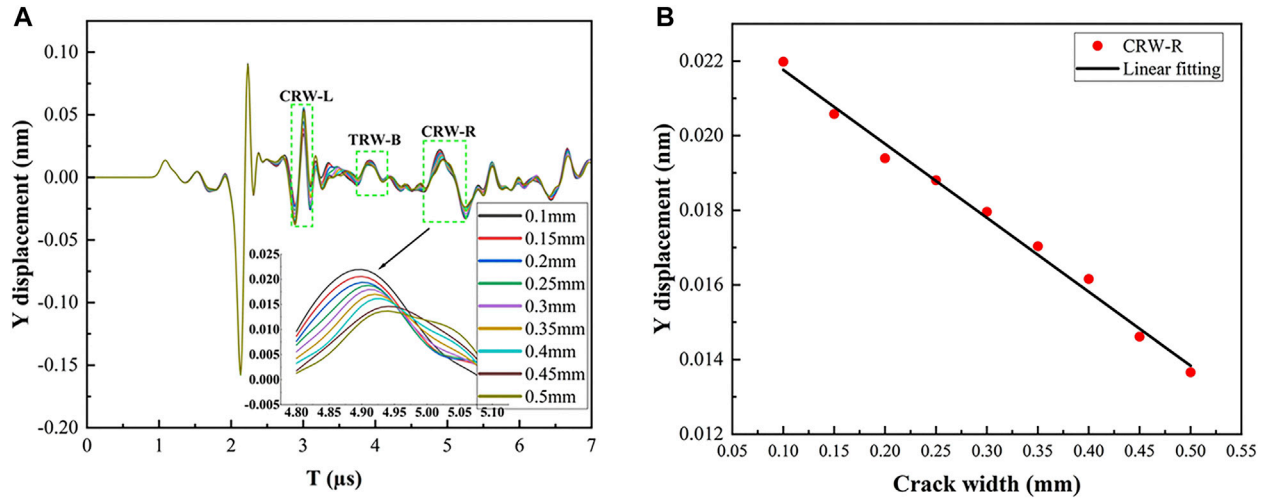

FIGURE 11
Y displacement and Fitting curve: **(A)** Different widths on the same side; **(B)** Fitting curve of CRW-R.

from −0.0631 to −0.0369 nm as the crack width grows, indicating a positive correlation between displacement and width. TRW-B's displacement falls from 0.0559 to 0.0413 nm, indicating a negative correlation.

$$Y_6 = -0.0740181 \times \exp\left(\frac{-W}{0.74738}\right) + 0.00134864 \quad (13-1)$$

$$Y_7 = 0.0280565 \times \exp\left(\frac{-W}{0.032585}\right) + 0.0354521 \quad (13-2)$$

where Y_6 is the min Y displacement of the TRW and W is the width of the crack. Y_7 is the TRW-B. TRW with better fitting effect was introduced here. The fitting curve's fitting regression coefficient R^2 is 99.846%. MSE is 1.30148×10^{-13}. The maximum fitting error is 1.18% at a width of 0.4 mm. The essential crack width information can be obtained by detecting the TRW's Y displacement extremes and substituting the calculation, which also proves that TRW can quantitatively identify the width while the D/λ is 0.34.

4 Discussion

Most researchers rely on expensive scanning equipment and interferometers to analyze defects in metals. Their method is effective, but it is also costly, which is one of the reasons why laser

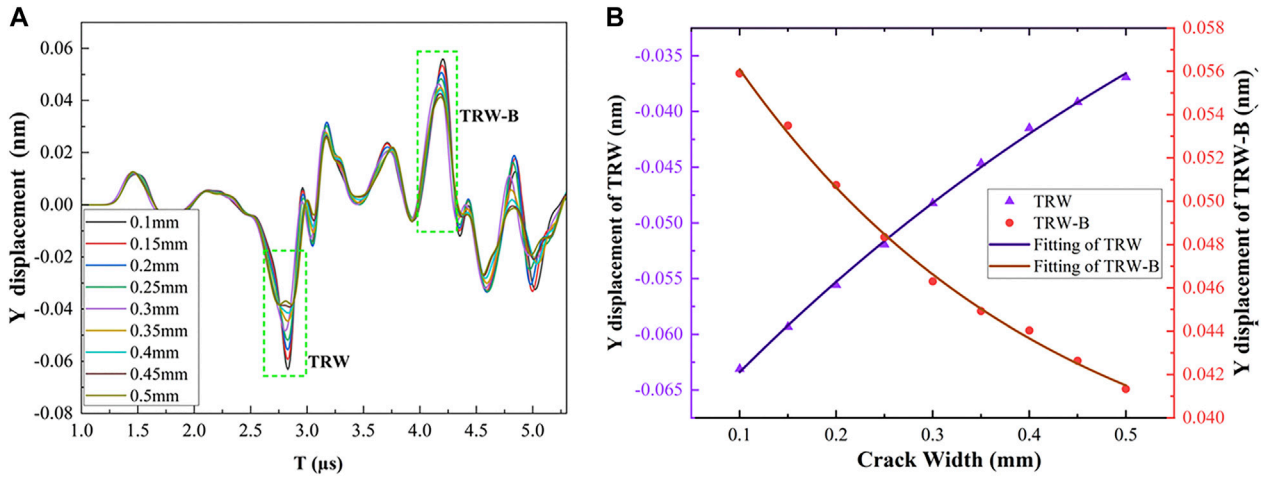

FIGURE 12
Y displacement and Fitting curves: **(A)** Different widths on the opposite side; **(B)** Fitting curve of TRW (purple) and TRW-B (red).

ultrasonic inspection has not yet reached the industrial scale. In the past, researchers have often used frequency spectrum or correlation transmission or reflection coefficients to qualitatively analyze the defects on metal surfaces without quantitative analysis. This paper proposed a simpler method to quantitatively detect surface angled defects.

This method aims at the mode transformation and the related waveform displacement signal change during the propagation of ultrasonic waves for the angled cracks, which has good applicability. Not only did the approach of fitting different waveform displacements complete the angle detection, but it also accomplished the depth and width detection. As a result, this method can be used to quantitatively characterize metal surface defects and the maximum error between fitting and simulation is only 2.7%. The advantage of this method is that a certain defect-displacement fitting expression can be obtained according to the relationship between the measured ultrasonic displacement and the defect. According to these fitting expressions, the defect information can be obtained from the measured displacement in the subsequent measurement, reducing a certain amount of work, and all the data are carried out in the time domain. The method could be confirmed with a low-cost transducer and lead to the use of laser ultrasound as a simple industrial detection approach.

In the simulation model, parameters such as 0.7 mJ, 10 ns, and 0.4 mm were chosen to match the laser equipment used in later studies. The physical structure of the model was isotropic material and was analyzed using the a-scan results. The research will be more inclined to detect multilayer materials or composites in future experiments and investigations.

5 Conclusion

In this paper, the finite element model is used to simulate the process of laser ultrasonic testing. The effects of time function, laser pulse width and spot radius on the excitation ultrasound signals were investigated. Different time functions have a considerable impact on the power spectrum density, according to the simulation results. The narrower the pulse width and the smaller the spot radius, the more efficient it is to excite the ultrasound signals, and this trend is more pronounced for small pulse width or radius parameters. Different Rayleigh wave modes can be useful in detecting surface-angled cracks. The peak-to-valley difference of the Y displacement component of the RW is related to the angle of the crack. When the excitation and detection points are on the same side of the crack, the width and depth of the crack can be quantified by fitting the Y displacement of the CRW. The maximum error of the fit is 1.98% for defect feature values within 0.5 mm. When the excitation and detection points are on the opposite side, the extreme value of the Y displacement of TRW or TRW-B is related to the depth and width of the crack, whose max error of the fitting curve is 2.7%.

This paper provides a feasible method for quantitative crack analysis. The method has the potential to reduce detection analysis time and could facilitate the application of laser ultrasound detection.

Data availability statement

The raw data supporting the conclusions of this article will be made available by the authors, without undue reservation.

Author contributions

Conceptualization, SH and YL; methodology, YL; software, SH; validation, LX, QH, and JD; formal analysis, SH; investigation, YW; resources, ZL; data curation, SH; writing—original draft preparation, SH; writing—review and editing, SH; visualization, YL; supervision, YL; project administration, YL; funding acquisition, YL. All authors have read and agreed to the published version of the manuscript.

Funding

This research was funded in part by National Natural Science Foundation of China (61905062); in part by China Postdoctoral Science Foundation (2020M670613); and in part by Hebei Postdoctoral Scholarship Project (B2020003026).

Conflict of interest

The authors declare that the research was conducted in the absence of any commercial or financial relationships that could be construed as a potential conflict of interest.

Publisher's note

References

1. Zhang J, Zhao X, Yang B, Li J, Liu Y, Ma G, et al. Nondestructive evaluation of porosity in additive manufacturing by laser ultrasonic surface wave. *Measurement* (2022) 193:110944. doi:10.1016/j.measurement.2022.110944

2. Gupta R, Mitchell D, Blanche J, Harper S, Tang W, Pancholi K, et al. A review of sensing technologies for non-destructive evaluation of structural composite materials. *J Compos Sci* (2021) 5(12):319. doi:10.3390/jcs5120319

3. Vyas J, Kažys RJ. A review on nondestructive techniques and characteristics of composite materials for the aerospace system. In: MATEC web of conferences: 8th EASN-CEAS international workshop on manufacturing for growth & innovation; September 4-7, 2018; Glasgow, UK. Scotland, UK: EDP Sciences (2018).

4. Zhenwei Z, Jing X, Rui J, Yinghong W, Hao G, Siyi H, et al. Terahertz non-destructive testing and imaging of high-voltage cables. *Front Phys* (2022) 10:893145. doi:10.3389/fphy.2022.893145

5. Bai Z, Zhang Z, Wang K, Gao J, Zhang Z, Yang X, et al. Comprehensive thermal analysis of diamond in a high-power Raman cavity based on fvm-fem coupled method. *Nanomaterials* (2021) 11(6):1572. doi:10.3390/nano11061572

6. Chen H, Bai Z, Yang X, Ding J, Qi Y, Yan B, et al. Enhanced stimulated brillouin scattering utilizing Raman conversion in diamond. *Appl Phys Lett* (2022) 120(18): 181103. doi:10.1063/5.0087092

7. Davis G, Nagarajah R, Palanisamy S, Rashid RAR, Rajagopal P, Balasubramaniam K. Laser ultrasonic inspection of additive manufactured components. *Int J Adv Manuf Technol* (2019) 102(5):2571–9. doi:10.1007/s00170-018-3046-y

8. Werr F, Eppelt U, Müllers L, Ligny D. Ultra-short-pulse laser filaments for float glass cutting: Influence of laser parameters on micro cracks formation. *Front Phys* (2022) 10:862419. doi:10.3389/fphy.2022.862419

9. Nomura K, Deno S, Matsuida T, Otaki S, Asai S. *In situ* measurement of ultrasonic behavior during lap spot welding with laser ultrasonic method. *NDT E Int* (2022) 130:102662. doi:10.1016/j.ndteint.2022.102662

10. Keyvani M, Garcin T, Militzer M, Fabregue D. Laser ultrasonic measurement of recrystallization and grain growth in an L605 cobalt superalloy. *Mater Characterization* (2020) 167:110465. doi:10.1016/j.matchar.2020.110465

11. Selim H, Delgado-Prieto M, Trull J, Picó R, Romeral L, Cojocaru C. Defect reconstruction by non-destructive testing with laser induced ultrasonic detection. *Ultrasonics* (2020) 101:106000. doi:10.1016/j.ultras.2019.106000

12. Choe J, Jon S, Ryang W, Yun Y, So J. Research of laser ultrasonic defect statistics recognition technology based on radial basis function neural network. *Opt Laser Technol* (2022) 150:107857. doi:10.1016/j.optlastec.2022.107857

13. Kusano M, Hatano H, Watanabe M, Takekawa S, Yamawaki H, Oguchi K, et al. Mid-infrared pulsed laser ultrasonic testing for carbon fiber reinforced plastics. *Ultrasonics* (2018) 84:310–8. doi:10.1016/j.ultras.2017.11.015

14. Jiang Y, Wang H, Chen S, Tian G. Visual quantitative detection of rail surface crack based on laser ultrasonic technology. *Optik* (2021) 237:166732. doi:10.1016/j.ijleo.2021.166732

15. Klose J, Esch S, Kohns P, Ankerhold G. Assessment of the intrinsic damage to refractory materials at high temperatures using the laser ultrasonic pulse method. *Open Ceramics* (2022) 9:100221. doi:10.1016/j.oceram.2022.100221

16. Yi K, Liu P, Park S-H, Sohn H. Femtosecond laser ultrasonic inspection of a moving object and its application to estimation of silicon wafer coating thickness. *Opt Lasers Eng* (2022) 148:106778. doi:10.1016/j.optlaseng.2021.106778

17. Guo H, Zheng B, Liu H. Numerical simulation and experimental research on interaction of micro-defects and laser ultrasonic signal. *Opt Laser Technol* (2017) 96:58–64. doi:10.1016/j.optlastec.2017.04.004

18. Arias I, Achenbach JD. Thermoelastic generation of ultrasound by line-focused laser irradiation. *Int J Sol Structures* (2003) 40(25):6917–35. doi:10.1016/S0020-7683(03)00345-7

19. Xu B, Shen Z, Ni X, Lu J. Numerical simulation of laser-generated ultrasound by the finite element method. *J Appl Phys* (2004) 95(4):2116–22. doi:10.1063/1.1637712

20. Wang J, Shen Z, Xu B, Ni X, Guan J, Lu J. Numerical simulation of laser-generated ultrasound in non-metallic material by the finite element method. *Opt Laser Technol* (2007) 39(4):806–13. doi:10.1016/j.optlastec.2006.01.009

21. Guan J. Numerical simulation of ultrasonic guide waves generated by pulsed laser line source in thermoelastic regime. *J Nanjing Univ Posts Telecommunications (Natural Science)* (2011) 31(3):108–13. doi:10.14132/j.cnki.1673-5439.2011.03.002

22. Rajagopal S, Cox BT. Modelling laser ultrasound waveforms: The effect of varying pulse duration and material properties. *J Acoust Soc Am* (2021) 149(3): 2040–54. doi:10.1121/10.0003558

23. Cavuto A, Martarelli M, Pandarese G, Revel GM, Tomasini EP. Fem based design of experiment for train wheelset diagnostics by laser ultrasonics. *Ultrasonics* (2021) 113:106368. doi:10.1016/j.ultras.2021.106368

24. Bustamante L, Jeyaprakash N, Yang C-H. Hybrid laser and air-coupled ultrasonic defect detection of aluminium and cfrp plates by means of Lamb mode. *Results Phys* (2020) 19:103438. doi:10.1016/j.rinp.2020.103438

25. Dutton B, Clough AR, Rosli MH, Edwards RS. Non-contact ultrasonic detection of angled surface defects. *NDT E Int* (2011) 44(4):353–60. doi:10.1016/j.ndteint.2011.02.001

26. Zhang Z, Zhao J, Pan Y. Surface circular-arc defects interacted by laser-generated Rayleigh wave. *Ultrasonics* (2020) 103:106085. doi:10.1016/j.ultras.2020.106085

27. Zeng W, Qi S, Liu L, Yao Y. Research on laser-generated Rayleigh waves with angled surface crack by finite element method. *Optik* (2019) 181:57–62. doi:10.1016/j.ijleo.2018.11.105

28. Zhou Z, Zhang K, Zhou J, Sun G, Wang J. Application of laser ultrasonic technique for non-contact detection of structural surface-breaking cracks. *Opt Laser Technol* (2015) 73:173–8. doi:10.1016/j.optlastec.2015.04.026

29. Wang Y, Han S, Yu Y, Qi X, Zhang Y, Lian Y, et al. Numerical simulation of metal defect detection based on laser ultrasound. *IEEE Photon J* (2021) 13(4):1–9. doi:10.1109/JPHOT.2021.3097997

30. Park S-H, Liu P, Yi K, Choi G, Jhang K-Y, Sohn H. Mechanical properties estimation of additively manufactured metal components using femtosecond laser ultrasonics and laser polishing. *Int J Machine Tools Manufacture* (2021) 166:103745. doi:10.1016/j.ijmachtools.2021.103745

31. Liu P, Nazirah AW, Sohn H. Numerical simulation of damage detection using laser-generated ultrasound. *Ultrasonics* (2016) 69:248–58. doi:10.1016/j.ultras.2016.03.013

32. Dai Y, Xu BQ, Luo Y, Li H, Xu GD. Finite element modeling of the interaction of laser-generated ultrasound with a surface-breaking notch in an elastic plate. *Opt Laser Technol* (2010) 42(4):693–7. doi:10.1016/j.optlastec.2009.11.012

33. Zeng W, Yao Y, Qi S, Liu L. Finite element simulation of laser-generated surface acoustic wave for identification of subsurface defects. *Optik* (2020) 2019: 163812. doi:10.1016/j.ijleo.2019.163812

34. Ji B, Zhang Q, Cao J, Li H, Zhang B. Non-contact detection of delamination in stainless steel/carbon steel composites with laser ultrasonic. *Optik* (2021) 226:165893. doi:10.1016/j.ijleo.2020.165893

frontiers | Frontiers in Physics

TYPE Original Research
PUBLISHED 30 August 2022
DOI 10.3389/fphy.2022.993297

OPEN ACCESS

EDITED BY
Baitao Zhang,
Shandong University, China

REVIEWED BY
Xiaofei Yang,
Shanghai Institute of Optics and Fine Mechanics (CAS), China
Jinbao Xia,
Shandong University, China

*CORRESPONDENCE
Yajun Pang,
yjpang@hebut.edu.cn

SPECIALTY SECTION
This article was submitted to Optics and Photonics,
a section of the journal
Frontiers in Physics

RECEIVED 13 July 2022
ACCEPTED 10 August 2022
PUBLISHED 30 August 2022

CITATION
Miao R, Liu X, Pang Y and Lang L (2022), Design of a mobile 3D imaging system based on 2D LIDAR and calibration with levenberg–marquardt optimization algorithm.
Front. Phys. 10:993297.
doi: 10.3389/fphy.2022.993297

Design of a mobile 3D imaging system based on 2D LIDAR and calibration with levenberg–marquardt optimization algorithm

Ruikai Miao[1,2], Xinyue Liu[1,2], Yajun Pang[1,2]* and Liying Lang[1,2]

[1]Center for Advanced Laser Technology, Hebei University of Technology, Tianjin, China, [2]Hebei Key Laboratory of Advanced Laser Technology and Equipment, Tianjin, China

LIDAR is an excellent means to obtain the information of buildings, forests, bridges, tunnels and many other big scenes, but the high price of 3D LIDAR currently limits its further application. To meet this challenge a mobile 3D imaging system based on 2D LIDAR is proposed. The system has the characteristics of large imaging range and low cost. The composition and implementation principle of each module of the system are introduced in detail and a calibration method for the 3-axis assembly error is proposed. In this method Levenberg-Marquardt (LM) optimization algorithm is used to obtain the optimal value of the 2D LIDAR 3-axis attitude angle, which is used to compensate for the point cloud distortion caused by the assembly error. The experimental results show that the proposed method can effectively reduce the point cloud distortion caused by assembly error. This system can meet the application demand of big scenes 3D imaging.

KEYWORDS

lidar, 3D imaging, point cloud, calibration, mobile

Introduction

3D imaging technology can accurately obtain environmental digital information, and is also the key to realize the "digital twin" technology [1]. Indoor buildings such as rooms and tunnels are essential parts of human life, and these environments have rich structural features. 3D reconstruction of the interior of such buildings can achieve geometric parameter measurement, facilitate monitoring and evaluation of static and dynamic assets to achieve optimal decision-making, such as providing environmental data support for VR, AR and mobile robot navigation.

As a kind of high-precision active detection technology with high resolution and strong anti-interference capability, LIDAR [2] has received wide attention from researchers, which is widely used in autonomous driving [3], remote sensing [4] and 3D reconstruction [5]. 3D LIDAR is certainly capable of 3D detection, but the current high price leads to its poor cost-performance radio in some specific applications. While

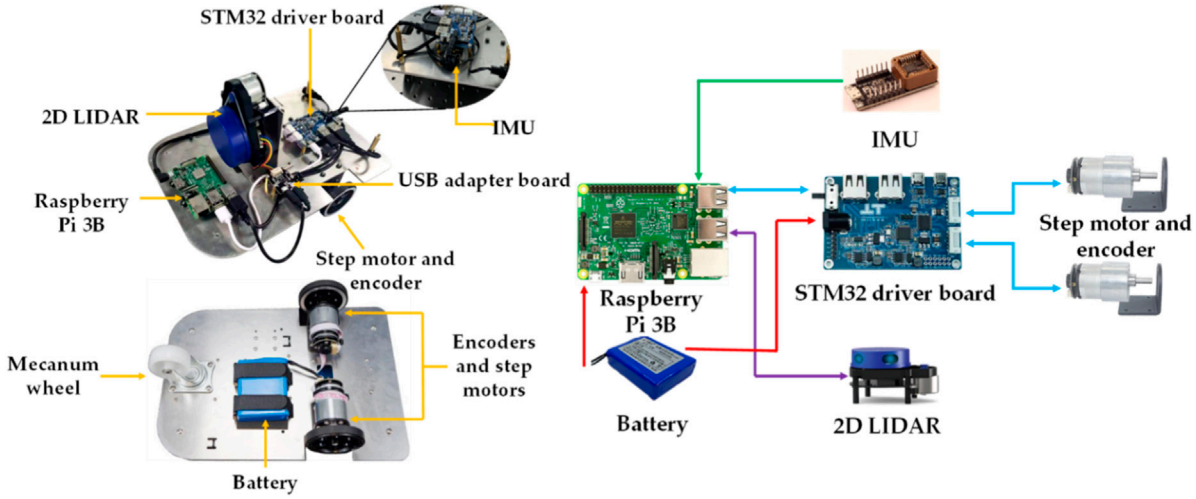

FIGURE 1
Hardware and software structure of the 3D imaging system.

2D LIDAR [6] is inexpensive and has achieved more mature commercialization, it is widely used in simultaneous localization and mapping (SLAM) [7] for mobile robots. Compared to 3D LIDAR, 2D LIDAR has higher cost-performance and a more flexible field of view [8], but it can only obtain 2D plane information. If 3D information can be obtained by combining another dimension movement of 2D LIDAR, such a scheme will be more competitive.

At present, the widely used method is to combine 2D LIDAR with a rotating device [9, 10] such as a Pan-Tilt Unit to achieve low-cost 3D scanning of the environment by supplementing the third dimension with rotational scanning of the device. Although such solutions can achieve 3D scanning of the environment, these solutions have the disadvantage of poor detection range. Considering that the actual working environment may be complex or narrow scenes (e.g., offices and hallways), there may also be some obstacles and other objects in the environment. Thus there will be problems such as occlusion, resulting in partial absence of the point cloud, making it difficult to achieve a complete image of the environment in one scan. The device must be moved at multiple locations for multiple scans. The complete point cloud can only be formed after registration at a later stage. So we can see that such operation is complicated, inefficient and may generates registration errors.

Two key points [11] need to be solved in the scheme using 2D LIDAR as the core sensor: one is to reduce the point cloud distortion due to the assembly error [12], and the other is to carry out accurate motion estimation of the device during scanning. Inaccurate motion estimation and assembly errors of the attitude angle will lead to significant point cloud deformation, resulting in global point cloud images unusable.

In view of the characteristics and shortcomings of the above methods, a low-cost 3D imaging system based on 2D LIDAR is proposed in this paper. The 2D LIDAR is mounted vertically on the mobile platform. The scanning plane of the 2D LIDAR is perpendicular to the horizontal plane, and the range data of the vertically mounted 2D LIDAR is combined with the movement data of the mobile platform. When the scanning plane sweeps across a volume in space, the 3D scene information is obtained. This solution overcomes the scanning range of the fixed device and is capable of large-scale scanning task. In this paper, we propose the composition of each module of the system, the implementation principle, and the calibration method for the 3-axis attitude angle. Various experiments are performed to test the superior performance of the system. The experiment results show that point cloud distortion caused by the assembly error of the system is significantly improved and can be used in the measurement of regions and in the complete scene reconstruction.

The remainder of this paper is organized as follows: the components and parameters of the 3D imaging system are described in Section 2, the working principle of the system including the transformation relations between coordinate systems, and the mathematical model for motion estimation, are described in Section 3, Section 4 focuses on the calibration method of the 3-axis attitude angle and revises the complete coordinate generation formula after calibration, Section 5 presents our experimental validation in different scenes to verify the excellent performance of our system. Finally, the summary of our work is outlined in Section 6.

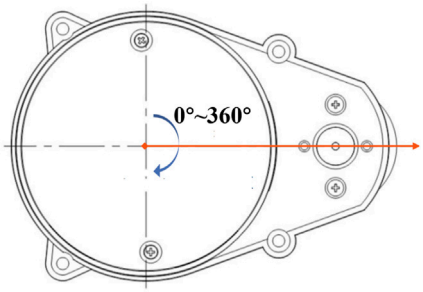

FIGURE 2
The definition of the scanning angle.

System overview

Hardware system

The whole hardware structure of the system is shown in Figure 1. The hardware consists of 2D LIDAR, step motors, IMU, STM32 driver board, Raspberry Pi 3B and power supply. The 2D LIDAR is installed vertically on the center of the mobile platform. The step motors are controlled by STM32 driver board The speed of step motors is read by its optical encoder. The speed is used to achieve wheel odometer. 2D LIDAR, step motors, IMU obtain 2D point cloud, speed and attitude angle respectively. The obtained information is transmitted to Raspberry Pi 3B, and fused to generate the whole 3D point cloud by multi-sensor fusion algorithm.

The 2D LIDAR we use in this study is YDLIDAR X4, this sensor is based on the laser triangulation principle. The built-in rotating module drives the ranging module to rotate 360° to achieve 360° rotational scan, then the sampled laser points information of the ranging distance and its scanning angle can be obtained. The definition of the scanning angle is shown in Figure 2. The scanning angle is the angle between the laser measurement optical path and the vertical direction. The specific parameters are shown in Table 1. It has high cost-performance and can meet the performance requirements of general indoor applications. The IMU is HI 219, and its specific accuracy is shown in Table 2. The speed accuracy of the step motors is 1% per meter.

Software system

Our software system is based on Robot Operating System (ROS), and the software system is divided into three levels, namely, hardware driver, coordinate transformation, and multi-sensor fusion. The software architecture is shown in Figure 3.

The hardware driver is responsible for controlling and reading the range data from 2D LIDAR, pose data from IMU, and sending velocity control commands to the STM32 driver board. And the driver board controls the motor speed through PID algorithm and receives motor velocity which is transmitted back to Raspberry Pi for motion estimation of the wheel odometer. The relative position of each sensor is defined in the coordinate transformation module. And the coordinate transformation module is also responsible for fusing the pose data from IMU and the wheel odometer to complete motion estimation of the platform by Extended Kalman Filter (EKF). The data fusion module fuses the transformation matrix obtained from the motion estimation and the range data from 2D LIDAR to generate the coordinates in the world coordinate system. The complete point cloud is generated by adding up the coordinates in the world coordinate system frame by frame.

TABLE 2 The specific accuracy of HI 219.

Parameter	Roll/pitch (static)	Roll/pitch (dynamic)	Yaw
Value	0.2°–0.4°	0.5°–2.0°	0.5°

Operation principle

Coordinate system model

In this section we define the coordinate systems of multiple sensors in the system, and the coordinate systems are all in Cartesian right-handed coordinate system. The transformation relationship between the coordinate systems is elaborated.

As shown in Figure 4, we define Body as the center of motion, Laser as the coordinate system of 2D LIDAR, and Imu as the coordinate system of IMU. The coordinate system Body is used as the origin to establish the reference coordinate system. The world coordinate system is the geodetic coordinate system, which coincides with the initial position of the Body coordinate system. As shown in Figure 4, h is the distance from the origin of the 2D LIDAR coordinate system to the xOy plane of the reference coordinate system, *wheel_distance* is the distance from the center of the wheel to the center of motion, l_1 is the displacement from the center of the 2D LIDAR coordinate system to the reference coordinate system along the x-axis direction, and l_2 is the

TABLE 1 The specific parameters of YDLIDAR X4.

Parameter	Distance range	Distance accuracy	Angular resolution	Sample frequency (kHz)	Scan frequency (Hz)
Value	0.12–10 m	<1%	0.5°	5	7

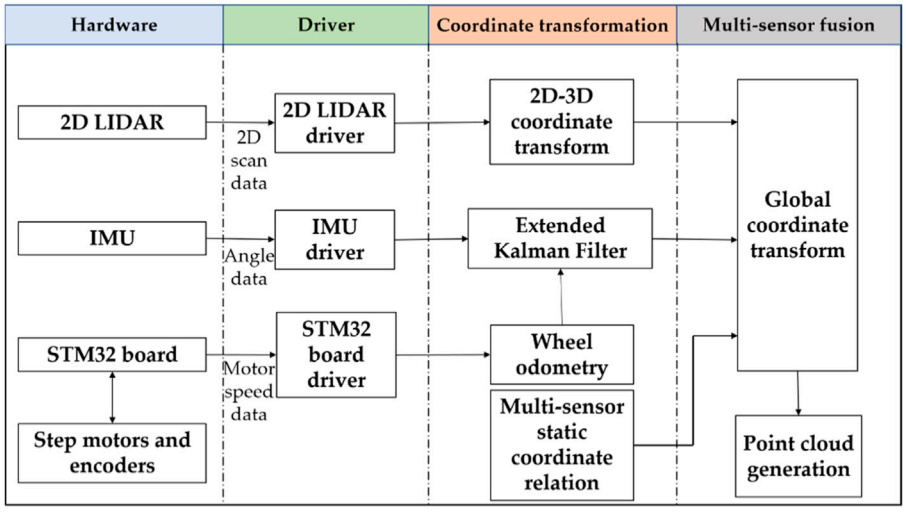

FIGURE 3
Software architecture of the 3D imaging system.

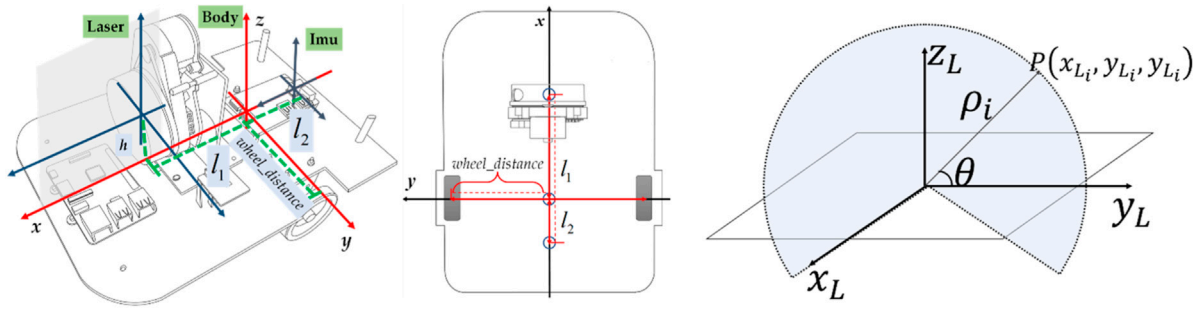

FIGURE 4
The schematic design and parameters of the 3D imaging system.

displacement from the center of the IMU coordinate system to the reference coordinate system along the x-axis direction. A 2D point in the lidar frame is obtained by converting a range measurement ρ from polar to Cartesian coordinate using the current position of the lidar rotating angle θ in Eq. 1.

$$\begin{cases} x_{L_i} = 0 \\ y_{L_i} = \rho_i \times \cos\theta_i \\ z_{L_i} = \rho_i \times \sin\theta_i \end{cases}. \tag{1}$$

Wheel odometer

The motion of the platform can be regarded as the rigid body plane motion, which can be decomposed into two kinds of motion: translation and rotation, which contains the translation in x-y direction, and the rotation around z-axis. So the motion of the platform can be decomposed into 3 degrees of freedom. When the speed of the left and right driving wheels are the same, the position of the platform changes and the heading direction remains the same, while different, the position and the heading direction both change at the same time. We use the optical encoder on the driving wheels to read the rotational speed of the left and right driving wheels. The wheel odometer model is established based on the rotational speed of the two wheels, respectively.

The velocity of the geometric center is $[v_c\ \omega]^{\mathrm{T}}$. The linear velocity v_c is positive when the heading direction is the same as the x-axis direction, and negative when opposite; the angular velocity ω is positive when the car rotates counterclockwise, and negative when opposite.

$$\begin{bmatrix} v_c \\ \omega \end{bmatrix} = \begin{bmatrix} \frac{1}{2} & \frac{1}{2} \\ \frac{1}{2 \times wheel\_distance} & -\frac{1}{2 \times wheel\_distance} \end{bmatrix} \begin{bmatrix} v_r \\ v_l \end{bmatrix} \tag{2}$$

Then we have the kinematic recurrence relation matrix

$$\begin{bmatrix} X_O(k) \\ Y_O(k) \\ \theta_O(k) \end{bmatrix} = \begin{bmatrix} X_O(k-1) \\ Y_O(k-1) \\ \theta_O(k-1) \end{bmatrix} + \begin{bmatrix} \cos\theta_O & -\sin\theta_O & 0 \\ \sin\theta_O & \cos\theta_O & 0 \\ 0 & 0 & 1 \end{bmatrix} \begin{bmatrix} dX_O \\ dY_O \\ d\theta_O \end{bmatrix} \tag{3}$$

Where $[\, X_O(k) \;\; Y_O(k) \;\; \theta_O(k) \,]^T$ is the position of the platform in the world coordinate system derived by the wheel odometer at the current moment, $[\, X_O(k-1) \;\; Y_O(k-1) \;\; \theta_O(k-1) \,]^T$ is the position of the platform in the world coordinate system derived by the wheel odometer at the previous moment, and $[\, dX_O \;\; dY_O \;\; d\theta_O \,]^T$ is the kinematic increment solved at the current moment. Where,

$$\begin{cases} dX_O = v_c dt \cos\theta_O \\ dY_O = v_c dt \sin\theta_O \\ d\theta_O = \omega dt \end{cases}. \tag{4}$$

Extended kalman filter

Since wheel slippage is inevitable, using the wheel odometer model alone for track deduction will result in errors, leading to inaccurate motion estimation. To obtain more accurate motion estimation, we use an EKF to fuse the wheel odometer and IMU.

Extended Kalman Filter is divided into two parts: prediction and update.

The complete state variables of the platform are defined as $x_k = [X_k, Y_k, \theta_k]^T$, control variables are defined as $u_k = [v, \omega]^T$. The complete state of the platform is used as the prediction model, and the wheel odometer and IMU are used as the observation model.

The equation of state of the system is defined as:

$$x_k = \left[\, X_{k-1} + v_{k-1} dt \cos\theta_{k-1} \;\; Y_{k-1} + v_{k-1} dt \sin\theta_{k-1} \;\; \theta_{k-1} + \omega_{k-1} dt \,\right]^T. \tag{5}$$

Then the system state transfer equation is defined as:

$$x_k = f(x_{k-1}, u_k) + w_{k-1}. \tag{6}$$

Where $f(x_{k-1}, u_k)$ is the state transfer matrix of the system at moment k-1.u_k is the system control input and w_{k-1} is the Gaussian noise of the system at moment k-1. z_k is the observation equation of the system

$$z_k = h(x_k) + v_k. \tag{7}$$

Where $h(x_k)$ is the observed model transfer matrix, v_k is the observed Gaussian noise.

1) Prediction. Calculate the predicted value $\hat{x}_k = f(\hat{x}_{k-1}, u_k)$ and covariance matrix $\hat{P}_k = F_{k-1} P_{k-1} F_{k-1}^T + Q_{k-1}$. Where F is the Jacobi matrix of the state transfer function and Q is the variance of the normal distribution at moment k-1.

2) Update. Calculate Kalman gain, optimal estimate and error covariance matrix:

$$K_k = P_k H_k^T \left[R_k + H_k P_k H_k^T \right]^{-1}; \tag{8}$$

$$\hat{x}_k = \hat{x}_{k-1} + K_k [z_k - h(\hat{x}_{k-1})]; \tag{9}$$

$$P_k = [I - K_k H_k] \hat{P}_k. \tag{10}$$

In this section we define the coordinate systems of multiple sensors in the system, and the coordinate systems are all in Cartesian right-handed coordinate system. The transformation relationship between the coordinate systems is elaborated.Where H_k is the Jacobi matrix of the sensor function and R_k is the variance of the normal distribution at moment k.

Extended Kalman Filter can get more accurate coordinates of the car in the world coordinate system. So the transformation matrix from the reference coordinates to world coordinates can be obtained as follows

$$A = \begin{bmatrix} \cos\theta_i & -\sin\theta_i & 0 & X_i \\ \sin\theta_i & \cos\theta_i & 0 & Y_i \\ 0 & 0 & 1 & 0 \\ 0 & 0 & 0 & 1 \end{bmatrix} \tag{11}$$

Then we can obtain the global point cloud coordinate equation.

$$P_W = A(P_L + T_1). \tag{12}$$

Calibration method and strategy

Calibration method

The quality of the point cloud depends on the accuracy of its coordinates which are obtained by the precise transformation matrix between coordinate systems [13]. Since assembly errors will inevitably exist during assembly, it is not physically possible to install the 2D LIDAR perfectly vertically. So angular deviations will inevitably occur, that is, the actual 2D LIDAR coordinate system L' may not coincide with the theoretical coordinate system L. The bias includes three rotational degrees of freedom (coordinate system rotational angle γ along the x-axis, angle β along the y-axis, angle α along the z-axis), which will result in the ideal scanning plane being different from the actual, as shown in Figure 5.

Therefore, the bias will cause the actual rotation matrix to be different from the theoretical rotation matrix, which in turn will lead

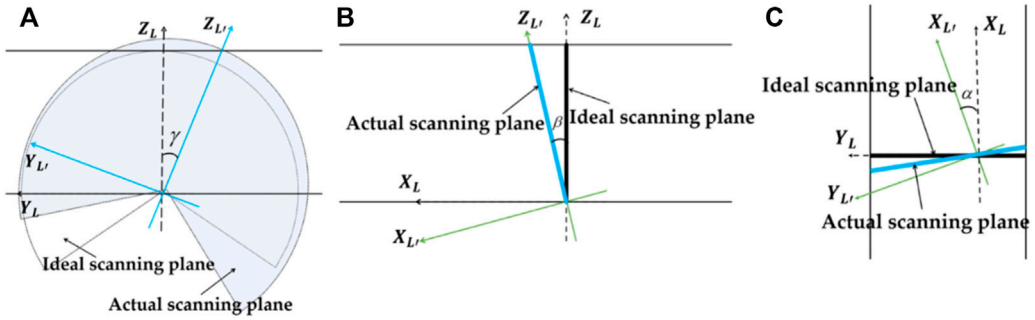

FIGURE 5
The comparison of the ideal and actual laser scanning plane due to the angular error about the three axes **(A)** *x*-axis **(B)** *y*-axis **(C)** *z*-axis.

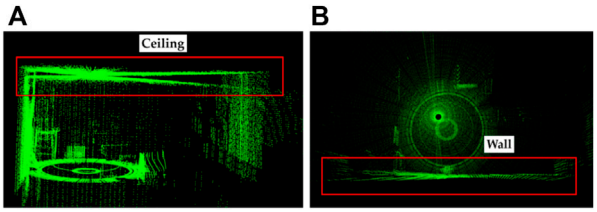

FIGURE 6
Original scan captured by our system without calibration, visible distortion is marked in red box **(A)** distortion in ceiling **(B)** distortion in wall.

to distortions in the global point cloud. When the car drives along a complete circle, the certain object will be repeatedly scanned twice and this distortion becomes a particularly noticeable ghost image, as shown in Figure 6. We can find distortion between two parts of the ceiling and the vertical wall after two scans.

Therefore, it is necessary to calibrate the three-axis attitude angle of the 2D LIDAR accurately to obtain the accurate transformation matrix between the actual and ideal coordinate systems. The traditional measurement-based methods are difficult to obtain accurate calibration results, so after the equipment is built, real point cloud need to be collected for calibration. Some calibration methods have been proposed for such problems. The methods provided in the literature [14–16] require the addition of camera and checkerboard, etc. For calibration, which is complex to operate and the added sensors may introduce more uncertainties. The method provided in the literature [17] calibrate only one angle rather than three, so the final result still has some errors. The calibration method based on planar alignment proposed in this paper is able to perform a complete calibration of the three-axis attitude angle without adding another sensor, and obtain an accurate three-axis attitude angle.

The rotation matrix of the 2D LIDAR is defined as

$$R = \begin{bmatrix} \cos\alpha\cos\beta & \cos\alpha\sin\beta\sin\gamma - \sin\alpha\cos\gamma & \cos\alpha\sin\beta\cos\gamma + \sin\alpha\sin\beta \\ \sin\alpha\cos\beta & \sin\alpha\sin\beta\sin\gamma + \cos\alpha\cos\gamma & \sin\alpha\sin\beta\cos\gamma - \cos\alpha\sin\gamma \\ -\sin\beta & \cos\beta\sin\gamma & \cos\beta\cos\gamma \end{bmatrix} \tag{13}$$

So the complete coordinate transformation is defined correctly as

$$P'_W = A(RP_L + T_1). \tag{14}$$

Calibration is carried out according to the following steps:

1) Actuate the car to drive along a circle at a constant rate;

2) Extract the calibration target and determine the corresponding points, establish the cost function;

3) Calculate the three-axis attitude angle when the cost function is minimized using the LM nonlinear optimization algorithm;

4) Adjust the transformation matrix according to the calibration results and regenerate the point cloud;

5) Fit the ceiling plane using the RANSAC algorithm and analyze the fitting effect.

The calibration target is stuck on the window so that it is convenient to extract the target plane. When the car is actuated according to the above steps, and the point cloud of the calibration target can be obtained after two scans. As the car drives along a circle at a constant rate, the calibration target is actually scanned twice, which can be used to construct two point clouds. However, the corresponding points of the two scans cannot be overlapped due to the bias of the 2D LIDAR, as shown in Figure 7.

LM Optimized Algorithm.

We define the distance between the corresponding laser points in the two point clouds as

$$d = \left\| P'_{WT}\, P'_{W2} \right\|. \tag{15}$$

Where P'_{W1} and P'_{W2} are the corresponding points of the two scans in the world coordinate system, respectively. The purpose of the calibration is to find the three-axis attitude angle of the LIDAR to make the corresponding points of the two scans coincide,

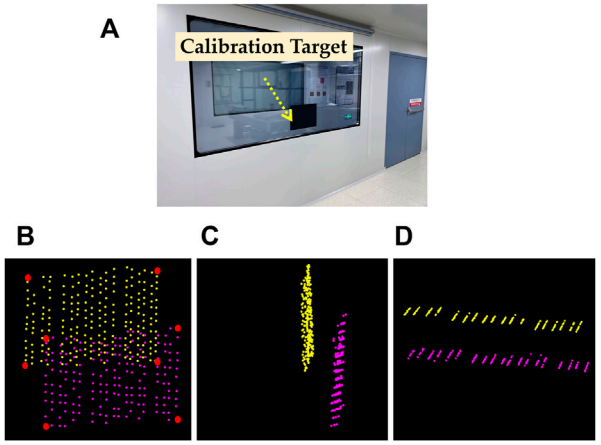

FIGURE 7
Experiment environment and different views of the point cloud obtained by two scans of the calibration target **(A)** experiment environment **(B)** front view **(C)** side view **(D)** top view.

specifically to optimize the minimum distance d between the corresponding laser points of the two point clouds, as shown in the following equation:

$$[\alpha, \beta, \gamma] = \underset{\alpha,\beta,\gamma}{argmin}\{F(\alpha, \beta, \gamma)\}. \quad (16)$$

Where the cost function is defined as

$$F(\alpha, \beta, \gamma) = \frac{1}{m}\sum_{k=1}^{m} d(k)^2 = \frac{1}{m}\sum_{k=1}^{m}\left\|P_{W1}^{'k} - P_{W2}^{'k}\right\|^2 = \frac{1}{m}\sum_{k=1}^{m}\left\|A_1^k\left(RP_{L1}^k + T_1\right) - A_2^k\left(RP_{L2}^k + T_1\right)\right\|^2 \quad (17)$$

Four corresponding edge points are selected in each scan, as shown in Figure 7B. The selected four matching pairs of points are used in Equation 17 to obtain the optimal calibration parameters. The calibration problem is a nonlinear optimization problem, and we apply the LM algorithm to solve it.

Experiments and analysis

After the establishment of system and the calibration model, we performed the calibration experiment and scanning experiment in practical indoor environment, and analyzed the measurement accuracy of the system respectively.

Calibration experiment

In the calibration experiment, we actuate the car according to the steps mentioned in Section 4, the radius of the driving circle of the center of motion is 0.83 m, and the calibration target is placed in the environment, as shown in Figure 7A. The LM algorithm is used to optimize the calibration formula, and the mean square error variation curve of the point cloud and the variation curve of the three-axis attitude angle with the number of iterations during the iteration are shown in Figure 8.

After adopting LM algorithm, the final result is $\boldsymbol{\alpha}$ = -0.0058 rad, β = 0.0126 rad, γ = 0.0355 rad. We use the calibration results into Equation 14 to reconstruct the point cloud. As shown in Figures 9A,B, the distortion of the ceiling and wall has been improved significantly. To characterize the accuracy of the calibration, we calculate the deviation and normal vector between the measured plane and the actual plane to evaluate the accuracy of our method, where the plane normal vector is obtained by plane fitting using RANSAC algorithm, and the obtained normal vector is $(-0.012, 0.011, 0.099)^T$, which is very close to $(0,0,1)^T$. As shown in Figure 9C D, the deviation comparison of calibrated and uncalibrated plane is visualized by histogram.

Similarly, we performed a comparison test in a stairwell, an environment with more structured scenes for observing the aberrations. We controlled the car to scan a specific area twice and calibrated the point cloud distortion according to the optimal value in Section 5.1. By comparing the point clouds obtained before and after calibration, we can see that the distortion of the point cloud has improved significantly. The results of the test are shown in Figure 10.

Scanning experiment

We performed a complete scan of the laboratory, tested the good performance of Extended Kalman Filter, point cloud density and measurement accuracy. The environment is a 10*5*2.5 m room, the car drives in a closed loop, moving at a speed about 0.20 m/s. The experiment scene and results are shown in Figure 11. Due to the wheel odometer's error, the trajectory is inaccurate and the loop cannot be closed. During the scanning process, some areas were scanned twice and we can see some mismatch in those areas. As shown in Figures 11C,D, we can see some details in the zoomed-in region, which shows the improvement of the EKF optimization. After the application of EKF optimization, the trajectory is more accurate, so the mismatch of the point cloud is significantly improved. As shown in Figures 11E,F, some objects in the lab can be displayed in the point cloud, but some objects cannot due to the different scattering and absorption of the laser by the object material.

We used a representation based on the average distance to represent the sparsity of the point cloud distribution. In a point cloud **C** with number of points N, $dis(p,q)$ denotes the distance between point p and any other point q, and d_p denotes the minimum distance between point p and other points, then the average distance density of the point cloud is defined as

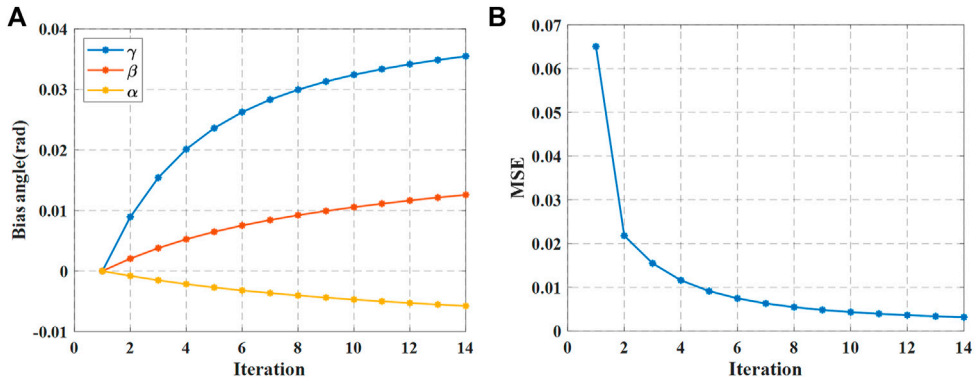

FIGURE 8
LM algorithm optimization results of calibration **(A)** optimization results of three-axis attitude Angle under different iterations **(B)** MSE of two point clouds.

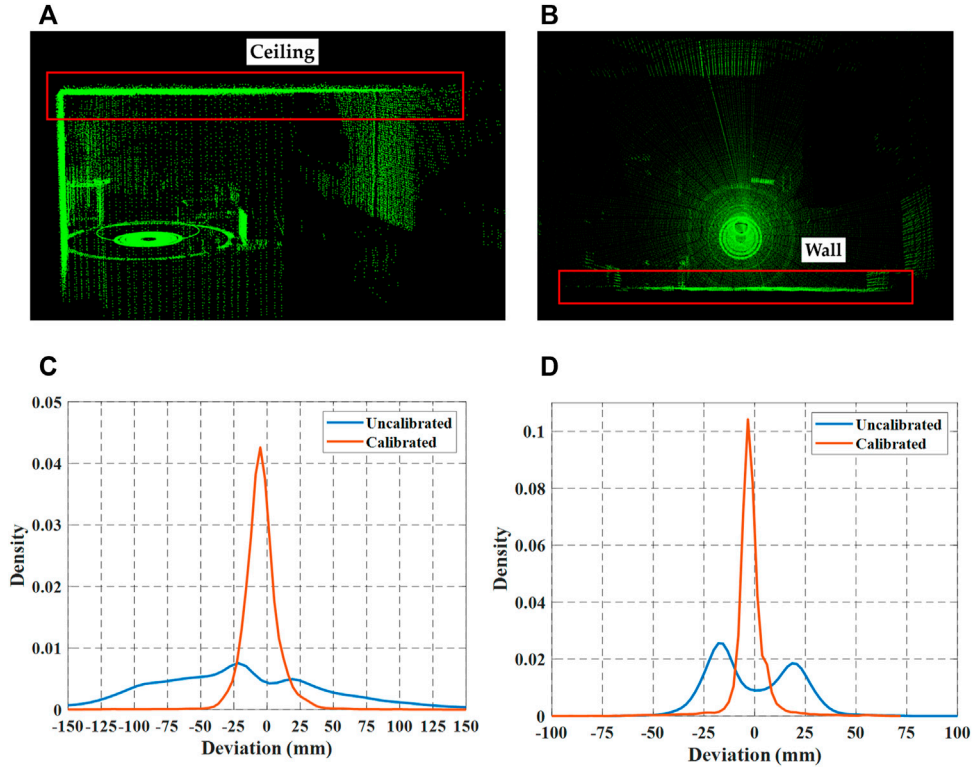

FIGURE 9
Deviation comparison of the uncalibrated plane and the calibrated plane, respectively **(A)** ceiling plane **(B)** wall plane **(C)** ceiling plane histogram **(D)** wall plane histogram.

$$\bar{d} = \frac{1}{N}\sum_{p=1}^{N} d_p. \tag{18}$$

Where

$$d_p = min\left(dis\left(p,q\right)\right), q = 1, 2, \cdots, N, p \neq q. \tag{19}$$

The smaller the $\bar{d}$, the denser the point cloud distribution, and vice versa. The obtained point cloud density $\bar{d}$ is 0.1325.

In order to evaluate the measurement accuracy of the system, we first filter the point cloud to reduce noise, and then use RANSAC algorithm to fit different wall and ceiling planes to

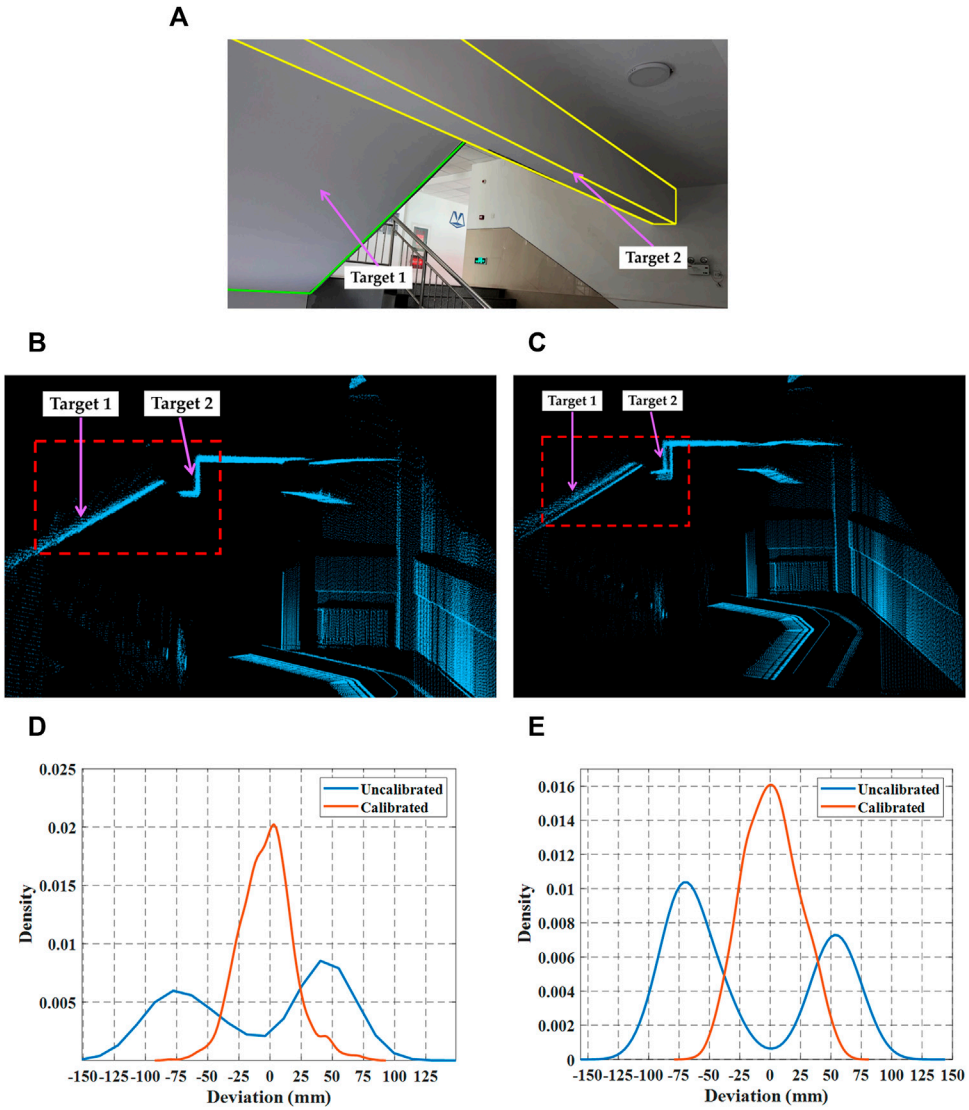

FIGURE 10
Deviation comparisons in a stairwell. The ladder plate and platform beam are used as the contrast objects, namely, Target one and Target 2 **(A)** the experiment scene: stairwell **(B)** target point cloud before calibration **(C)** target point cloud after calibration **(D)** deviation comparison of Target 1 **(E)** deviation comparison of Target 2.

obtain the plane equations of the corresponding planes, as shown in Figure 12A. The fitting results are listed in Equations 20–24. Then, we use the distance of the corresponding plane to represent the experimental value of L_1, L_2 and L_3 respectively. The statistical results are presented by boxplots, as shown in Figure 12B.

$$P_{11}: \ -1.0000x - 0.0072y + 0.0061z + 6.2418 = 0 \quad (20)$$

$$P_{12}: \ 0.9998x + 0.0189y + 0.0055z - 4.1121 = 0 \quad (21)$$

$$P_{21}: \ 0.0081x - 1.0000y + 0.0042z - 1.0315 = 0 \quad (22)$$

$$P_{22}: \ -0.0396x + 0.9992y + 0.0049z + 4.9593 = 0 \quad (23)$$

$$P_3: \ 3.1652e - 4x + 0.0018y - 1.0000z + 2.3575 = 0 \quad (24)$$

The comparison of experimental and actual value is shown in Table 3. From the results, we can see that the accuracy of the system is acceptable.

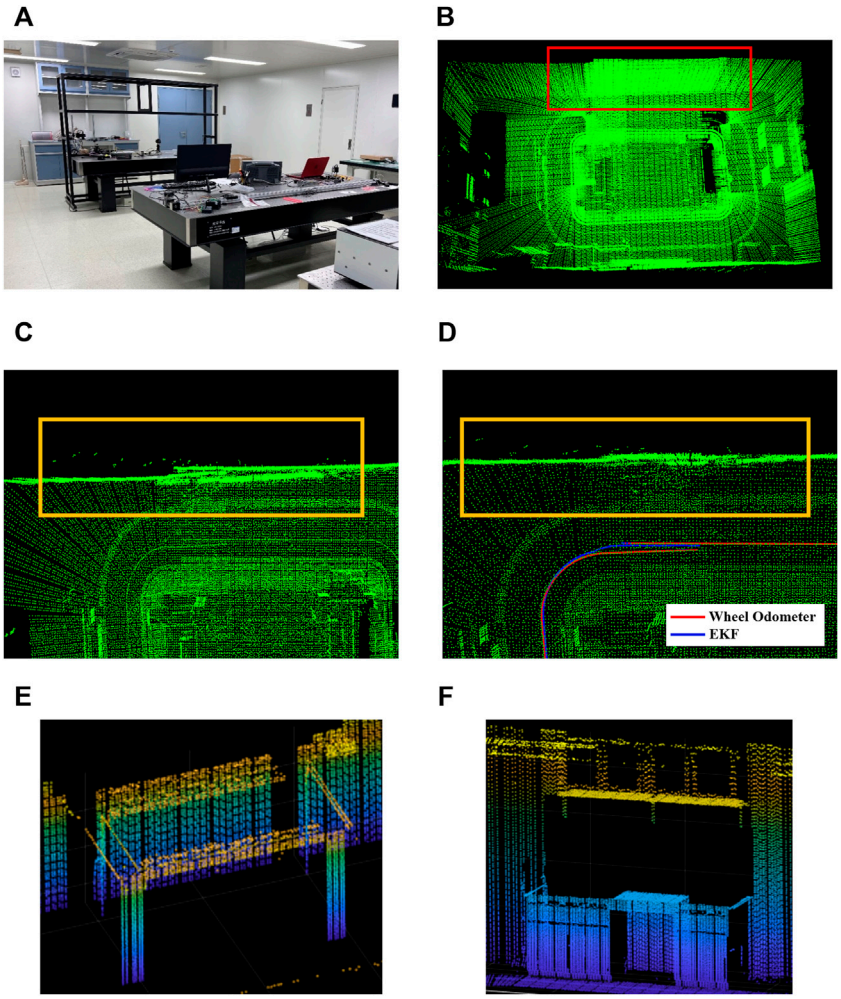

FIGURE 11
Different views of the point cloud **(A)** the experiment environment **(B)** top view of the point cloud **(C)** the mismatch before EKF optimization **(D)** the mismatch after EKF optimization **(E)** worktop **(F)** laboratory casework.

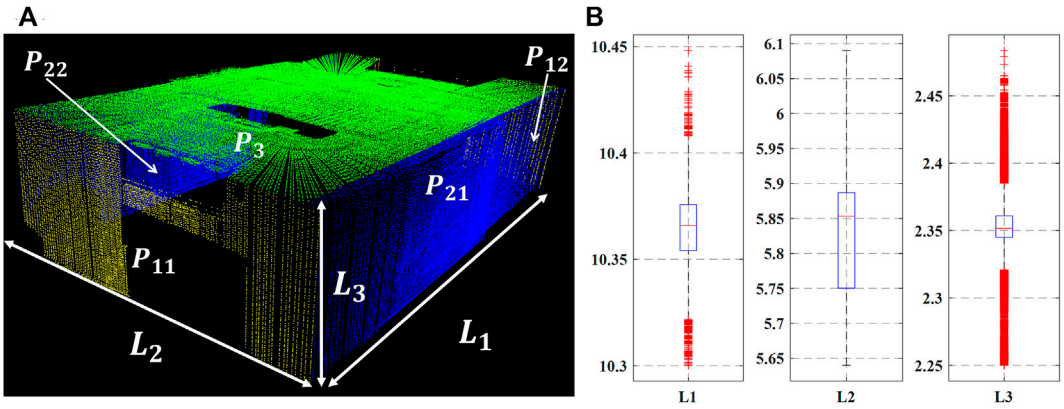

FIGURE 12
Accuracy results **(A)** plane segmentation results **(B)** measurement statistical results shown in boxplots.

TABLE 3 Comparison of experimental and actual value.

Item	L_1	L_2	L_3
Experiment Value	10.354 m	5.859 m	2.358 m
Actual Value	10.330 m	5.850 m	2.350 m

Conclusion

In summary, this paper proposes a low-cost mobile 3D imaging system based on 2D LIDAR. The software and hardware components are introduced, and the theoretical model is derived. The system can realize a wide range of 3D scanning of the environment, which can be used for big scenes 3D mapping and reconstruction. For this system, the assembly error of 2D LIDAR is an important cause of point cloud distortion. To solve this problem, we propose a calibration method based on targeted calibration plane registration, which can calibrate the 3-axis error angles without adding extra sensor. LM nonlinear optimization algorithm is used to calculate the results. The experiments verify the superior performance of the system and the validity of the calibration method. The system not only reduces the cost but also ensures the accuracy. It is anticipated that this system will greatly expand the availability of LIDAR in a wide range of applications.

Data availability statement

The original contributions presented in the study are included in the article/Supplementary Material, further inquiries can be directed to the corresponding author.

Author contributions

Writing-original draft preparation, conceptualization was provided by RM Data curation was provided by XL Investigation, methodology was provided by YP Validation, formal analysis was provided by LL.

Funding

This research was funded by the National Natural Science Foundation of China (NSFC) (61905063, 61905061); the Natural Science Foundation of Hebei Province, China (F2020202055).

Acknowledgments

The authors are thankful to other colleagues in their laboratory for their understanding and help.

Conflict of interest

The authors declare that the research was conducted in the absence of any commercial or financial relationships that could be construed as a potential conflict of interest.

Publisher's note

All claims expressed in this article are solely those of the authors and do not necessarily represent those of their affiliated organizations, or those of the publisher, the editors and the reviewers. Any product that may be evaluated in this article, or claim that may be made by its manufacturer, is not guaranteed or endorsed by the publisher.

References

1. Baek J, Park J, Cho S, Lee C. 3D global localization in the underground mine environment using mobile LiDAR mapping and point cloud registration. *Sensors* (2022) 22:2873. doi:10.3390/s22082873

2. Williams K, Olsen MJ, Roe GV, Glennie C. Synthesis of transportation applications of mobile LIDAR. *Remote Sensing* (2013) 5:4652–92. doi:10.3390/rs5094652

3. Li Y, Ibanez-Guzman J. Lidar for autonomous driving: The principles, challenges, and trends for automotive lidar and perception systems. *IEEE Signal Process Mag* (2020) 37:50–61. doi:10.1109/msp.2020.2973615

4. Liu K, Ma HC, Ma HC, Cai Z, Zhang L. Building extraction from airborne LiDAR data based on min-cut and improved post-processing. *Remote Sensing* (2020) 12:2849. doi:10.3390/rs12172849

5. Wu QY, Yang HB, Wei MQ, Remil O, Wang B, Wang J. Automatic 3D reconstruction of electrical substation scene from LiDAR point cloud. *ISPRS J Photogrammetry Remote Sensing* (2018) 143:57–71. doi:10.1016/j.isprsjprs.2018.04.024

6. Konolige K, Augenbraun J, Donaldson N, Fiebig C, Shah P. Ieee. A low-cost laser distance sensor. In: *Proceedings of IEEE international conference on robotics and automation*. Pasadena, CA (2008). p. 3002–+. doi:10.1109/ROBOT.2008.4543666

7. Hess W, Kohler D, Rapp H, Andor D. Real-time loop closure in 2D LIDAR SLAM. *Ieee Int Conf Robotics Automation (Icra)* (2016) 1271–8. doi:10.1109/icra.2016.7487258

8. Wang H, Lin Y, Wang Z, Yao Y, Zhang Y, Wu L. Validation of a low-cost 2D laser scanner in development of a more-affordable mobile terrestrial proximal sensing system for 3D plant structure phenotyping in indoor environment. *Comput Elect Agric* (2017) 140:180–9. doi:10.1016/j.compag.2017.06.002

9. Xu X, Luo M, Tan Z, Zhang M, Yang H. Plane segmentation and fitting method of point clouds based on improved density clustering algorithm for laser radar. *Infrared Phys Tech* (2019) 96:133–40. doi:10.1016/j.infrared.2018.11.019

10. Bauersfeld L, Ducard G. Low-cost 3D laser design and evaluation with mapping techniques review. In: *Proceedings of 2019 IEEE sensors applications symposium* (2019). (SAS).

11. Bi S, Yuan C, Liu C, Cheng J, Wang W, Cai Y. A survey of low-cost 3D laser scanning technology. *Appl Sci* (2021) 11:3938. doi:10.3390/app11093938

12. Yuan C, Bi S, Cheng J, Yang D, Wang W. Low-cost calibration of matching error between lidar and motor for a rotating 2D lidar. *Appl Sci* (2021) 11:913. doi:10.3390/app11030913

13. Zhao Haipeng H, Du Yuhong Y, Ding Juan J, Zhao Di D, Shi Yijun Y. LiDAR ranging angle measurement calibration method in mobile robot. 红外与激光工程 (2019) 48(68):630002–0630002. doi:10.3788/irla201948.0630002

14. Olivka P, Krumnikl M, Moravec P, Seidl D. Calibration of short range 2D laser range finder for 3D SLAM usage. *J Sensors* (2016) 3715129. doi:10.1155/2016/3715129

15. So E, Basso F, Menegatti E. Calibration of a rotating 2D laser range finder using point-plane constraints. *J Automation Mobile Robotics Intell Syst* (2013). doi:10.1007/978-3-319-10774-5_15

16. Kurnianggoro L, Hoang V, Jo KH. Calibration of a 2D laser scanner system and rotating platform using a point-plane constraint. *Comsis J* (2015) 12:307–22. doi:10.2298/csis141020093k

17. Zeng Y, Yu H, Dai H, Song S, Lin M, Sun B, et al. An improved calibration method for a rotating 2D LIDAR system. *Sensors* (2018) 18:497. doi:10.3390/s18020497

frontiers | Frontiers in Physics

TYPE Mini Review
PUBLISHED 30 August 2022
DOI 10.3389/fphy.2022.982640

OPEN ACCESS

EDITED BY
Zhi-Han Zhu,
Harbin University of Science and Technology, China

REVIEWED BY
Zhongming Yang,
Shandong University, China
Yang Cao,
Polytechnique Montréal, Canada

*CORRESPONDENCE
Yajun Pang,
yjpang@hebut.edu.cn
Liying Lang,
langliying@hebut.edu.cn

SPECIALTY SECTION
This article was submitted to Optics and Photonics,
a section of the journal
Frontiers in Physics

RECEIVED 30 June 2022
ACCEPTED 08 August 2022
PUBLISHED 30 August 2022

CITATION
Hu Q, Wei X, Pang Y and Lang L (2022), Advances on terahertz single-pixel imaging.
Front. Phys. 10:982640.
doi: 10.3389/fphy.2022.982640

Advances on terahertz single-pixel imaging

Qiao Hu[1,2], Xudong Wei[1,2], Yajun Pang[1,2]* and Liying Lang[1,2]*

[1]Center for Advanced Laser Technology, Hebei University of Technology, Tianjin, China, [2]Hebei Key Laboratory of Advanced Laser Technology and Equipment, Tianjin, China

Single-pixel imaging is a novel imaging technique that can obtain image information through a single-pixel detector. It can effectively avoid the problem of lack of high-quality area array detectors in the terahertz band, and has attracted the attention of a large number of researchers in recent years. In this paper, the basic imaging principles, terahertz beam modulation methods and typical image reconstruction algorithms for terahertz single-pixel imaging are introduced and discussed, as well as its research progresses and developing trends.

KEYWORDS

terahertz imaging, single-pixel imaging, terahertz beam modulation, compressed sensing, reconstruction algorithm

1 Introduction

Terahertz [1] (THz) waves (0.1–10 THz, 3 mm-30 um) have the characteristics of high penetration, low photon energy and spectral resolution, which makes terahertz imaging a widely technology used in various fields, such as nondestructive testing [2–4], safety monitoring [5–7] and medical applications [8–10].

According to different detection methods, terahertz imaging can be divided into array imaging and point-by-point scanning imaging [11]. Array imaging usually uses CCD cameras [12], CMOS cameras [13] or microbolometer cameras [14] as the detectors, which has advantages of high integration and real-time imaging. However, due to the limitation of THz array detectors, the resolution of array imaging cannot be very high. Point-by-point scanning imaging [15] scans the sample mechanically to obtain the value of every pixel, thereby realizing the imaging of the object. Its spatial resolution is higher than that of array imaging, but the scanning speed will limit the imaging efficiency. So it is impossible to realize high-speed imaging. Based on the shortcomings of the above imaging methods, some researchers applied single-pixel imaging in the field of terahertz imaging. Single-pixel imaging [16] is a new computational imaging technology, whose basic idea is to use a single-pixel detector to collect spatial intensity information of objects and then reconstruct the image using the correlation calculation of intensities between the collected light and the original light with a specific spatial distribution. Since only a single-pixel detector is needed to obtain the image of the object, the system structure can be simplified and the cost can be reduced, which provides a new method for terahertz imaging [17].

2 Basic principle

Single-pixel imaging is a computational imaging method that can be described by a mathematical model. An image can be regarded as a one-dimensional matrix I with a size of $1 \times N$. The mask pattern is P_i ($i = 1, 2, \ldots, M$ represents the $i-th$ measurement), which modulate the light source spatially. So the intensity of the detected light S_i can be expressed as $P_i \times I_i$. Using a single-pixel system for M measurements, linear equations can be obtained:

$$\boldsymbol{S} = \boldsymbol{P} \times \boldsymbol{I}. \tag{1}$$

Where $\boldsymbol{P}$ is the measurement matrix with a size of $M \times N$, and $\boldsymbol{S}$ is a one-dimensional matrix composed of M measured intensity values. By this way, the problem of reconstructing the object image is transformed into the problem of solving N independent unknowns by using M linear equations. Generally speaking, when $M = N$and P is an orthogonal matrix, the image can be reconstructed according to Eq. 2, otherwise Eq. 1 is an underdetermined equation. Image reconstruction is the process of matrix inversion:

$$\boldsymbol{I} = \boldsymbol{P}^{-1}\boldsymbol{S} \tag{2}$$

When the measurement matrix adopts random matrix, it takes more measurement time to recover the object image with considerable quality.

3 Development of terahertz single-pixel imaging

According to the basic principle of single-pixel imaging, the key points is the spatial modulation of the beam, the selection of modulation matrix and the reconstruction algorithm of the image. In the view of the beam modulation methods and imaging algorithms, this section introduces the development of terahertz single-pixel imaging.

3.1 Spatial modulation of terahertz wave

The existing spatial light modulators, such as digital micromirror devices and liquid crystal spatial light modulations, generally work in visible and infrared bands, which cannot directly be used to modulate terahertz waves. Therefore, studying the spatial light modulation methods in the terahertz band is a very important topic to THz single-pixel imaging. Recently, researchers have put forward a great many different solutions to this challenge.

3.1.1 Metallic masks modulation

As metals have strong absorption and reflection properties for terahertz waves, it is an effective method to modulate terahertz waves by metal masks. As shown in Figure 1AChan et al. partially printed copper on the transparent PCB as a random mask [18] and combined it with the CS algorithm to achieve 32×32 pixels terahertz single-pixel imaging. However, making a large number of masks is cumbersome and its mechanical switching speed limits the imaging speed of the system. Duan et al. [19] proposed a metal mask structure that shares the adjacent mask matrices and used a linear motor to drive a metal plate to achieve automatic modulation of terahertz. The imaging system uses a terahertz Tunable Parametric Oscillator (TPO) as the radiation source and obtains identifiable results for hole imaging of the circular, rectangular and shape image letter "H." The sharing mode of adjacent mask matrices greatly simplifies the complicated process of making a large number of mask plates, improves the switching speed of mask matrices, and eliminates the problem of optical path alignment caused in the process of mask replacement. However, with the improvement of resolution, the length of mask will greatly increase, which makes the whole system cumbersome.

Some researchers have proposed the use of rotating masks to modulate terahertz waves. In 2012, the University of Liverpool [20] demonstrated for the first time that continuously rotating PCB circular disks with masks can be used to rapidly modulate terahertz. For terahertz imaging, 160 measurements (about 16%) can provide images with acceptable quality. Similarly, Vallés et al. [21] used metal ring with a series of direct perforation random masks to realize 2D imaging with high pixel resolution (1200 × 1200) in the entire terahertz frequency range (3–13 THz). Moreover, the Chinese Academy of Sciences uses the rotation of double amplitude modulation plates [22, 23] to generate reusable measurement matrices, which further improved the acquisition speed of the measurement matrix and imaging quality (7 mm resolution).

3.1.2 Optically controlled semiconductor modulation

In addition to the direct modulation of terahertz waves by metal mask, there is also photo-induced semiconductor modulation technology [23, 24] to be commonly used in recent years. As shown in Figure 1B, its modulation mechanism is that the area of the semiconductor illuminated by light will excite the internal photo-generated carriers, forming a transient region with high absorption or high reflection of terahertz waves, so that the modulation of terahertz waves is converted into modulation of the current carrier in the semiconductor. Therefore, the modulation of terahertz waves can be realized by combining traditional spatial light modulators and semiconductors. Because of its own characteristics, silicon has a band gap width suitable for laser pumping and it is the first time semiconductor material that has been proved to be used to realize optically controlled terahertz modulation devices. In

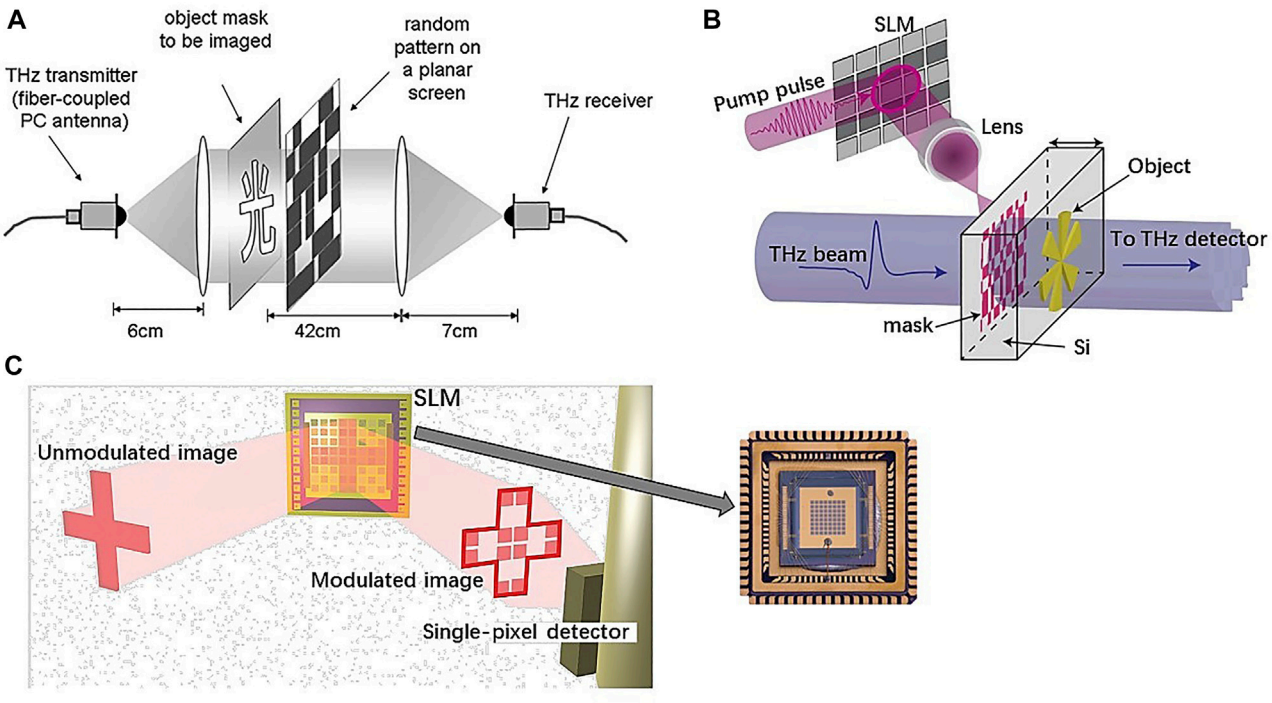

FIGURE 1
(A) Terahertz single-pixel imaging based on metal mask modulator [18], **(B)** Terahertz single-pixel imaging based on optically controlled semiconductor modulation [25], **(C)** Terahertz single-pixel imaging based on metamaterial modulation [38].

addition, materials such as germanium and gallium arsenic have also been proved to be used as modulation semiconductors.

Busch et al. applied the modulation technology of optically pumped semiconductor materials (25% modulation depth) to terahertz beam control and imaging [25], and obtain a 64 × 64 pixels image of a cross-shaped aluminum sheet by using a series of masks. Hendry's group [26] used spatially modulated femtosecond laser pulses to pump high-resistance Si, and achieved single-pixel imaging of terahertz with a spatial resolution of $103\,\mu m \pm 7\,\mu m (\sim \frac{\lambda}{4}$, the central wavelength of the terahertz pulse $\lambda = 375\,\mu m$) under a 115 mm thick silicon wafer. Subsequently, they also studied the effect of silicon wafer thickness at this resolution [27]. By reducing the silicon wafer thickness to $6\,\mu m$, a resolution of $9\,(\pm 4)\,\mu m$ $(\sim \frac{\lambda}{45})$ can be achieved, which is about 3 times faster than scanning imaging. In a similar way, Stantchev [28] et al. used a continuous wave source to optically excite charge carriers in high-resistance silicon to form a light-controlled terahertz modulator with depth of up to 80%. By optimizing the modulation geometry (total internal reflection TIR) and post-processing algorithm, a single-pixel fiber-coupled photo-conductive detector was used to obtain a real-time terahertz video with a resolution of 32×32 at a speed of about 6 frames per second. Besides, Zanotto et al. proposed far-field imaging based on single-pixel imaging with THz-TDS system [29]. Without mechanical grating scanning, they reconstructed the terahertz electric field waveform in the time domain at each spatial position of the object, and obtained the time-of-flight images of high-density polyethylene samples with different thicknesses. This achievement combines the powerful functions of THz-TDS and compressed sensing, and the sampling efficiency is greatly improved.

To improve the modulation depth of silicon-based modulators, many researchers have used micro-nano structures to cover the silicon surface, such as graphene [30], metal gratings [31], and so on. Zhu et al. performed a comparative analysis of the THz imaging results between a micro-structure silicon modulator and a conventional high-resistance silicon modulator [32]. The results showed that the micro-structure greatly improved the absorption and utilization rate of silicon for laser and improved the imaging effect.

Graphene has also been proved to be useful for the modulation of terahertz waves due to its unique structure and high carrier mobility. Wen et al. designed a graphene based all-optical spatial terahertz modulator [33]. They transferred a layer of graphene on the top of doped germanium, and controlled the transmission of terahertz waves by irradiating the germanium substrate with a laser to generate carriers to diffuse into the graphene layer, thereby realizing the modulation of terahertz waves. The maximum modulation depth of the optically controlled modulator is as high as 90%. In addition, Shenzhen

TABLE 1 Comparison of modulation methods in THz single-pixel imaging.

Research units	System	Modulation mode	Modulation efficiency
Rice University [18]	Fiber-coupled antennas (100 GHz)	PCB	100%
Tianjin University [19]	Terahertz parametric oscillator	Coded sheet metal	100%
University of Liverpool [20]	IR and THz	Rotating circular disks with masks	100%
Chiba University [21]	Monochromatic terahertz source	A perforated metallic ring mask	—
Philipps-Universität Marburg [25]	fiber coupled THz-TDS system	DMD + fs laser pump high resistance silicon	25%
University of Glasgow [26]	THz-TDS system	DMD + fs laser pump high resistance silicon	>90%
Chinese University of Hong Kong [28]	CW and single-pixel photoelectricity Conductive antenna	DMD pumped triangular silicon	~80%
Institut National de la Recherche Scientifique [29]	THz-TDS system	DMD + fs laser pump Si-plate	95%
University of Electronic Science and Technology of China [33]	THz-TDS system	Germanium-based monolayer graphene	94%
Tianjin University [35]	Wideband pump probe THz-TDS system	Metal gratings are integrated into SOS	>60%
University of Science and Technology of China [36]	THz-TDS system	VO_2	60%
Los Alamos National Laboratory [37]	THz-TDS system	Split-ring resonators	50%
Boston University [38]	Blackbody radiation (>4.6 THz)	Metamaterial THz absorber	33%

Institute of Advanced Technology used the mono-layer graphene on a high-resistance silicon substrate illuminated by a coded laser beam as a terahertz modulator to realize Fourier single-pixel terahertz imaging [34]. Though the sampling ratio is only 1.6%, the image reconstruction can be completed with a signal-to-noise ratio as large as 5.11. The modulation depth of graphene combined with semiconductor is still limited and its working frequency is narrow. Tianjin University [35] proposed to integrate sub-wavelength metallic grating into silicon on sapphire to design a high-efficiency, ultra-thin and fast THz SLM with high modulation depth (over 60% THz peak amplitude modulation depth at the pump flux of $80\,\mu\,J/cm^2$). Besides silicon, vanadium dioxide, a phase change material, is also a common used material. The University of Science and Technology of China proposed to exploit the photo-metallic-insulating phase transition properties of the phase-changing material vanadium dioxide (VO_2) to achieve efficient spatial modulation of coherent terahertz pulses [36]. They achieved a modulation depth of 60% and the THz single-pixel imaging with a spatial resolution of $4.5\,\mu m$was realized by using VO_2 with a thickness of 180 nm. Moreover, the spatial resolution exceeded less than one percent of the central wavelength ($\frac{\lambda_0}{133}$).

3.1.3 Metamaterial modulation

Artificial metamaterials combined with tunable semiconductor structures can realize high-speed terahertz modulators. This class of modulators mainly involves fabricating metallic metamaterial structures on semiconductor materials and controls the resonant strength of the metamaterial structure by applying a bias voltage between the metamaterial and the substrate. In 2006, Chen et al. proposed a terahertz modulator [37] with a semiconductor metamaterial structure to obtain a modulation depth of 50% at 0.72 THz. As shown in Figure 1C, Padilla's team proposed a reconfigurable terahertz spatial light modulator based on metamaterial absorber in 2014, which uses an electronically controlled 8×8 mask. In the mask each pixel is composed of dynamic, polarization sensitive absorbers, so real-time adjustment of terahertz wave transmittance can be achieved [38].

Terahertz SLMs (Spatial Light Modulator) are widely adopted in single-pixel imaging, in Table 1, we summarize the representative results of current THz single-pixel imaging. The metal mask controllability over terahertz is not strong, which affects the quality of reconstructed images. The photo-induced carrier concentration in photo-induced semiconductor modulation will directly affect the modulation efficiency. At present, it is difficult for the existing semiconductor materials to meet the requirements of modulation speed and modulation depth at the same time. Therefore, how to improve the carrier concentration in photo-induced semiconductors is a research hotpot. Artificial metamaterial modulation can better control the transmission of terahertz waves, but the design is complex and provides very few controllable pixels.

3.2 Imaging algorithm

Another important factor that affects the imaging quality of terahertz single-pixel is the post-imaging reconstruction algorithm. With the development of single-pixel imaging, many reconstruction algorithms have been proposed to improve imaging quality and efficiency, which can be broadly classified as follows: traditional

terahertz single-pixel imaging algorithms developed from computational ghost imaging algorithms, single-pixel imaging algorithms based on compressed sensing, single-pixel imaging algorithms based on base scanning, single-pixel imaging algorithm based on deep learning, etc.

Computational ghost imaging based on spatial light modulation was proposed by Bromberg et al. [39] in 2008. In terms of imaging nature, conventional terahertz single-pixel imaging and computational ghost imaging are mathematically equivalent, as in Eq. 3, which uses an iterative approach for image reconstruction based on correlation algorithms.

$$\boldsymbol{I} = \frac{\boldsymbol{1}}{\boldsymbol{M}} \sum_{i=1}^{M} (\boldsymbol{S_i} - \langle \boldsymbol{S} \rangle)(\boldsymbol{P_i} - \langle \boldsymbol{P} \rangle) \tag{3}$$

It can be seen from the formula that the reconstructed image is equivalent to a weighted sum of modulation masks, where the weight is the detection value of a single-pixel. Usually, this method can only obtain images with high SNR for a larger number of measurements ($M \gg N$). In order to improve the quality of terahertz single-pixel imaging, some researchers have proposed differential ghost imaging [40] and normalized ghost imaging [41] based on the traditional imaging algorithms. Differential ghost imaging removes noise by using the differential value of the barrel detector instead of the total light intensity value to improve the SNR of the imaging results. Normalized ghost imaging improves the noise immunity of the system by normalizing the detection value of the signal optical path with the total intensity value of the reference optical path, and this method has a similar SNR to differential ghost imaging. Although these methods further improve the imaging quality, they are still inferior to traditional imaging methods and require a very large number of samples.

In order to overcome the problems of large amount of sampled data and long time in imaging, some studies have proposed combining compressed sensing (CS) techniques with optically controllable terahertz spatial light modulators in single-pixel imaging. Compressed sensing theory [42–44] was first proposed in 2006 by Candès and Donoho et al. It breaks away from the traditional Nyquist sampling theorem by exploiting the sparsity of natural images in the orthogonal transform domain to accurately reconstruct the original target image using a small number of sampled measurements. The CS theory solves the problem of solving the uncertain inverse problem with more unknown values than the available data. In single-pixel imaging [17], this means that the number of mask patterns is less than the total number of pixels used to restore the image, which provides a new method for single-pixel imaging. After the CS theory was proposed, Rice University [45] conducted a single-pixel imaging experiment using the theory, which used a digital micromirror array to modulate visible light, combined the pre-designed observation matrix with the one-dimensional measurements obtained from the single-pixel detector, and then used the compressed sensing reconstruction algorithm to obtain the original image.

Although the introduction of CS algorithms [38, 46, 47] reduces the number of samples and effectively reduces the imaging time, it requires a long time for computation and high computational complexity in the image reconstruction process. In addition to the random matrix modulation, terahertz single-pixel imaging can also be modulated with deterministic orthogonal bases, such as Fourier bases [34, 48, 49], Hadamard bases [50–52], discrete cosine bases [53], and wavelet transform bases [54, 55], etc. This imaging method is also known as base-scan terahertz single-pixel imaging. Since these substrate patterns are orthogonal, by determining the illumination projection of the patterns, the spatial information of the object image in the transform domain can be obtained and the corresponding inverse transformation can be performed to recover the target image. In addition, taking advantage of the sparsity of natural images in the transform domain, it is possible to reconstruct clear images using under-sampled data by measuring coefficients of larger amplitude.

Although the base-scan terahertz single-pixel imaging approach effectively solves the problem of long data acquisition time, the sampling frequency is subjectively selected in the sampling process, which leads to selective loss of image information and does not always exactly match the frequency distribution of the image. In recent years, many researchers have demonstrated the advantages of deep learning [56–63] in the field of single-pixel imaging, which is widely used in the fields of information encryption [64] and image super-resolution [65]. For single-pixel imaging, the image quality is proportional to the number of samples, and how to get effective recovery of the target image under low sampling is an important issue nowadays. Combining deep learning with single-pixel imaging and relying on the deep learning ability of the model can obtain better image quality. In 2017, Lyu et al. applied deep learning [66] to a traditional computational ghost imaging algorithm by using a large number of reconstructed low-quality images at low sampling rates as network inputs and the original images as labels for the network, and iteratively trained the network to obtain high-quality target images at 10% sampling rate. In addition, some researchers used the single-pixel detection signal sequence as the input of the neural network and the image reconstruction result as the output of the neural network to train the neural network to achieve deep learning single-pixel imaging [67]. In terahertz waves single-pixel imaging, most of the existing research uses deep learning techniques to improve the quality of imaging [68–70], and it is also a research direction to investigate how to train modulation masks suitable for terahertz single-pixel imaging to improve the imaging speed in response to the current problems.

4 Discussion and conclusion

Applying single-pixel imaging technique to THz imaging can effectively solve some problems existing in traditional method. With the continuous development of spatial modulation techniques, many terahertz single-pixel imaging techniques have been investigated as described above. This paper summarizes the initial physical metal masks to later methods based on light modulation in

semiconductors and artificial metamaterial modulation. In terms of imaging algorithms, the main imaging algorithms applied to terahertz single-pixel imaging are introduced, including the traditional terahertz single-pixel imaging algorithm developed from computational ghost imaging algorithm, single-pixel imaging algorithm based on compressed sensing, single-pixel imaging algorithm based on basic scanning and single-pixel imaging algorithm based on deep learning. At present, how to improve the sampling speed to achieve real-time imaging while ensuring the image SNR is the problem that needs to be solved for terahertz single-pixel imaging. In addition, further improvement of terahertz modulation techniques and exploration of more optimized algorithms are the two most important research directions for terahertz single-pixel imaging.

Author contributions

QH: investigation, writing—original draft. XW: investigation, writing—review and editing. YP: investigation, writing—original draft, writing—review and editing, supervision. LL: investigation, writing—review and editing.

Funding

This work was funded by the Key R&D Program of Hebei Province (20371802D), the National Natural Science Foundation of China (61905063), and the Natural Science Foundation of Hebei Province (F2020202055).

Conflict of interest

The authors declare that the research was conducted in the absence of any commercial or financial relationships that could be construed as a potential conflict of interest.

Publisher's note

References

1. Siegel PH. Terahertz technology. *IEEE Trans Microwave Theor Techn* (2002) 50:910–28. doi:10.1109/22.989974

2. Wang J, Zhang J, Chang T, Liu L, Cui HL. Terahertz nondestructive imaging for foreign object detection in glass fibre-reinforced polymer composite panels. *Infrared Phys Technol* (2019) 98:36–44. doi:10.1016/j.infrared.2019.02.003

3. Zhang D, Ren J, Gu J, Li LJ, Zhang JY, Xiong WH, et al. Nondestructive testing of bonding defects in multilayered ceramic matrix composites using THz time domain spectroscopy and imaging. *Compos Structures* (2020) 251:112624. doi:10.1016/j.compstruct.2020.112624

4. Zhang X, Chang T, Wang Z, Cui HL. Three-dimensional terahertz continuous wave imaging radar for nondestructive testing. *IEEE Access* (2020) 8:144259–76. doi:10.1109/access.2020.3014170

5. Tong H, Pei S, Jiang L, Zhu Y, Xiao L *Seventh international green and sustainable computing conference (IGSC)*. Hangzhou, China: IEEE (2016). 1–5.A low-power-consumption and high efficiency security system for automatic detection of concealed objects in human body

6. Hu S, Chen X, Alfadhl Y. *43rd international conference on infrared, millimeter, and terahertz waves (IRMMW-THz)*. Nagoya: IEEE (2018). 1–2.A THz imaging system using sparse antenna array for security screening

7. Tzydynzhapov G, Gusikhin P, Muravev V, Dremin A, Nefyodov Y, Kukushkin I. New real-time sub-terahertz security body scanner. *J Infrared Millim Terahertz Waves* (2020) 41(6):632–41. doi:10.1007/s10762-020-00683-5

8. Yang X, Zhao X, Yang K, Liu Y, Liu Y, Fu W, et al. Biomedical applications of terahertz spectroscopy and imaging. *Trends Biotechnol* (2016) 34:810–24. doi:10.1016/j.tibtech.2016.04.008

9. Cao Y, Huang P, Li X, Ge W, Hou D, Zhang G. Terahertz spectral unmixing based method for identifying gastric cancer. *Phys Med Biol* (2018) 63:035016. doi:10.1088/1361-6560/aa9e1a

10. Rong L, Latychevskaia T, Chen C, Wang D, Yu Z, Zhou X, et al. Terahertz in-line digital holography of human hepatocellular carcinoma tissue. *Sci Rep* (2015) 5:8445. doi:10.1038/srep08445

11. Guerboukha H, Nallappan K, Skorobogatiy M. Toward real-time terahertz imaging. *Adv Opt Photon* (2018) 10:843–938. doi:10.1364/aop.10.000843

12. Trichopoulos GC, Mosbacker HL, Burdette D, Sertel K. A broadband focal plane array camera for real-time THz imaging applications. *IEEE Trans Antennas Propagat* (2013) 61:1733–40. doi:10.1109/tap.2013.2242829

13. Schuster F, Coquillat D, Videlier H, Sakowicz M, Teppe F, Dussopt L, et al. Broadband terahertz imaging with highly sensitive silicon CMOS detectors. *Opt Express* (2011) 19:7827–32. doi:10.1364/oe.19.007827

14. Simoens F, Meilhan J, Gidon S, Lasfargues G, Lalanne Dera J, Ouvrier-Buffet JL, et al. Antenna-coupled microbolometer based uncooled 2D array and camera for 2D real-time terahertz imaging. *Proc SPIE 8846 Terahertz Emitters, Receivers, Appl* (2013) IV:88460O.

15. Hu B, Nuss MC. Imaging with terahertz waves. *Opt Lett* (1995) 20:1716–8. doi:10.1364/ol.20.001716

16. Edgar MP, Gibson GM, Padgett MJ. Principles and prospects for single-pixel imaging. *Nat Photon* (2019) 13:13–20. doi:10.1038/s41566-018-0300-7

17. Duarte MF, Davenport MA, Takhar D, Laska JN, Sun T, Kelly KF, et al. Single-pixel imaging via compressive sampling. *IEEE Signal Process Mag* (2008) 25:83–91. doi:10.1109/msp.2007.914730

18. Chan WL, Charan K, Takhar D, Kelly KF, Baraniuk RG, Mittleman DM. A single-pixel terahertz imaging system based on compressed sensing. *Appl Phys Lett* (2008) 93:121105. doi:10.1063/1.2989126

19. Duan P, Wang Y, Xu D, Yan C, Yang Z, Xu W, et al. Single pixel imaging with tunable terahertz parametric oscillator. *Appl Opt* (2016) 55:3670–5. doi:10.1364/ao.55.003670

20. Shen H, Gan L, Newman N, Dong Y, Li C, Huang Y, et al. Spinning disk for compressive imaging. *Opt Lett* (2012) 37:46–8. doi:10.1364/ol.37.000046

21. Vallés A, He J, Ohno S, Omatsu T, Miyamoto K. Broadband high-resolution terahertz single-pixel imaging. *Opt Express* (2020) 28:28868–81. doi:10.1364/oe.404143

22. Yan H, Zhao C, Xu W, Li Shuofeng. Terahertz ghost imaging based on imaging-transformation measurement matrices. *Chin. J. Lasers* (2019) 46:1214001. (in Chinese). doi:10.3788/cjl201946.1214001

23. Shang Y, Wang X, Sun W, Han P, Ye J, Feng S, et al. Terahertz image reconstruction based on compressed sensing and inverse Fresnel diffraction. *Opt Express* (2019) 27:14725–35. doi:10.1364/oe.27.014725

24. Shrekenhamer D, Watts CM, Padilla WJ. Terahertz single pixel imaging with an optically controlled dynamic spatial light modulator. *Opt Express* (2013) 21(10): 12507–18. doi:10.1364/oe.21.012507

25. Busch S, Scherger B, Scheller M, Koch M. Optically controlled terahertz beam steering and imaging. *Opt Lett* (2012) 37:1391–3. doi:10.1364/ol.37.001391

26. Stantchev RI, Sun B, Hornett SM, Hobson PA, Gibson GM, Padgett MJ, et al. Noninvasive, near-field terahertz imaging of hidden objects using a single-pixel detector. *Sci Adv* (2016) 2(6):e1600190. doi:10.1126/sciadv.1600190

27. Stantchev RI, Phillips DB, Hobson P, Hornett SM, Padgett MJ, Hendry E. Compressed sensing with near-field THz radiation. *Optica* (2017) 4:989–92. doi:10.1364/optica.4.000989

28. Stantchev RI, Yu X, Blu T, Pickwell-MacPherson E. Real-time terahertz imaging with a single-pixel detector. *Nat Commun* (2020) 11(1):2535. doi:10.1038/s41467-020-16370-x

29. Zanotto L, Piccoli R, Dong J, Caraffini D, Morandotti R, Razzari L. Time-domain terahertz compressive imaging. *Opt Express* (2020) 28:3795–802. doi:10.1364/oe.384134

30. Mittendorff M, Li S, Murphy TE. Graphene-based waveguide-integrated terahertz modulator. *ACS Photon* (2017) 4:316–21. doi:10.1021/acsphotonics.6b00751

31. Wen T, Zhang D, Wen Q, Liao Y, Zhang C, Li J, et al. Enhanced optical modulation depth of terahertz waves by self-assembled monolayer of plasmonic gold nanoparticles. *Adv Opt Mater* (2016) 4:1974–80. doi:10.1002/adom.201600248

32. Zhu Y, Shen Z, Zhang H, He Y, Wen Q Fast imaging technology of terahertz wave based on spatial modulator. *J Terahertz Sci Electron Inf Tech* (2020) 18(3): 351~357. (in Chinese).

33. Wen Q, Tian W, Mao Q, Chen Z, Liu WW, Yang QH, et al. Graphene based all-optical spatial terahertz modulator. *Sci Rep* (2015) 4:7409. doi:10.1038/srep07409

34. She R, Liu W, Lu Y, Zhou Z, Li G. Fourier single-pixel imaging in the terahertz regime. *Appl Phys Lett* (2019) 115:021101. doi:10.1063/1.5094728

35. Yang X, Tian Z, Chen X, Hu M, Yi Z, Ouyang C, et al. Terahertz single-pixel near-field imaging based on active tunable subwavelength metallic grating. *Appl Phys Lett* (2020) 116:241106. doi:10.1063/5.0010531

36. Chen S, Du L, Meng K, Li J, Zhai ZH, Shi QW, et al. Terahertz wave near-field compressive imaging with a spatial resolution of over λ/100. *Opt Lett* (2019) 44: 21–4. doi:10.1364/ol.44.000021

37. Chen H, Padilla WJ, Zide JMO, Gossard AC, Taylor AJ, Averitt RD. Active terahertz metamaterial devices. *Nature* (2006) 444:597–600. doi:10.1038/nature05343

38. Watts CM, Shrekenhamer D, Montoya J, Lipworth G, Hunt J, Sleasman T, et al. Terahertz compressive imaging with metamaterial spatial light modulators. *Nat Photon* (2014) 8:605–9. doi:10.1038/nphoton.2014.139

39. Bromberg Y, Katz O, Silberberg Y. Ghost imaging with a single detector. *Phys Rev A (Coll Park)* (2009) 79(5):053840. doi:10.1103/physreva.79.053840

40. Ferri F, Magatti D, Lugiato LA, Gatti A. Differential ghost imaging. *Phys Rev Lett* (2010) 104:253603. doi:10.1103/physrevlett.104.253603

41. Sun B, Welsh SS, Edgar MP, Shapiro JH, Padgett MJ. Normalized ghost imaging. *Opt Express* (2012) 20:16892–901. doi:10.1364/oe.20.016892

42. Candes EJ, Romberg J, Tao T. Robust uncertainty principles: Exact signal reconstruction from highly incomplete frequency information. *IEEE Trans Inform Theor* (2006) 52:489–509. doi:10.1109/tit.2005.862083

43. Tsaig Y, Donoho DL. Extensions of compressed sensing. *Signal Process.* (2006) 86:549–71. doi:10.1016/j.sigpro.2005.05.029

44. Donoho DL. Compressed sensing. *IEEE Trans Inform Theor* (2006) 52: 1289–306. doi:10.1109/tit.2006.871582

45. Takhar D, Laska J, Wakin M, Duarte MF, Baraniuk RG *Proc IS&T/SPIE symposium on electronic imaging* (2006).A new Compressive Imaging camera architecture using optical-domain compression

46. Clemente P, Durán V, Tajahuerce E, Andres P, Climent V, Lancis J. Compressive holography with a single-pixel detector. *Opt Lett* (2013) 38(14): 2524–7. doi:10.1364/ol.38.002524

47. Zhao C, Gong W, Chen M, Li E, Wang H, Xu W, et al. Ghost imaging lidar via sparsity constraints. *Appl Phys Lett* (2012) 101:141123. doi:10.1063/1.4757874

48. Zhang Z, Ma X, Zhong J. Single-pixel imaging by means of Fourier spectrum acquisition. *Nat Commun* (2015) 6:6225. doi:10.1038/ncomms7225

49. Zhang Z, Wang X, Zheng G, Zhong J. Hadamard single-pixel imaging versus Fourier single-pixel imaging. *Opt Express* (2017) 25:19619. doi:10.1364/oe.25.019619

50. Wang L, Zhao S. Fast reconstructed and high-quality ghost imaging with fast Walsh–Hadamard transform. *Photon Res* (2016) 4(6):240–4. doi:10.1364/prj.4.000240

51. Radwell N, Mitchell KJ, Gibson GM, Edgar MP, Bowman R, Padgett MJ. Single-pixel infrared and visible microscope. *Optica* (2014) 1:285–9. doi:10.1364/optica.1.000285

52. Vasile T, Damian V, Coltuc D, Petrovici M. Single pixel sensing for THz laser beam profiler based on Hadamard Transform. *Opt Laser Tech* (2016) 79:173–8. doi:10.1016/j.optlastec.2015.12.009

53. Liu BL, Yang ZH, Liu X, Wu LA. Coloured computational imaging with single-pixel detectors based on a 2D discrete cosine transform. *J Mod Opt* (2017) 64(3):259–64. doi:10.1080/09500340.2016.1229507

54. Li M, Yan L, Yang R, Liu YX. Fast single-pixel imaging based on optimized reordering Hadamard basis. *Acta Phys Sin* (2019) 68(6):064202. doi:10.7498/aps.68.20181886

55. Alemohammad M, Stroud JR, Bosworth BT, Foster MA. High-speed all-optical Haar wavelet transform for real-time image compression. *Opt Express* (2017) 25(9):9802–11. doi:10.1364/oe.25.009802

56. Shimobaba T, Endo Y, Nishitsuji T, Takahashi T, Nagahama Y, Hasegawa S, et al. Computational ghost imaging using deep learning. *Opt Commun* (2018) 413: 147–51. doi:10.1016/j.optcom.2017.12.041

57. Rizvi S, Cao J, Zhang K, Hao Q. DeepGhost: Real-time computational ghost imaging via deep learning. *Sci Rep* (2020) 10:11400. doi:10.1038/s41598-020-68401-8

58. Sui L, Zhang L, Cheng Y, Zhaolin X, Ailing T, Anand A. Computational ghost imaging based on the conditional adversarial network. *Opt Commun* (2021) 492: 126982. doi:10.1016/j.optcom.2021.126982

59. Wu H, Wang R, Zhao G, Xiao H, Liang J, Wang D, et al. Deep-learning denoising computational ghost imaging. *Opt Lasers Eng* (2020) 134:106183. doi:10.1016/j.optlaseng.2020.106183

60. Wang F, Wang H, Wang H, Li G, Situ G. Learning from simulation: An end-to-end deep-learning approach for computational ghost imaging. *Opt Express* (2019) 27:25560. doi:10.1364/oe.27.025560

61. He Y, Wang G, Dong G, Zhu S, Chen H, Zhang A, et al. Ghost imaging based on deep learning. *Sci Rep* (2018) 8:6469. doi:10.1038/s41598-018-24731-2

62. Zhang L, Bian Z, Ye H, Zhang D, Wang K. Research on photon-level ghost imaging restoration based on deep learning. *Opt Commun* (2022) 504:127479. doi:10.1016/j.optcom.2021.127479

63. Wu H, Wang R, Zhao G, Xiao H, Wang D, Liang J, et al. Sub-Nyquist computational ghost imaging with deep learning. *Opt Express* (2020) 28:3846. doi:10.1364/oe.386976

64. Sui L, Du C, Xu M, Ailing T, Anand A. Information encryption based on the customized data container under the framework of computational ghost imaging. *Opt Express* (2019) 27(12):16493–506. doi:10.1364/oe.27.016493

65. Tian C, Fei L, Zheng W, Xu Y, Zuo W, Lin CW. Deep learning on image denoising: An overview. *Neural Networks* (2020) 131:251–75. doi:10.1016/j.neunet.2020.07.025

66. Lyu M, Wang W, Wang H, Li G, Chen N, et al. Deep-learning-based ghost imaging. *Sci Rep* (2017) 7(1):17865–6. doi:10.1038/s41598-017-18171-7

67. Shang R, Hoffer-Hawlik K, Wang F, Situ G, Luke GP. Two-step training deep learning framework for computational imaging without physics priors. *Opt Express* (2021) 29(10):15239–54. doi:10.1364/oe.424165

68. Wang Y, Qi F, Wang J. Terahertz image super-resolution based on a complex convolutional neural network. *Opt Lett* (2021) 46(13):3123–6. doi:10.1364/ol.422684

69. Li Y, Hu W, Zhang X, Xu Z, Ni J, Ligthart LP. Adaptive terahertz image super-resolution with adjustable convolutional neural network. *Opt Express* (2020) 28(15): 22200–17. doi:10.1364/oe.394943

70. Long Z, Wang T, You C, Yang Z, Wang K, Liu J. Terahertz image super-resolution based on a deep convolutional neural network. *Appl Opt* (2019) 58(10): 2731–5. doi:10.1364/ao.58.002731

frontiers | Frontiers in Physics

TYPE Original Research
PUBLISHED 31 August 2022
DOI 10.3389/fphy.2022.986795

OPEN ACCESS

EDITED BY
Baitao Zhang,
State Key Laboratory of Crystal Materials, Shandong University, China

REVIEWED BY
Xiaohui Li,
Shaanxi Normal University, China
Haiyong Zhu,
Wenzhou University, China

*CORRESPONDENCE
Shande Liu,
pepsl_liu@163.com
Jinlong Xu,
longno.2@163.com

SPECIALTY SECTION
This article was submitted to Optics and Photonics,
a section of the journal
Frontiers in Physics

RECEIVED 05 July 2022
ACCEPTED 12 August 2022
PUBLISHED 31 August 2022

CITATION
Chen B, Li K, Jin Y, Wang P, Zhang N, Zhang K, Liu S and Xu J (2022), GaInSn liquid nanospheres as a saturable absorber for an Er:CaF_2 laser at 2.75 μm. *Front. Phys.* 10:986795.
doi: 10.3389/fphy.2022.986795

GaInSn liquid nanospheres as a saturable absorber for an Er:CaF_2 laser at 2.75 μm

Bo Chen[1], Kuan Li[1], Yicheng Jin[1], Peifu Wang[1], Ning Zhang[1], Ke Zhang[1], Shande Liu[1]* and Jinlong Xu[2]*

[1]College of Electronic and Information Engineering, Shandong University of Science and Technology, Qingdao, China, [2]School of Electronic Science and Engineering, Nanjing University, Nanjing, China

High-quality GaInSn liquid nanospheres are successfully fabricated by the ultrasonic method as a novel saturable absorber in the mid-infrared range. An open-aperture Z-scan technique is applied to study the saturation absorption property, presenting a modulation depth of 34.3% and a saturable fluence of 0.497 GW/cm^2 at 2.3 μm, respectively. With GaInSn nanospheres as a saturable absorber, a stable Q-switched Er:CaF_2 crystal laser operating at 2.75 μm is realized. The maximum Q-switched output power of 361 mW is obtained under the absorbed pump power of 2.9 W. The shortest pulse width of 500 ns and the highest repetition rate of 67 kHz are generated, corresponding to maximum peak power and single pulse energy of 10.78 W and 5.39 μJ, respectively. These findings indicate a promising potential of GaInSn nanospheres SA for generating nanosecond mid-infrared laser pulses.

KEYWORDS

3 μm mid-infrared laser, GaInSn nanospheres, liquid metal, passively Q-switched lasers, saturable absorber

Introduction

The mid-infrared (MIR) pulsed lasers play a crucial role in technological developments because of its wide application value in environmental monitoring, optoelectronic countermeasure, space communication, frontier physics, and so on [1–5]. Especially, the high absorption coefficient of water at 3 μm makes it great potential to be utilized in medical treatments. An effective and concise way to acquire high energy pulsed lasers is the passively Q-switched (PQS) method in which the saturable absorber (SA) is the key component. For the past few years, SAs based on one-dimensional (1D) and two-dimensional (2D) materials have attracted much attention and some encouraging application results in the mid-infrared region have been demonstrated [6–10]. However, there are still some intrinsic drawbacks which limit their further application. For example, the weak absorption efficiency of graphene, the selective absorption of carbon nanotubes, the heavy inherent defects of TIs, and the instability of BP in the ambient environment need to be improved [11]. Besides, zero-dimensional metal nanoparticles have been studied and then applied to realize mid-infrared pulsed lasers due to their localized surface plasmon resonance (LSPR). In 2018, Duan *et al.* realized a 734 ns

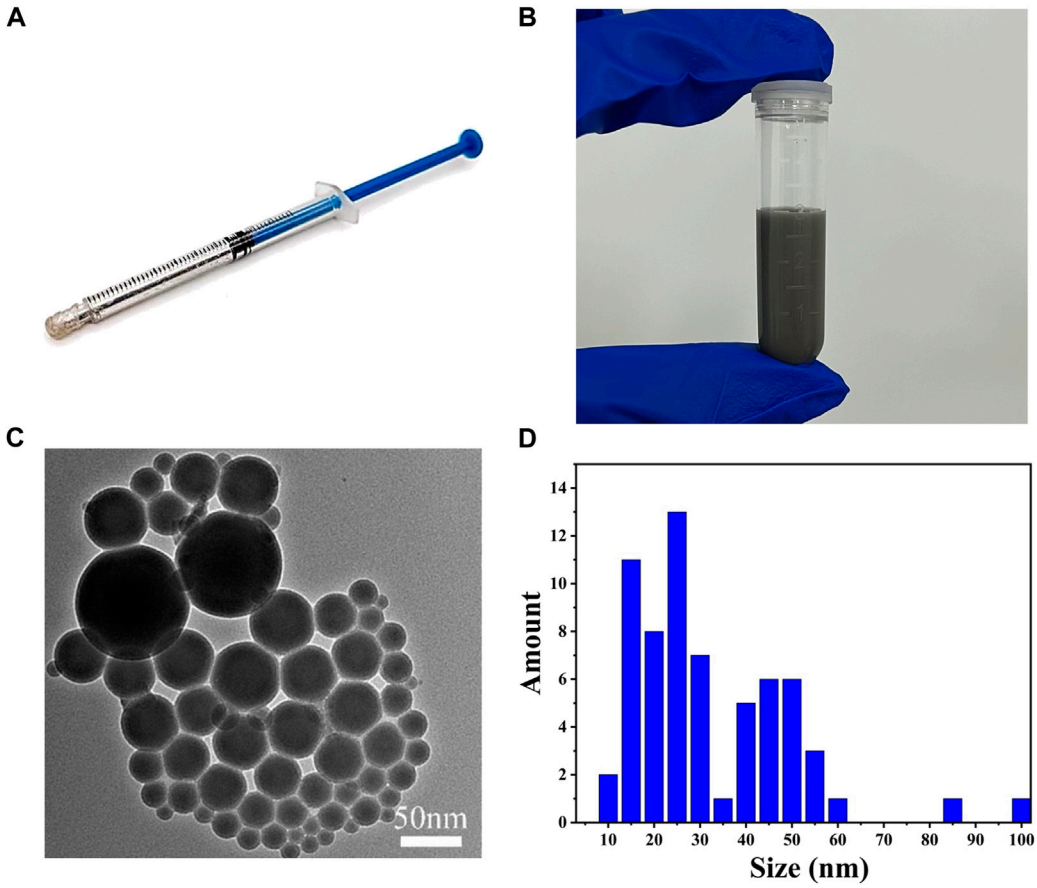

FIGURE 1
(A) GaInSn liquid alloy encapsulated in needle tubing. **(B)** As-prepared suspension of the GaInSn nanospheres. **(C)** TEM image. **(D)** The corresponding size distribution.

Q-switched Ho,Pr:LLF laser at 3 μm by using gold nanoparticles (Au-NPs) as a SA [11]. In addition, a 2 μm Q-switched laser based on Ag-NPs SA has also been developed [12]. Nevertheless, the disadvantage of the high cost of these noble metals has limited the incentive for further research.

In recent years, a novel nano-liquid metal material, GaInSn, has attracted great attention due to its excellent physico-chemical properties [13–16]. Nevertheless, most studies on GaInSn have focused on electrons and thermal conductivity, while few researches have been done on its nonlinear optical properties. Similar to the properties of most zero-dimensional materials, the saturation absorption characteristics of GaInSn nanospheres are also caused by LSPR [17]. It is worth noting that the amorphous form and high ductility of the liquid metal materials could produce diverse plasma microcavities, which may exhibit a broader LSPR response region than the traditional nanometals, such as Au-NPs and Ag-NPs. In 2020, Zhang *et al.* reported broadband saturation absorption characteristics of the GaInSn nanospheres and successfully realized Q-switched laser operations at 1.3 μm and 2 μm, separately [17]. Considering its broader LSPR response range, the nonlinear optical properties at ~3 μm, especially its performance as a SA applied in a Q-switched pulse laser, need to be further investigated.

In this paper, high-quality GaInSn nanospheres were successfully prepared by the ultrasonic method. The saturation absorption property of the GaInSn nanospheres was measured via the open-aperture Z-scan technique, presenting a modulation depth of 34.3% and a saturable fluence of 0.497 GW/cm^2, respectively. By utilizing GaInSn nanospheres as a SA in a 2.75 μm all-solid-state laser, a maximum Q-switched output power of 361 mW was obtained with the shortest pulse width of 500 ns.

Characterization of liquid metal GaInSn nanospheres

The GaInSn nanospheres were fabricated by the ultrasonic method. The ultrasonic method is a simple, rapid, and large-scale

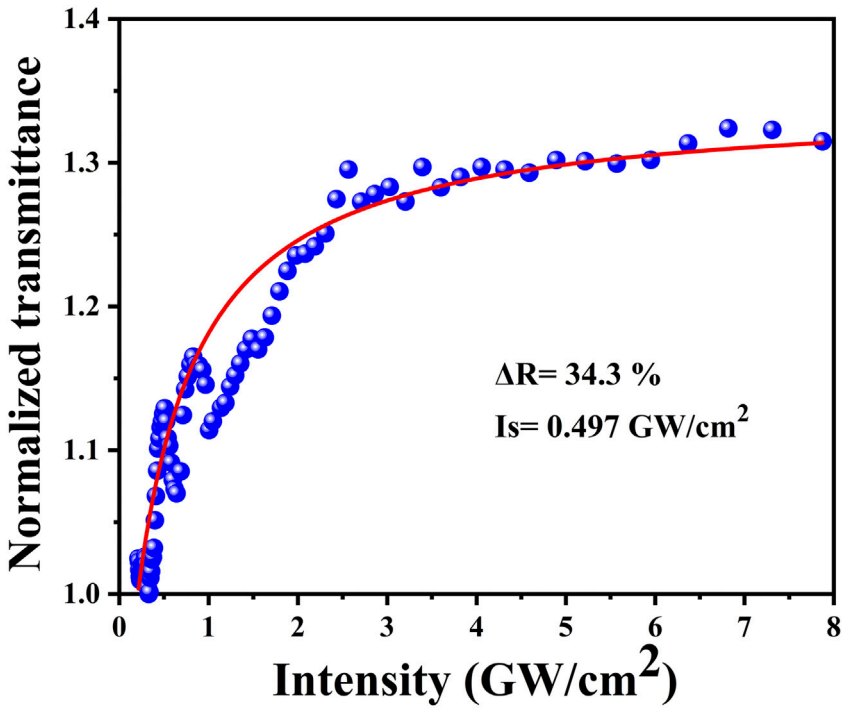

FIGURE 2
The normalized nonlinear transmittance versus the pump energy intensity.

method for the preparation of liquid metal nanospheres. First, the three metals were mixed with the proportions of 68% Ga, 22% In, and 10% Sn and then heated for 10 min at 350°C to form GaInSn alloy. The prepared alloy was encapsulated in a needle tubing, as shown in Figure 1A. To comminute it into nanospheres, the alloy was subjected to ultrasonic in acetone for 20 h. By optimizing the ultrasonic process parameters and multiple sedimentations, GaInSn nanospheres with uniform shapes and diameters less than 100 nm could be obtained. Figure 1B displays the suspension of the GaInSn nanospheres. The morphology of GaInSn nanospheres was characterized by transmission electron microscope (TEM), as described in Figure 1C. The TEM image showed that the as-prepared GaInSn nanospheres were almost spherical and the corresponding size distribution was illustrated in Figure 1D.

To explore the nonlinear saturable absorption property of the as-prepared GaInSn nanospheres, the open-aperture Z-scan technique was employed. The longest wavelength of the optical parametric laser applied in our Z-scan measurement is at 2.3 μm with a pulse width of 120 fs and a repetition rate of 5 kHz. The saturation absorption curve at 2.3 μm was fitted by the following formula [18]:

$$T(I) = 1 - \frac{\Delta R}{1 + I/I_s} - A_{ns}$$

where I_s, ΔR, and A_{ns} represent saturable fluence, modulation depth, and non-saturable loss, respectively. The saturation fluence and modulation depth of the as-prepared GaInSn nanospheres was fitted to be 0.497 GW/cm^2 and 34.3%, respectively. The fitting curve was shown in Figure 2. The experimental results confirm that the GaInSn nanospheres possess excellent saturation absorption characteristics and could be adopted as a saturable absorber in the mid-infrared range.

Experimental setup

The experimental setup of the GaInSn nanospheres Q-switched Er:CaF_2 laser was illustrated in Figure 3. A 3 × 3 × 11 mm^3 Er:CaF_2 crystal with a doped concentration of 1.7 at % was employed and both end surfaces of the laser crystal were well polished. To mitigate the thermal load, the laser crystal was wrapped with indium foil and embedded in a copper fixture. The copper was water-cooled with a temperature of 12.8°C. A plane-concave laser cavity was selected with the cavity length of 23 mm. The input mirror (IM) had a curvature radius of R = −100 mm with anti-reflectivity (AR) coated around 972 nm and high reflectivity (HR) coated near 3 μm. Three plane mirrors were adopted as output couplers (OCs) with different transmittance of

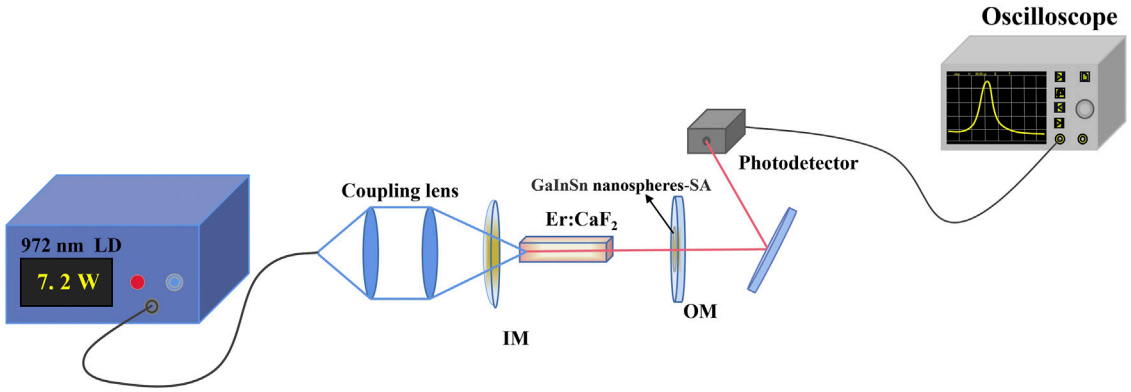

FIGURE 3
Schematic diagram of the GaInSn nanospheres Q-switched Er:CaF_2 laser.

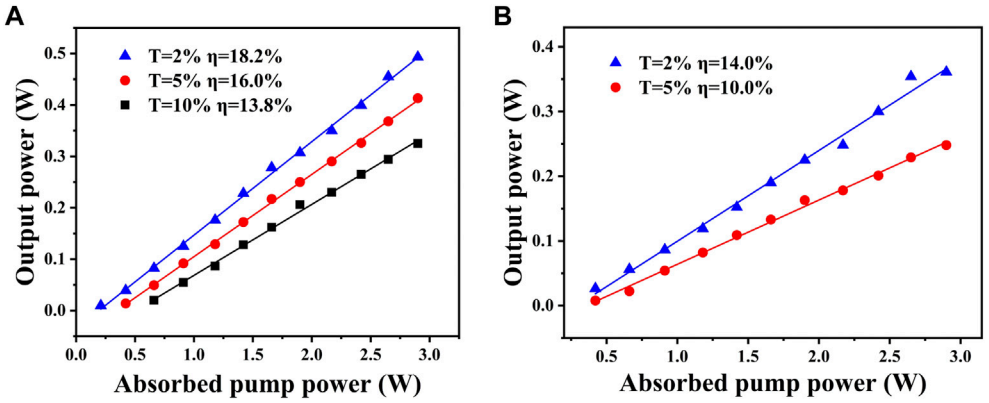

FIGURE 4
The dependence of output power on absorbed pump power for **(A)** CW laser, **(B)** PQS laser.

2%, 5%, and 10% at 2.8–3.0 μm. The pump source was a commercial 972 nm fiber-coupled laser diode (LD) with a numerical aperture (N.A.) of 0.22 and core diameter of 200 μm. The pump light was focused into the Er:CaF_2 crystal with a diameter size of 400 μm by an optical couple lenses. Moreover, a dichroic beam splitter was placed behind OCs to filter the residual pump light.

Results and discussions

The CW laser output power was first achieved by using the three different transmittances of OCs. The absorption efficiency of the Er:CaF_2 crystal at 972 nm was measured to be about 54.8%. Figure 4A shows the variation of average output powers with absorbed pump powers. In order to prevent the crystal from thermal damage, the absorbed pump power was limited to 2.9 W. Under a maximum absorbed pump power, a maximum average output power of 0.493 W was achieved with an output mirror transmittance of 2%, corresponding to a slope efficiency of 18.2% and an optical-to-optical conversion efficiency of 9.6%.

The GaInSn nanospheres were directly spin-coating on the two output couplers with the transmittance of 2% and 5%, which can reduce insertion loss. The relationships between Q-switching output powers and absorbed pump power are displayed in Figure 4B. Under a maximum absorbed pump power of 2.9 W, the highest Q-switching output power of 0.361 W was achieved with the transmission of 2%, corresponding to a slope efficiency of 14%. The slope efficiency is much higher than the previous result obtained by Graphene as SA [19], which may attribute to the low insertion loss of the GaInSn nanospheres.

A mid-infrared detector (VIGO System S.A., PVI-4TE-6) with a response time of 50 ns was used to detect the signal and the Q-switched pulses were synchronously displayed on a digital

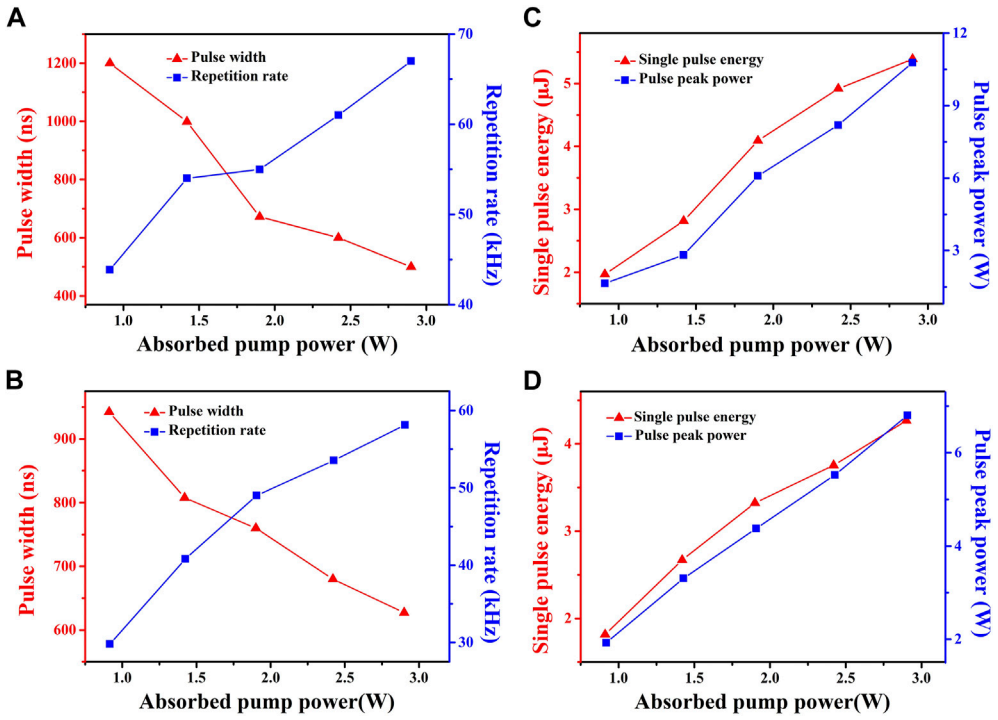

FIGURE 5
Pulse repetition rate and pulse duration versus absorbed pump power at **(A)** T = 2%, **(B)**T = 5%; the dependence of pulse energy and peak power on the absorbed pump power at **(C)** T = 2%, **(D)**T = 5%.

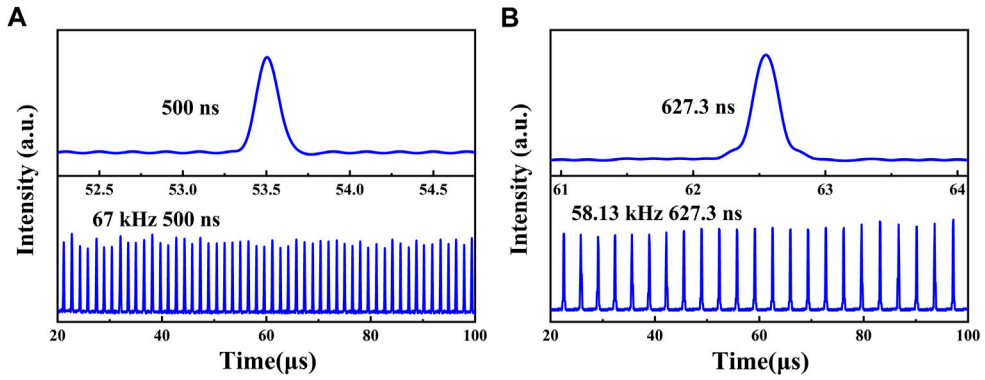

FIGURE 6
Typical pulse trains and single pulse profiles **(A)** T = 2%, **(B)** T = 5%.

oscilloscope (Rohde & Schwarz, RTO2012, 1 GHz bandwidth, 10 Gs/s sampling rates). Figure 5A,B show the pulse width and pulse repetition frequency as a function of the absorbed pump power. The pulse repetition rate increased with increasing absorbed pump power, while the pulse width decreased. Under the maximum absorbed pump power, the shortest pulse width and maximum pulse repetition rate with the transmittance of 2% are 500 ns and 67 kHz, respectively. A maximum single-pulse energy was reached to 5.39 μJ, corresponding to a maximum peak power of 10.78 W, as

described in Figure 5C,D. Typical pulse trains and a single pulse profile in Q-switching operation are illustrated in Figure 6. The output performance of Q-switched laser is obviously superior to that of graphene and graphdiyne as SA [19–21]. Beyond the absorbed pump power of 2.9 W, the pulse width increased, which resulted from the full saturation of the SA and the thermal lens effect in the gain medium. The regular Q-switched pulse could be recovered by slightly decreasing the pump power.

Conclusion

In conclusion, high-quality GaInSn nanospheres were fabricated by employing the ultrasonic method. The saturation absorption property and its application as a Q-switcher in the mid-infrared region were demonstrated. The saturation absorption property at 2.3 μm was studied through the open aperture Z-scan technique, presenting a saturable intensity and a modulation depth of 0.497 GW/cm^2 and 34.3%, respectively. Using the OC transmittance of 2%, the maximum Q-switching output power of 0.361 W was obtained, corresponding to a slope efficiency of 14%. The shortest pulse width of 500 ns was generated with the highest repetition rate of 67 kHz. The corresponding maximum peak power and single pulse energy were 10.78 W and 5.39 μJ, respectively. The findings indicate that the GaInSn nanospheres could act as an outstanding optical switcher device at 2.75 μm, which may help to explore potential applications in mid-infrared nonlinear optics.

Data availability statement

The original contributions presented in the study are included in the article/Supplementary Material, further inquiries can be directed to the corresponding authors.

Author contributions

BC was responsible for investigation, experiment, and writing. KL was responsible for experiment and editing. YJ was responsible for review. PW was responsible for data curation. NZ was responsible for experiment. KZ was responsible for data curation. SL was responsible for conceptualization, methodology, writing, and funding acquisition. JX was responsible for experiment, data curation, and editing.

Funding

This work was supported by National Key R&D Program of China (2017YFA0303700), National Natural Science Foundation of China (62175133), the Natural Science Foundation of Shandong Province (ZR2020MF115), and the SDUST Research Fund (skr21-3-049, 2019TDJH103).

Conflict of interest

The authors declare that the research was conducted in the absence of any commercial or financial relationships that could be construed as a potential conflict of interest.

Publisher's note

All claims expressed in this article are solely those of the authors and do not necessarily represent those of their affiliated organizations, or those of the publisher, the editors and the reviewers. Any product that may be evaluated in this article, or claim that may be made by its manufacturer, is not guaranteed or endorsed by the publisher.

References

1. Fan M, Li T, Zhao S, Li G, Ma H, Gao X, et al. Watt-level passively Q-switched Er:Lu_2O_3 laser at 2.84 μm using MoS_2. *Opt Lett* (2016) 41:540. doi:10.1364/OL.41.000540

2. Schliesser A, Picqué N, Hänsch TW. Mid-infrared frequency combs. *Nat Photon* (2012) 6:440–9. doi:10.1038/nphoton.2012.142

3. Arslanov DD, Spunei M, Mandon J, Cristescu SM, Persijn ST, Harren FJM. Continuous-wave optical parametric oscillator based infrared spectroscopy for sensitive molecular gas sensing: Cw OPO spectroscopy for chemical gas sensing. *Laser Photon Rev* (2013) 7:188–206. doi:10.1002/lpor.201100036

4. Popmintchev T, Chen M-C, Popmintchev D, Arpin P, Brown S, Ališauskas S, et al. Bright coherent ultrahigh harmonics in the keV X-ray regime from mid-infrared femtosecond lasers. *Science* (2012) 336:1287–91. doi:10.1126/science.1218497

5. Li X, Guo Y, Ren J, Liu J, Wang C, Zhang H, et al. Narrow-bandgap materials for optoelectronics applications. *Front Phys (Beijing)* (2022) 17:13304. doi:10.1007/s11467-021-1055-z

6. Yao Y, Zhang F, Chen B, Zhao Y, Cui N, Sun D, et al. Nonlinear optical property and mid-infrared Q-switched laser application at 2.8 μm of $PtSe_2$ material. *Opt Laser Tech* (2021) 139:106983. doi:10.1016/j.optlastec.2021.106983

7. Yao Y, Li X, Song R, Cui N, Liu S, Zhang H, et al. The energy band structure analysis and 2 μm Q-switched laser application of layered rhenium diselenide. *RSC Adv* (2019) 9:14417–21. doi:10.1039/C9RA02311A

8. Fan M, Li T, Zhao S, Li G, Gao X, Yang K, et al. Multilayer black phosphorus as saturable absorber for an Er:Lu_2O_3 laser at ~3 μm. *Photon Res* (2016) 4:181. doi:10.1364/PRJ.4.000181

9. Fan M, Li T, Li G, Zhao S, Yang K, Zhang S, et al. Passively Q-switched Ho, Pr:$LiLuF_4$ laser with graphitic carbon nitride nanosheet film. *Opt Express* (2017) 25:12796. doi:10.1364/OE.25.012796

10. Liu J, Liu J, Guo Z, Zhang H, Ma W, Wang J, et al. Dual-wavelength Q-switched Er:SrF_2 laser with a black phosphorus absorber in the mid-infrared region. *Opt Express* (2016) 24:30289. doi:10.1364/OE.24.030289

11. Duan W, Nie H, Sun X, Zhang B, He G, Yang Q, et al. Passively Q-switched mid-infrared laser pulse generation with gold nanospheres as a saturable absorber. *Opt Lett* (2018) 43:1179. doi:10.1364/OL.43.001179

12. Ahmad H, Samion MZ, Muhamad A, Sharbirin AS, Ismail MF. Passively Q-switched thulium-doped fiber laser with silver-nanoparticle film as the saturable absorber for operation at 2.0 μm. *Laser Phys Lett* (2016) 13:126201. doi:10.1088/1612-2011/13/12/126201

13. Chen B, Wang P, Zhang N, Li K, Zhang K, Liu S, et al. GaInSn liquid nanospheres as a saturable absorber for Q-switched pulse generation at 639 nm. *Opt Express* (2022) 30:28242. doi:10.1364/OE.467944

14. Liu Y, Chen H, Zhang H, Li Y. Heat transfer performance of lotus-type porous copper heat sink with liquid GaInSn coolant. *Int J Heat Mass Transfer* (2015) 80: 605–13. doi:10.1016/j.ijheatmasstransfer.2014.09.058

15. Zavabeti A, Daeneke T, Chrimes AF, O'Mullane AP, Zhen Ou J, Mitchell A, et al. Ionic imbalance induced self-propulsion of liquid metals. *Nat Commun* (2016) 7:12402. doi:10.1038/ncomms12402

16. Ou M, Qiu W, Huang K, Feng H, Chu S. Ultrastretchable liquid metal electrical conductors built-in cloth fiber networks for wearable electronics. *ACS Appl Mater Inter* (2020) 12:7673–8. doi:10.1021/acsami.9b17634

17. Zhang T, Wang M, Xue Y, Xu J, Xie Z, Zhu S. Liquid metal as a broadband saturable absorber for passively Q-switched lasers. *Chin Opt Lett* (2020) 18:111901. doi:10.3788/COL202018.111901

18. Liu S, Cui N, Liu S, Wang P, Dong L, Chen B, et al. Nonlinear optical properties and passively Q-switched laser application of a layered molybdenum carbide at 639 nm. *Opt Lett* (2022) 47:1830. doi:10.1364/ol.454047

19. Li C, Liu J, Jiang S, Xu S, Ma W, Wang J, et al. 2.8 μm passively Q-switched Er:CaF_2 diode-pumped laser. *Opt Mater Express* (2016) 6:1570. doi:10.1364/OME.6.001570

20. Zong M, Yang X, Liu J, Zhang Z, Jiang S, Liu J, et al. Er:CaF_2 single-crystal fiber Q-switched laser with diode pumping in the mid-infrared region. *J Lumin* (2020) 227:117519. doi:10.1016/j.jlumin.2020.117519

21. Zong M, Zu Y, Guo J, Zhang Z, Liu J, Ge Y, et al. Broadband nonlinear optical response of graphdiyne for mid-infrared solid-state lasers. *Sci China Phys Mech Astron* (2021) 64:294214. doi:10.1007/s11433-021-1720-3

frontiers | Frontiers in Physics

TYPE Original Research
PUBLISHED 05 September 2022
DOI 10.3389/fphy.2022.999637

OPEN ACCESS

EDITED BY
Zhenxu Bai,
Hebei University of Technology, China

REVIEWED BY
Can Cui,
Hebei University of Technology, China
Chenyu Hu,
Hangzhou Institute for Advanced Study, University of Chinese Academy of Science, China

*CORRESPONDENCE
Meixuan Li,
limx@jlenu.edu.cn
Yanqiu Li,
liyanqiu@jlenu.edu.cn

SPECIALTY SECTION
This article was submitted to Optics and Photonics, a section of the journal Frontiers in Physics

RECEIVED 21 July 2022
ACCEPTED 09 August 2022
PUBLISHED 05 September 2022

CITATION
Li M, Li Y and Wang H (2022), Research on target recognition technology of GISC spectral imaging based on active laser lighting.
Front. Phys. 10:999637.
doi: 10.3389/fphy.2022.999637

Research on target recognition technology of GISC spectral imaging based on active laser lighting

Meixuan Li[1,2]*, Yanqiu Li[3]* and Hong Wang[4]

[1]Institute for Interdisciplinary Quantum Information Technology, Jilin Engineering Normal University, Changchun, China, [2]Jilin Engineering Laboratory for Quantum Information Technology, Changchun, China, [3]School of Data Science and Artificial Intelligence, Jilin Engineering Normal University, Changchun, China, [4]Department of Physics, Changchun University of Science and Technology, Changchun, China

Aiming at the application requirements of spectral imaging technology in satellite remote sensing, biomedical diagnosis, marine detection and rescue, agricultural and forestry monitoring and classification, military camouflage identification, etc., this paper uses 532 and 650 nm lasers as light sources, and uses multi-spectral intensity correlation imaging equipment—snapshot spectroscopic cameras based on ghost imaging via sparsity constraints (GISC) enable precise identification of targets. In this paper, the principle of snapshot GISC spectral imaging is expounded, and the experimental research work of GISC spectral imaging target recognition technology based on active laser illumination is carried out. The experimental results show that using a 532 nm laser as the light source to illuminate the target object can accurately identify the green target letter "I"; using a 650 nm laser as the light source to illuminate the target object can accurately identify the red target letter "Q". And gives spectral imaging results of the color target "QIT" acquired by the GISC spectroscopic camera through a single exposure at the wavelength range from 446 to 698nm, with both pseudo-color map and color fusion map. In order to further illustrate the feasibility of the experiment, the spectral distribution of the reconstructed image is analyzed, which has important practical significance and engineering value.

KEYWORDS

ghost imaging (GI), spectral imaging, target recognition, compressed sensing (CS), laser active lighting

1 Introduction

Spectral imaging technology based on ghost imaging via sparsity constraints (GISC) is a brand-new imaging system [1], which has the advantages of non-locality and strong anti-interference ability, and has great application potential in the fields of remote sensing imaging, microscopic imaging and medical imaging [2]; [3]. In GISC

spectral imaging, the spectral image information can be retrieved from the high-order correlation between detected light fields and pre-measured light fields, thus it is actually a variant of the ghost imaging [4]; [5]; [6] system. In 1988, [7] proposed spontaneous parametric downconversion (SPDC) to generate entangled two-photons, and proposed an entangled two-photon quantum correlation imaging scheme. Later, both ghost image and diffraction were demonstrated to be realized by intensity correlation using classical light sources [8]; [9]; [10]. Also, apart from the correlation algorithm, other reconstruction algorithms have been further developed. In 2017, Situ Guohai [11] proposed a "GIDL" scheme based on computational quantum correlation imaging and deep learning, which is one of the representative works in the domestic quantum correlation imaging field combined with cutting-edge technologies. In 2018, [12] combined computational imaging technology with artificial intelligence, providing a new perspective for imaging technology, which has important application prospects in the fields of sensors and data analysis. In the same year, Xu Zhuo et al. [13] proposed a new type of deep learning quantum correlation imaging combined with artificial intelligence technology, which can obtain faster and more accurate target images at low sampling rates. In addition to those studies on active illuminating ghost imaging schemes, the researchers found that collecting light information of objects illuminated by natural light can also achieve image restoration through correlation computing, which is called passive quantum correlation imaging. Furthermore, the associated image formed by this light source-less imaging mechanism has the function of a single exposure, and can obtain a multispectral, three-dimensional image. In 2014, the research group of Han Shensheng of the Shanghai Institute of Optics and Mechanics [14] proposed a snapshot-type sparsely constrained quantum correlation imaging (GISC) spectral imaging system, and verified the feasibility of the imaging scheme in principle through compression imaging experiments. In 2018, the research group [15] used an 800-m-high tethered balloon to carry a snapshot-type GISC spectroscopic camera to achieve snapshot-type passive optical multispectral quantum correlation imaging of natural scenes. In the same year, the research group [16] proposed adding a flat-field grating to the snapshot GISC spectroscopic camera, which can increase the spectral resolution to 1 nm and realize the imaging function of the GISC hyperspectral camera, but the system structure is complex, which is not conducive to engineering applications. From 2020 to 2021, the research group will improve the anti-noise capability and imaging signal-to-noise ratio of the GISC spectroscopic camera through the optimized design of the hyper-Rayleigh speckle field and polarization characteristics [17]; [18]. In this paper, 532 and 650 nm solid-state lasers are used as the light source [19], and the GISC snapshot spectroscopic camera is used to realize the accurate identification of the target and carry out experimental research work.

2 Theoretical analysis

The optical path of the GISC spectral imaging system based on active laser illumination is shown in Figure 1. The coherent light source required for the test is provided by a solid-state laser, and the reflected light irradiated on the target object is 50% reflected and 50% transmitted through the beam splitter. The transmitted light images the target scene on the area array photodetector CCD1, which is an RGB camera and is used to determine the target shooting area. The reflected light passes through the filter, so that the light beam in the range of 440–700 nm is transmitted. The diffraction optical element (DOE) randomly phase modulates the light field emitted by each point on the broadband image on the pre-imaging surface, and after modulation, forms a speckle pattern in which two-dimensional spatial information and one-dimensional spectral information are aliased. The detection signal is obtained on the area array photodetector CCD2, and then according to the detection signal and the calibration obtained measurement matrix, a high-performance server is used to obtain a three-dimensional multispectral image by means of computational imaging.[1]

The detection process of the GISC spectral imaging system can be expressed by the following formula [1]; [20]:

$$\begin{bmatrix} y_{11} \\ \vdots \\ y_{m1} \\ y_{12} \\ \vdots \\ y_{mn} \end{bmatrix} = \begin{bmatrix} a^{\lambda_1}_{11,11} & \cdots & a^{\lambda_1}_{11,p1} & a^{\lambda_1}_{11,12} & \cdots & a^{\lambda_1}_{11,pq} & \cdots & a^{\lambda_S}_{11,11} & \cdots & a^{\lambda_S}_{11,pq} \\ \vdots & & \vdots & \vdots & & \vdots & & \vdots & & \vdots \\ a^{\lambda_1}_{m1,11} & \cdots & a^{\lambda_1}_{m1,p1} & a^{\lambda_1}_{m1,12} & \cdots & a^{\lambda_1}_{m1,pq} & \cdots & a^{\lambda_S}_{m1,11} & \cdots & a^{\lambda_S}_{m1,pq} \\ a^{\lambda_1}_{12,11} & \cdots & a^{\lambda_1}_{12,p1} & a^{\lambda_1}_{12,12} & \cdots & a^{\lambda_1}_{12,pq} & \cdots & a^{\lambda_S}_{12,11} & \cdots & a^{\lambda_S}_{12,pq} \\ \vdots & & \vdots & \vdots & & \vdots & & \vdots & & \vdots \\ a^{\lambda_1}_{mn,11} & \cdots & a^{\lambda_1}_{mn,p1} & a^{\lambda_1}_{mn,12} & \cdots & a^{\lambda_1}_{mn,pq} & \cdots & a^{\lambda_S}_{mn,11} & \cdots & a^{\lambda_S}_{mn,pq} \end{bmatrix} \begin{bmatrix} x^{\lambda_1}_{11} \\ \vdots \\ x^{\lambda_1}_{p1} \\ x^{\lambda_1}_{12} \\ \vdots \\ x^{\lambda_1}_{pq} \\ \vdots \\ x^{\lambda_S}_{11} \\ \vdots \\ x^{\lambda_S}_{pq} \end{bmatrix} + \begin{bmatrix} \varepsilon_{11} \\ \vdots \\ \varepsilon_{m1} \\ \varepsilon_{12} \\ \vdots \\ \varepsilon_{mn} \end{bmatrix} \tag{1}$$

1 For the calibration, a monochormatic point source is used as the object rather than a real target, and a series of responses of the GISC camera system to the point source at different positions and wavelengths can be achieved by performing scanning-type pre-measurements.

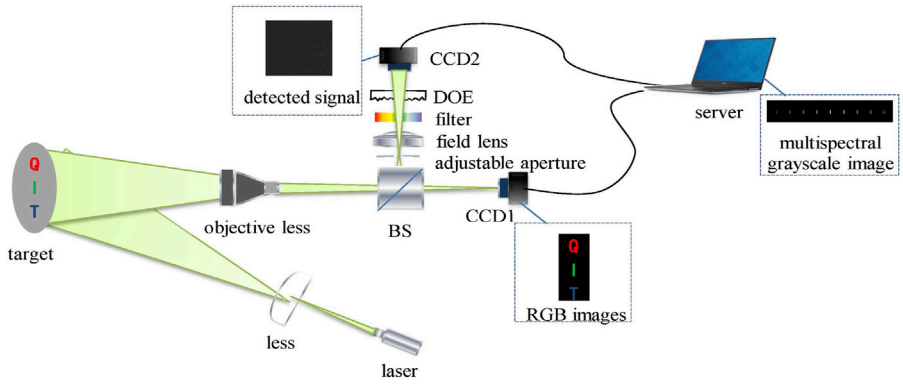

FIGURE 1
Optical path diagram of GISC spectral imaging system based on active laser illumination.

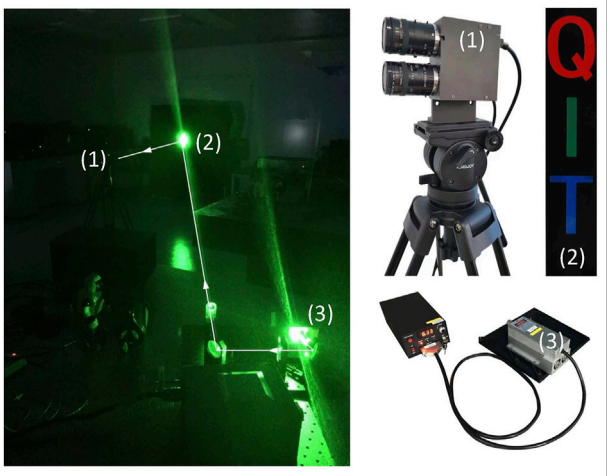

FIGURE 2
The left subfigure shows GISC spectral imaging experimental system based on active laser illumination, lights from the laser (3) pass through a reflector and an expander to illuminate the object (2), and the illuminated object is detected by the GISC camera (1). The subfigure in the right shows appearances of those three experimental parts in the left subfigure.

In the formula, $X_{pq}^{\lambda_s}(p = 1, \ldots, P, \quad q = 1, \ldots, Q)$ represents the multispectral image information reconstructed by $s(s = 1, \ldots, S)$ in the s spectral bands of the pixels in the pth row and the q column on the object surface, and $a_{mn,pq}^{\lambda_s}(m = 1, \ldots, M, \quad n = 1, \ldots, N)$ represents the point light source used for the calibration of the imaging system on the pth row and qth columns on the object surface. When moving up, the light intensity value obtained by the pixel in the mth row and nth column of the CCD on the detection surface. y_{mn} represents the intensity distribution of the detection signal in the mth row and nth column on the detection surface during imaging, ε represents probe signal noise. According to Eq. 1, the reconstruction of multispectral images can be achieved by solving the following optimization problem [21]; [1]:

$$\min_{x} \|Y - AX\|_2^2 + \mu_1 \left\|\nabla_{i,j} X\right\|_1 + \mu_2 \|X\|_*, \text{ s.t. } X \geq 0, \qquad (2)$$

where $\|\nabla_{i,j} X\|_1$ is the gradient norm, which is equivalent to extracting the segmented edge of the image, making the transformed image more sparse; $\|X\|_*$ is the matrix nuclear norm, indicating the low rank of the multispectral image matrix; μ_1, $\mu_2 \geq 0$ is the constraint item weight factor. In this paper, the TV-RANK compressed sensing algorithm is used for image reconstruction.

3 GISC spectral imaging scheme and experiment based on active laser illumination

3.1 Experimental setup

The GISC spectral imaging experimental system based on active laser illumination is shown in Figure 2. Among them, (1) is the imaging system; (2) is the target to be measured; (3) is the 532 nm solid-state laser. The experimental parameters are set as: the spectral range of the GISC camera is 440–700nm, there are 16 spectral channels, the spectral resolution is <20 nm, and the pixel resolution is ≥ 0.5 mrad. The exposure time of the camera is 1 s, and the exposure time of the RGB camera is 0.3 s. The target to be tested is the color letter "QIT", and the height of the letters is 3.3 cm. A 532 nm solid-state laser is used as the illumination light source, the target object to be measured is 3.5 m away from the imaging system, and the imaging field of view is 61 mm × 619 mm wide.

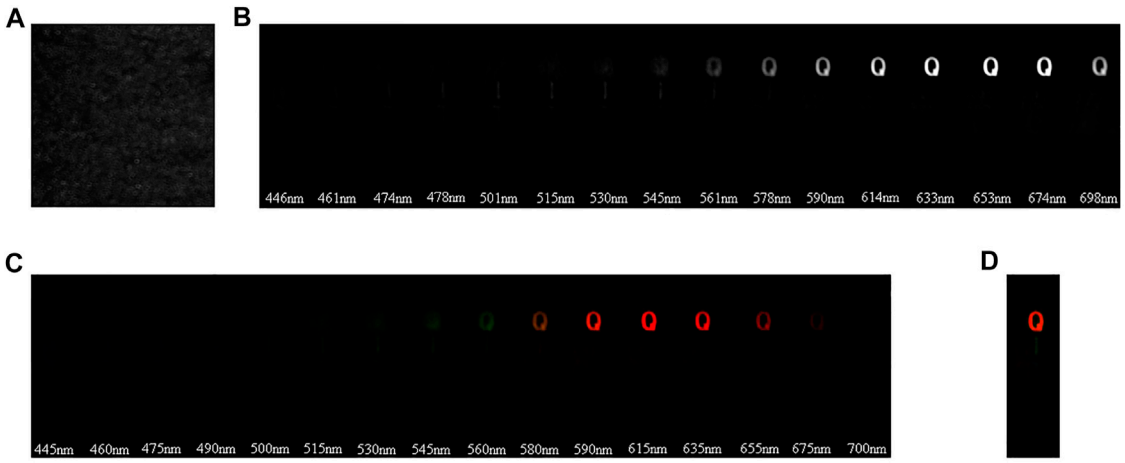

FIGURE 3
Experimental results of spectral imaging of the target object irradiated by a 532 nm laser. **(A)** Detection signal; **(B)** Spectral grayscale image; **(C)** Multispectral false color image; **(D)** Multispectral fusion image.

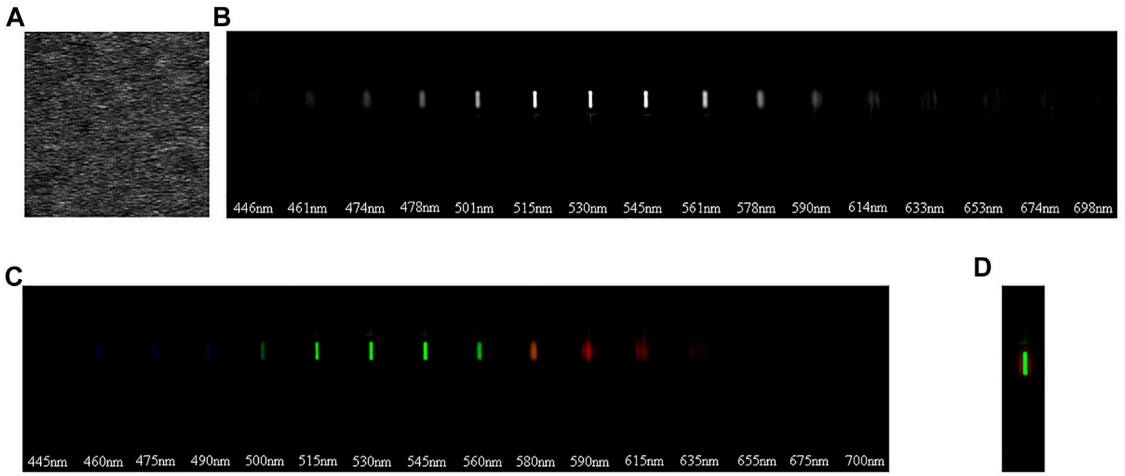

FIGURE 4
Experimental results of spectral imaging of the target object irradiated by 650 nm laser. **(A)** Detection signal; **(B)** Spectral grayscale image; **(C)** Multispectral false color image; **(D)** Multispectral fusion image.

3.2 Experimental results and data analysis

Figure 3 shows the experimental results of spectral imaging of the target object irradiated by a 532 nm laser. When the average number of electrons recorded by the CCD is 402e-, the CCD detection signal obtained by the GISC camera through a single exposure is shown in Figure 3A. The image is shown in Figure 3B; the pseudo-color corresponding to the wavelength is added to Figure 3B, and its multispectral image is shown in Figure 3C; Figure 3D is 445, 460, 475 nm, 490, 500, 515, 530, 545, 560, 580, 590, 615, 635, 655, 675, 700 nm, the color fusion map of the 16 spectral channels is compared with Figure 2 in Figure 2, the shape and spectrum of the letter I The information restoration degree is high.

Figure 4 shows the experimental results of spectral imaging of the target object irradiated by a 650 nm laser. When the average number of electrons recorded by the CCD

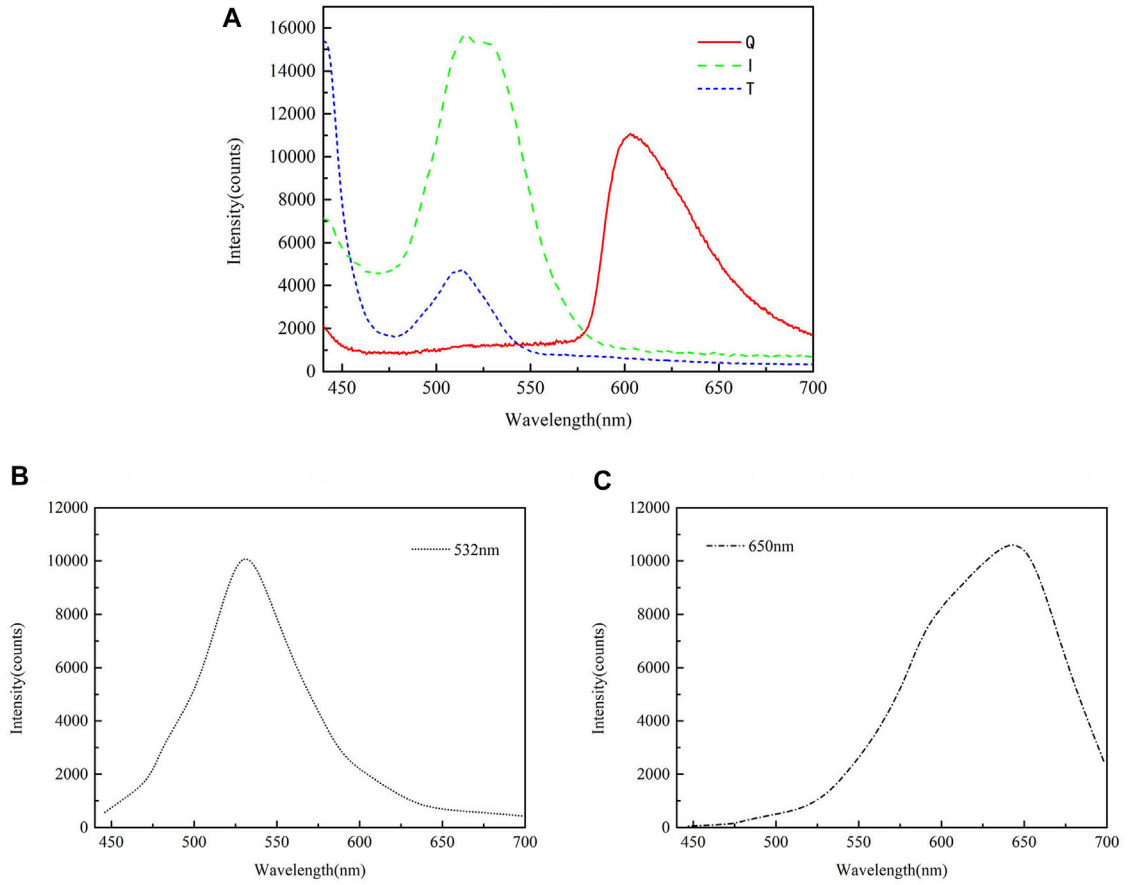

FIGURE 5
Spectral distribution of USB4000-VIS-NIR spectrometer and color targets in multispectral images. **(A)** The spectral distribution curve of letter QIT in the test target of USB4000-VIS-NIR spectrometer **(B)** The spectral distribution curve of the letter "I″ in the reconstructed image of the target object irradiated by 532 nm laser **(C)** The spectral distribution curve of the letter "Q" in the reconstructed image of the target object irradiated by 650 nm laser.

is 693e-, the CCD detection signal obtained by the GISC camera through a single exposure is shown in Figure 4A. The image is shown in Figure 4B; then add the false color corresponding to the wavelength to Figure 4B, which are 446, 461, 4745, 487, 501, 515, 530, 545, 561, 578, 590, 614 nm, 633, 653, 674, 698 nm, the multi-spectral grayscale image of 16 spectral channels is shown in Figure 4C; Figure 4D is the color fusion map compared with Figure 2 in Figure 2, the shape of the letter Q and spectral information reduction degree is high.

In order to further illustrate the feasibility of the experiment, the spectral distribution of different colors in the target object from 440 to 700 nm was tested using the USB4000-VIS-NIR spectrometer, as shown in Figure 5A. The USB4000-VIS-NIR spectrometer was tested at 532 nm, and the intensity value of the target letter "Q" was 1264, the intensity value of the letter "I" was 14919, and the intensity value of the letter "T" was 2530. The intensity value of the letter "I" is the highest at 532 nm, so the target letter "I" can be accurately identified by irradiating the target object with 532 nm laser light. The spectral distribution curve of the letter "I" in the reconstructed image of the target object irradiated by 532 nm laser light is shown in Figure 5B. The USB4000-VIS-NIR spectrometer was tested at 650 nm, and the intensity value of the target letter "Q" was 5118, the intensity value of the letter "I″ was 852, and the intensity value of the letter "T" was 405. The intensity value of the letter "Q" is the highest at 650nm, so the target letter "Q" can be accurately identified by irradiating the target object with 650 nm laser light. The spectral distribution curve of the letter "Q" in the reconstructed image of the target object irradiated by 650 nm laser light is shown in Figure 5C. Those intensity value data representing spectral information of targets are detailed listed in Table 1.

TABLE 1 List of intensity values of targets "Q" and "I" corresponding to Figure 5. Bold numbers show that the reconstructed intensity values of both letters reach the highest at the wavelengths correspond to the illuminated lasers.

Wavelength/nm	Letter "I"		Letter "Q"	
	Illuminated by LED	Illuminated by 532 nm laser	Illuminated by LED	Illuminated by 650 nm laser
446	4680	565	1470	43
461	4793	1217	907	90
474	4664	1869	852	130
481	5054	3130	847	260
501	11347	5000	1048	521
515	15670	8000	1213	695
530	15126	**10913**	1233	1173
545	10282	8695	1240	2217
561	4526	6043	1303	3521
578	1949	4000	1789	5478
590	1270	2565	7318	7652
614	940	1608	10195	9217
633	917	869	7649	10434
653	737	652	4628	**11000**
674	807	565	2966	6304
698	740	434	1758	2500

4 Conclusion

Aiming at the problems of low detection sensitivity, many sampling times and serious light energy loss in traditional spectral imaging technology, a GISC spectral imaging target recognition scheme based on active laser illumination is proposed. This scheme combines laser technology, spectral imaging technology, correlated imaging technology and compressed sensing. The combination of theory has the advantages of high energy utilization rate and fast information acquisition efficiency. The imaging principle of GISC camera is theoretically analyzed, and the GISC spectral imaging target recognition experiment based on active laser illumination is completed in the laboratory environment. The results show that by selecting the appropriate wavelength of the laser light source, the GISC spectral imaging technology can be used to accurately identify the target spectral information. Next, how to establish the imaging quality evaluation and analysis system of the experimental results is a problem that needs to be solved in the future work.

Data availability statement

The raw data supporting the conclusions of this article will be made available by the authors, without undue reservation.

Author contributions

ML and HW conceived the idea and designed the experiment. YL supervised the experiment and data analysis. HW performed the experiment. ML analyzed the data, conducted the image reconstruction. YL and ML wrote the manuscript.

Funding

This work is supported by the Department of science and technology of Jilin Province (Grant No. 20220204106YY and 20220401098YY).

Acknowledgments

The authors would like to thank Lijun Song in Jilin Engineering Laboratory for Quantum Information Technology and YL in Jilin Engineering Normal University for their meaningful discussion and helpful advice.

Conflict of interest

The authors declare that the research was conducted in the absence of any commercial or financial relationships that could be construed as a potential conflict of interest.

Publisher's note

References

1. Liu Z, Tan S, Wu J, Li E, Shen X, Han S. Spectral camera based on ghost imaging via sparsity constraints. *Sci Rep* (2016) 6:25718–0. doi:10.1038/srep25718

2. Bai Z, Williams RJ, Kitzler O, Sarang S, Spence DJ, Wang Y, et al. Diamond brillouin laser in the visible. *APL Photon* (2020) 5:031301. doi:10.1063/1.5134907

3. Chen H, Bai Z, Yang X, Ding J, Qi Y, Yan B, et al. Enhanced stimulated brillouin scattering utilizing Raman conversion in diamond. *Appl Phys Lett* (2022) 120:181103. doi:10.1063/5.0087092

4. Shapiro JH, Boyd RW. The physics of ghost imaging. *Quan Inf Process* (2012) 11:949–93. doi:10.1007/s11128-011-0356-5

5. Shih Y. The physics of ghost imaging. In: *Classical, semi-classical and quantum noise*. Berlin, Germany: Springer (2012). p. 169–222.

6. Han S, Yu H, Shen X, Liu H, Gong W, Liu Z. A review of ghost imaging via sparsity constraints. *Appl Sci* (2018) 8:1379. doi:10.3390/app8081379

7. Shih YH, Alley CO. New type of einstein-podolsky-rosen-bohm experiment using pairs of light quanta produced by optical parametric down conversion. *Phys Rev Lett* (1988) 61:2921–4. doi:10.1103/PhysRevLett.61.2921

8. Bennink RS, Bentley SJ, Boyd RW. two-photon" coincidence imaging with a classical source. *Phys Rev Lett* (2002) 89:113601. doi:10.1103/physrevlett.89.113601

9. Gatti A, Brambilla E, Bache M, Lugiato LA. Ghost imaging with thermal light: Comparing entanglement and classicalcorrelation. *Phys Rev Lett* (2004) 93:093602. doi:10.1103/physrevlett.93.093602

10. Cheng J, Han S. Incoherent coincidence imaging and its applicability in x-ray diffraction. *Phys Rev Lett* (2004) 92:093903. doi:10.1103/physrevlett.92.093903

11. Lyu M, Wang W, Wang H, Wang H, Li G, Chen N, et al. Deep-learning-based ghost imaging. *Sci Rep* (2017) 7:17865–6. doi:10.1038/s41598-017-18171-7

12. Altmann Y, McLaughlin S, Padgett MJ, Goyal VK, Hero AO, Faccio D. Quantum-inspired computational imaging. *Science* (2018) 361:eaat2298. doi:10.1126/science.aat2298

13. He Y, Wang G, Dong G, Zhu S, Chen H, Zhang A, et al. Ghost imaging based on deep learning. *Sci Rep* (2018) 8:6469–7. doi:10.1038/s41598-018-24731-2

14. Wu J, Shen X, Yu H, Liu Z, Tan S, Han S, et al. Snapshot compressive imaging by phase modulation. *Acta Optica Sinica* (2014) 34:1011005. doi:10.3788/aos201434.1011005

15. Wu J, Li E, Shen X, Yao S, Tong Z, Hu C, et al. Experimental results of the balloon-borne spectral camera based on ghost imaging via sparsity constraints. *IEEE Access* (2018) 6:68740–8. doi:10.1109/access.2018.2879849

16. Liu S, Liu Z, Wu J, Li E, Hu C, Tong Z, et al. Hyperspectral ghost imaging camera based on a flat-field grating. *Opt Express* (2018) 26:17705–16. doi:10.1364/oe.26.017705

17. Liu S, Liu Z, Hu C, Li E, Shen X, Han S. Spectral ghost imaging camera with super-Rayleigh modulator. *Opt Commun* (2020) 472:126017. doi:10.1016/j.optcom.2020.126017

18. Chu C, Liu S, Liu Z, Hu C, Zhao Y, Han S. Spectral polarization camera based on ghost imaging via sparsity constraints. *Appl Opt* (2021) 60:4632–8. doi:10.1364/ao.417022

19. Cui C, Wang Y, Lu Z, Bai Z, Yuan H, Chen Y, et al. High-visibility pseudothermal light source based on a cr4+: Yag passively q-switched single-longitudinal-mode laser. *Int J Opt* (2020) 2020:1–7. doi:10.1155/2020/3160837

20. Meixuan L, Hong W, Xiaohan L, Ming L, Lijun S. Research on multispectral correlation imaging of moving target based on phase modulation. *Infrared Laser Eng* (2021) 50:20210184–1.

21. Tan S. *The application research of structured compressed sensing in multispectral ghost imaging*. Ph.D. thesis. Shanghai: Shanghai Institute of Optics and Fine Mechanics, University of Chinese Academy of Sciences (2015).

frontiers | Frontiers in Physics

TYPE Brief Research Report
PUBLISHED 28 September 2022
DOI 10.3389/fphy.2022.1019480

OPEN ACCESS

EDITED BY
Baitao Zhang,
Shandong University, China

REVIEWED BY
Xinmin Fan,
Weifang University, China
Hong Zhang,
Sichuan University, China

*CORRESPONDENCE
Chengyu Zhu,
zhuchy@hit.edu.cn

SPECIALTY SECTION
This article was submitted to Optics and Photonics,
a section of the journal
Frontiers in Physics

RECEIVED 15 August 2022
ACCEPTED 12 September 2022
PUBLISHED 28 September 2022

CITATION
Yuan H, Hao J, Dan Z, Zhu C and Li Y (2022), Theoretical studies of high-power laser beam smoothing via stimulated brillouin scattering in plasma. *Front. Phys.* 10:1019480.
doi: 10.3389/fphy.2022.1019480

Theoretical studies of high-power laser beam smoothing *via* stimulated brillouin scattering in plasma

Hang Yuan, Jianing Hao, Ziqiang Dan, Chengyu Zhu* and Yuxin Li

National Key Laboratory of Science and Technology on Tunable Laser, Harbin Institute of Technology, Harbin, China

To achieve uniform irradiation, the focal spot from a high-power laser system must be homogeneous; thus, laser beam smoothing is required. In this study, we theoretically demonstrated a novel spatial smoothing method based on stimulated Brillouin scattering (SBS) in a plasma. As SBS is sensitive to pump intensity, the area of higher intensity in the laser beam has a higher reflectivity, leading to a more homogeneous passed beam. From the theoretical simulation, the laser beam modulation significantly decreased in SBS, while the fluence contrast decreased from 15.9% to 9.7%.

KEYWORDS

stimulated brillouin scattering, beam smoothing, high power laser, plasma, nonlinear optics

Introduction

Inertial confinement fusion requires perfectly controlled laser beams to compress a deuterium-tritium target and achieve nuclear fusion. Laser fusion has extremely high energy requirements. From theoretical analysis, the laser energy deposition must be above 1 MJ, and is spread to dozens of beams. Generally, the energy of a single beam is approximately 10 kJ in high-power laser systems, such as the National Ignition Facility (NIF) [1], Laser MegaJoule [2, 3] and SG-III [4, 5].

The construction of such a system requires specific development of optical techniques. Before the laser energy is deposited at the target, the laser beam undergoes a frequency conversion of the third harmonic (3ω) to 351 nm. After the third harmonic, the UV optical module has the highest risk of damage to the entire system. In actual laser system operation, the laser flux is far below the optical element bulk damage threshold, and most optical damage originates from defects in the subsurface microstructure [6–8]. The laser spatial modulation caused by frequency conversion and beam coherence increases the local laser light intensity, which further increases the optical damage risk.

To reduce the optical damage risk, optical beam smoothing techniques such as liquid crystal spatial light modulators (SLMs) can help improve the near-field beam quality before the main amplifier system [9, 10]. A continuous phase plate (CPP) [11] and

smoothing via spectral dispersion [12] have been developed and applied in engineering to realize homogeneous focal spots. However, SLMs have low laser energy transmittance [13]. The smoothing element (e.g., CPP) itself also suffers from damage risk. Moreover, such elements involve complex processing procedures, so any corresponding damage is difficult to repair.

The processing of traditional optical materials has faced bottlenecks: plasma, as an ionized substance, has almost no damage threshold. Accordingly, the plasma density and temperature span are extremely large, which significantly affect interaction of the laser [14–16]. Therefore, making full use of the plasma is crucial to improve laser beam performance [17].

In this study, we developed an optical smoothing method with high energy efficiency based on stimulated Brillouin scattering (SBS) in plasma. SBS, excited by the interaction of the standing wave acoustic field formed by ions, can be applied for beam smoothing. Because SBS has a significant threshold characteristic, scattering is proportional to the square of the injected laser intensity [18–21]. The transmitted light power is restricted to a certain level. Thus, high-frequency modulation of the near-field of the laser can be reduced, and optical smoothing can be achieved.

Theory

During propagation of a 351-nm (3ω) laser with high photon energy, traditional liquid or solid medium are not suitable. For liquid Brillouin medium, the weaker chemical bonds in medium (eg., heavy fluorocarbon) has a greater probability of being directly broken down. For solid Brillouin medium, this pump intensity is easily to cause irreversible damage to components.

The nonlinear effect in the plasma can manifest an "optical limiting" effect, demonstrating beam smoothing. In comparison with the traditional liquid or solid Brillouin medium, the backscattering angle of the SBS in plasma will be larger. The effect of nonlinear scattering further destroys the spatial and temporal coherence of the main laser and enhances the beam smoothing effect.

To theoretically simulate laser beam smoothing in plasma, coupling of the electromagnetic wave equation and the ion acoustic wave equation was realized as follows:

$$\left(\frac{\partial^2}{\partial t^2} - c^2\nabla^2 + \omega_{pe}^2\right)\vec{A}_s = -\frac{4\pi e^2}{m_e}\tilde{n}_e\vec{A}_0 \tag{1}$$

$$\left(\frac{\partial^2}{\partial t^2} - C_s^2\nabla^2\right)\tilde{n}_e = -\frac{Zn_0e^2}{m_im_ec^2}\nabla^2\left(\vec{A}_0\cdot\vec{A}_s\right) \tag{2}$$

where $\vec{A}_0$and $\vec{A}_S$are the incident and scattered light wavefield vector potentials, respectively; $\tilde{n}_0/\tilde{n}_e$represents the density disturbance of the plasma; C_s is the ion speed of sound; Z is the ionic charge; m_i is the ion mass; m_e is the electron mass; and ω_{pe} is the plasma frequency.

At the strong damping limit, the vibration and density perturbation of electrons can be expressed using the same formula for both the electron plasma wave and the ion plasma soundwave as:

$$\tilde{n}_e = -\frac{k^2e^2}{m_e^2c^2\omega_{pe}^2}\frac{\chi_e(1+\chi_i)}{\varepsilon}a_0a_s^* \tag{3}$$

where a_0 and a_s represent the ramping amplitudes of the pump and scattered light, respectively; χ_e and χ_i represent the electron and ion polarizability, respectively; and $\varepsilon = 1+\chi_e+\chi_i$ is the dielectric function of the plasma.

The energy flow is expressed as: $J_0 = \omega_0\nu_{g0}|a_0|^2$, and $J_s = \omega_s\nu_{gs}|a_s|^2$.

Under one-dimensional (1D) conditions, ignoring the time differential term yields the following equation:

$$\frac{\partial|J_s|}{\partial x} = \frac{k^2e^2}{m_e^2c^2\omega_s\nu_{gs}}\mathrm{Im}\left[\frac{\chi_e(1+\chi_i)}{\varepsilon}\right]|a_0|^2 \tag{4}$$

The above equation was solved to obtain:

$$|J_S(0)| = |J_S(L)|\times\exp(\mathrm{G}) \tag{5}$$

$$G = -\int_0^L\frac{k^2e^2|a_0|^2}{m_e^2c^2\omega_s\nu_{gs}}\mathrm{Im}\left[\frac{\chi_e(1+\chi_i)}{\varepsilon}\right]dx \tag{6}$$

$$G_{SBS} \approx \frac{1}{8}\frac{\omega_0}{c}\frac{n_e}{n_c}\frac{v_0^2}{v_{te}^2}\frac{\omega_{IAW}}{\nu_{IAW}}L \tag{7}$$

where n_e/n_c is the electron density normalized to the critical density of the interaction wavelength. The scattering intensity and energy reflectivity of the plasma SBS can be estimated using the gain, and the influence of nonlinear scattering on the light field distribution can be numerically analyzed.

The injected and the scattered light are given by:

$$J_0(x) = J_0(0) + J_S(0) - J_S(x) \tag{8}$$

$$\frac{\partial|\bar{J}_S|}{\partial x} = -\Gamma[1-|\bar{J}_S(0)| + |\bar{J}_S|]|\bar{J}_S| \tag{9}$$

$$\Gamma = \frac{k^2e^2|a_0|^2}{m_e^2c^2\omega_s\nu_{gs}}\mathrm{Im}\left[\frac{\chi_e(1+\chi_i)}{\varepsilon}\right] \tag{10}$$

Using the above 1D model, SBS of light and the respective properties could be theoretically simulated.

Numerical simulation and analysis

A schematic of plasma SBS beam smoothing is presented in Figure 1. The laser beam was amplified, and the third harmonic was obtained before it was focused on the target. The plasma-smoothing cell was placed in the focused path to realize nonlinear effects in the plasma, which requires a high-power laser, and the plasma was excited using a femtosecond laser. A laser beam with space modulation was introduced into the plasma-smoothing cell. Additionally, an isolator was

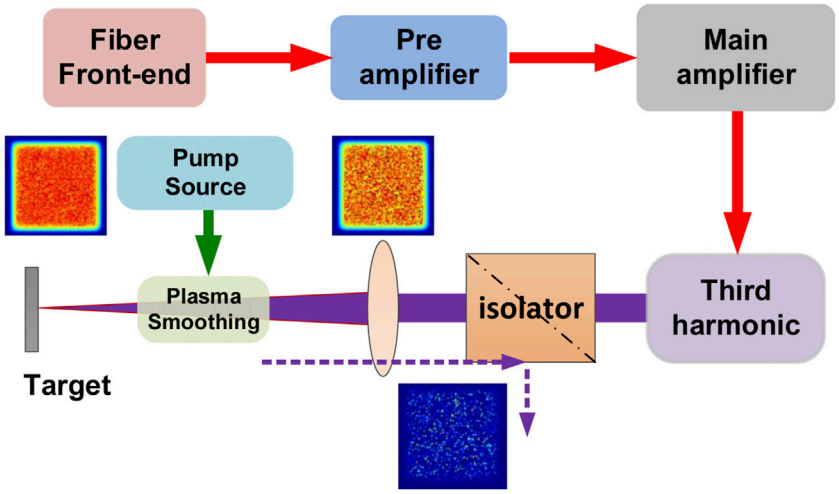

FIGURE 1
Schematic of simulated Brillouin scattering in plasma for beam smoothing.

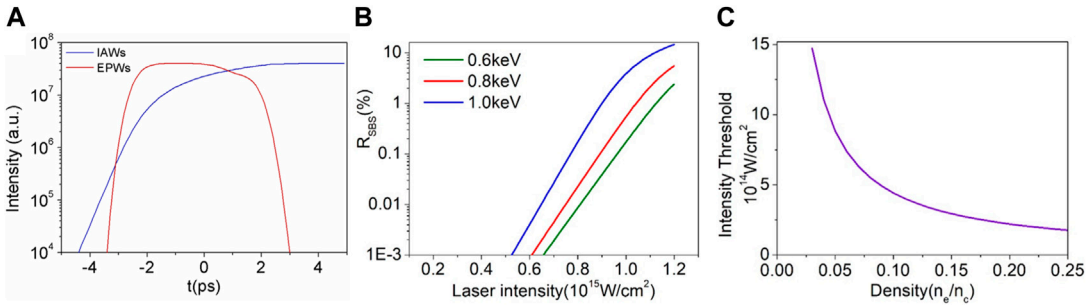

FIGURE 2
Theoretical simulation results of SBS proprieties in plasma. **(A)** Temporal evolution of scattered intensities of ion acoustic waves (IAWs) and electron plasma wave (EPW) driven by the 2-ps laser pulse. **(B)** Reflectivity results as a function of laser intensity for T_e of 0.6, 0.8, and 1.0 keV. **(C)** Intensity at which SBS reaches 1% (intensity threshold) as a function of plasma density.

employed to prevent scattered light. Owing to the threshold properties of the SBS, hotspots in the laser beam exhibited higher reflectivity. The transmitted laser was then smoothed according to this optical limiting property.

For SBS in plasma, the Stokes signal arises from the ion acoustic wave that interacts with the injected laser. Figure 2A presents the theoretically simulated ion acoustic wave (IAW) with SBS at the pump intensity of 10^{17} W/cm^2 and FWHM Gaussian laser pulse of 2 ps. The intensities of the driven waves were plotted as a function of time, and $t = 0$ refers to the peak of the pump pulse. In theoretical simulation, since the electron mass is much smaller than the ion mass, the temporal evolution of EPWs(electron plasma wave) has a short relaxation time. When the pump laser injection is over, it doesn't last for a while like IAW, but it decays quickly and fades away. It can be observed that IAWs grow slowly and develop over 3 ps before reaching the saturation area. As the pump pulse falls, IAWs remain in the plasma and dampen slowly. The IAW decay time is much longer than the pump laser falling time, which is comparable to that of Landau damping $T_e >> T_i$, and no ions move at the phase velocity rate. Thus, in the simulation, the ion movement can be regarded as a steady state.

By numerically solving the electromagnetic wave equation and the ion acoustic wave equation, the SBS reflectivity was found to vary with the injected laser intensity at different temperatures, as detailed in Figure 2. The normalized electron density n_e/n_c was set to 8%. As can be seen in Figure 2B, the SBS threshold decreased with an increase in the plasma temperature. Apparent optical limiting characteristics can be achieved by controlling the laser intensity distribution around 0.5–1.5 × 10^{15} GW/cm^2.

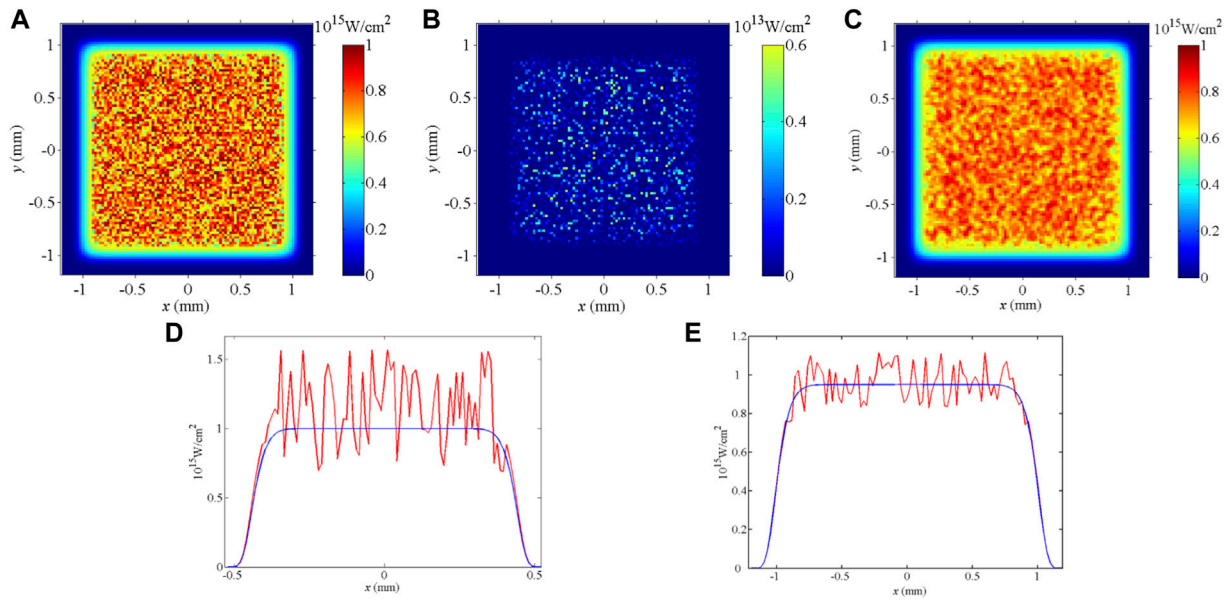

FIGURE 3
Intensity distributions of laser beam: **(A)** injected laser beam; **(B)** scattered laser beam; **(C)** output smoothed laser beam; **(D)** 1D curve of injected light; **(E)** 1D curve of output light. To quantitatively analyze the beam smoothing effect, the fractional power above intensity (FOPAI) was evaluated using Eq. 11.

Using these simulation results, the pump laser and plasma parameters could be set.

Figure 2C shows that the intensity threshold strongly depends on the plasma density. The electron density was simulated in a 1-mm-long target and varied from 3% to 25% n_c. The plasma temperature was maintained at 1 keV. The SBS reflectivity above was determined as the SBS threshold. This indicates that the SBS threshold decreased quickly before 10%n_c. In the density range of 10%n_c, the thresholds decreased slowly with increasing plasma density. Instantaneous backscatter was determined at the saturation part of the IAWs. It was demonstrated that the increase in scattering was sensitive to the laser intensity and plasma density.

Based on the simulation results in Figure 2, the properties of SBS in plasma depend on the plasma temperature and density. SBS in plasma is driven by the ion acoustic waves. The intensity of ion acoustic waves are affected by the plasma temperature and density and will significantly affect Brillouin gain in plasma. These parameters significantly influence the SBS reflectivity and threshold values [18, 19]. To apply this beam-smoothing method, these parameters must be matched with the intensity of the injected laser to achieve optical limiting and reduce the energy loss of SBS scattering.

As shown in Figure 3, the beam intensity distributions were numerically investigated through the plasma SBS theory. The mean intensity of the injected light was set to

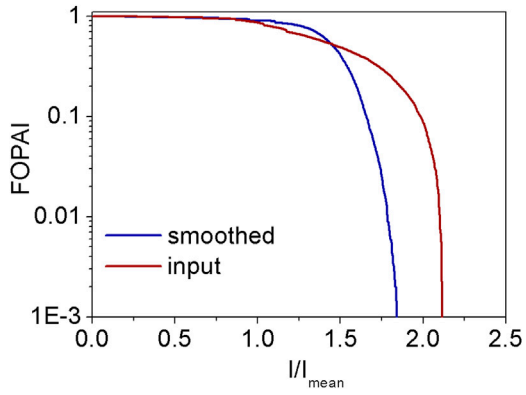

FIGURE 4
Fractional power above intensity (FOPAI) comparisons for the smoothed beam and the input beam.

1×10^{15} GW/cn^2, the beam size was set to 2 mm × 2 mm, the plasma length was set to 2 mm, the electron density was 8%n_c, and temperature T_e was 1 keV. Figures 3A,D present the 2D and 1D distributions of the pump light, (b) depicts the scattered light, and (c) and (e) show the distributions of the smoothed light. It is clear that the beam distribution was smoothed by transmission through the plasma.

$$\mathrm{FOPAI}(I_0) = \frac{\iint\limits_{I_f(x_f,y_f)\geq I_0 \wedge (x_f,y_f)\in A} I_f(x_f,y_f)\mathrm{d}x_f\mathrm{d}y_f}{\iint\limits_{(x_f,y_f)\in A} I_f(x_f,y_f)\mathrm{d}x_f\mathrm{d}y_f} \quad (11)$$

The resulting FOPAI plots for the input and smoothed beams are displayed in Figure 4. In general, if the FOPAI curve is closer to the left side, the proportion of high-intensity laser beams is lower. As shown in Figure 4, the high-intensity hotspot inside the beam was effectively suppressed after beam smoothing via SBS. The initial fluence distribution was relatively dispersed, with the fluence contrast degree of 15.9%. After beam smoothing, the fluence distribution was more centralized with the contrast degree of 9.7%.

The potential optical damage strongly correlates with the laser fluence. Beam smoothing elements (such as CPP) in conventional focusing beam paths suffer from a high damage risk. The plasma has virtually no damage threshold, and the passed laser fluence can be extremely high. Thus, this plasma beam smoothing technology will provide new ideas for solving optical element damage.

In high-power laser systems, dozens of optical elements are distributed along the beam path from the front seed to the final target. Each optical element may contain a number of inner defects generated during the material growth process or surface defects generated from component processing. These defects can cause strong local diffraction effects and light intensity enhancement in the laser beam. In addition, inhomogeneity further increases the amplification and frequency conversion, which seriously affects the irradiation uniformity of the subsequent laser. Beam smoothing before the focal spot presents a complicated practical situation. In future research, we will further develop the dynamic control capability of the plasma to achieve dynamic beam smoothing of the focal spot.

Conclusion

In this paper, we present a novel laser beam spatial smoothing method based on SBS in plasma. The key elements of this beam smoothing result from the optical limiting properties of the SBS. Plasma parameters and SBS proprieties are theoretically calculated. Theoretical simulation results show that The SBS reflectivity of the hot spot in the beam is significantly higher than that of the smooth part. High-intensity hotspots were significantly reduced following beam smoothing via SBS. The beam smoothing effect was simulated theoretically, and the results indicate that the fluence contrast decreased from 15.9% to 9.7% after beam smoothing. This approach to spatial beam smoothing is flexible and does not introduce optical damage issues.

Data availability statement

The raw data supporting the conclusions of this article will be made available by the authors, without undue reservation.

Author contributions

HY: Conceptualization, Programming, Acquisition of data, Drafting the manuscript, Funding acquisition JH: Analysis of data, Data Curation ZD: Investigation, Visualization CZ: Writing–Review and Editing YL: Investigation, Validation.

Funding

This work is supported by the National Natural Science Foundation of China No. 61905052.

Conflict of interest

The authors declare that the research was conducted in the absence of any commercial or financial relationships that could be construed as a potential conflict of interest.

Publisher's note

All claims expressed in this article are solely those of the authors and do not necessarily represent those of their affiliated organizations, or those of the publisher, the editors and the reviewers. Any product that may be evaluated in this article, or claim that may be made by its manufacturer, is not guaranteed or endorsed by the publisher.

References

1. Haynam CA, Wegner PJ, Auerbach JM, Bowers MW, Dixit SN, Erbert GV, et al. National ignition facility laser performance status. *Appl Opt* (2007) 46:3276–303. doi:10.1364/ao.46.003276

2. Fleurot N, Cavailler C, Bourgade JL. The Laser Megajoule (LMJ) Project dedicated to inertial confinement fusion: Development and construction status. *FUSION ENGINEERING DESIGN* (2005) 74:147–54. doi:10.1016/j.fusengdes.2005.06.251

3. Luce J. Beam shaping in the MegaJoule laser project. *Proc SPIE* (2011) 8130: 813002.

4. Dai W, Hu D, Zhou W, Zhao J, Jing F, Yang Z, et al. Beam wavefront control of a thermal inertia laser for inertial confinement fusion application. *Appl Opt* (2009) 48:3691–4. doi:10.1364/ao.48.003691

5. Yu H, Jing F, Wei X, Zheng W, Zhang X, Sui Z, et al. Status of prototype of SG-III high-power solid-state laser. *Proc SPIE* (2009) 7131:713112.

6. Negres RA, Raman RN, Bude JD, Feit MD, Demos SG. Dynamics of transient absorption in bulk DKDP crystals following laser energy deposition. *Opt Express* (2012) 20:20447–58. doi:10.1364/oe.20.020447

7. Raman RN, Negres RA, Demos SG. Kinetics of ejected particles during breakdown in fused silica by nanosecond laser pulses. *Appl Phys Lett* (2011) 98: 051901. doi:10.1063/1.3549193

8. Zheng Y, Ba R, Zhou X, Ding L, Li J, Yuan J, et al. Characteristics of precursors responsible for bulk damage initiation in doubler KDP crystal at different wavelengths. *Opt Laser Technol* (2017) 96:196–201. doi:10.1016/j.optlastec.2017.05.034

9. Ko S-W, Lin T-H, Huang Y-H, Jau H-C, Chu S-C, Chen Y-Y, et al. Electrical control of shape of laser beam using axially symmetric liquid crystal cells. *Appl Opt* (2012) 51:1540–5. doi:10.1364/ao.51.001540

10. Li S, Wang Y, Lu Z, Ding L, Du P, Chen Y, et al. High-quality near-field beam achieved in a high-power laser based on SLM adaptive beam-shaping system. *Opt Express* (2015) 23:681–9. doi:10.1364/oe.23.000681

11. Marozas JA. Fourier transform-based continuous phase-plate design technique: A high-pass phase-plate design as an application for OMEGA and the national ignition facility. *J Opt Soc Am A* (2007) 24:74–83. doi:10.1364/josaa.24.000074

12. Duluc M, Penninckx D, Loiseau P, Riazuelo G, D'Humieres E. Optical smoothing with reduced FM-to-AM conversion in high-power lasers using spectral distribution. *Phys Rev Appl* (2019) 12:054055. doi:10.1103/physrevapplied.12.054055

13. Chen HX, Li DH, Chen ZP. Measuring phase modulation characteristics of LC-SLM by using phase-shift interference. *Proc SPIE* (2000) 4231:384–6.

14. Thaury C, Guillaume E, Döpp A, Lehe R, Lifschitz A, Ta Phuoc K, et al. Demonstration of relativistic electron beam focusing by a laser-plasma lens. *Nat Commun* (2015) 6:6860. doi:10.1038/ncomms7860

15. Wang HY, Lin C, Sheng ZM, Liu B, Zhao S, Guo ZY, et al. Laser shaping of a relativistic intense, short Gaussian pulse by a plasma lens. *Phys Rev Lett* (2011) 107: 265002. doi:10.1103/physrevlett.107.265002

16. Wilson R, King M, Gray RJ, Carroll DC, Dance RJ, Armstrong C, et al. Ellipsoidal plasma mirror focusing of high power laser pulses to ultra-high intensities. *Phys Plasmas* (2016) 23:033106. doi:10.1063/1.4943200

17. Weng X, Zhong Z, Li J, Zhang B. Filamentation of spatiotemporal smoothed focal spot in plasma by Beam Smoothing scheme. *OPTICS COMMUNICATIONS* (2019) 436:216–21. doi:10.1016/j.optcom.2018.12.039

18. Lu ZW, Hasi WLJ, Gong HP, Li Q, He WM. Generation of flat-top waveform by double optical limiting based on stimulated Brillouin scattering. *Opt Express* (2006) 14:5497–501. doi:10.1364/oe.14.005497

19. Zhu X, Yang H, Wang G, Wu D, Qiu Y. Optimising of the material and laser parameters for high-power laser spatial beam smoothing based on stimulated Brillouin scattering. *Laser Phys* (2019) 29:075402. doi:10.1088/1555-6611/ab232a

20. Depierreux S, Michel DT, Tassin V, Loiseau P, Stenz C, Labaune C. Effect of the laser wavelength on the saturated level of stimulated Brillouin scattering. *Phys Rev Lett* (2009) 103:115001. doi:10.1103/physrevlett.103.115001

21. Rousseaux C, Baton SD, Benisti D, Gremillet L, Loupias B, Philippe F, et al. Experimental investigation of stimulated Raman and Brillouin scattering instabilities driven by two successive collinear picosecond laser pulses. *Phys Rev E* (2016) 93:043209. doi:10.1103/physreve.93.043209

frontiers | Frontiers in Physics

TYPE Original Research
PUBLISHED 07 October 2022
DOI 10.3389/fphy.2022.1034973

OPEN ACCESS

EDITED BY
Zhenxu Bai,
Hebei University of Technology, China

REVIEWED BY
Yaoyao Qi,
Hebei University of Technology, China
Bo Guo,
Harbin Engineering University, China

*CORRESPONDENCE
Bingyuan Zhang,
bingyuanzhang@lcu.edu.cn

SPECIALTY SECTION
This article was submitted to Optics and Photonics,
a section of the journal
Frontiers in Physics

RECEIVED 02 September 2022
ACCEPTED 20 September 2022
PUBLISHED 07 October 2022

CITATION
Liu C, Li G, Su X, Wang Y, Gao F, Xie Y, Kumar S and Zhang B (2022), Generation of h–Shaped pulse in a mode–Locked erbium-doped fiber laser.
Front. Phys. 10:1034973.
doi: 10.3389/fphy.2022.1034973

Generation of h–Shaped pulse in a mode–Locked erbium-doped fiber laser

Chao Liu, Guoru Li, Xiancui Su, Yiran Wang, Feilong Gao, Yiyan Xie, Santosh Kumar and Bingyuan Zhang*

Shandong Key Laboratory of Optical Communication Science and Technology, School of Physics Science and Information Technology, Liaocheng University, Liaocheng, China

In this paper, the generation of h-shaped pulse is demonstrated in a nonlinear polarization rotation mode-locked erbium-doped fiber laser (MLEDFL). The length of the entire cavity is about 2506 m to enhance the nonlinear effect in the cavity. The multi-pulse state is obtained firstly under the certain pump power and polarization state. By further adjusting the polarization controller the h-shaped pulse with sharp top and flat bottom is generated under the pump power of ~100 mW. And the duration of pulse is tuned with a range of 54.63–470 ns. The width and intensity of pulse trailing part vary differently during the process of increasing pulse width. The results indicate that the peak power clamping effect and weak birefringence effect dominate in different h-shaped pulse forming process.

KEYWORDS

h-shaped pulse, ultra-long cavity, mode-locked, fiber laser, nonlinear effect

Introduction

Passively mode-locked fiber lasers (MLFLs) have attracted a lot of interest in the area of academia and industry in recent decades, for instance, optical sensing [1, 2], materials micromachining [3, 4] and biomedicine [5]. A strong nonlinear effect exists in MLFLs as a result of the unique structure of the fiber core. And the complex dynamic processes occur in fiber lasers under the action of nonlinear effects. Therefore, various pulse shapes will be generated from passively MLFLs, for example bunched multi-solitons [6], rectangular-wave pulses [7–9], step-like pulses [10, 11], chair-like pulses [12, 13], and h-shaped pulses [14, 15].

In 1991, the square pulse was firstly observed by Richardson based on figure-eight passively MLFLs [16]. The features of rectangular-wave pulses, however, have not been fully investigated. Komarov et al. theoretically researched the dynamics of the rectangular-wave pulses in an NPR fiber laser subsequently [17]. The mechanism for suppressing the formation of additional pulses was established based on numerical simulation in a laser resonator as pump power increased [18]. Since then, more and more researchers have begun to study the rectangular-wave pulse in fiber lasers. Zhang realized the rectangular-wave pulse with tuning range of 10–1710 ns by enhancing intracavity nonlinearity and cavity length [8]. The results show that the stronger nonlinearity in the cavity has a

positive impact on the pulse duration. Liu reported that the multiwavelength square pulses were generated by utilizing a NALM-based cavity filtering effect in a passively MLFL with anomalous dispersion using a figure-eight structure [19]. The results indicate that as pump power increases, the width of rectangular-wave pulses broadens linearly, yet the peak power remains practically constant.

In addition to rectangular-wave pulses, another h-shaped pulse has also drawn a lot of interest in a unique structure with a sharper peak on the leading edge and a longer flat-top bunch on the trailing edge. In 2018, Luo found that the h-shaped pulses as the pump source could realize high repetition gain-switching [14]. In the same year, Zhao investigated the influences of weak birefringence in the cavity on pulse characteristics [20]. In 2019, Zheng demonstrated that nanoscale h-shaped pulses with μJ-level pulse energy could be generated in the figure-of-9 fiber laser [21]. The generation of h-shaped pulse was realized by Zhao by employing an ultralong fiber laser resonator, revealing that by increasing pump power or varying intra-cavity polarization state, the h-shaped pulse could be generated with different orders of harmonic mode-locking state [15]. Compared to low-dimensional material SAs [22], nonlinear multimode interference (NLMMI) [23, 24] mode-locked technology, the mode-locked principle of NPR is based on the accumulation of different nonlinear phase shifts in the cavity. And the strong nonlinear effect is conducive to reducing the nonlinear polarization switching threshold, which means that it is easy to obtain h-type pulses at lower pump power.

In this work, the evolution of h-shaped pulse is demonstrated in a passively MLEDFL based on NPR technique. By varying the polarization, the h-shaped pulses can be switched from the multi-pulse state under the fixed pump power. The pump power varies from 100 mW to 350 mW, and the pulse width changes from 54.63 to 470 ns. The width and intensity of the pulse trailing part change during the process of pulse width increase. The results indicate that the peak power clamping effect and weak birefringence effect dominate in different h-shaped pulse forming processes. It may be helpful to further enhance understanding the physical properties of the h-shaped pulses which generate in MLFLs.

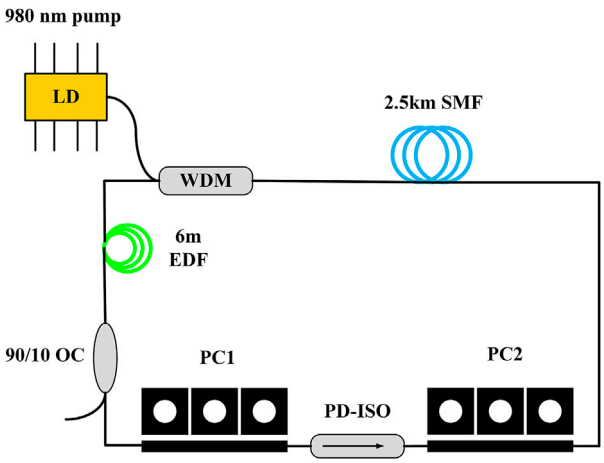

FIGURE 1
Schematic diagram of the MLFL based on NPR technique.

Experimental setup

The experimental schematic diagram of the passively MLFL is shown in Figure 1. The length of the entire cavity is around 2506 m. The erbium-doped fiber (EDF, 4/125 μm) as gain medium is pumped by a 980 nm laser diode (LD) through a 980/1550 nm wavelength division multiplexed (WDM) coupler. The Er-doped fiber is low-gain fiber, so we use the length of 6 m Er-doped fiber as the gain fiber. The cavity length of 2506m is to increase the nonlinear effect in the cavity and reduce the nonlinear polarization switching threshold, so as to achieve a wide range h-shaped pulse output in time domain. The optical coupler (OC) is used to extract 10% of the power from the cavity.

Two three-paddle type polarization controllers (PC1 and PC2) are used to adjust the polarization state of the propagation light. In addition, the polarization-dependent isolator (PD-ISO) is used to ensure the unidirectional transmission in the ring cavity. A 2.5 km long single mode fiber (SMF) is added to the cavity to prolong the cavity length and enhance the cumulative nonlinearity. The temporal pulse profile and output spectrum are monitored by using a 1 GHz digital oscilloscope (Tektronix MDO3102) and an optical spectrum analyzer with a scanning range of 600–1700 nm (Yokogawa AQ6370), respectively. The net dispersion of the ring cavity is calculated to be -53.87 ps^2.

Results and analysis

In our experiment, with launched pump power fixed at 100 mW, three tight pulses emerge from the laser cavity by altering the PCs properly. Figures 2A,B illustrate the temporal profile of the pulse and optical spectrum, respectively. It can be observed the temporal distance between adjacent pulses is not equidistant and interval is large, showing that the interaction of the pulse is weak. The whole output spectrum is broad with no Kelly sideband features of conventional-soliton pulse. And the central wavelength is located at 1573 nm with ~23 nm 3 dB spectral bandwidth.

Figures 3A,B illustrate the evolution of the number of round-trip pulses and the output spectra with increasing pump power, respectively, to further examine the behaviors of multi-pulses in MLFL. The intensity of the output spectrum enhances slightly with the increase of pump power. The corresponding number of the round-trip pulses varies from

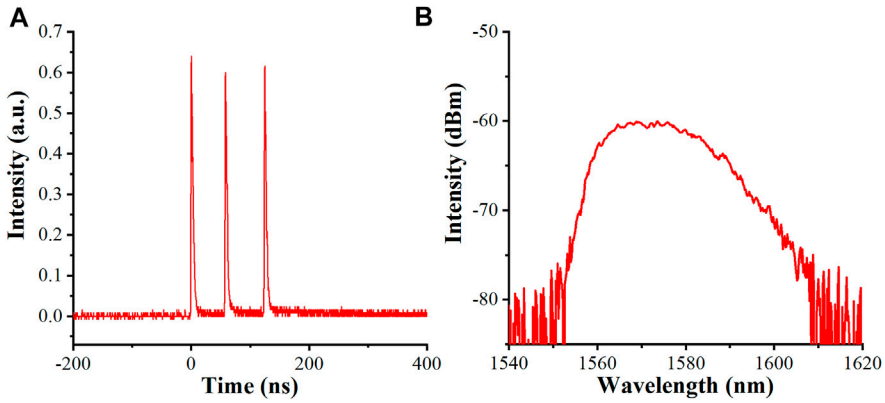

FIGURE 2
(A) The temporal pulse profile of the three pulses. **(B)** The corresponding optical spectrum.

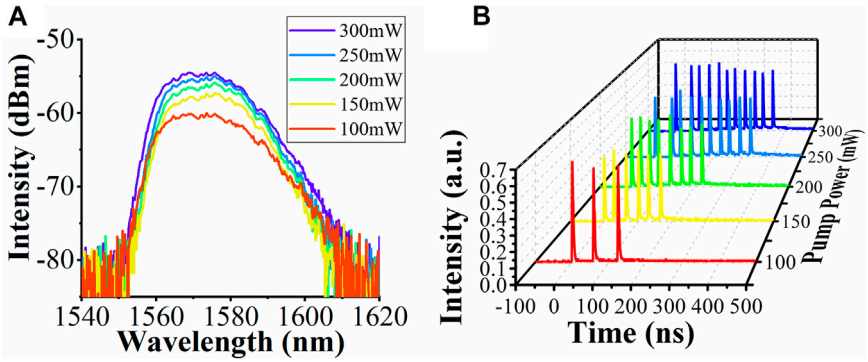

FIGURE 3
The evolution of **(A)** the output spectra and **(B)** the temporal pulse profile with increasing pump powers.

6 to 11, during the pump power increases to 300 mW. The temporal spacing between adjacent pulses is not equivalent, but the shape and width of pulses are essentially uniform. This is because gain competition between neighboring pulses and experimental ambient noise may induce pulse intensity inconsistency [25]. It is similar to the harmonic mode-locked (HML) regime in that the excess energy in the cavity is converted to build up the number of pulses. In fact, the operation of multi-pulses in NPR MLFLs can be attributed to weakly birefringent effects in optical fiber, gain dynamics, and nonlinearity [20].

The h-shaped pulse is obtained at the pump power of ~100 mW by slightly adjusting the PC again. Figures 4A,B show the output spectra and temporal profiles, respectively. It can be observed that there are dual central bands in the output spectrum. The first band has a central wavelength and a 3 dB spectral bandwidth of 1543.5 nm and 3 nm, respectively. The second band has a central wavelength and a 3 dB spectral bandwidth of 1585 nm and 28 nm, respectively. The second segment has a wider spectrum with a depression in the center. The birefringence-related cavity-spectral-filtering (CSF) effect may be the reason why two independent spectra bands appear [20]. According to Ref. [26], there is a strong correlation between the time and spectral distribution of the J-shaped pulse. In this experiment, the intensity of the leading edge and the trailing edge of the h-shaped pulse is almost the same, meaning that the same effect on the wider spectrum. Although the ultra-long SMF cumulates the intracavity nonlinearity, it also increases intracavity birefringence, which changes the CFS effect related to the birefringence. Figure 4C shows the corresponding pulse train at 100 mW of pumping power, which corresponds to a repetition rate of 81.17 kHz. Meanwhile, the measured RF spectrum in the

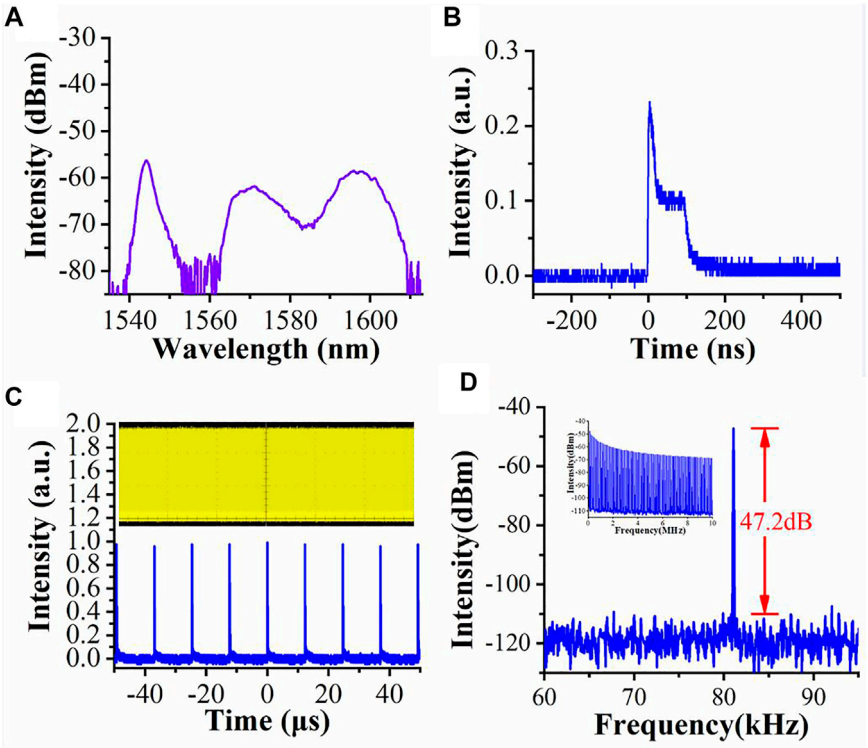

FIGURE 4
Output characteristics of the h-shaped pulse with ~100 mW pump power: **(A)** output spectra; **(B)** temporal profile; **(C)** pulse train (inset: a span of 1 ms); **(D)** the RF spectrum (insert: RF spectrum in 10 MHz range).

range of 0–10 MHz confirms that the operation of mode-locked has excellent stability.

Figure 5B shows the evolution of the h-shaped pulse at different pump powers. The pulse width ranges from 94 to 292 ns as the pump power increases from 100 to 240 mW. As the pump power increases, the peak power of the pulse does not increase due to the clamping effect, but the gain is not saturated so the pulse width can increase continuously. The flat trailing portion broadens as pump power increases, while the sharp spike of the pulse narrows slowly. This is similar to the properties of dissipative soliton resonance (DSR) pulse in fiber lasers [27, 28]. It is noteworthy that the repetition frequency of the mode-locked pulse is 81kHz, it is not so easy to induce amplified spontaneous emission (ASE) in the pulse interval. So, the properties of trailing portion are just caused by the peak power clamping (PPC) effect rather ASE. The PPC effect contributes to the formation of h-shaped pulses and inhibits pulse splitting by flattening the lengthy trailing section [15]. Meanwhile, the PPC effect is associated with the nonlinearity in the laser resonant cavity, which implies the intensive nonlinearity can reduce the switching threshold [29]. As seen in Figure 5A, the intensity of corresponding output spectra increases slightly as the pump power increases, while the central wavelength remains almost invariable, which is consistent with the previously proven features of an h-shaped pulse [14, 20, 30, 21, 15]. As the pump power reaches 240 mW, the temporal pulse profile becomes unstable. Then, we rotate the PCs slightly, and the mode-locked pulse reappears again. Figures 5C,D, respectively, display the output spectra and temporal pulse profile. It is found that the central wavelength of the optical spectrum has changed. The band has a central wavelength of 1572 nm. The measured pulse duration widens from 368 to 470 ns as the pump power changes from 260 to 340 mW. And the complete pulse profile is observed by adjusting the vertical resolution of the oscilloscope. It can be seen the amplitude of sharp peak is higher than previously mentioned, the amplitude of trailing portion remains almost invariant. Theoretically, rotating the PCs will change the local birefringence of the fiber, resulting in a change in the amount of intracavity birefringence and further impacting the characteristics of the output pulse [20]. For the h-shape pulse with higher amplitude of sharp peak, the PPC effect plays a weak role in the formation of sharp peak, but it contributes to inhibit pulse splitting by flattening the lengthy trailing section. The energy of whole pulse is more

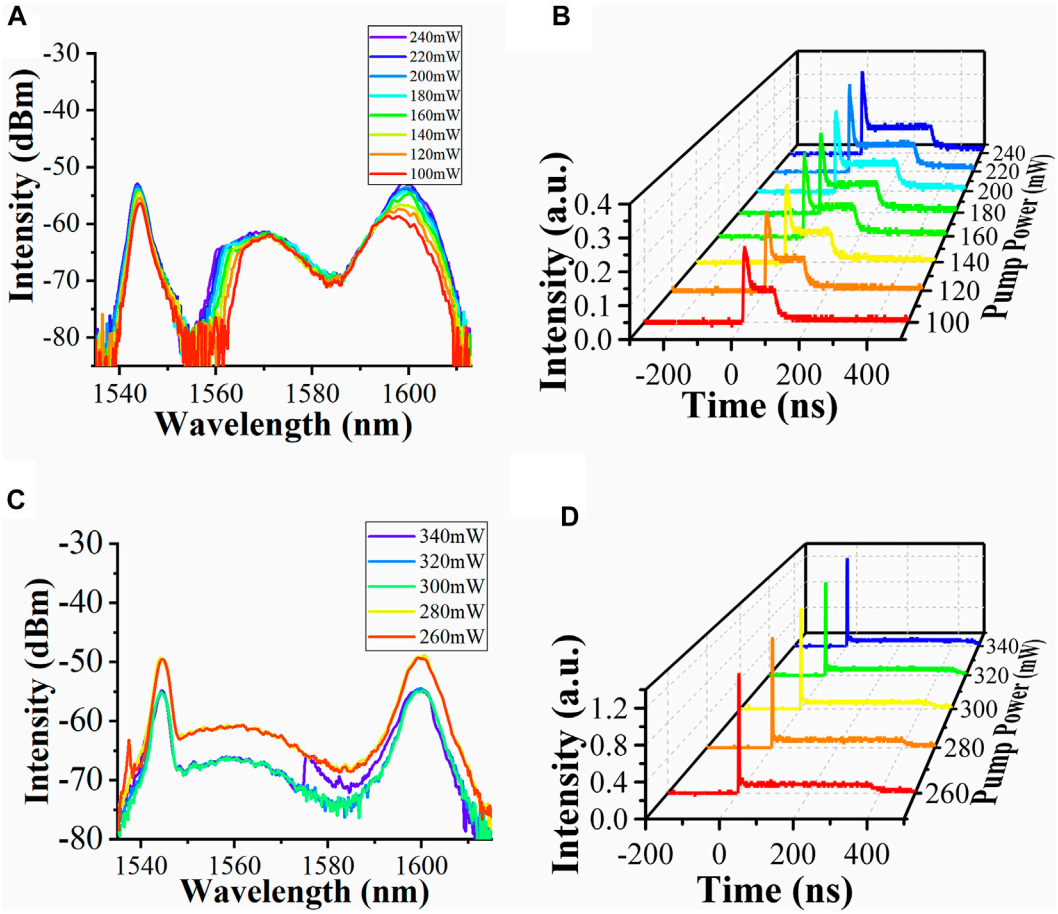

FIGURE 5
(A) Output spectra and **(B)** the temporal pulse profile variations *versus*versus different pump powers. **(C)** Changes of the spectra after adjusting the PCs and **(D)** the corresponding variations of the temporal pulse profile.

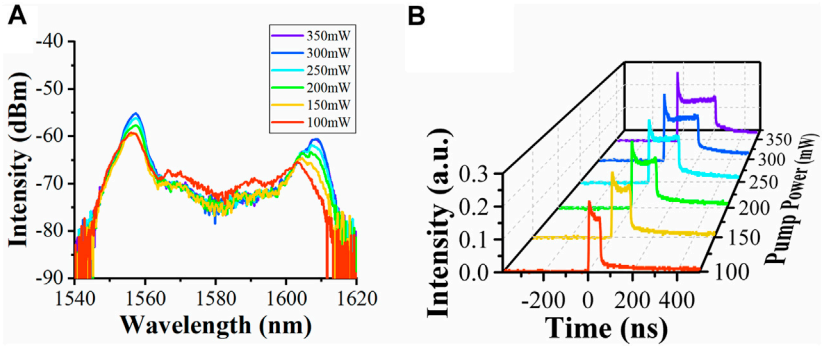

FIGURE 6
(A) The variations of the output spectra under different pump powers after adjusting the PCs. **(B)** Corresponding temporal pulse profile as increasing pump power.

concentrated on the peak of pulse instead of splitting into pulses with the same power.

In order to further investigate the characteristics of the h-shaped pulse, another h-shaped pulse is generated by rotating the angle of the PCs. Figures 6A,B show the output spectra and the corresponding temporal pulse profile as increasing pump power respectively. The corresponding pulse width ranges from 54.63 to 245.9 ns as the pump power increases from 100 to 350 mW. The output spectrums have changed, and the central wavelength reduced from two to one, which can be attributed to the different intensity of CSF effect caused by the angle of PCs. As can be noticed, there are no-Signiant change with the amplitude of the flat-top portion. According to Ref. [30], it could be found that the sharp peak at the top of an h-shaped pulse might be restrained by inserting a piece of unpumped doped-fiber into the cavity. Similarly, this function can be realized by adjusting the PC in this experiment. It may be helpful to further enhance understanding the physical properties of the h-shaped pulses in MLFLs.

Conclusion

In conclusion, the evolution of h-shaped pulses in an ultralong NPR MLEDFL is experimentally realized. The 2.5 km long SMF is employed in the cavity to enhance the nonlinear effect. By adjusting the polarization, the h-shaped pulse can evolve from the multi-pulse state. And the duration of pulse is tuned with a range of 54.63–470 ns. The width and intensity of pulse trailing part vary differently during the process of increasing pulse width. The results indicate that the peak power clamping effect and weak birefringence effect dominate in different h-shaped pulse forming process. The experimental results may be helpful to investigate the output performances of the h-shaped pulse in MLEDFLs.

Data availability statement

The original contributions presented in the study are included in the article/supplementary material, further inquiries can be directed to the corresponding author.

Author contributions

All authors listed have made a substantial, direct, and intellectual contibution to the work and approved it for Publication.

Funding

Natural Science Foundation of Shandong Province (ZR2021QF025, ZR2020QF093); National Natural Science Foundation of China (62105134, 61905104).

Conflict of interest

The authors declare that the research was conducted in the absence of any commercial or financial relationships that could be construed as a potential conflict of interest.

Publisher's note

All claims expressed in this article are solely those of the authors and do not necessarily represent those of their affiliated organizations, or those of the publisher, the editors and the reviewers. Any product that may be evaluated in this article, or claim that may be made by its manufacturer, is not guaranteed or endorsed by the publisher.

References

1. Zhao X, Hu G, Zhao B, Li C, Pan Y, Liu Y, et al. Picometer-resolution dual-comb spectroscopy with a free-running fiber laser. *Opt Express* (2016) 24(19): 21833–45. doi:10.1364/oe.24.021833

2. Cao Y, Wang L, Lu Z, Wang G, Wang X, Ran Y, et al. High-speed refractive index sensing system based on Fourier domain mode locked laser. *Opt Express* (2019) 27(6):7988–96. doi:10.1364/oe.27.007988

3. Kerse C, Kalaycıoğlu H, Elahi P, Çetin B, Kesim DK, Akçaalan Ö, et al. Ablationcooled material removal with ultrafast bursts of pulses. *Nature* (2016) 537(7618):84–8. doi:10.1038/nature18619

4. Malinauskas M, Žukauskas A, Hasegawa S, Hayasaki Y, Mizeikis V, Buividas R, et al. Ultrafast laser processing of materials: From science to industry. *Light Sci Appl* (2016) 5(8):e16133. doi:10.1038/lsa.2016.133

5. Wilson CR, Hutchens TC, Hardy LA, Irby PB, Fried NM. A miniaturized, 1.9F integrated optical fiber and stone basket for use in thulium fiber laser lithotripsy. *J Endourol* (2015) 29(10):1110–4. doi:10.1089/end.2015.0124

6. Chen Y, Wu M, Tang P, Chen S, Du J, Jiang G, et al. The formation of various multi-soliton patterns and noise-like pulse in a fiber laser passively mode-locked by a topo-logical insulator based saturable absorber. *Laser Phys Lett* (2014) 11:055101. doi:10.1088/1612-2011/11/5/055101

7. Li S, Dong Z, Li G, Chen R, Gu C, Xu L, et al. Chirp-adjustable square-wave pulse in a passively mode-locked fiber laser. *Opt Express* (2018) 26(18):23926–34. doi:10.1364/oe.26.023926

8. Zhang X, Gu C, Chen G, Sun B, Xu L, Wang A, et al. Square-wave pulse with ultra-wide tuning range in a passively mode-locked fiber laser. *Opt Lett* (2012) 37(8):1334–6. doi:10.1364/ol.37.001334

9. Semaan G, Braham FB, Fourmont J, Salhi M, Bahloul F, Sanchez F. 10 μJ dissipative soliton resonance square pulse in a dual amplifier figure-of-eight double-clad Er:Yb mode-locked fiber laser. *Opt Lett* (2016) 41(20):4767–70. doi:10.1364/ol.41.004767

10. Mao D, Liu X, Wang L, Lu H, Duan L. Dual-wavelength step-like pulses in an ultra-large negative-dispersion fiber laser. *Opt Express* (2011) 19(5):3996–4001. doi:10.1364/oe.19.003996

11. Guo B, Yao Y, Xiao J, Wang R, Zhang J. Topological insulator-assisted dual-wavelength fiber laser delivering versatile pulse patterns. *IEEE J Sel Top Quan Electron* (2016) 22(2):0900108–15. doi:10.1109/jstqe.2015.2426951

12. Dong Z, Lin J, Li H, Li S, Tao R, Gu C, et al. Generation of mode-locked square-shaped and chair-like pulse based on reverse saturable absorption effect of nonlinear multimode interference. *Opt Express* (2019) 27(20):27610–7. doi:10.1364/oe.27.027610

13. Gupta PK, Singh CP, Singh A, Sharma SK, Mukhopadhyay PK, Bindra KS. Chair-like pulses in an all-normal dispersion Ytterbium-doped mode-locked fiber laser. *Appl Opt* (2016) 55(35):9961–7. doi:10.1364/ao.55.009961

14. Luo H, Liu F, Li J, Liu Y. High repetition rate gain-switched Ho-doped fiber laser at 2.103 μm pumped by h-shaped mode-locked Tm-doped fiber laser at 1.985 μm. *Opt Express* (2018) 26(20):26485–94. doi:10.1364/oe.26.026485

15. Zhao J, Li L, Zhao L, Tang D, Shen D, Su L. Tunable and switchable harmonic h-shaped pulse generation in a 3.03 km ultralong mode-locked thulium-doped fiber laser. *Photon Res* (2019) 7(3):332–40. doi:10.1364/prj.7.000332

16. Richardson DJ, Laming RI, Payne DN, Matsas V, Phollips MW. Selfstarting, passively modelocked erbium fibre ring laser based on the amplifying Sagnac switch. *Electron Lett* (1991) 27:542. doi:10.1049/el:19910341

17. Komarov A, Leblond H, Sanchez F. Multistability and hysteresis phenomena in passively mode-locked fiber lasers. *Phys Rev A (Coll Park)* (2005) 71(5):053809. doi:10.1103/physreva.71.053809

18. Komarov A, Amrani F, Dmitriev A, Komarov K, Sanchez F. Competition and coexistence of ultrashort pulses in passive mode-locked lasers under dissipative-soliton-resonance conditions. *Phys Rev A (Coll Park)* (2013) 87(2):023838. doi:10.1103/physreva.87.023838

19. Liu H, Zheng X, Zhao N, Ning Q, Liu M, Luo Z, et al. Generation of multiwavelength noise-like square-pulses in a fiber laser. *IEEE Photon Technol Lett* (2014) 26(19):1990–3. doi:10.1109/lpt.2014.2344505

20. Zhao J, Li L, Zhao L, Tang D, Shen D. Cavity-birefringence-dependent h-shaped pulse generation in a thulium-holmium-doped fiber laser. *Opt Lett* (2018) 43(2):247–50. doi:10.1364/ol.43.000247

21. Zheng Z, Ren X, Zhu K, Ouyang D, Wang J, Guo C, et al. Fundamental and harmonic mode-locked h-shaped pulse generation using a figure-of-9 thulium-doped fiber laser. *Opt Express* (2019) 27(26):37172–9. doi:10.1364/oe.27.037172

22. Qi YY, Yang S, Wang JJ, Li L, Bai ZX, Wang YL, et al. Recent advance of emerging low-dimensional materials for vector soliton generation in fiber lasers. *Mater Today Phys* (2022) 23:100622. doi:10.1016/j.mtphys.2022.100622

23. Qi YY, Zhang Y, Yang S, Bai ZX, Ding J, Wang YL, et al. Controllable multiple-pulse dynamic patterns in the mode-locking ultrafast laser with a GIMF-YDF-based saturable absorber. *Opt Laser Tech* (2022) 153:108274. doi:10.1016/j.optlastec.2022.108274

24. Qi YY, Liu MY, Luan NN, Yang S, Bai ZX, Yan BZ, et al. Recent research progress of nonlinear multimode interference mode-locking technology based on multimode fibers. *Infrared Phys Tech* (2022) 121:104017. doi:10.1016/j.infrared.2021.104017

25. Kokhanovskiy A, Kuprikov E, Kobtsev S. Single- and multi-soliton generation in figure-eight mode-locked fibre laser with two active media. *Opt Laser Technol* (2020) 131:106422. doi:10.1016/j.optlastec.2020.106422

26. Gupta PK, Singh CP, Mukhopadhyay PK, Bindra KS. Generation of J-shaped pulses in ultra-long Ytterbium doped mode locked fiber laser. *Laser Phys* (2022) 30(6):065105. doi:10.1088/1555-6611/ab8797

27. Chang W, Ankiewicz A, Soto-Crespo JM, Akhmediev N. Dissipative soliton resonances. *Phys Rev A (Coll Park)* (2008) 78(2):023830. doi:10.1103/physreva.78.023830

28. Wu X, Tang DY, Zhang H, Zhao LM. Dissipative soliton resonance in an all-normal-dispersion erbium-doped fiber laser. *Opt Express* (2009) 17(7):5580–4. doi:10.1364/oe.17.005580

29. Li G, Liu J, Wang F, Nie H, Wang R, Yang K, et al. Third-order nonlinear optical response of few-layer MXene Nb_2C and applications for square-wave laser pulse generation. *Adv Mater Inter* (2021) 8(6):2001805. doi:10.1002/admi.202001805

30. Zhao J, Zhou J, Li L, Klimczak M, Komarov A, Su L, et al. Narrow-bandwidth h-shaped pulse generation and evolution in a net normal dispersion thulium-doped fiber laser. *Opt Express* (2019) 27(21):29770–80. doi:10.1364/oe.27.029770

frontiers | Frontiers in Physics

TYPE Original Research
PUBLISHED 14 October 2022
DOI 10.3389/fphy.2022.1021950

OPEN ACCESS

EDITED BY
Zhi-Han Zhu,
Harbin University of Science and Technology, China

REVIEWED BY
Yajun Pang,
Hebei University of Technology, China
Wei Li,
Beijing Institute of Technology, China

*CORRESPONDENCE
Pengge Ma,
mapenge@163.com

SPECIALTY SECTION
This article was submitted to Optics and Photonics,
a section of the journal
Frontiers in Physics

RECEIVED 18 August 2022
ACCEPTED 27 September 2022
PUBLISHED 14 October 2022

CITATION
Guo X, Ma P, Meng D, Sun J, Jin Q and Wei H (2022), Research on laser center positioning under CV model segmentation.
Front. Phys. 10:1021950.
doi: 10.3389/fphy.2022.1021950

Research on laser center positioning under CV model segmentation

Xingchen Guo[1], Pengge Ma[1]*, Dongdong Meng[2], Junling Sun[1], Qiuchun Jin[1] and Hongguang Wei[1]

[1]College of Intelligent Engineering, Zhengzhou University of Aeronautics, Zhengzhou, China, [2]Aerospace Information Research Institute, Chinese Academy of Sciences, Beijing, China

Spot positioning accuracy is an important index of laser processing system and ranging system. When the laser spot is noisy or the gray level is not uniform, the positioning accuracy is easily affected. Aiming at the above problems, this paper proposes a laser spot segmentation method based on the Chan-Vese model, which can improve the accuracy of spot center localization in combination with the gray centroid method. Firstly, the laser spot image is decomposed by two-dimensional wavelet, and the high-frequency component is suppressed by soft threshold function to eliminate the noise in the laser spot image. Secondly, the level set algorithm based on Chan-Vese model is used to segment the laser spot image with adaptive improvement of the initial coordinates of the evolution curve. Finally, the center coordinates are calculated inside the segmentation curve using the gray centroid method. Experimental results show that the method is more accurate and robust.

KEYWORDS

laser spot, wavelet transform, CV model, level set, centralized positioning

Introduction

Laser has many advantages, such as energy concentration, good directivity and low divergence, etc. It is widely used in machining, guidance, ranging and other fields. Laser spot location is the key technology of the whole system, so many algorithms are proposed [1]. The common methods to detect the center of laser spot include the Hough transform method [2], the circular fitting method [3], and the gray centroid method [4], Hough transform is a feature detection method proposed by Hough in 1962. It can detect the shape of the image by constructing functions to describe the edge pixels [5]. The Hough transform is required to vote-by-point, which accuracy is only of pixel level [6]. The circle fitting method is to use the least squares to fit the geometric features of the image, which is easily affected by the noise [3]. The gray centroid method needs to use the light intensity received by each pixel on the two-dimensional image, and requires high uniformity of the laser spot brightness [7]. In order to improve the positioning accuracy, many improved algorithms have been proposed in recent years. Liu et al. proposed a curve fitting sub-pixel location algorithm of barycenter, only few data points are calculated by the algorithm which meets the accuracy requirements of micro distortion measurement [8], The algorithm is more suitable for laser spot image of Gauss Distribution. Jiang et al put forward a nonlinear least square fitting algorithm to compensate the system error, so

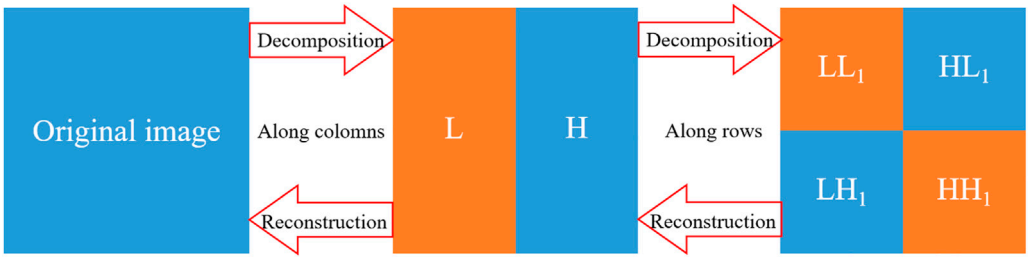

FIGURE 1
Discrete wavelet decomposition and reconstruction of images.

as to improve the positioning accuracy of gray centroid method [9]. Liu et al used an algorithm based on the optimal arc to obtain the center for the laser spot by fitting the circle center [10]. It is found that image denoising and laser spot boundary location are important prerequisites for measuring the center position of laser spot, so we focuses on laser spot denoising and image segmentation [11, 12].

In this paper, combining with the gray centroid method, the proposed laser spot segmentation method based on Chan-Vese [13] model can further improve the accuracy of laser spot positioning. The image is pre-processed by wavelet decomposition and reconstruction to solve the problem of uneven gray scale of the image and reduce the interference of noise on the contour. The laser spot boundary is calculated using the level set method based on the CV model. The grayscale center of mass is calculated within the closed shape to obtain the exact center coordinates. The method is fully validated in experiments.

Theoretical analysis

Wavelet decomposition denoising

Wavelet transform is a local transform of space and frequency, which can separate noise information from signal effectively [14]. The 2D discrete wavelet decomposition and reconstruction of the image can be represented as Figure 1. First, perform one-dimensional discrete wavelet transform and down-sampling on the row direction of the image, so as to calculate the low-frequency component L and high-frequency component H of the image in the row direction. Repeat the above process in column direction, finally get the four subgraphs A, H, V, D. A represents the low frequency part of the image, H, V, D represent the high-frequency parts of the image in the horizontal, vertical, and diagonal directions, respectively. The low-frequency sub-image reflects the overall information of the image, and the high-frequency sub-images reflect the local details of the image [15, 16]. Continue to repeat the process of Figure 2 for the low-frequency sub-images, that is, to obtain the multi-layer wavelet decomposition of the image.

In this paper, two-layer wavelet decomposition is performed on the laser spot image, and the process can be expressed as Figure 2.

After image wavelet decomposition, the image noise is reflected in the high-frequency components, and the absolute value of the wavelet coefficient is small; while the part with uniform laser energy is reflected in the high-frequency component, and the wavelet coefficient is large. According to the idea of wavelet threshold denoising proposed by John Stone [17], when the wavelet coefficient is less than a certain threshold, it is considered to be mainly noise components, and the part larger than the threshold is retained.

We chose the VisuShrink [17] method to generate the threshold, the formula is

$$T = \sigma\sqrt{2\lg N} \tag{1}$$

where σ is the image standard deviation and N is the image size. Generally, the threshold function is divided into two types: hard threshold function and soft threshold function. Because the hard threshold function is prone to Ringingeffect [18], We chooses the soft threshold method to process the estimated wavelet coefficients, which can be expressed as:

$$\widehat{w}_{j,k} = \begin{cases} sign\left(w_{j,k}\right)\left(\left|w_{j,k}\right| - T\right), & \left|w_{j,k}\right| \geq T \\ 0, & \left|w_{j,k}\right| < T \end{cases} \tag{2}$$

Where: *sign* (*) is the sign function, $w_{j,k}$is the wavelet coefficient before processing, $\widehat{w}_{j,k}$ is the wavelet coefficient after processing. The threshold T is given by Eq. 1.

Figure 3 shows the comparison effect of the spot image before and after denoising. After denoising, the edge high-frequency noise texture and radial light are better suppressed, and the image Grayscale Value image is smoother.

Laser spot segmentation based on CV model

This section will discuss the applicability of the CV model to laser spot segmentation. The key of the CV model is to use the image grayscale information to construct the energy function $E(C)$, so as to evolve the curve to a certain target area. The energy function can be expressed as

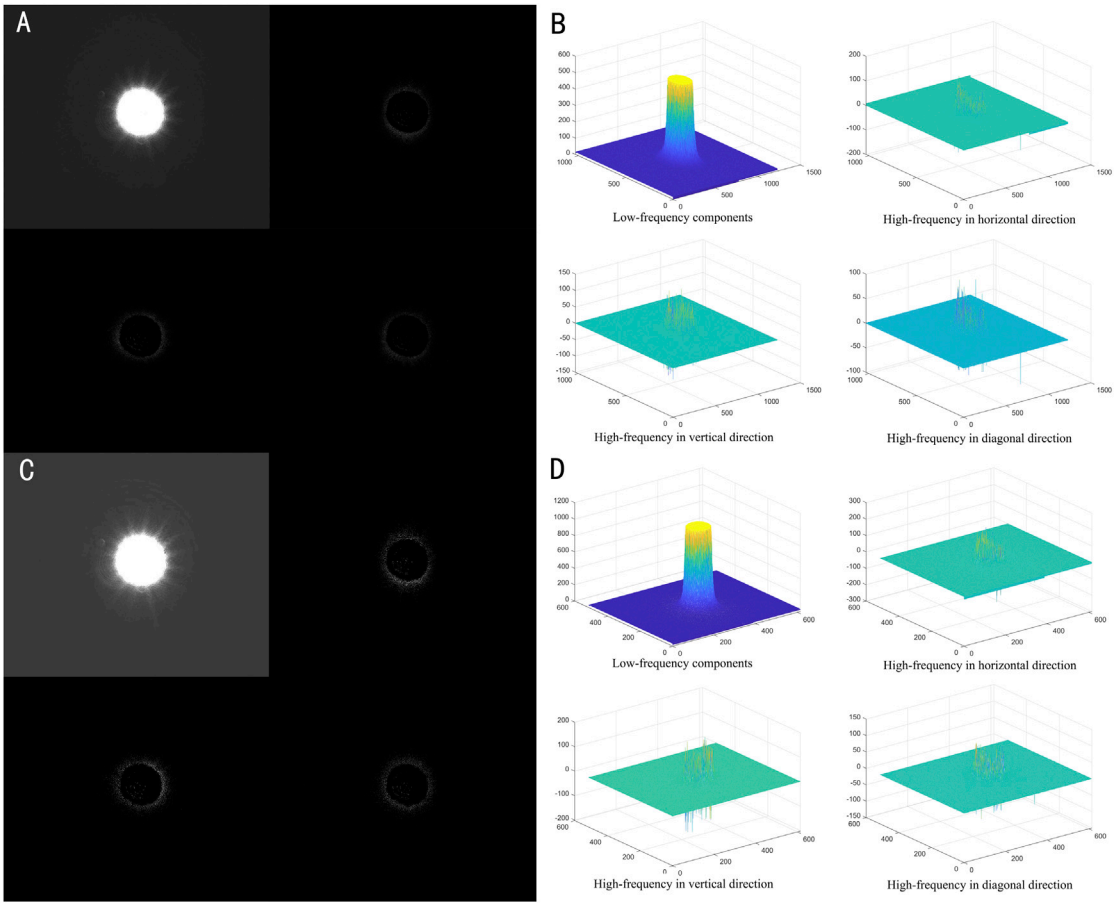

FIGURE 2
Wavelet Decomposition Results and Wavelet Coefficient Distribution of Laser Spot Image. **(A)**: The first layer of wavelet decomposition; **(B)**: The first layer of wavelet coefficient distribution; **(C)**: The second layer of wavelet decomposition; **(D)**: The second layer of wavelet coefficient distribution.

$$E^{cv}(c_1,c_2,C) = \mu \cdot Length(C) + \lambda_1 \cdot \int_{inside(C)} |u_0(x,y) - c_1|^2 dxdy + \lambda_2 \cdot \int_{outside(C)} |u_0(x,y) - c_2|^2 dxdy \quad (3)$$

Where, μ is the length weight of the contour line; C is the contour line of the target, u is the target image; and λ_1 and λ_2 are the correction weights; c_1 and c_2 are the mean image gray levels inside and outside the evolution curve C, respectively. The formula is divided into three items; the first item is the regularization item, which is used to constrain the length of the contour line to ensure that the contour line is the shortest under the current conditions; the second and third items are the contour line condition items, which are responsible for controlling the current contour line evolution trend. Use level set functions to control curve evolution, The level set function is expressed as

$$\varphi(x,y)\begin{cases} > 0; & x,y \in inside(C) \\ = 0; & x,y \in boundary(C) \\ < 0; & x,y \in outside(C) \end{cases} \quad (4)$$

Eq. 4 is substituted into Eq. 3. Also, the energy function $E(C)$ is be written as

$$E^{cv}(c_1,c_2,\varphi) = \mu \cdot \int_{\Omega} \delta_\varepsilon(\varphi(x,y))|\nabla\varphi(x,y)|dxdy + \lambda_1 \cdot \int_{\Omega} |u_0(x,y) - c_1|^2 H_\varepsilon(\varphi(x,y))dxdy + \lambda_2 \cdot \int_{\Omega} |u_0(x,y) - c_2|^2 (1 - H_\varepsilon(\varphi(x,y)))dxdy \quad (5)$$

H_ε is Heaviside Function, Use its approximate form

$$H_\varepsilon(z) = \frac{1}{2}\left(1 + \frac{2}{\pi}\arctan\left(\frac{z}{\varepsilon}\right)\right) \quad (6)$$

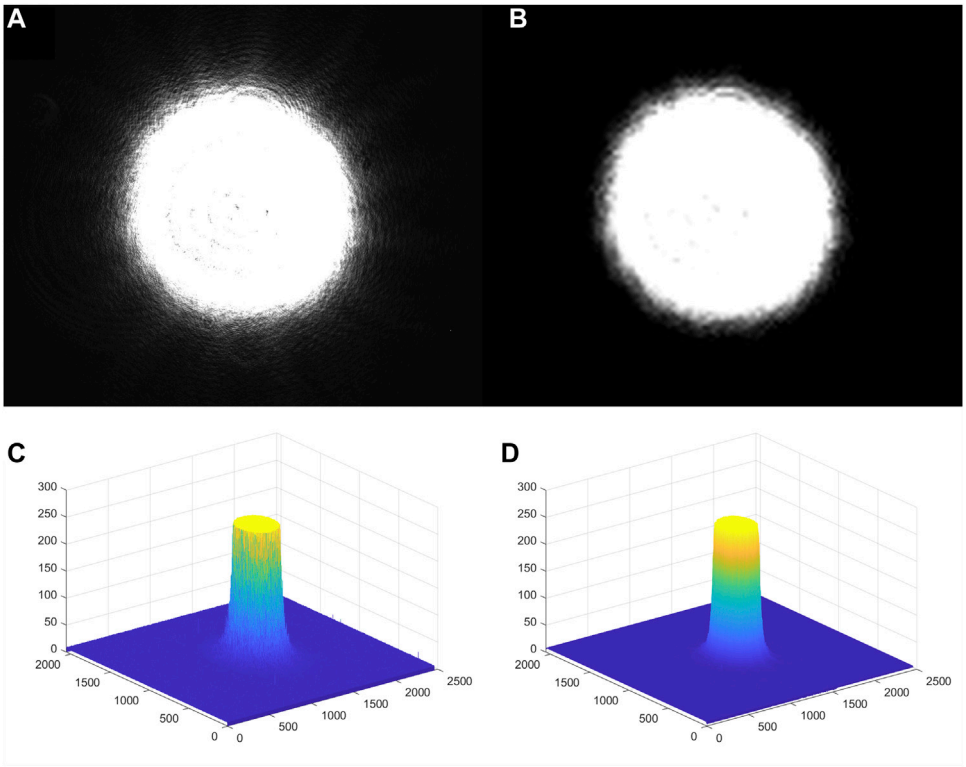

FIGURE 3
Comparison of before and after laser spot image denoising. **(A)**: Image before denoising; **(B)**: Image after denoising; **(C)**: Grayscale Value distribution before denoising; **(D)**: Grayscale Value distribution after denoising.

FIGURE 4
Adaptive initial curve coordinates and evolutionary results. **(A)**: Images of laser spot at different positions; **(B)**: Fitting results of laser spot images at different positions.

10.3389/fphy.2022.1021950

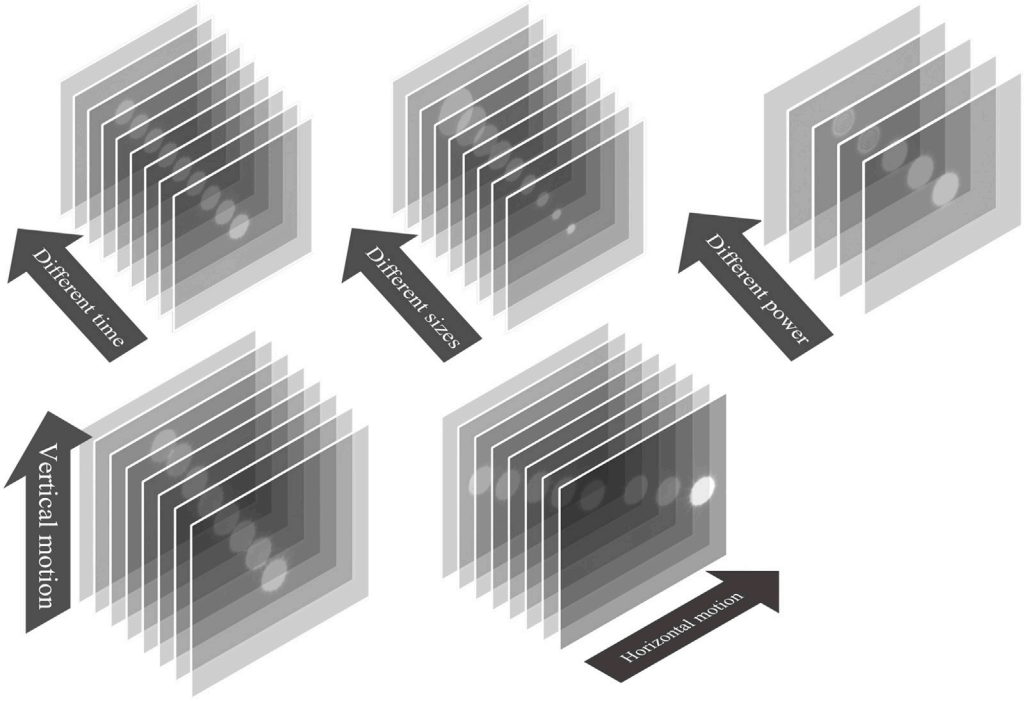

FIGURE 5
Experimental image data.

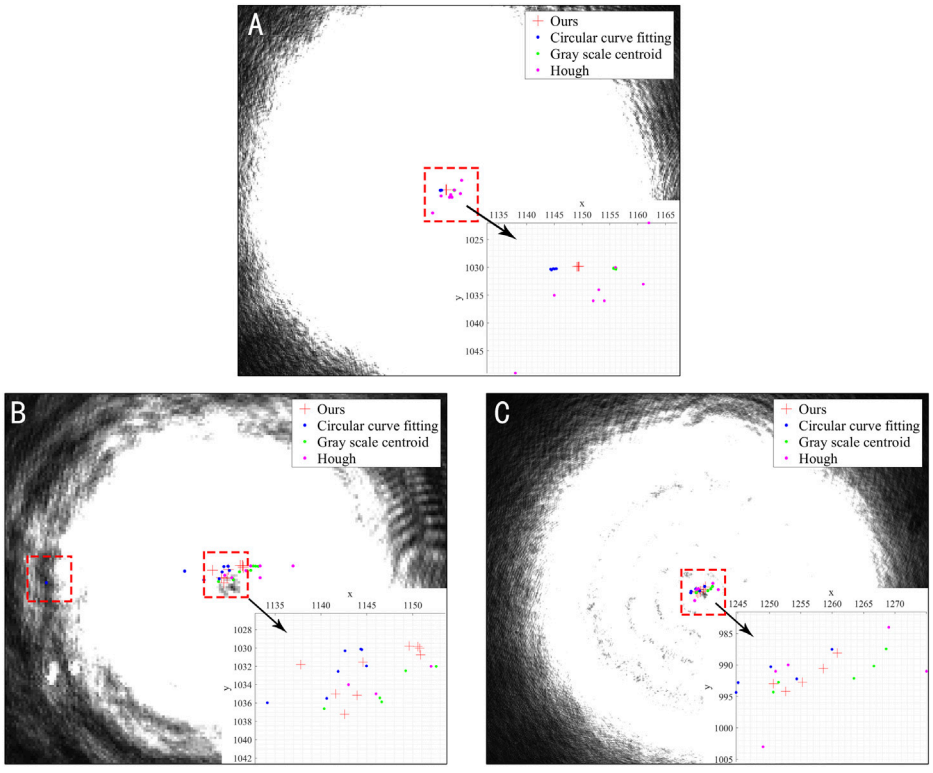

FIGURE 6
Experimental results under the stationary spot position. **(A)**: Different time at the same position; **(B)**: Different sizes at the same position; **(C)**: Different power at the same position.

TABLE 1 Standard deviation of coordinate x and coordinate y resulting from different methods.

Algorithm	Group1		Group2		Group3		Average
	x	y	x	y	x	y	
Ours	0.140	0.024	4.806	2.745	4.174	2.406	2.383
Circular curve fitting	0.388	0.079	24.993	2.679	6.468	2.632	6.207
Gray scale centroid	0.176	0.076	5.574	2.604	8.517	2.646	3.266
Hough transform	7.463	7.038	8.353	2.369	11.781	6.907	7.319

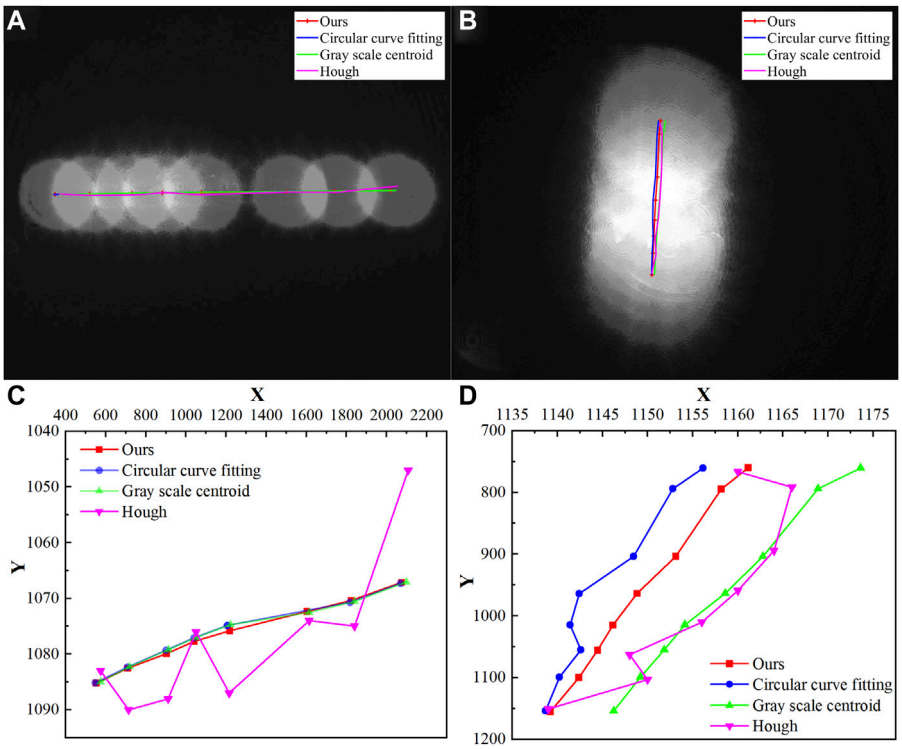

FIGURE 7
Experimental results under the moving spot position. **(A)**: Horizontal direction; **(B)**: Vertical direction; **(C)**: Details in horizontal direction experiment; **(D)**: Details in vertical direction experiment.

$$\delta_\varepsilon(z) = \frac{1}{\pi} \cdot \frac{\varepsilon}{\varepsilon^2 + \pi^2} \tag{7}$$

The minimization problem is solved by solving the Euler-Lagrange equation corresponding to Eq. 5. Using Variation and Gradient Descent to Solve the Extreme Values of Energy Functionals, as in Eq. 8. Finally, the energy equation evolution curve is obtained.

$$\frac{\partial \varphi}{\partial t} = \delta(\varphi)\left[\mu div\left(\frac{\nabla \varphi}{|\nabla \varphi|}\right) - \lambda_1 (u - c_1)^2 + \lambda_2 (u - c_2)^2\right] \tag{8}$$

In order to speed up the evolution process, optimize the initial position of the level set function, Compute the global image grayscale centroid. Obviously the center of mass coordinates are inside the laser spot. This is a rough estimate and cannot be used for precise positioning, But it is enough to make the level set function get a suitable initial position, so that the gradient descent is faster.

In Figure 4A, the laser spot positions are different, but the initial curve positions of the level set algorithm are all inside the spot. The curve evolution results are shown in Figure 4B. The

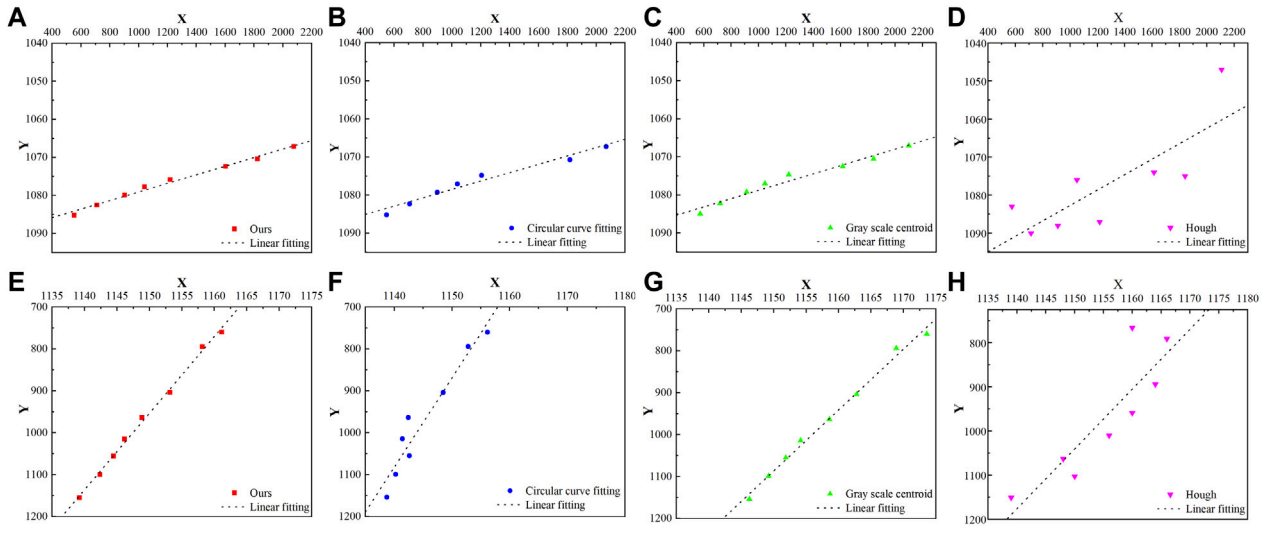

FIGURE 8
Results of fitting straight lines with different methods. **(A)**: Results of our method in horizontal direction; **(B)**: Results of Circular curve fitting method in horizontal direction; **(C)**: Results of Gray scale centroid method in horizontal direction; **(D)**: Results of Hough transform method in horizontal direction; **(E)**: Results of our method in vertical direction; **(F)**: Results of Circular curve fitting method in vertical direction; **(G)**: Results of Gray scale centroid method in vertical direction; **(H)**: Results of Hough transform method in vertical direction;

TABLE 2 The Residual sum of squares of the results under different methods.

Algorithm	Group4	Group5	Average
Ours	3.1	1.569	2.335
Circular curve fitting	9.915	20.034	14.975
Gray scale centroid	8.19	4.521	6.356
Hough transform	467.909	137.655	302.782

image is segmented according to the closed curve, and the grayscale center of mass is calculated again for the interior of the curve to obtain a more accurate center position.

Experiment and analysis

In this section, we design several sets of experiments and compare our method with the Hough transform method, the circular fitting method, and the grayscale center-of-mass method. The data used in the experiment comes from the real laser spot image we collected, in which the laser model is MSL-FN-532 and the size of the CCD camera is 2456 × 2048 pixels, The shooting is done on an optical platform.

Experimental data

Since the real data do not have *a priori* coordinate position information, we designed five sets of experiments to verify the performance of the algorithm. The experimental images are shown in Figure 5. When taking the first three sets of images, the laser and the camera remain relatively fixed. The first group contains nine pictures, taken at different time points; The second group contains nine pictures, and the laser spot has different sizes by adjusting the beam expander; The third group contains five images, and by changing the attenuation ratio, laser spots of different powers are generated; The fourth group contains 8 images, with the laser moving horizontally as they were taken; The fifth group also contains 8 images, with the laser moving vertically. Theoretically, the position of the laser spot in the first three groups of images is fixed, and we evaluate the performance of each method by the repeatability of the calculation results of each method. For the latter two sets of images, although the laser can be displaced with high precision on the optical table, we cannot guarantee that the camera is perfectly level. Considering that the trajectory of the laser center coordinates is a straight line, we calculated the linear fitting ability of the calculated results of each method. Specific graphs and data are given below with detailed analysis.

Repeatability

The localization results of different methods can be seen in Figure 6. Figures 6A–C show the coordinates calculated by each method. The results show that the method based on the Hough transform is the least effective, and it calculates the coordinate positions very randomly. The effect of the circular arc fitting method is unstable, and in Figure 6B, its results have a large deviation in the x-direction. The performance of the gray centroid method is better, and it calculates the coordinate positions more centrally, which is very close to the effect of the method in this paper, we use standard deviation for quantitative analysis and the results are given by Table 1. The standard deviation reflects the degree of dispersion of the data, and when its value is smaller, it means that the data is more concentrated. From Table 1, it is easy to see that the method in this paper performs the best, and the standard deviation of the method in this paper is reduced by 27% on average compared with the traditional gray centroid method.

Linear fitting ability

In this section, the accuracy of different methods is examined by measuring the laser spot centers at different locations. The results of the experiments are shown in Figure 7. We have drawn the visualized paths on the coordinate system. It is easy to notice from Figures 7C,D that the results of Hough transform still look the worst and other method s need to be compared quantitatively.

Because the laser's travel path is straight, we perform a linear fit on the results of each algorithm, and the fitting results are shown in Figure 8. When the laser is moved horizontally, the fitting results of different methods are shown in Figures 8A–D. When the laser is moved vertically, the fitting results of different methods are shown in Figures 8E–H. The fitting ability of discrete points can be expressed as Residual Sum of Squares. The smaller the sum of squared residuals, the better the data fit, i.e., the closer the coordinate points are to the true laser spot movement path. For the first row of Figure 8, The laser moves horizontally, the residual at each point is the distance from the point to the vertical of the fitted line. Similarly, in the second row, the residual is the horizontal distance from the point to the fitted line. The detailed calculation results are given in Table 2.

From Table 2, we can intuitively see that our method fits the best, this means that each coordinate is very close to the trajectory of the laser's movement. The gray centroid method is the second most effective. The residual sum of squares of the Hough transform is the largest. According to the data in Table 2, Our method reduces the residual sum of squares of the results calculated by the gray scale centroid method by 63.3%, which shows that our method is effective.

Conclusion

This paper focuses on researching the effectiveness of image segmentation based on Chan-Vese model for laser spot center localization. In order to improve the segmentation accuracy, two improvements are made. First, we added image pre-processing to denoise the image using two layers of wavelet decomposition. Second, we improved the initialization coordinates of the level set curve, which drives the evolution of the curve from inside the laser spot. We selected three classical algorithms for comparison, among which the traditional gray centroid method significantly outperformed other algorithms in our dataset. Therefore, we combine our work with the gray scale centroid method and find that it can further improve the accuracy and stability of laser spot positioning, which proves that the image segmentation method based on Chan-Vese model can be applied to laser spot center detection, it provides an idea for method improvement.

Data availability statement

The original contributions presented in the study are included in the article/Supplementary Material, further inquiries can be directed to the corresponding author.

Author contributions

XG proposed the idea and wrote the original manuscript. XG and PM performed the simulation work. DM helped collect the data. PM helped in revising the original manuscript, JS and QJ supervised the research work. HW helped to complete the experiment.

Funding

This work was supported by the National Natural Science Foundation of China Civil Aviation Joint Fund (U1833203) and Graduate Education Innovation Program Fund of Zhengzhou University of Aeronautics (2021CX48).

Conflict of interest

The authors declare that the research was conducted in the absence of any commercial or financial relationships that could be construed as a potential conflict of interest.

Publisher's note

References

1. Zhuo H. Laser spot measuring and position method with sub-pixel precision. In: *International symposium on photoelectronic detection and imaging 2007: Related technologies and applications*, 6625 (2008). p. 66250A. doi:10.1117/12.790760

2. Krstinić D, Skelin AK, Milatić I. Laser spot tracking based on modified circular Hough transform and motion pattern analysis. *Sensors* (2014) 11:20112–33. doi:10.3390/s141120112

3. Kong B, Wang Z, Tan Y. Algorithm of laser spot detection based on circle fitting. *Infrared Laser Eng* (2002) 31:275–9.

4. Zhang K, Chen H, Li J, Xu J. An improved sub-pixel algorithm for laser spot center determination based on Zernike moments. *Proc SPIE - Int Soc Opt Eng* (2009) 7382:738244. doi:10.1117/12.836667

5. Ballard DH. Generalizing the Hough transform to detect arbitrary shapes. *Pattern Recognition* (1981) 13:111–22. doi:10.1016/0031-3203(81)90009-1

6. Ying J, He Y, Zhou Z. High speed gradient Hough transform algorithm for laser spot location. *Proc SPIE - Int Soc Opt Eng* (2007) 6625:66250J. doi:10.1117/12.790783

7. Moss RH. Optical projection and image processing approach for mine wall monitoring. *Opt Eng* (2007) 46:013601. doi:10.1117/1.2424914

8. Liu Z, Wang Z, Liu S, Shen C. Simulating multiple class urban land-use/cover changes by RBFN-based CA model. *Comput Geosci* (2011) 28:111–21. doi:10.1016/j.cageo.2010.07.006

9. Zhang J. Research on the measurement accuracy of different laser spot center location. *Int Conf Photon Opt Eng* (2019) 38. doi:10.1117/12.2521709

10. Hui L, Zheng S, Cao S, Wang Z. Algorithm of focal spot reconstruction for laser measurement using the schlieren method. *Optik* (2017) 145:61–5. doi:10.1016/j.ijleo.2017.07.033

11. Chen H, Bai Z, Yang X, Ding J, Qi Y, Yan B, et al. Enhanced stimulated Brillouin scattering utilizing Raman conversion in diamond. *Appl Phys Lett* (2022) 120(18):181103. doi:10.1063/5.0087092

12. Bai Z, Williams RJ, Kitzler O, Sarang S, Spence DJ, Wang Y, et al. Diamond Brillouin laser in the visible. *APL Photon* (2020) 5(3):031301. doi:10.1063/1.5134907

13. Wang X, Huang D, Xu H. An efficient local chan–vese model for image segmentation. *Pattern Recognition* (2010) 43:603–18. doi:10.1016/j.patcog.2009.08.002

14. Figueiredo M, Nowak RD. An EM algorithm for wavelet-based image restoration. *IEEE Trans Image Process* (2003) 12:906–16. doi:10.1109/TIP.2003.814255

15. Zhao Z, Bai Z, Jin D, Qi Y, Ding J, Yan B, et al. Narrow laser-linewidth measurement using short delay self-heterodyne interferometry. *Opt Express* (2022) 30(17):30600–10.

16. Hun X, Bai Z, Chen B, Wang J, Cui C, Qi Y, et al. Fabry–Pérot based short pulsed laser linewidth measurement with enhanced spectral resolution. *Results Phys* (2022) 37:105510. doi:10.1016/j.rinp.2022.105510

17. Donoho DL, Johnstone IM. Minimax estimation via wavelet shrinkage. *Ann Statist* (1999) 26:879–921. doi:10.1214/aos/1024691081

18. Yang L, Liu G, Shi Z. Research on Suppression Algorithms of the Ringing Effect Caused by Blind Image Restoration. *2015 Fifth International Conference on Instrumentation and Measurement, Computer, Communication and Control* (IMCCC) (2015) 1264-1267. doi:10.1109/IMCCC.2015.271

frontiers | Frontiers in Physics

TYPE Brief Research Report
PUBLISHED 17 October 2022
DOI 10.3389/fphy.2022.1034932

OPEN ACCESS

EDITED BY
Zhi-Han Zhu,
Harbin University of Science and Technology, China

REVIEWED BY
Aili Wang,
Harbin University of Science and Technology, China
Zhigang Peng,
Beijing University of Technology, China
Wang Gao,
North University of China, China

*CORRESPONDENCE
Li Li,
ll@cust.edu.cn

SPECIALTY SECTION
This article was submitted to Optics and Photonics,
a section of the journal
Frontiers in Physics

RECEIVED 02 September 2022
ACCEPTED 27 September 2022
PUBLISHED 17 October 2022

CITATION
Chang D and Li L (2022), Edge GPU cluster processing system for laser interference image collection.
Front. Phys. 10:1034932.
doi: 10.3389/fphy.2022.1034932

Edge GPU cluster processing system for laser interference image collection

Dajun Chang[1,2] and Li Li[1]*

[1]College of Computer Science and Technology, Changchun University of Science and Technology, Jilin, China, [2]School of Electrical Information, Changchun University of Architecture and Civil Engineering, Jilin, China

In order to realize the real-time processing and communication of multi-laser interference images, a GPU cluster processing system for laser interference images was designed. The measured target was illuminated by multiple lasers, and the image information of the multi-laser interference fringes was obtained by the CCD. The data of laser interference images from CPU was transmitted by the GPU cluster, and the image feature recognition and transmission were completed through the cluster image processing module. A multi-channel laser interference image transmission algorithm was designed by the multi-core and multi-buffer (MCMB) algorithm. In the experiment, the laser interference images were collected by the CPU, and then the real-time communication of multi-channel images data was completed by the GPU cluster. The packet loss rate experiment showed that when the data traffic reached 110, the data was lost with the traditional UDP communication algorithm, and the slope of the fitting curve was 0.6,053. When the data flow reached 160, the data was lost with MCMB algorithm, and the slope of the fitting curve was 0.2,181. In contrast, the GPU occupancy of this algorithm was improved, and it was still not saturated at 210 data streams. In a word, the system has better optimization effect in real-time processing and communication of multi-laser interference images.

KEYWORDS

laser interference image, GPU cluster, MCMB, data packet drop rate, GPU resource occupancy rate

Introduction

Spectral analysis of laser is an important method to analyze target features [1]. The analysis and recognition of laser interference images are used in many fields, such as laser warning, drug identification, and so on [2]. If a large amount of information can be quickly and accurately classified and communicated, it will be very practical.

With the continuous development of computer science and technology in recent years, its application has become more and more extensive in laser spectrum analysis and laser information processing [3–6]. The data mining technology for laser interference fringes can improve the processing capability of the system. According to the characteristics of frequency and amplitude of the laser interference images, the effective identification of similar targets and the suppression of similar noises can be realized. For the classification of laser

interference images, algorithms such as machine learning [7], deep learning [8], and adaptive parameter adjustment [9] can be used. Liu Xuan et al. [10] used machine learning algorithms to classify and identify hyperspectral vegetation data, and the obtained band characteristic interval provided data support for agricultural vegetation evaluation. The spectral resolution of the system was 5.0 pm, and it took 13.6 s to complete the spectral image transmission of the entire area. The main reason for the slow speed was the large amount of image data transmission. Yuan Shuping [11] used data mining technology to classify laser spectrum data, and greatly improved the classification speed through multi-node parallel processing. It worked well for fluorescence feature data, but for image data, the parallel communication speed was still limited. Yu Xiaoya et al. [12] completed the classification and recognition of algae images by partial least squares algorithm, and its average accuracy rate was over 80%. This method has a good effect on the acquisition of laser interference images, but when there are many features of the laser interference images, the recognition accuracy will drop significantly. Reference [13] proposed a network layering method, which was dynamically divided according to the resource situation of the terminal equipment. Due to the powerful computing power of GPU (Graphics Processing Unit), it had been widely used in laser interference images, artificial intelligence and other fields. According to this design idea, the paper applied the GPU cluster to the fast processing and communication of a large number of laser interference fringe images. Reference [14] used the efficient packet processing capability of DPDK (Data Plane Development Kit [15]) to implement a packet capture system, which greatly improved the data processing capability of the system. For a large amount of laser interference images data, the use of GPU cluster computing can improve the real-time computing capability of the system [16]. GPU cluster has the advantages of strong data processing capability and fast speed. And compared with multi-channel communication, it can also realize the reasonable allocation of core processing system resources according to the data flow state. In order to improve the data processing and communication capabilities of GPU clusters and meet the fast processing requirements for a large amount of laser interference images data, the GPU cluster processing and communication transmission system was proposed based on data stream processing. The efficient transmission of laser interference images data stream had been realized by the system.

System design

The system consists of two parts, the laser interference fringe acquisition module (module A) and the GPU cluster processing module (module B). The laser interference fringes can be dynamically collected in real time by module A. When the multi-laser signals are mixed into the interferometer, the CCD sensor at the end will collect the corresponding interference fringe image. With the increase of time, the system can obtain a large number of interference fringe images, which constitute the laser interference image dataset. These data can be used for analysis of the laser signal. Images data can be quickly classified, identified and transmitted in real time by module B. The system structure is shown in Figure 1.

As shown in Figure 1, the driver to complete the scanning of the laser intensity and wavelength is controlled by CPU, to realize the wide-band dynamic scanning of the target area. Any material, structure, *et c.* Whose spectral properties need to be obtained can be the target to be measured. The laser interference images data stream from module A is entered into the GPU cluster. When the laser irradiates the target, the diffusely reflected light will be received by the optical system. In order to obtain better laser interference images, multi-channel lasers were used to get interference fringes, so that it can reduce the impact on image processing and communication quality analysis. The optical system converges and collimates the incident light, making it more coherent. The light emitted from the optical system enters the interferometer, thereby forming an interference fringe image, which is imaged on the CCD sensor. The image is transmitted to the GPU cluster through the CPU, and the extraction of image features and data analysis are completed in the cluster operation. Finally, the signal is sent to the end user through the wireless reflection module. The innovation in the architectural design of this system is to match the processing power of the GPU cluster with a large number of laser interference fringe images. In the matching process, edge computing was used to realize the self-organization of terminal contacts, so as to optimize the data flow distribution in the process of laser interference fringe image communication.

Principles of the system

Laser interference images

The Fourier transform interferometer was used to complete the fast spectral analysis of the incident laser light. The interference module can generate two beams of coherent light, and control the optical path difference to make them interfere, thereby obtaining interference images. The Fourier transform interferometer was realized by frequency demodulation.

Assuming that the incident laser wave number is v, it is irradiated on the beam splitter (BS) plate with reflectivity r and transmittance t. The optical path difference of the two beams is l, so the interference spectrum image can be expressed as

$$\begin{cases} I(l, v) = 2RTB_0(v)(1 + \cos\varphi) \\ \varphi = 2\pi \times v \times l \end{cases} \tag{1}$$

Among them, $R = r \cdot r*$, which is the reflectivity of BS. B_o 5) is the incident beam intensity, and v is the wave number. $T = t \cdot t*$, which is the transmittance of BS. After the laser was selected, v

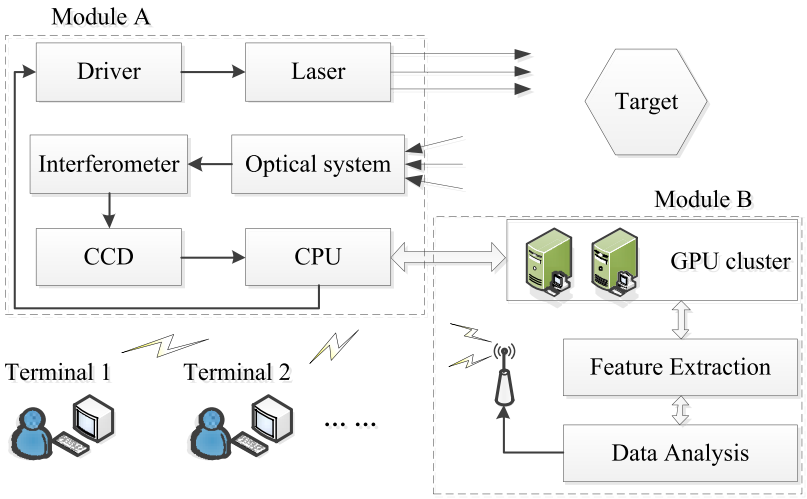

FIGURE 1
Laser interference images data processing system based on GPU cluster.

became a constant, so after substituting the constant, the independent variable was only l. The light source is usually an extended-spectrum light source in practical applications. It can be seen that in the full spectrum range, the interference images should be the integral of all wave numbers, and it is

$$I(l) = \int_0^\infty B(v)\cos(2\pi vl)dv \tag{2}$$

Among them, B (v) $= 2RTB_o(v)$, which is the light source intensity obtained by correcting various influences. The above formula represents an input beam, which wave number is v after passing through the interferometer. So the image surface curve of the relationship between strong $I(l)$ and optical path difference can be calculated. When the optical path difference of the two beams of light is Δ = (Z1-Z2), Z1 and Z2 represent the optical path distances of the laser light in the two directions in the interferometer, respectively. The light intensity measured by the detector is the sum of all frequency light intensities, which is

$$I_R(\Delta) = 2TR\left[\int_0^\infty E_{0(\sigma)}^2 d\sigma + \int_0^\infty E_{0(\sigma)}^2 \cos(2\pi\sigma\Delta)d\sigma\right] \tag{3}$$

Among them, R is the reflectance and T is the transmittance.

Because the interference images are a real even function, the cosine change is changed to a Fourier change, and the final spectral intensity is

$$B(\sigma) = \int_{-\infty}^\infty I(\Delta)e^{-i2\pi\sigma\Delta}d\Delta \tag{4}$$

Then the interference images can be obtained by

$$I(\Delta) = \int_{-\infty}^\infty B(\sigma)e^{i2\pi\sigma\Delta}d\sigma \tag{5}$$

GPU cluster

From the perspective of hardware architecture, the GPU cluster only connects the GPU as a peripheral device through the high-speed PCI bus to the inside of the node. The addition of GPU makes the cluster presentation node's internal computing resources heterogeneous. Since the GPU not only has computing resources that are heterogeneous to the CPU, the data transfer between the CPU and the GPU must be performed explicitly under the control of the CPU. As a computing resource for multi-scale data parallel computing, GPU clusters have multi-level parallel computing capabilities. GPU clusters can not only support single-program multi-data and multi-program multi-data computing capabilities of conventional granularity, but also support more fine-grained large-scale data-oriented single-program multi-data and single-instruction multi-data computing capabilities. It provides powerful large-scale data parallel processing capabilities to the cluster.

Since a large number of images data streams are generated during the real-time acquisition of laser interference images, it has significant advantages that the use of GPU clusters to classify, identify and communicate laser interference images.

Algorithm design

Data transfer protocol

The data of the laser interference images data stream was composed of a steady stream of numerical matrix data, including a large number of floating point numbers. In order to reduce the overhead of the data to be transmitted and realize the rapid classification and communication transmission of laser

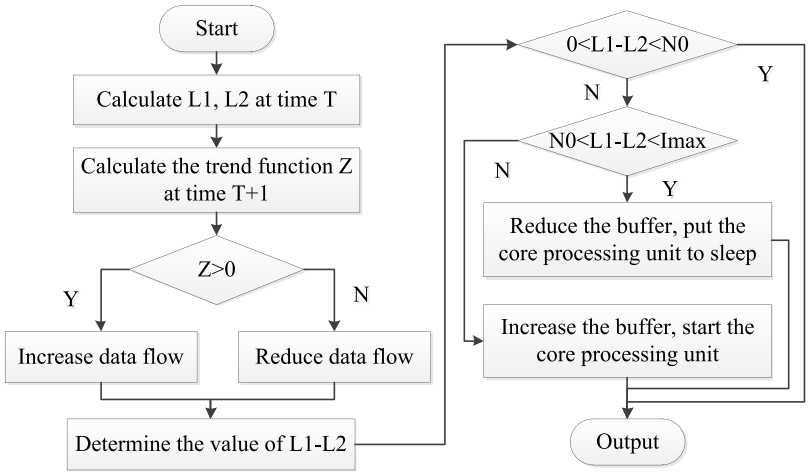

FIGURE 2
Flow chart of multi-buffer algorithm based on GPU cluster.

interference images, a message-based data transmission protocol was designed to reduce the amount of data, and according to the content of the protocol, the receiving end can directly obtain it with only one time.

The system maintained multiple cyclical laser interference images data stream buffers, and the number of buffers was dynamically adjusted with the changes of the laser interference images data stream. The circular data stream buffer was used to cache the laser interference images in a classified manner, and the images of each frame belonged to the processing cycle. DPDK used the memory pool to manage the data. After the data received, the received core applied for the object from the memory pool. After completing the data encapsulation, it cached the data packet to the write data packet according to the data packet identifier and processing cycle. In the cache line corresponding to the pointer, each frame was processed for a data stream with the same processing cycle. After the data was buffered, the communication was in a one by one correspondence with the buffer table of the data stream.

MCMB algorithm

In order to reduce the occupation of shared resources and improve the efficiency of data processing, the affinity of the data flow and the core was set. The data packets belonging to the same data flow were handed over to the designated core for processing. Among them, each forwarding core managed a circular laser interference images data stream buffer, which was responsible for forwarding the laser interference images in the managed buffer, and the selection of multi-frame images was dynamically selected according to the load balance of the ports. Thus, MCMB was constructed, and its flow is shown in Figure 2.

L1 and L2 represent two adjacent laser interference images, and T represents the sampling time for collecting the laser interference images. Z represents the data flow trend line, which is quantitatively analyzed by GPU work resource occupancy. And according to its size to increase or decrease the data flow control. N0 represents the amount of image feature difference, which is used to measure the total amount of feature data in the image. Imax represents the feature data amount of the laser interference image including the most feature data. The acquisition unit completed the acquisition of the interference fringe image data stream from the CCD, and performs matching calculation on the two images whose time interval was T. When the trend function $Z > 0$, increase the data flow. Conversely, when the trend function $Z < 0$, the data flow is reduced. This enables real-time adjustments to the data flow. The difference calculation was performed on the two sets of interference fringe image data, and the interval range was judged. When it was between (0, N0), it was directly reserved and output. When it was between (N0, Imax), reduce the buffer and put the core processing unit to sleep.

Experiments

Acquisition of laser interference images

Under laboratory conditions, real-time interference image processing and communication were performed for the aliased spectral data of three lasers at 639.1 nm, 654.5 nm and 660.1 nm. Different lasers entered the irradiation window at the same time through different pigtails, and then the beamforming and collimation module completed the optical path shaping. A Fourier transform interferometer

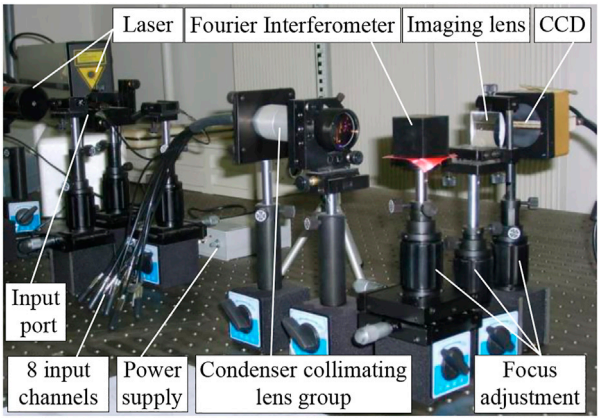

FIGURE 3
Laser interference image acquisition system.

was fixed at 4 cm from the output end, and an imaging lens was installed between the output end of the interferometer and the camera to focus the interference fringe image on the CCD sensor. The experimental structure is shown in Figure 3.

The aliasing spectrum is calibrated with a Q8344A spectrometer. The laser spectrum curve is shown in Figure 4.

From Figure 4, although the interference fringes entered the CCD sensor at the same time, there was a certain aliasing phenomenon, but the position of the main laser peak after inversion could still be easily identified, and the optimal response value was about -37.6 dB.

Data streaming test

In order to verify the performance of the scheme, eight ordinary servers were used to simulate eight channels of laser interference images to transmit data streams in real time. Three computer nodes were used to build a GPU cluster, and each node was configured with a gigabit network card. Each server can simulate multiple terminal devices at the same time. The GPU cluster was built by computing nodes with GPUs installed. The number of computing nodes in the cluster can be adjusted according to changes in the number of terminal devices in the actual application scenario. The traditional UDP (User Datagram Protocol) algorithm was selected to compare with MCMB algorithm. Comparing the algorithms applicable to different systems can characterize the pros and cons of the algorithms from the program running effect. In the next section, we will also compare the resource usage of hardware modules. When the flow of the data stream was continuously increased, the test result of the data packet drop rate is shown in Figure 5. At the same time, the GPU resource occupancy rates of the traditional communication algorithm and the optimized communication algorithm were compared, as shown in Figure 5.

In Figure 5, when the number of data streams exceeded 110 by the traditional UDP algorithm, packets started to drop during the transmission of images data. With the further increase of data traffic, the packet loss rate also increased. The change of the test curve is close to linear, which shows that the data communication capability of the system has reached its limit. As the data flow continues to grow, the number of lost packets will also increase linearly. The calculation shows that the fitting curvature of the curve is 0.6053. When the number of data

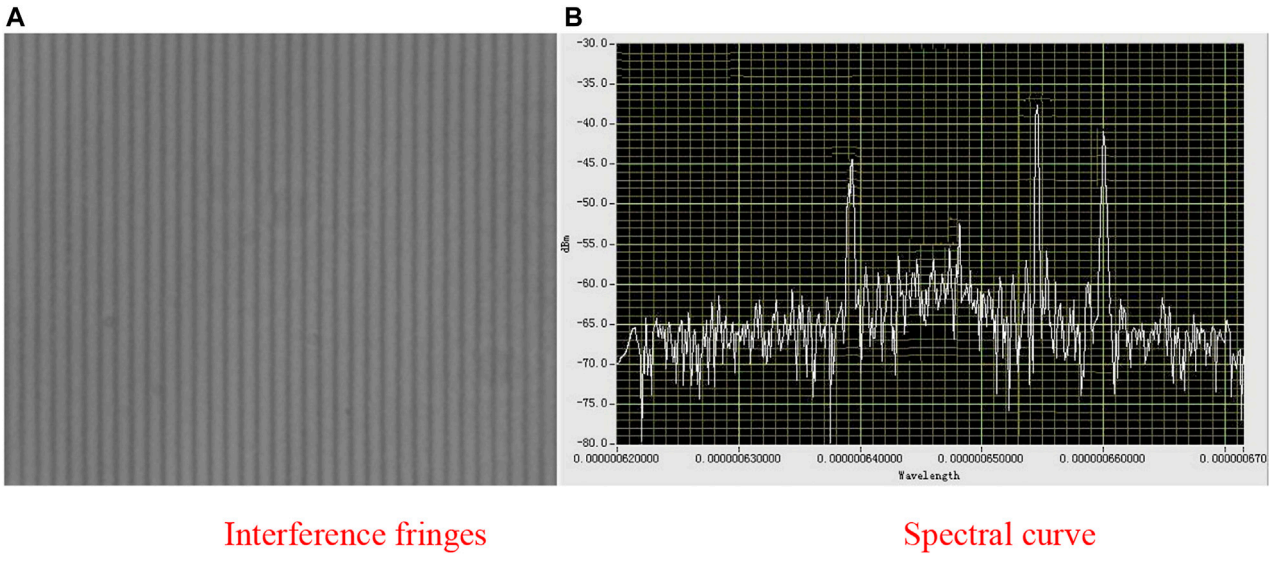

FIGURE 4
Three sets of laser spectrum calibration curves.

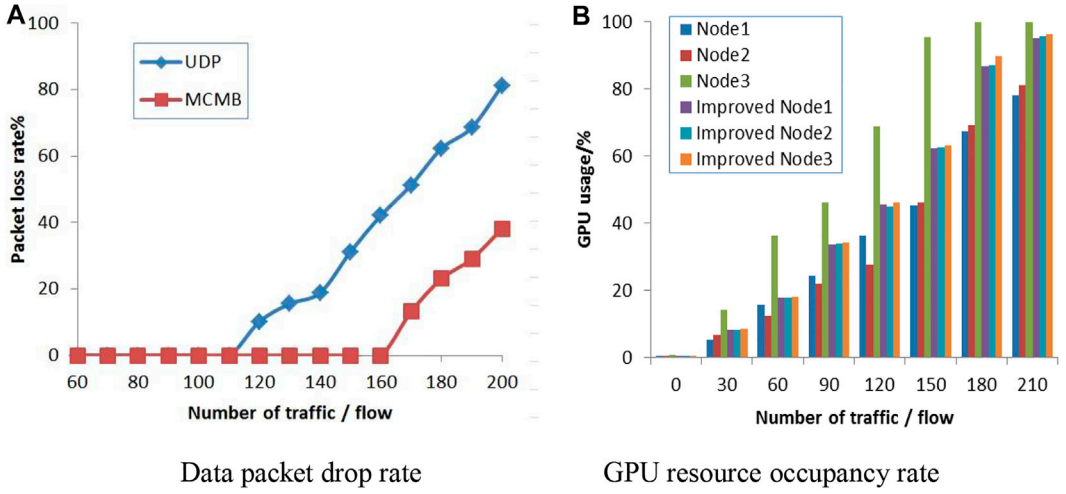

FIGURE 5
Data streaming test.

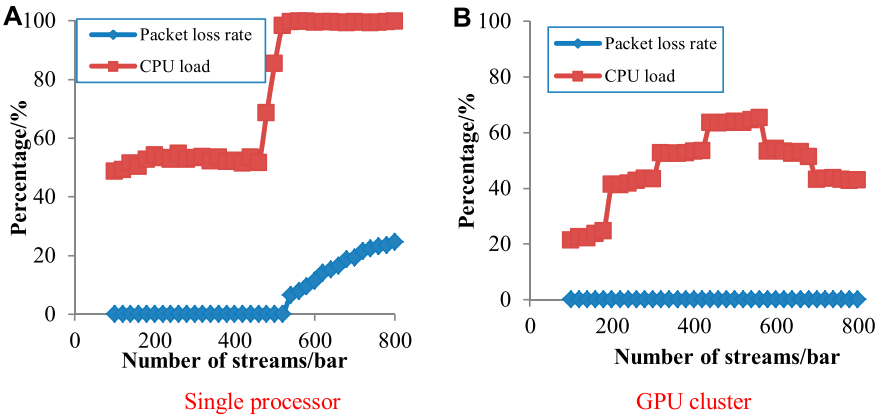

FIGURE 6
Packet loss rate and CPU load for two methods.

streams exceeded 160 by the MCMB algorithm, packets started to drop during the transmission of images data. Its packet loss curve is also close to linear, and the curve fitting curvature is 0.2181. It verifies that the improved algorithm has lower packet loss rate and stronger communication ability. In Figure 5, the GPU occupancy ratios on the three data nodes using the traditional method are significantly different, and the resource occupancy ratio of the third node is relatively high. As the data traffic increases, the third node overflows when the traffic reaches between 150 and 180, resulting in significant packet loss. After the optimization of this algorithm, the GPU occupancy difference of the three nodes is very small. They evenly distribute the total amount of data flow across the three nodes. When the data traffic reaches 210, the GPU occupancy rate of the three nodes reaches more than 95% without overflow, which avoids packet loss caused by excessive data traffic. At node 3, many data streams passed through this place, so the communication pressure was high and the resource occupancy rate was high. This also shows that when the communication network data flow is not evenly distributed, it will lead to a decrease in communication capacity.

Analysis of packet loss rate and load status

In order to verify that the GPU cluster can greatly improve the data transmission capability of laser interference images, a comparison test was carried out with the communication unit of

a single processor. The number of image data streams was increased from 100 to 800, and the packet loss rate and CPU core load status of the system were recorded for each additional 100. The test results were shown in Figure 6.

As shown in Figure 6, the test results of a single processor showed that when the data flow exceeds 520, the CPU load increased significantly. When there were more than 550 data streams, the CPU load basically remained around 99.5%. At the same time, the packet loss phenomenon occurred in the system, and the packet loss rate increases with the increase of the number of data streamed, reaching 24.6% in 800 data streams. As shown in Figure 6, the test results of the GPU cluster showed that there was no packet loss during the entire process from 100 to 800 data streams. After the load of each CPU in the system was increased by more than 60%, the data processing task was redistributed, so that the original CPU load was gradually reduced. When the offload of data processing was increased, the average CPU load was only 43.2% at 800 entries.

Conclusion

Aiming at the problem of fast processing and communication, a multi-laser interferometric image real-time processing and communication system was proposed based on GPU cluster. The multi-core multi-buffer algorithm was designed to improve the resource allocation of multi-nodes. It is a certain contribution to the resource optimization problem of simultaneous processing of multiple data streams by the GPU cluster design and improved algorithm proposed in the paper. The feature of the paper is to apply the image synchronization processing capability of GPU cluster to feature data extraction and real-time data communication of multi-laser interference images. However, it did not discuss the attenuation effect of the optical structure of the system on signals of different wavelengths, and the corresponding correction parameters of the GPU cluster. It will also be the main content of further in-depth research in the later stage of the thesis.

Data availability statement

The original contributions presented in the study are included in the article/supplementary material, further inquiries can be directed to the corresponding author.

Author contributions

DC is responsible for experimental testing and writing papers. LL is responsible for the design of the system structure and simulation analysis.

Conflict of interest

The authors declare that the research was conducted in the absence of any commercial or financial relationships that could be construed as a potential conflict of interest.

Publisher's note

All claims expressed in this article are solely those of the authors and do not necessarily represent those of their affiliated organizations, or those of the publisher, the editors and the reviewers. Any product that may be evaluated in this article, or claim that may be made by its manufacturer, is not guaranteed or endorsed by the publisher.

References

1. Palomares I, Martinez L, Herrera F. A consensus model to detect and manage non-cooperative behaviors in large scale group decision making. *IEEE Trans Fuzzy Syst* (2014) 22(3):516–30. doi:10.1109/tfuzz.2013.2262769

2. Leira R, Julian-Moreno G, Gonzalez I, Gomez-Arribas FJ, Lopez de Vergara JE. Performance assessment of 40 Gbit/s off-the-shelf network cards for virtual network Probes in 5G networks. *Computer Networks* (2019) 152(4):133–43. doi:10.1016/j.comnet.2019.01.033

3. Zhao Z, Bai Z, Jin D, Qi Y, Ding J, Yan B, et al. Narrow laser-linewidth measurement using short delay self-heterodyne interferometry. *Opt Express* (2022) 30(17):30600–10. doi:10.1364/OE.455028

4. Cui L, Chen Q. Dynamic monitoring model based on DPDK parallel communication. *J Comp Appl* (2020) 40(2):335–41. doi:10.11772/j.Issn.1001-9081.2019081405

5. Gao P, Zhao D, Chen X. Multi-dimensional data modelling of video image action recognition and motion capture in deep learning framework. *IET Image Process* (2020) 14(7):1257–64. doi:10.1049/iet-ipr.2019.0588

6. Ponsard R, Janvier N, Kieffer J, Houzet D, Fristot V. RDMA data transfer and GPU acceleration methods for high-throughput online processing of serial crystallography images. *J Synchrotron Radiat* (2020) 27(5):1297–306. doi:10.1107/s1600577520008140

7. Gao-xing Z, Hu S-H, Zhang J-X. Transfer protools for data center networks: A survey. *J Comp Res Development* (2020) 57(1):74–84. doi:10.1007/s11107-015-0550-y

8. Raychaudhuri D, Nagaraja K, Venkataramani A. Mobilityfirst: A robust and trustworthy mobility-centric architecture for the future internet. *SIGMOBILE Mob Comput Commun Rev* (2012) 16(3):2–13. doi:10.1145/2412096.2412098

9. Laoutaris N, Che H, Stavr Akakis I. The LCD interconnection of LRU caches and its analysis. *Perform Eval* (2006) 63(7):609–34. doi:10.1016/j.peva.2005.05.003

10. Liu X, Zhang Y, Teng Y. Estimation of vegetation water content based on Bi-inverted Gaussian fitting spectral feature analysis using hyperspectral data. *Remote Sensing Technology Appl* (2016) 31(06):1075–82. doi:10.11873/J.ISSN.1004-0323.2016.6.1075

11. Yuan S. Research on pattern recognition of laser fluorescence spectrum data in big data background. *Laser J* (2018) 39(5):124–7. doi:10.14016/j.cnki.jgzz.2018.05.124

12. Yu X, Zhang Y, Yin G, Xiao X, Zhao N, Duan J, et al. Feature wavelength selection of phytoplankton fluorescence spectra based on partial least squares. *Acta Optica Sinica* (2014) 34(9):0930002–7. doi:10.3788/aos201434.0930002

13. Qu-cheng C, Qing-kui C. Deep neural network layering strategy for embed deddevices. *J Chin Comp Sys Tems* (2019) 40(7):1455–61. doi:10.0012/20(2019)07-1455-07

14. Rui-lin L, Jun-feng L, Dan L. Realtime capture of high-speed traffic on multi-core platform. *J Comp Res Developer* (2017) 54(6):1300–13. doi:10.7544/issn1000-1239.2017.20160823

15. Matthew Helm J, Swiergosz AM, Haeberle HS, Karnuta JM, Schaffer JL, Krebs VE, et al. Machine learning and artificial intelligence: Definitions, applications, and future directions. *Curr Rev Musculoskelet Med* (2020) 13(10):69–76. doi:10.1007/s12178-020-09600-8

16. Nathali Silva B, Khan M, Kijun H. Internet of things: A comprehensive review of enabling technologies, architecture, and challenges. *IETE Tech Rev* (2018) 35(2):205–20. doi:10.1080/02564602.2016.1276416

frontiers | Frontiers in Physics

TYPE Brief Research Report
PUBLISHED 24 October 2022
DOI 10.3389/fphy.2022.1036346

OPEN ACCESS

EDITED BY
Zhi-Han Zhu,
Harbin University of Science and Technology, China

REVIEWED BY
Santosh Kumar,
Liaocheng University, China
Zilong Zhang,
Beijing Institute of Technology, China

*CORRESPONDENCE
Mingliang Long,
F_CEO_beifeng@126.com

SPECIALTY SECTION
This article was submitted to Optics and Photonics, a section of the journal Frontiers in Physics

RECEIVED 04 September 2022
ACCEPTED 07 October 2022
PUBLISHED 24 October 2022

CITATION
Long M, Zhang H, Yu RZ, Wu Z, Qin S and Zhang Z (2022), Satellite laser ranging at ultra-high PRF of hundreds of kilohertz all day.
Front. Phys. 10:1036346.
doi: 10.3389/fphy.2022.1036346

Satellite laser ranging at ultra-high PRF of hundreds of kilohertz all day

Mingliang Long[1]*, Haifeng Zhang[1,2], Rong Zong Yu[3], Zhibo Wu[1,2], Si Qin[1] and Zhongping Zhang[1,2,4]

[1]Shanghai Astronomical Observatory, Chinese Academy of Sciences, Shanghai, China, [2]Key Laboratory of Space Object and Debris Observation, Chinese Academy of Sciences, Nanjing, China, [3]School of Materials Science and Engineering, Shanghai University, Shanghai, China, [4]East China Normal University State Key Laboratory of Precision Spectroscopy, Shanghai, China

Satellite laser ranging (SLR) had been operated at a pulse repetition frequency (PRF) from ~10 Hz to 10 kHz; the ultra-high PRF of SLR (UH-SLR) is a trend of development. In this study, an alternate working mode of laser firing and gated pulse bursts is proposed to solve the problem of laser echo interference by laser backscattering. Through an ultra-high PRF of 200-kHz picosecond green laser with single-pulse energy of 80 μJ and a pulse width of 10 ps and a ranging gate device, UH-SLR has been built by an aperture of the 60-cm SLR system in the Shanghai Astronomical Observatory. By this UH-SLR, low-orbit to high-orbit and geostationary orbit satellites are measured night and day and also for low-orbit and medium-orbit satellites in the daytime. The normal point (NP) accuracy is ~30 μm for low-orbit satellites and ~100 μm for high-orbit satellites, which provides an effective method for the development of ultra-high PRF and high-precision space target laser ranging.

KEYWORDS

satellite laser ranging (SLR), picosecond laser, laser backscatter, pulse bursts, ultra-high pulse repetition frequency

Introduction

Satellite laser ranging (SLR) is applied to acquire the distance from satellites to ground stations with the time-of-flight measurement [1–4]. Its ranging accuracy is up to a millimeter or even more, which is a key source of information for satellite geodes [5–10]. A precise orbit determination (POD) can be obtained by SLR [6]; it is an original contribution to testing and verifying relativistic physics [11]. The post-fit root-mean-square residuals of the POD were 8.81 cm with 49 normal points (NPs) for Quasi-Zenith Satellite 1, and also, the corresponding three-dimensional orbital overlap error for 4 days was 160.564 m [10]. At present, the picosecond laser plays an important role in SLR. The pulse repetition frequency (PRF) of the kilohertz (kHz) picosecond laser was more widely used to provide more ranging measurement data and higher ranging accuracy [3, 6, 9]. The high PRF of laser ranging has the characteristic of a fast target search; it can increase the number of echoes within the ranging measurement NPs to obtain higher precision, so it has been rapidly developed [2, 3, 12–17]. In 2018, the Shanghai Astronomical

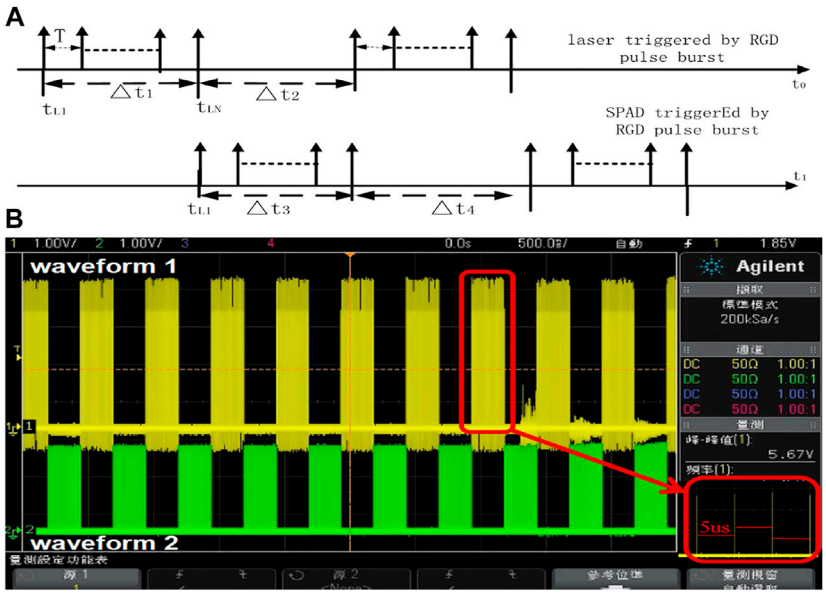

FIGURE 1
Time sequence of the alternated working mode for laser emission and the SPAD triggered **(A)** and pulse burst periodic signal **(B)** by the RGD.

Observatory (SHAO) analyzed the ranging data to show that the NP ranging accuracy at a PRF of 4 kHz was about 2.62 times higher than that of 1 kHz [12]. In the following year, the 10-kHz laser ranging from a low orbit to a geostationary orbit was realized by upgrading the laser and distance gate device [3].

The ultra-high PRF (above 100 kHz) of SLR (UH-SLR) is mainly realized by pulse bursts and the single-photon detector (SPAD). A small fiber nanosecond laser was used to achieve a PRF of 100 kHz UH-SLR, whose measured range was up to 20,000 km, and the NP ranging accuracy was 5~15 mm; this ranging system size was only 1.8 × 1.2 × 1.6 m with a weight of 200 kg [14, 15]. At the Global Technology Conference organized by the International Laser Ranging Service (ILRS) in Stuttgart, D. Dequal analyzed the NP ranging accuracy at a PRF of 100 kHz. UH-SLR was expected to be at a sub-millimeter level [16]; after a few years, they had realized 100 kHz UH-SLR [17]. The SLR station in Graze reported a PRF of 500 kHz UL-SLR, and a few years later, they achieved a PRF of 1 MHz UH-SLR in 2021 [2]. A PRF of 100 kHz lunar laser ranging was built by Vladimir Zharov in Russia to obtain a sub-millimeter ranging accuracy. The aperture of the telescope was 2.5 m with 150 W in a PRF of 150 kHz pulse laser [18]. However, for UH-SLR, the laser backscattered (LBS) under laser transmission in the atmosphere very easily interferes with the laser echoes, which increases the difficulty of laser echo identification [19]. In this study, pulse bursts in the alternating mode are proposed to solve the question of the LBS, and also, the SPAD with low noise worked in the Geiger mode.

Analysis of the SLR detection ability and ranging accuracy

The radar link equation is the basis of evaluating the measurement capability for the SLR system; the equation is as follows [20]:

$$n_0 = \frac{16}{\pi^2} \bullet \frac{\lambda \eta_q}{hc} \bullet \frac{E_t A_r A_s}{R^4 \theta_t^2 \theta_s^2} \bullet T^2 \bullet K_t \bullet K_r \bullet \alpha, \quad (1)$$

where n_0 is the average photo-electrons produced by laser echoes from satellites, λ is the wavelength of the laser, h is the Planck's constant, c is light velocity, η_q is the quantum efficiency of the SPAD, E_t is single-pulse laser energy, A_r is the effective receiving area of the telescope, A_S is the reflection area of the reflector, T is the laser transmission efficiency in the atmosphere, K_t is the efficiency of the transmitting optical telescope, Kr is the efficiency of the receiving optical telescope, α is the attenuation factor, θ_t is the divergence of the laser beam, θ_t is the reflector divergence angle on satellites, and R is the distance from ground stations to satellites. When the SPAD detects background and dark noise, the laser echoes from satellites will not be detected, so the detection probability of the laser echoes from the satellite is as follows:

$$P(0, n_0) = e^{-(n_1+n_2)}(1 - e^{-n_0}), \quad (2)$$

where n_1 is the background photon noise and n_2 is the dark photon noise by the SPAD. It can be seen from the aforementioned formula that in order to improve the detection probability of n_0, n_1 and n_2 should be reduced.

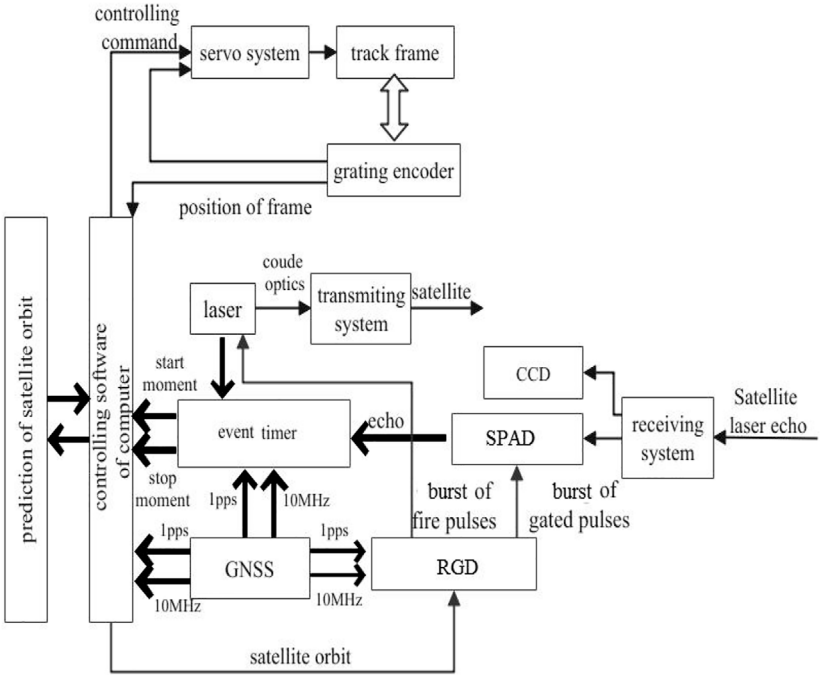

FIGURE 2
Diagram for the UH-SLR system.

Under the PRF of f and combined with the radar link (1), the average number of laser echo points N per unit of time is as follows:

$$N = f e^{-(n_1+n_2)}\left(1 - e^{-\frac{16}{\pi^2}\bullet\frac{\lambda\eta_q}{hc}\bullet\frac{E_t A_r A_s}{R^4\theta_t^2\rho_s^2}\bullet T^2\bullet K_t\bullet K_r\bullet\alpha}\right) \quad (3)$$

From the aforementioned formula, in order to increase the average number of laser echo points N, the PRF of laser ranging should be increased. At the same time, supposing N is constant, increasing the PRF can reduce the single-pulse energy of the laser or the effective receiving area of the system, so a small-aperture telescope and a low-pulse energy laser with a high PRF can be used for SLR, like the minimal SLR system in [14].

The single-ranging accuracy of the SLR system is estimated as follows [14–17]:

$$\sigma_{\text{single}} = \sqrt{\sigma_L^2 + \sigma_{D1}^2 + \sigma_{D2}^2 + \sigma_{ET}^2 + \sigma_S^2} \quad (4)$$

σ_L is the time deviation caused by the pulse width of the laser, σ_{D1} is the deviation of opening time with the SPAD gate, σ_{D2} is the deviation of SPAD closing time of the gate, σ_{ET} is the event timer response deviation, and σ_s is the impulse response deviation of the ranging target. At present, the ILRS uses NPs to reflect the ranging accuracy, and the calculation formula is as follows [12, 17, 20]:

$$\sigma = \frac{\sigma_{\text{single}}}{\sqrt{N}}, \quad (5)$$

where N is the number of data points in the NP duration time, which is defined by the ILRS (https://ilrs.gsfc.nasa.gov/data_and_products/data/npt/index.html). From Eq. 5, it is observed that the PRF of raised SLR can increase the number of echoes in N so that a higher NP ranging accuracy can be obtained.

System construction of UH-SLR and the result

Under UH-SLR, because the PRF is up to 100 kHz (the space-time of laser pulses is 10 μs), the space-time between the laser pulses is short. The LBS from the laser pulse transmission in the atmosphere is relatively strong, and also, the continuing time of the LBS would be more than 10 μs. If the SPAD is opened at the continuing time of the LBS, on one hand, it is easy to cause the SPAD to be saturated and damaged; on the other hand, the LBS will interfere with the laser echoes from satellites; when the SPAD detects photons from the LBS, photons from laser echoes cannot be detected, which will increase the identification difficulty for SLR [19]. The LBS will be avoided in our mode of alternating pulse bursts. The working mode is shown in Figure 1A. The laser

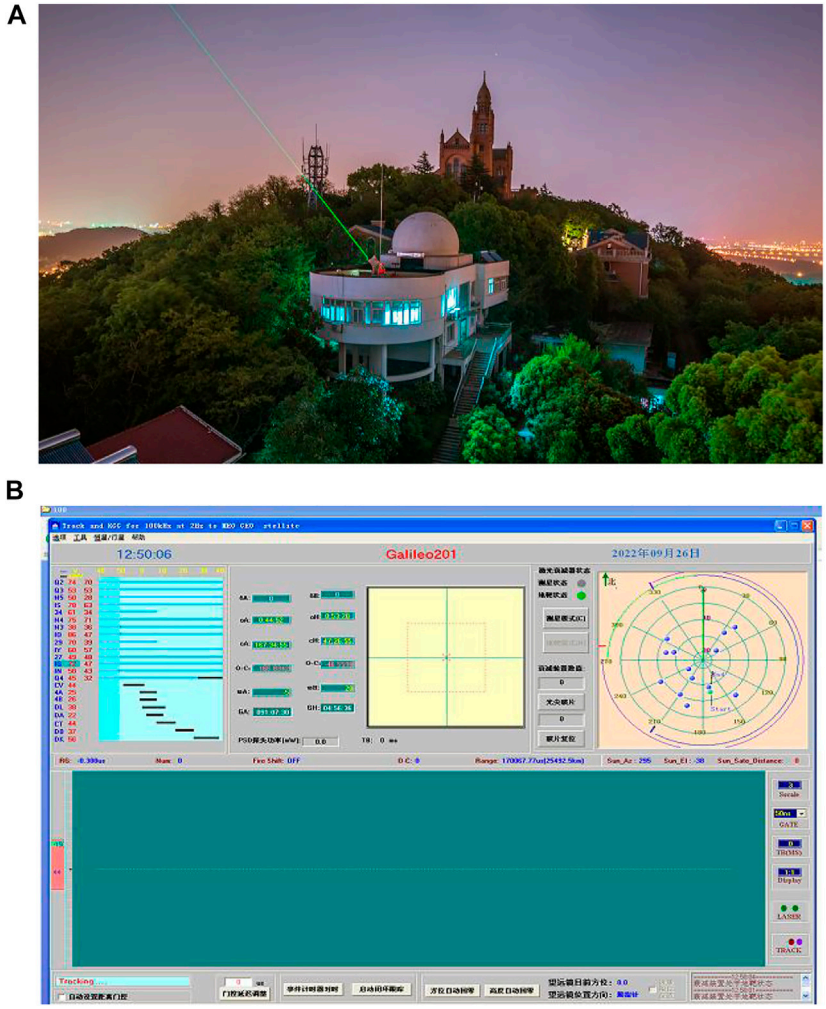

FIGURE 3
SLR system: **(A)**aperture of 60 cm at the SHAO (mountain of SheShang in Shanghai city); **(B)** software for UH-SLR.

outputs pulse bursts, and it stops from a ranging gate device (RGD). Since the output of the laser has stopped, the SPAD is turned on to collect laser echoes from satellites; therefore, it avoids the interference of the LBS. After the SPAD receives the laser echoes, it then stops working, while at this time, the laser would be emitted, so this cycle repeats again; it is shown in Figure 1B.

In Figure 1A, the maximum continuous working time of the trigger signal for pulse bursts is as follows:

$$\Delta t_1 = \frac{2L}{c} \tag{6}$$

where c is the speed of light and L is the distance between the satellite and the SLR station, which varies with the azimuth and elevation of the satellite. The maximum number of pulses emitted from the laser is as follows:

$$N_L = \frac{2L}{cT} \tag{7}$$

where T is the period of the laser PRF; at this time, there is no external trigger signal within $\triangle t_2$, so the laser pulse is not emitted; however, the SPAD is turned on by the gate pulse burst signal from the RGD. The continuous working time $\triangle t_3$ of the corresponding SPAD is equal to $\triangle t_2$, and $\triangle t_2$ is equal to $\triangle t_1$, so the pulse burst period T_L of the laser output is as follows:

$$T_L = \Delta t_1 + \Delta t_2 = \frac{4L}{c}. \tag{8}$$

For satellites with different orbital distances, the corresponding pulse burst periods can be obtained from Eq. 8. For example, for a satellite with a distance of 37,500 km from the SLR station, the pulse burst period T_L will be 500 ms, the

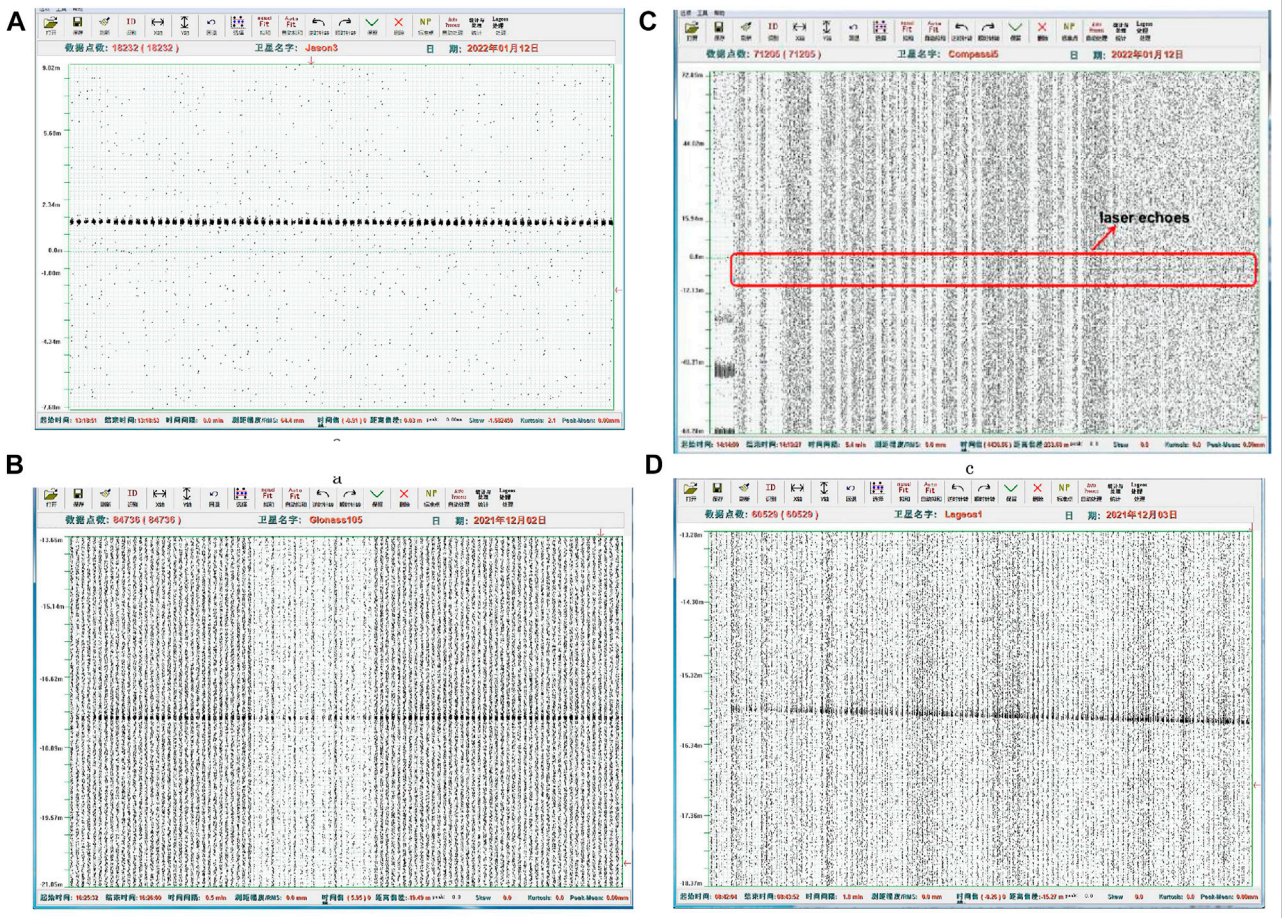

FIGURE 4
Measurement data processing for the satellite Jason3 **(A)**, Glonass105 **(B)**, Compassi5 **(C),** and Lageos2 **(D)** with UH-SLR at the SHAO.

alternating frequency is 2 Hz, and the maximum time of pulse emission within the corresponding burst is 250 ms; for a PRF of 200 kHz, T is 5 μs, so the maximum number of pulses emitted from the laser is 50,000. In the actual ranging process, the satellite distance is changed, so T_L would be changed. For different satellite orbit prediction distances, the repetition frequency of the pulse bursts and the number of pulses in the bursts can be calculated according to Eqs 7 and 8. We design an RGD for our UH-SLR using this. The pulse burst periodic signal of geostationary orbit satellites is generated by RGD, as shown in Figure 1B; waveform 1 is the pulse bursts of the laser ignition signal generated by Eq. 7, and waveform 2 is the SPAD trigger signal generated by Eq. 8; the interval between pulses for waveform 1 and 2 is 5 μs.

Taking the SLR system at the SHAO as a platform with the basic framework of laser ranging in [21], the block diagram of UH-SLR is shown in Figure 2.

In Figure 2, the satellite orbit prediction parameters are downloaded to the controlling software of the computer, and it is converted to a controlling command for the servo system, which controls the telescope mount to track the satellite with an accurate feedback track from the grating encoder. The satellite would be monitored by the receiving system's monitoring charge-coupled device (CCD). At this time, the laser is ignited by the burst fire of pulses from the RGD, through the coupé optics and transmitting system to the satellite, and also, the laser pulse is processed by using a photoelectric detector, and it is sent to the event timer (ET). The ET (USB, A033 origin Latvia) would start to record and send the start time of laser pulses t_1 to the computer. Bursts of gate pulses from the RGD would be sent to the SPAD (by East China Normal University, China). Spectral filtering (0.15 nm) and spatial filtering are performed to reduce background noise. When the laser pulses are emitted, the SPAD is turned off, and when the SPAD is turned on, the laser pulse would be stopped; thus, it realizes the alternating mode of pulse burst sending and receiving. The laser echoes pass through the receiving system to the SPAD, and the return time t_2 is obtained by the ET. Altogether, the RGD, computer, and ET are provided high precision time from the GNSS′ clock.

TABLE 1 Ranging data results for satellites from the UH-SLR system at the SHAO.

Num	Satellite name	Points	RMS (cm)	Num of NP	Num of NP (mm)	Orbit
1	Stella	221,532	0.69	4	0.029	Low
2	Hy2b	522,403	0.81	8	0.032	Low
3	CryoSat-2	513,359	0.9	8	0.036	Low
4	Starlette	358,812	0.97	5	0.036	Low
5	Geoik2	95,496	0.98	2	0.045	Low
7	Ajisai	203,465	1.59	2	0.050	Low
8	Hy2c	10,306	0.7	1	0.069	Low
9	Beacon	334,495	1.81	5	0.070	Low
10	Lageos2	60,077	1.01	4	0.082	Medium
11	Glonass132	6,171	0.89	1	0.113	High
12	Glonass106	9,786	1.31	1	0.132	High
13	Galileo203	8,401	1.27	1	0.139	High
14	Galileo210	4,747	1.1	1	0.160	High
15	Jason3	22,649	1.07	7	0.188	Low
16	Glonass105	9,736	2.03	1	0.206	High
17	Lageos1	10,381	1.23	3	0.209	Medium
18	Glonass133	8,712	2.17	1	0.232	High
19	Glonass128	2,267	1.2	1	0.252	High
20	Galileo218	5,154	0.98	8	0.386	High
21	TerraSAR-X	236	0.66	1	0.430	Low
22	Glonass134	539	2.78	1	1.197	High
23	Glonass121	334	1.84	2	1.424	High
24	Compassi5	202	3.87	1	2.723	Geostationary

Considering the delay of $\triangle t_0$ from the UH-SLR system, the range of satellite R is as follows:

$$R = \frac{(t_2 - t_1 - \Delta t_0)\bullet C}{2}. \quad (9)$$

A PRF of the 200-kHz picosecond laser is used, the average output power of the laser is 16 W, the single-pulse energy is 80 uJ, and the pulse width is 10ps. Based on the aperture of the 60-cm SLR system at the SHAO (as shown in Figure 3A), the UH-SLR system is established; UH-SLR software is shown in Figure 3B. Under the coordinated universal time (UTC) in the SHAO, satellite measurement data processing with satellites Jason3 in the low orbit, Glonass105 in the high orbit, and Compassi5 in the geostationary orbit, Lageos2 is ~6000 km away, as shown in Figure 4, respectively. The satellite Lageos2 (Figure 4D) is measured in the UTC time of 8:42:04; this is daytime for the SHAO in the east eight time zones. The laser echoes in Figure 3 show that the SPAD operates in an alternate way, and it reflects the alternate mode of sending and receiving pulse bursts.

Many satellites are measured during the night and daytime, as shown in Table 1; a part of the global navigation satellite system for Russia (Glonass), China (Beidou), and Europe (Galileo) is measured, especially the satellite Compassi5, which is about 37,000 km away. The single-ranging accuracy root mean square (RMS) is around 1 cm. The best NP ranging accuracy is 29 um with the satellite of Stella, and the satellite of Glonass132 is up to 113 μm. Compared with the NP ranging accuracy of the fiber nanosecond laser [15, 16], it achieves an order of magnitude improvement, which shows the advantages of a picosecond laser in UH-SLR.

Conclusion

According to the radar link equation, the relationship between the average number of laser echoes, PRF, and the echo detection probability per unit of time is obtained. The SLR transmission time period with UH-SLR is separated from the laser echoes to solve the LBS interference; UH-SLR is achieved at the SHAO with a picosecond laser and RGD. Low- to high-orbit and geostationary orbits are measured night and day, and Lageos1 (about 6,000 km far away) is realized in the daytime. The NP ranging accuracy is up to 29 μm for low-orbit satellites and 113 μm for high-orbit satellites. Through the research and experiment in this study, pulse bursts in the alternating mode will become an effective method to realize UH-SLR, which strongly promotes the development and application of laser ranging technology.

Data availability statement

The original contributions presented in the study are included in the article/Supplementary Material; further inquiries can be directed to the corresponding author.

Author contributions

ML conceived the project. ML, HZ, RY, ZW, and SQ conducted the experiment. ML and RY wrote the manuscript, and all authors contributed to discussions during its preparation. ZZ supervised the project.

Funding

This work was supported by the National Natural Science Foundation of P. R. China (12003056), the Natural Science Foundation of Shanghai (20ZR1467500), and the Shanghai Science and Technology Innovation Action (21142201900).

Conflict of interest

The authors declare that the research was conducted in the absence of any commercial or financial relationships that could be construed as a potential conflict of interest.

Publisher's note

All claims expressed in this article are solely those of the authors and do not necessarily represent those of their affiliated organizations, or those of the publisher, the editors, and the reviewers. Any product that may be evaluated in this article, or claim that may be made by its manufacturer, is not guaranteed or endorsed by the publisher.

References

1. Steindorfer MA, Kirchner G, Koidl F, Wang P, Jilete B, Flohrer T. Daylight space debris laser ranging. *Nat Commun* (2020) 11:3735. doi:10.1038/s41467-020-17332-z

2. Wang P, Steindorfer MA, Koidl F, Kirchner G, Leitgeb E. Megahertz repetition rate satellite laser ranging demonstration at Graz observatory. *Opt Lett* (2021) 46: 937. doi:10.1364/ol.418135

3. Long M, Zhang H, Meng L, Wu Z, Deng H, Qin S, et al. Satellite laser ranging at high-repetition 10 kHz in all day[J]. *J.Infrared Millim Waves* (2020) 39:778~785.

4. Bai Z, Chen H, Gao X, Li S, Qi Y. Highly compact nanosecond laser for space debris tracking. *Opt Mater* (2019) 98:109470. doi:10.1016/j.optmat.2019.109470

5. Strugarek D, Sonica K, Arnold D, Jäggi A, Zajdel R, Bury G. Satellite laser ranging to GNSS-based Swarm orbits with handling of systematic errors[J]. *GPS Solutions* (2022) 26:104. doi:10.1007/s10291-022-01289-1

6. Zhang z, Cheng z, Zhang h, Zhao g, Deng h, Wu z Global laser ranging observation of Beidou Satellites and data application[J]. *Chin J Lasers* (2017) 44:1–9.

7. Zhang L, Sun W. Progress and prospect of GRACE Mascon product and its application. *Rev Geophys Planet Phys* (2022) 53:18.

8. Song C, Liang ZP, Lin HY, Zhao CY, Dong HP. Rotation state estimation of slow-rotating multi-reflector defunct spacecraft through laser ranging measurements from a single short arc. *Celest Mech Dyn Astron* (2022) 134:30. doi:10.1007/s10569-022-10083-7

9. Kucharski D, Kirchner G, Lim H-C, Koidl F. Optical response of nanosatellite BLITS measured by the Graz 2 kHz SLR system. *Adv Space Res* (2011) 48:1335–40. doi:10.1016/j.asr.2011.06.016

10. Oh H, Park E, Lim H-C, Lee S-R, Choi J-D, Park C Orbit determination of high-earth-orbit satellites by satellite laser ranging[J]. *Astron Space Sci* (2017) 34: 271–9. doi:10.5140/JASS.2017.34.4.271

11. Ulrich Schreiber K, Jan K. The application of coherent local time for optical time transfer and the quantification of systematic errors in satellite laser ranging. *Space Sci Rev* (2018) 214:22. doi:10.1007/s11214-017-0457-2

12. Deng H, Zhang H, Long M, Wu Zhibo 吴, Tang Kai 汤, Zhang Zhongping 张. 4 kHz repetition rate satellite laser ranging system and its application. 光学学报 (2019) 39:0314002. doi:10.3788/aos201939.0314002

13. Sung K-P, Choi E-J, Lim H-C, Kim IY, Choi JS. Development of operation software for high repetition rate satellite laser ranging. *J Korean Soc Aeronaut Space Sci* (2016) 44:1103–11. doi:10.5139/jksas.2016.44.12.1103

14. Daniel H, Paul W, Schafer E, Riede W (2018). Concept for a new minimal SLR system[C]. 21st International Laser Ranging Workshop. Canberra, Australia.

15. Schafer D, Sproll E, sproll F, Otsubo T, Wagner P, Riede W. Satellite laser ranging at 100 kHz pulse repetition rate. *CEAS Space J* (2019) 11:363–70. doi:10.1007/s12567-019-00247-x

16. Dequal D, Agnesi C, Sarrocco D, Amoto LS, Cumis MS, Vallone G, et al. 100 kHz satellite laser ranging demonstration at Matera Laser Ranging Observatory [C]. ILRS Technical Workshop. Stuttgart, Germany (2019).

17. Dequal D, Agnesi C, Sarrocco D, Calderaro L, Santamaria Amato L, Siciliani de Cumis M, et al. 100 kHz satellite laser ranging demonstration at Matera Laser Ranging Observatory. *J Geod* (2021) 95:26. doi:10.1007/s00190-020-01469-2

18. Zharov V, Milyukov V, Ivlev O. Sub-millimeter lunar laser ranging: Novel approach to moon reference frame[C]. 21st International Laser Ranging Workshop. Canberra,Australia (2018). Available at: https://cddis.nasa.gov/lw21/docs/2018/presentations/Session9_Zharov_presenta-tion.pdf.

19. Iqbal F, Kirchner G, Koidl F, Leitgeb E. Laser back scatter: Limitation to higher repetition rate [kHz] Satellite Laser Ranging system. *Geodesy and Geodynamics* (2021) 12:48–53. doi:10.1016/j.geog.2020.08.002

20. Zhang C, Gao T, Cao Y, Fan Z, Fu H, Gu DF, et al. The facilities and performance of TianQin laser ranging station. *Class Quan Gravity* (2022) 39: 125005. doi:10.1088/1361-6382/ac6d3e

21. Wu Z, Deng H, Zhang H, Kai T, Long M-L, Wang N, et al. Analysis and improvement on stability of satellite laser ranging system[J]. *J.Infrared Millim.Waves* (2019) 38:479–84.

frontiers | Frontiers in Physics

TYPE Original Research
PUBLISHED 03 November 2022
DOI 10.3389/fphy.2022.1026517

OPEN ACCESS

EDITED BY
Liyuan Chen,
Hilase Center, Czechia

REVIEWED BY
Haochong Huang,
China University of Geosciences, China
Hairui Suo,
Hangzhou Dianzi University, China

*CORRESPONDENCE
Jiao Xiao-Xue,
xxjiao@hebeu.edu.cn

SPECIALTY SECTION
This article was submitted to Optics and Photonics,
a section of the journal
Frontiers in Physics

RECEIVED 24 August 2022
ACCEPTED 27 September 2022
PUBLISHED 03 November 2022

CITATION
Hui Z, Yong-Jian Z, Lei Z, Xiao-Xue J and Li-Ying L (2022), Fast color point cloud registration based on virtual viewpoint image.
Front. Phys. 10:1026517.
doi: 10.3389/fphy.2022.1026517

Fast color point cloud registration based on virtual viewpoint image

Zhao Hui[1], Zhang Yong-Jian[1], Zhang Lei[2], Jiao Xiao-Xue[2]* and Lang Li-Ying[3]

[1]School of Information and Electrical Engineering, Hebei University of Engineering, Handan, Hebei, China, [2]School of Mathematics and Physics Science and Engineering, Handan, Hebei, China, [3]Advanced Laser Technology Research Center, Hebei University of Technology, Tianjin, China

With the increase of point cloud scale, the time required by traditional ICP-related point cloud registration methods increases dramatically, which cannot meet the registration requirements of large-scale point clouds. In this paper, a fast registration technique for large scale point clouds based on virtual viewpoint image generation is studied. Firstly, the projection image of color point cloud is generated by virtual viewpoint. Then, the feature is extracted based on ORB and the rotation and translation matrix is calculated. The experimental results show that the registration time of the proposed method is about 1s when the size of the point cloud is from 300,000 to 2 million, which is improved by 17–258 times compared with the traditional ICP registration method, and the registration error is reduced by 80% from ICP 5.0 to 1.0. This paper provides a new idea and method for large-scale color point cloud registration.

KEYWORDS

point cloud, registration, virtual viewpoint, ICP, ORB

Introduction

The optical 3D sensor based on structured light illumination is affected by the limitation of the depth of field and the range of field of view of the lens as well as the self-occlusion of the object. It needs to conduct multi-angle point cloud imaging of the measured object, and then unify the point cloud data to the global coordinate system through point cloud registration [1, 2], so as to obtain the complete 3D point cloud data of the target object.

There are four main methods for point cloud registration: direct registration, feature-based, deep learning and image-based. 1) Based on point cloud direct registration, there are mainly ICP [3, 4], GO-ICP [5, 6] and other algorithms. Theoretically, the accuracy is high, but when the scale of the point cloud is large, the computation is too large, and the time is too long. 2) Feature-based point cloud registration mainly includes PFH, FPFH, 4PCS and super-4PCS [7]. It is mainly limited by the fact that the feature extraction algorithm cannot completely and accurately describe the point cloud features, and the high computational amount and complexity

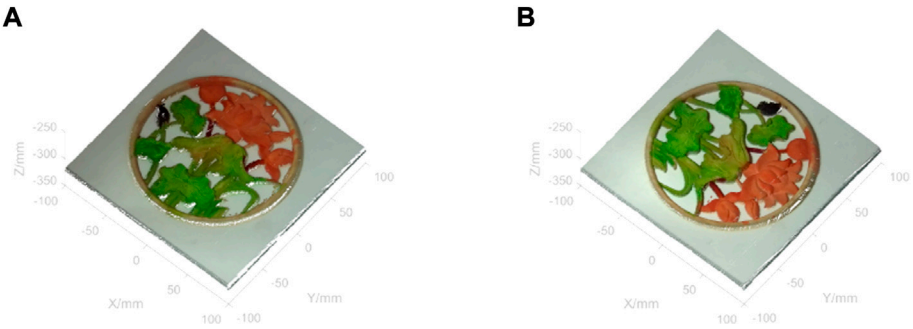

FIGURE 1
Registration of the first two clusters of point clouds.

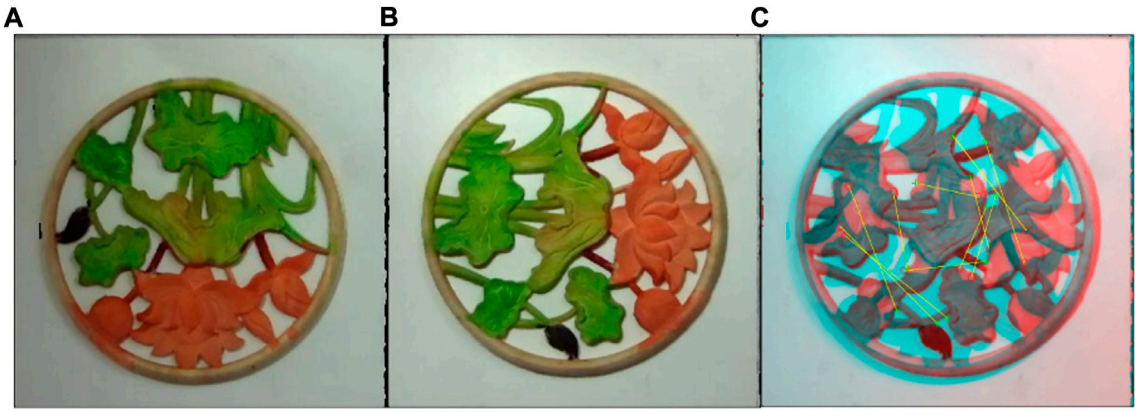

FIGURE 2
Virtual view imaging and feature extraction and matching of two cluster point clouds. **(A)** the virtual view image of Figure 1A, **(B)** the virtual view image of Figure 1B.

of some feature extraction and description algorithms affect the practical application of the registration algorithm. 3) Point cloud registration based on deep learning [8–10] mainly includes PointNet, PointNet+, PointNet++, PointNetLk [8] and other network structures. Limited by the point cloud disorder and no spatial structure, it cannot be sampled on regular grids and processed as image pixels, and lacks color information, deep learning can generally only be used to process the relative positions of points, which limits the application of this technology. 4) Based on the point cloud registration of intermediate media such as image [3, 4, 11–13], the projection image, optical image or depth map is used to convert the 3D point cloud registration problem to the 2D image matching problem, and the transformation parameters between point clouds are indirectly calculated by using the 2D image registration algorithm. Such algorithms often have high timeliness and matching accuracy. However, most applications do not have corresponding optical images or intensity images, so there are certain limitations.

In this paper, large-scale color point cloud registration is realized based on ORB feature extraction [14] and matching of virtual viewpoint projection images. Firstly, the color image is obtained by the color point cloud projection based on the virtual viewpoint. Then, the ORB is used to extract the image features and registration, and the rotation and translation matrix between the virtual viewpoint images is solved. The rotation and translation matrix are used to register the point cloud. Experimental results show that, compared with ICP method, the registration can be achieved with high precision without the limitation of initial pose and rotation at any Angle. At the same time, different from the ICP method, the registration time increases with the increase of the size of the point cloud, the registration time of the proposed method is about 1s, and the registration accuracy is 20% of the ICP registration accuracy

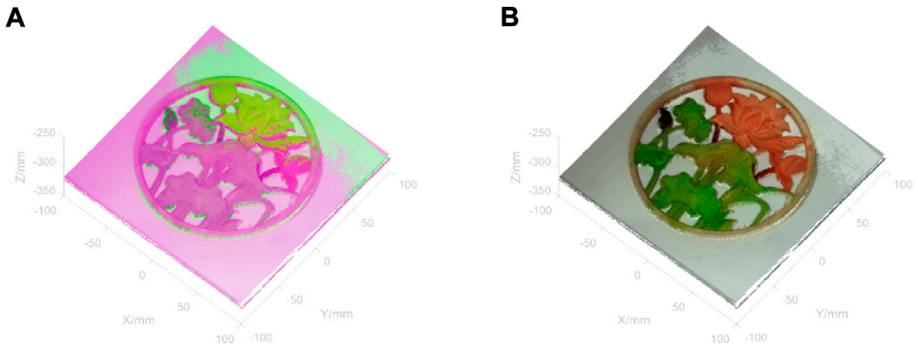

FIGURE 3
Registration results of two clusters of point clouds **(A)** registration results of point clouds **(B)** fusion results of two clusters of point clouds.

TABLE 1 Rotation and translation parameters of point cloud B.

The serial number	Rotation(R)	Translation(t)
1	Around the Z axis: 30°	[-3.3, 1.0, -2.4]
2	Around the Z axis:60°	[1.5, 1.9, 2.5]
3	Around the Z axis:90°	[-0.5, -4.2, -2.7]
4	Around the Z axis:120°	[4.1, -3.5, 3.3]
5	Around the Z axis:150°	[0.4, 5.0, -4.2]
6	Around the Z axis:180°	[-0.6, -3.9, 4.6]
7	Around the Z axis:210°	[-4.9, 2.7, 3.2]
8	Around the Z axis:240°	[3.7, -4.2, -1.0]
9	Around the Z axis:270°	[-2.4, 3.0, -0.7]
10	Around the Z axis:300°	[4.1, -3.2, -2.4]
11	Around the Z axis:330°	[-3.5, -3.7, 3.7]
12	Around the Z axis:360°	[0.8, 0.5, -3.6]

TABLE 2 Comparison of registration time and error of different rotation and translation matrices.

Number of point cloud	Time(s)		Error (mm)	
	Our method	ICP	Our method	ICP
1	0.92	26.72	0.79	36.16
2	0.84	33.57	0.97	107.6
3	0.79	32.01	1.75	132.46
4	0.77	34.83	1.88	156.15
5	0.76	29.84	2.41	194.45
6	0.80	28.85	1.86	198.68
7	0.80	30.16	2.44	194.25
8	0.77	33.56	1.56	156.18
9	0.88	29.61	1.48	132.83
10	0.76	32.9	1.27	107.11
11	0.86	29.35	0.35	36.05
12	0.92	11.53	0.62	0.53

when the scale of the point cloud is 300,000 ~2 million. The experimental results confirm that the virtual viewpoint based large-scale point cloud registration technology proposed in this paper can achieve high speed and high precision point cloud registration. It provides a new idea for the registration of large-scale point clouds.

ORB color point cloud fast registration technology based on virtual viewpoint

Rigid point cloud registration is essentially for the transformation matrix between the two group of point cloud clusters [R|t], in which R is rotation matrix, t is translation matrix. This paper proposes a rapid image registration technique based on virtual view images, will first XYZ color point cloud images projected into 2d images in the *Z* axis direction, and then use the ORB in the 2D image feature extraction algorithm for matching feature points, then according to the matching feature points by using SVD decomposition or least square method to solve R, t matrix. Finally using the transformation matrix [R|t] to coordinate transformation of color point cloud, so as to realize two clusters of color of point cloud registration.

Figures 1A,B show two clusters of colored point clouds before registration, and the scale of point clouds is about 500,000 points. The point cloud of Figure 1B is obtained by rotation and translation of the point cloud of Figure 1A. Two group of point cloud clusters to get *Z* axis direction projection direction of the virtual view image (Figures 2A,B), according to the virtual view + *Z* direction projection image, respectively, using the ORB to feature extraction and feature matching to get

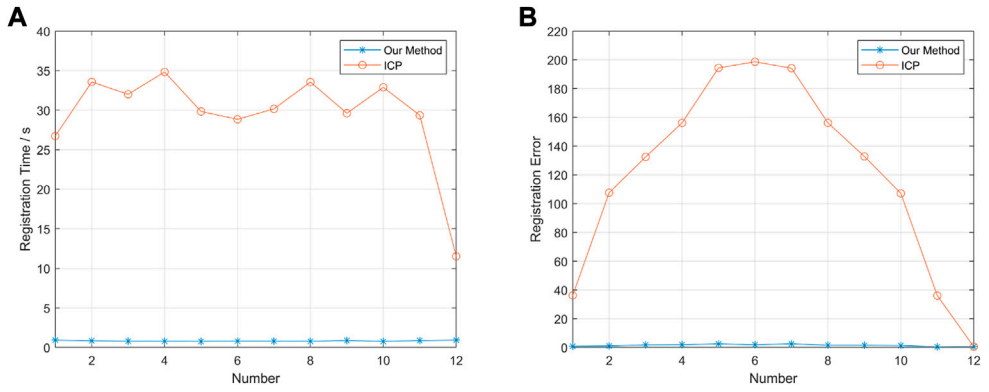

FIGURE 4
Comparison of results: **(A)** point cloud registration time,**(B)** registration error.

TABLE 3 Comparison of registration time and error of different scales.

Number of point cloud	Time(s)		Error	
	Our method	ICP	Our method	ICP
2,044,145	0.88	227.65	0.54	5.20
1,022,073	0.67	64.43	1.58	5.13
511,037	0.81	46.29	0.34	5.02
292,021	1.10	18.82	0.54	4.91

the rotation of the virtual view image translation matrix [R|t], registration results as shown in Figure 2C.

The virtual view image to extract the [R|t] is applied to the second point cloud clusters, the second point cloud clusters rotating shift to make it and the first bunch of point cloud registration and two clusters of point cloud registration after image, the Figure 3A is the difference in two clusters of point cloud registration after color figure, one orange said first point cloud clusters, green said the second point cloud clusters. Figure 3B is the color result after the fusion of two clusters of point clouds. Direct observation can show that the point cloud registration method based on virtual viewpoint proposed in this paper can realize the registration of two clusters of point clouds.

Comparison of ICP and ORB registration results and registration time under different angle transformation

Taking the collected color point cloud as the reference point cloud data A, the point cloud contains A total of 464,966 color points, and each data packet contains three-dimensional spatial coordinates XYZ and color data RGB. The reference point cloud data were rotated 30° counterclockwise around the Z-axis, and the random translation of XYZ was increased within the range of ±5 mm to generate color point cloud B to be registered. The reference point cloud data A was rotated 12 times in total, with the rotation Angle ranging from 30° to 360°, and 12 groups of color point clouds to be matched were generated. The transformation parameters of 12 groups of point clouds to be registered are shown in the following Table 1 and in Figure 4.

Will then respectively stay 12 groups B using traditional ICP registration color point cloud point cloud registration algorithm and proposed in this paper, based on the virtual view of the ORB image feature point cloud registration algorithm with A benchmark color point cloud registration, and calculate the registration after the color point cloud B′ and benchmark color point cloud registration results: the mean absolute error of specific formula is as follows:

$$\Delta = \frac{1}{N}\sum_{i=1}^{N}\left(|x_i - x_0| + |y_i - y_0| + |z_i - z_0|\right)$$

Where xi, yi, zi is the spatial coordinates of the color point cloud after registration. and x0, y0, z0 is the base color point cloud space coordinate. N = 464,966 indicates the total number of point clouds in a point cloud cluster.

The registration time and error of 12 groups of color point cloud B to be registered and reference color point cloud A are shown in Table 2.

Compared with the traditional ICP method, the registration time of the proposed method is about 3% of the traditional ICP method, and the registration time is about 1s for the color point cloud with a scale of 500,000 points. In terms of registration accuracy, the error of the traditional ICP registration method increases with the increase of the point cloud offset Angle. When

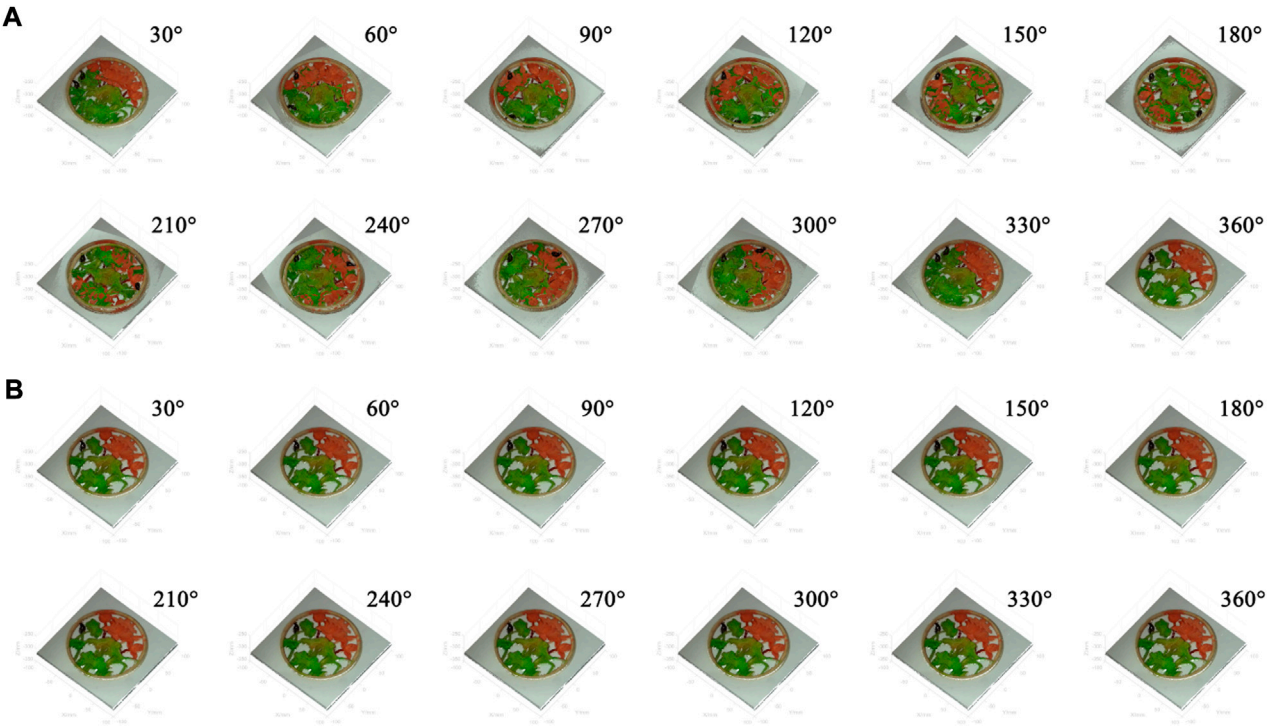

FIGURE 5
Registration results of two cluster point clouds, **(A)** ICP **(B)** Our method.

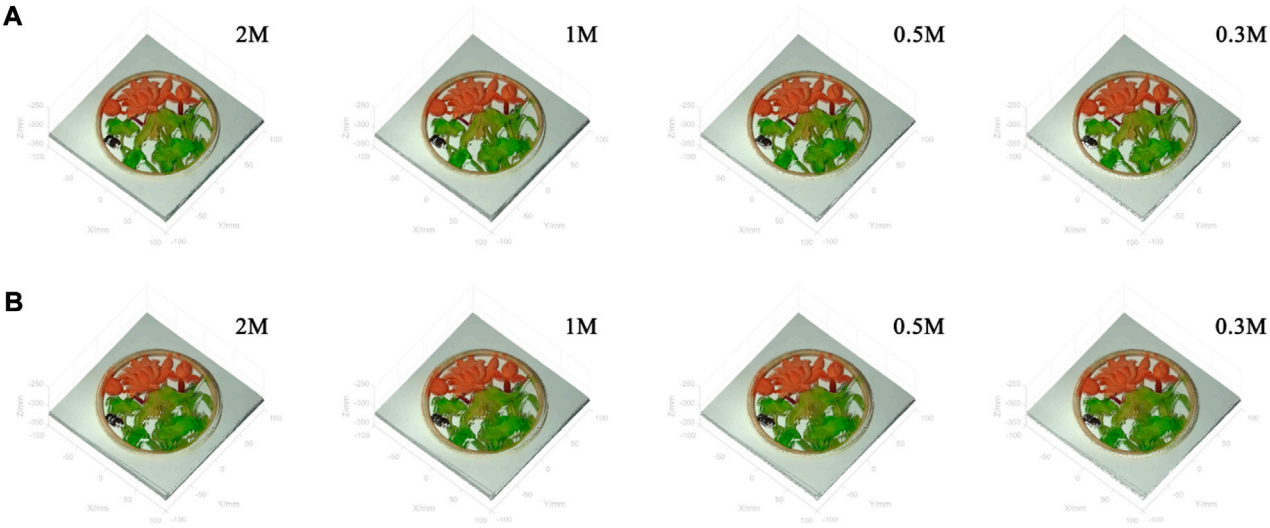

FIGURE 6
Registration results of different scale point clouds, **(A)** Our method, **(B)** ICP.

the two-point clouds rotate 180°, the error reaches the maximum, which is about 4 times of the error when the two group point clouds rotate 30°. However, the registration error of the proposed method is less affected by the rotation Angle, and the average error is 2 mm at most, which is 2% of the traditional ICP registration error. The registration result is shown in Figure 5,

where Figure 5A is the registration result of traditional ICP, and Figure 5B is the registration result of the proposed method.

Registration results and registration times of ICP and ORB point clouds of different sizes

A cluster of color point cloud with 2.04 million size was collected by the color three-dimensional imaging equipment with high precision acquisition mode, and four groups of reference color point cloud A of different sizes were obtained after simplification. By rotating 3° counterclockwise and adding random displacements within a range of ±5 mm in the XYZ direction, four groups of color point cloud data B with different sizes to be registered were obtained. The proposed method and ICP are used for point cloud registration test, and the test results are shown in Table 3.

The registration results of four different scale point clouds are shown in Figure 6, where Figure 6A is the registration results of the proposed method, and Figure 6B is the registration results of ICP. From the comparison results, it can be seen that with the increase of the scale of point clouds, the time required for the registration of traditional ICP point clouds is increasing continuously, from 18.82 s for 300,000 point clouds to 227.65 s for 2 million point clouds. However, the registration time of the proposed method has little correlation with the scale of the point cloud, and the registration time is about 1s. From the perspective of registration error, for small Angle point cloud rotation of 3°, ICP has a high accuracy, which is not correlated with the scale of point cloud, and the overall error is about 5 mm. However, the registration accuracy of the method proposed in this paper is also not correlated with the scale of the point cloud, and the overall error is about 1mm, which is 20% of the traditional ICP.

Discussion

Limited by the field of view of 3D optical imaging equipment and the self-occlusion of the target to be measured, it is necessary to image the target several times, and then achieve coordinate unification through point cloud registration. As the precision of data becomes higher and higher, the scale of point cloud becomes larger and larger. With the increase of the scale of point cloud, the registration time of existing global registration and semi-global registration algorithms becomes longer and longer, which limits the rapid development and application of optical 3D imaging technology.

In this paper, a large-scale point cloud registration algorithm is proposed based on ORB feature extraction and matching of virtual viewpoint projection images. Firstly, the color image is obtained by the color point cloud projection based on the virtual viewpoint. Then, the ORB is used to extract the image features and registration, and the rotation and translation matrix between the virtual viewpoint images is solved. The rotation and translation matrix is used to register the point cloud. Compared with ICP method, it is not limited by the initial pose and can achieve high precision registration with any rotation Angle. At the same time, the registration time of the proposed method is about 1 s, and the registration accuracy is 20% of the ICP registration accuracy when the scale of point clouds ranges from 300,000 to 2 million. The experimental results confirm that the virtual viewpoint based large-scale point cloud registration technology proposed in this paper can achieve high speed and high precision point cloud registration. It provides a new idea for the registration of large-scale point clouds and expands the application scope and application scenarios of large-scale point clouds.

Data availability statement

The original contributions presented in the study are included in the article/supplementary material, further inquiries can be directed to the corresponding author.

Author contributions

All authors listed have made a substantial, direct, and intellectual contribution to the work and approved it for publication.

Funding

S&T Program of Hebei (20371802D).

Conflict of interest

The authors declare that the research was conducted in the absence of any commercial or financial relationships that could be construed as a potential conflict of interest.

Publisher's note

References

1. Li J, Zhan J. Review on 3D point cloud registration method. *JOURNAL IMAGE GRAPHICS* (2022) 27(02):349–67. doi:10.11834/jig.210243

2. Sui Y-L. *Research on large-scale 3D point cloud registration technology*. Zheng Zhou: PLA Strategic Support Force Information Engineering University (2020).

3. Su B-Y, Han W, Peng Y-S, Sheng M. 4D-ICP point cloud registration method for RGB-D data. *JOURNAL NANJING UNIVERSITY (NATURAL SCIENCE)* (2018) 54(04):829–37. doi:10.13232/j.cnki.jnju.2018.04.019

4. Men H, Gebre B, Pochiraju K. Color point cloud registration with 4D ICP algorithm. In: 2011 IEEE International Conference on Robotics and Automation; 09-13 May 2011; Shanghai, China (2011). doi:10.1109/ICRA.2011.5980407

5. Lu W, Wan G, Zhou Y, Fu X, Yuan P, Song S. DeepICP: An end-to-end deep neural network for 3D point cloud registration. In: 2019 IEEE/CVF International Conference on Computer Vision (ICCV); 27 October 2019 - 02 November 2019; Seoul, Korea (South) (2019). doi:10.1109/ICCV.2019.00010

6. Yang J, Li H, Campbell D, Jia Y. Go-ICP: A globally optimal solution to 3D ICP point-set registration. *IEEE Trans Pattern Anal Mach Intell* (2015) 38(11):2241–54. doi:10.1109/TPAMI.2015.2513405

7. Mellado N, Mitra N, Aiger D. Super4pcs: Fast global pointcloud registration via smart indexing. *COMPUT GRAPH FORUM* (2014) 5(33):205–15. doi:10.1111/cgf.12446

8. Aoki Y, Goforth H, Srivatsan RA. PointNetLK: Robust & efficient point cloud registration using PointNet (2019). Available at: https://arxiv.org/abs/1903.05711.

9. Wang Y, Solomon JM. PRNet: Self-Supervised learning for partial-to-partial registration (2019). Available at: https://arxiv.org/abs/1910.12240.

10. Pais GD, Ramalingam S, Govindu VM, Nascimento JC, Chellappa R, Miraldo P. *3DRegNet: A deep neural network for 3D point registration* (2020).

11. Bao Z, Xie L, Lu N-N, et al. A point cloud registration algorithm using depth image. *NAVIGATION OF CHINA* (2019) 42(02):8–11.

12. Zhong S, Li Y, Liu Z, Xie Z, Chen J, Wang W, et al. Robust rigid point cloud registration via RGB-D images. *J Computer-Aided Comput Graphics* (2022) 34(01):25–35. doi:10.3724/SP.J.1089.2022.18823

13. Sheng M, Peng Y-S, Su B-Y, et al. RGBD point cloud registration based on feature similarity. *JOURNAL GRAPHICS* (2019) 40(05):829–34.

14. Li Y-C. *Research on 3D point cloud registration algorithm based on image features and ICP*. Gui Yang: GuiZhou University (2020).

frontiers | Frontiers in Physics

TYPE Brief Research Report
PUBLISHED 10 November 2022
DOI 10.3389/fphy.2022.1047445

OPEN ACCESS

EDITED BY
Zhi-Han Zhu,
Harbin University of Science and Technology, China

REVIEWED BY
Zhanda Zhu,
Beijing University of Technology, China
Lijun Qiao,
Taiyuan University of Technology, China

*CORRESPONDENCE
Xinmin Fan,
xinminfan@163.com

SPECIALTY SECTION
This article was submitted to Optics and Photonics,a section of the journal Frontiers in Physics

RECEIVED 18 September 2022
ACCEPTED 31 October 2022
PUBLISHED 10 November 2022

CITATION
Li S, Zhang J, Cheng X, Shao M, Liu Q, An J, Li S and Fan X (2022), Research on beam quality control technology of 2 μm antimonide semiconductor laser. *Front. Phys.* 10:1047445. doi: 10.3389/fphy.2022.1047445

Research on beam quality control technology of 2 μm antimonide semiconductor laser

Sensen Li[1], Jingsheng Zhang[1], Xiangzheng Cheng[2], Ming Shao[2], Qianghu Liu[1], Jiashuo An[3], Shun Li[4,5] and Xinmin Fan[4,5]*

[1]Science and Technology on Electro-Optical Information Security Control Laboratory, Tianjin, China, [2]Key Laboratory of Electro-Optical Countermeasures Test and Evaluation Technology, Luoyang, China, [3]Center for Advanced Laser Technology, Hebei University of Technology, Tianjin, China, [4]School of Physics and Electronic Information, Weifang University, Weifang, China, [5]Weifang Key Laboratory of Laser Technology and Application, Weifang University, Weifang, China

Antimonide semiconductor laser is a new type of laser with unique advantages in the 2 μm band. However, employing FP cavities causes multiple transverse modes to degrade beam quality despite achieving higher power output. In this paper, an antimonide semiconductor laser operating in 2 μm band is realized by utilizing fiber coupling and combining. Fiber combining results in higher output power, while the uniform patterns in both near-field and far-field are obtained, and the beam quality is improved. The experimental results illustrate that the output power reaches 1.2 W after 7-channel beam combination, and the near-field distribution is approximately Gaussian, while the far-field distribution is a flat-top.

KEYWORDS

shortwave infrared laser, antimonide, semiconductor laser, fiber combining, beam quality

Introduction

The laser in 2 μm band is superior to the low atmospheric extinction ratio and human eye safety, and has absorption peaks at various molecules such as H_2O and CO_2 [1, 2]. Therefore, the 2 μm band laser has a vital role in the fields of laser remote sensing, laser ranging, spectroscopy and medical treatment [3–6]. In particular, antimonide semiconductor lasers are gradually occupying an increasingly important position in short-wave infrared lasers due to their small size, high photoelectric conversion efficiency, and good temperature stability [7].

As narrow-bandgap semiconductor materials, antimonide covers the bandwidth of 1.5–5 μm, and thus becomes an ideal material system for mid-infrared semiconductor laser. Antimonide semi-conductor laser is a new type of laser. Since its invention in 1986, the short-wave infrared (2 μm) laser generated by antimonide semiconductor laser has been a research hotspot, and become a high-quality light source for infrared laser countermeasure, biological microscope, medical illumination, laser pumping, plastic welding and other fields [8]. In recent years, antimonide infrared lasers have been widely concerned and developed rapidly. In

2009, Li et al. reported a quantum well antimonide semiconductor laser with a 43 mW CW output at 2.2 μm [9]. In 2010, Niu et al. achieved a 2 μm laser output at room temperature for the first time using an F-P cavity [10]. Subsequently, the wavelength of the output laser was extended to 2.4 μm [11], and the output power was further increased to 1.4 W [12]. In 2011, Reboul et al. reported a GaSb-based semiconductor laser output in the 2 μm band [13]. In 2013, Apiratikul et al. achieved a 40 mW single longitudinal mode laser output in the 2 μm band through laterally coupled distributed feedback [14]. In 2016, Hosoda et al. reported a high-power cascaded antimonide semiconductor laser that achieved a continuous-light laser output with an average power of 2 W at room temperature [15]. In recent years, Niu Zhichuan's team at the Chinese Academy of Sciences has also achieved a series of research results in antimonide semiconductor lasers [12, 16, 17].

Similar to other semiconductor lasers, the 2 μm antimonide semiconductor laser also has problems such as multimode output, large divergence angle, and asymmetric laser pattern, which seriously restrict its development and application. To solve these problems, Rong et al. proposed a fishbone-shaped microstructure in 2016 to reduce the transverse divergence angle of the beam by 55% [18]. In this paper, we employ fiber coupling and combining to improve the beam quality of 2 μm antimonide semiconductor laser. Through 7-channel beam combination, the laser with a center wavelength of 2,055 nm and a line width of 30 nm has an average output power of 1.2 W, while possessing an approximate Gaussian near-field distribution and a flat-topped far-field distribution.

Fiber homogenization theory

A simple and effective beam shaping method is to couple the semiconductor laser into a large-core multimode fiber with a certain length. The outgoing beam is homogenised after transmission due to the limitations of the multimode fibre waveguide structure.

The high-order mode fiber applied to beam shaping is essentially a multimode fiber. The normalized frequency is given by

$$V = \frac{2\pi aNA}{\lambda} \tag{1}$$

where NA is the numerical aperture of the fiber. It can be seen that a larger NA and core diameter results in a more significant normalized frequency of the fiber and a larger number of modes allowed in the fiber, which can be expressed as

$$M \cong \frac{V^2}{2} \tag{2}$$

Due to the larger core diameter and NA of the multimode fiber, i.e., more supported modes, the laser coupling into multimode fiber excites higher-order modes, and most of the energy of the fundamental mode is transferred to the higher-order modes supported by the multimode fiber, and the energy coupling between these modes occurs. Assuming that the intensity of the incident beam is E_{in} $(x, y, z = 0)$, the intensity at the fusion surface after the beam enters the multimode fiber becomes the result of the superposition of each mode:

$$E_{in}(x, y, z = 0) = \sum_{1}^{M}\sum_{1}^{N} C_{mn} e_{mn}(x, y, z = 0) \tag{3}$$

where $e_{mn}(x, y, z = 0)$ is the intensity distribution of the mn-th order guided mode in the multimode fiber, M × N is the number of excited modes in the multimode fiber, C_{mn} is the modal expansion coefficient and can be expressed as

$$C_{mn} = \frac{\iint_s E_{\text{in}}(x, y, 0) \times e^{*}_{mn}(x, y, 0) ds}{\iint_s \left| e_{mn}(x, y, 0) \right|^2 ds} \tag{4}$$

After these modes propagate for a certain distance in the fiber, the power carried by each conduction mode becomes stable, and the energy is redistributed among the higher-order modes. The final beam intensity distribution from the fiber is the superposition of the various-order modes:

$$E_{out}(x, y, L) = \sum_{1}^{M}\sum_{1}^{N} C_{mn} e_{mn}(x, y, 0) e^{-i\beta_{mn} L} \tag{5}$$

where mn is the propagation constant of the mn-th order excitation mode of the waveguide in the multimode fiber. The more significant the difference between the diameter of the incident laser pattern and the core diameter of the multimode fiber, the more high-order modes are excited, and the better the homogenization effect of the laser pattern is.

Experimental results and discussion

Direct output performance

In this experiment, the antimonide semiconductor laser chip operating in 2 μm band is designed with a high-reliability ridge waveguide structure and a Fabry-Perot cavity type, using antimonide substrate, grown by quantum well epitaxy, and then packaged in COS. We measured the intensity distribution of the laser direct output, as shown in Figure 1. Figure 1 shows the near-field distribution of the beam at three different positions, 20, 100, and 200 mm from the laser output port, respectively. Obviously, the beam quality is relatively poor, and there are problems such as multimode output, large divergence angle, asymmetric laser pattern, etc. Next, we investigated how to improve the beam quality through multi-beam combination through the fibers.

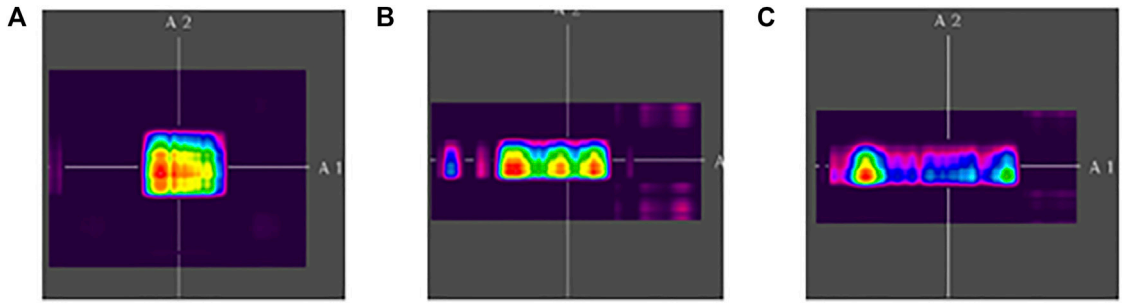

FIGURE 1
The beam near-field distribution at different transmission distances **(A)** 20 mm, **(B)** 100 mm and **(C)** 200 mm.

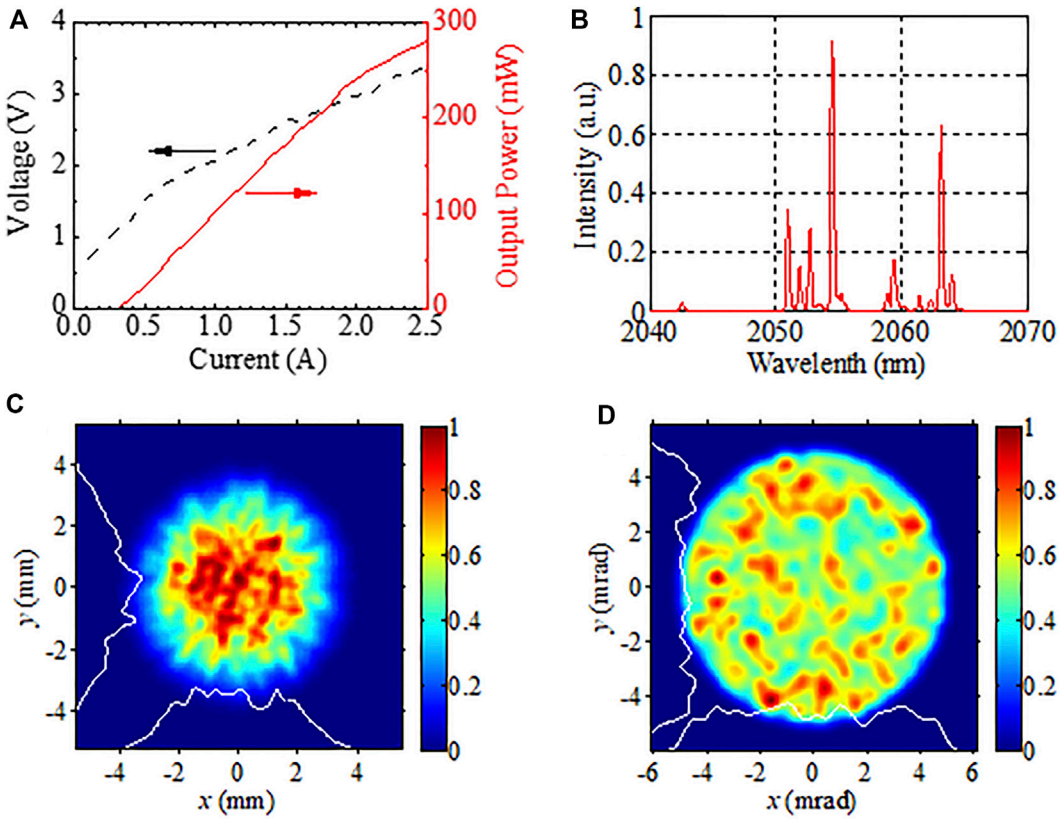

FIGURE 2
Laser output performance of antimonide fiber-coupled semiconductor laser module: **(A)** PIV curve, **(B)** laser spectrum, **(C)**near-field pattern and **(D)**far-field pattern of output beam. The near-field distribution is Gaussian and the far-field distribution is flat-topped.

Single fiber-coupled output performance

The experiments first examined the output of a single laser chip coupled to a quartz fibre with the core diameter of 105 μm. Although the larger the fiber core diameter and numerical aperture, the higher the coupling efficiency, the coupling fiber core diameter must not be too large and must be smaller than the core diameter of the combining fiber. So

we choose a core diameter of 105 μm for the coupling fiber. The coupling method adopts a wedge-shaped fiber lens for direct coupling, and the structure of the fiber output port is SMA905.

The variation curve of fiber output power with current is shown in Figure 2A. The overall linearity is relatively good, and the coupling efficiency at the highest power point reaches 56% (when the fiber input power is 0.5 W, the output power is 0.28 W). The end face of the fiber lens is not coated, and the coupling efficiency will be further improved if the coating is applied. The output laser spectrum has a dendritic spectral distribution, about 2,050–2,065 nm, the line width is up to 15 nm, and there are multiple longitudinal modes, as shown in Figure 2B. This is due to the limited frequency selection capability of the FP cavity. If the DFB structure is employed, the narrow linewidth output can be achieved, although the output power will be significantly reduced [19]. Figure 2C shows the near-field distribution of the laser at the output end of the fiber, which is Gaussian as a whole and has modulation inside; Figure 2D shows the far-field distribution of the laser output, which has a flat-top distribution as a whole, and the internal modulation is still evident. It can be seen that the beam quality of the antimonide semiconductor laser in the 2 μm band is still relatively poor after coupling the fiber, because the semiconductor chip itself has multi-transverse mode output and the coupling fiber is a multi-mode fiber. However, compared to Figure 1, it can be seen that the intensity distribution of the beam after transmission through the coupling fiber and tends to be uniformly smooth overall, and the horizontal divergence angle becomes smaller and almost equal to the vertical one, that's because the laser coupling into multimode fiber excites higher-order modes, and most of the energy of the fundamental mode is transferred to the higher-order modes supported by the multimode fiber, and the energy coupling between these modes occurs. From this it can be assumed that if such multi-channel beams are combined into a single multimode fiber, this results in a number of light intensity components with different intensity distributions in different modes being coupled and superimposed, and the beam quality should be further improved, and the greater the number of fiber channels the greater the probability that the intensity of the beam-combining will be uniform. In our experiment, we combine 7-channel optical fiber outputs to explore the feasibility of this method, and verify its effect on the beam quality.

Comparing Figures 1, 2, it can be seen that the intensity distribution of the beam after transmission through the coupling fiber and tends to be uniformly smooth overall, that's because the laser coupling into multimode fiber excites higher-order modes, and most of the energy of the fundamental mode is transferred to the higher-order modes supported by the multimode fiber, and the energy coupling between these modes occurs. But the quality of this beam is still relatively poor and the transverse distribution of the intensity is very uneven. If such multi-channel beams are combined into a single multimode fiber, this results in a number of light intensity components with different intensity distributions in different modes being coupled and superimposed, and the beam quality should be further improved, and the greater the number of fiber channels the greater the probability that the intensity of the beam-combining will be uniform. In our experiment, we combine 7-channel optical fiber outputs to explore the feasibility of this method, and verify its effect on the beam quality.

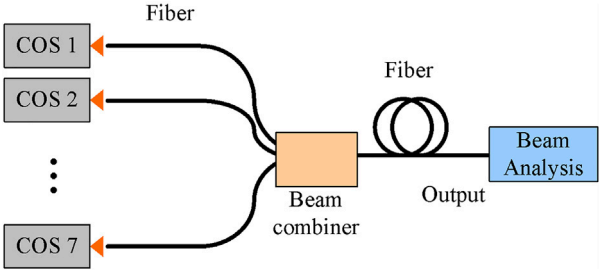

FIGURE 3
The structure of the 7-channel fiber combining.

7-Channel beam combining output performance

Figure 3 is a schematic diagram of the 7-channel fiber combining. Seven identical antimonide semiconductor lasers are respectively coupled and output through the same 105 μm core-diameter fibers, and then combined into another fiber with a core diameter of 200 μm through a beam combiner.

Figures 4A,B shows the output optical power and spectral line characteristics of the 7-channel beam combination. The output laser power of the single-tube COS chip is 0.5 W, the output power of the 7-channel combined beam reaches 1.25 W, and the overall beam combining efficiency of the system is 35.7%. The output laser spectral distribution is from 2,040 to 2,070 nm, showing a dendritic spectral distribution with a line width of up to 30 nm. The near-field and far-field distributions of the output beam are shown in Figures 4C,D, presenting a Gaussian distribution and a flat-top distribution, respectively. Compared with Figures 2C,D, it can be seen that the beam quality is greatly improved after combining, this is consistent with the previous speculation, if increase the number of channels the beam quality and intensity distribution will be further improved.

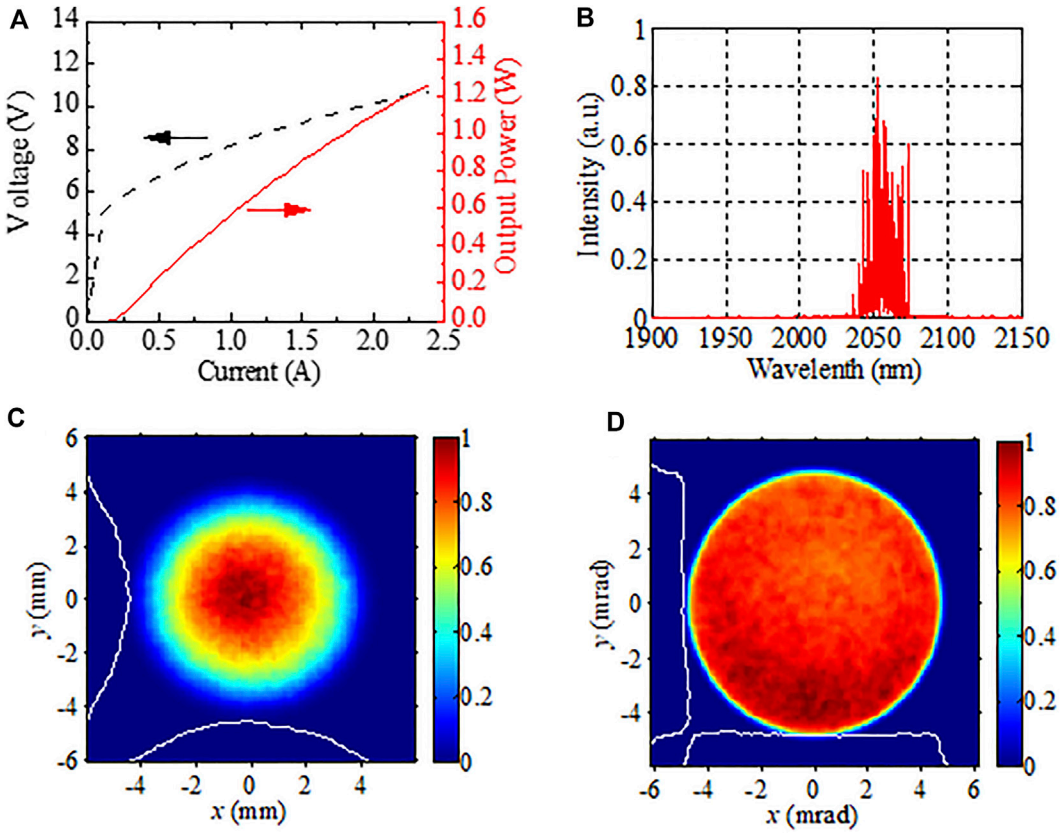

FIGURE 4
Laser output performance of 7-channel beam combining: **(A)** PIV curve, **(B)** laser spectrum, **(C)** near-field pattern and **(D)** far-field pattern.

Conclusion

To address the poor beam quality of antimonide semiconductor lasers in the 2 μm band, we propose a solution to improve the beam quality by using multi-channel fibres to combine beam. In the experiment, the fiber was employed to study the beam combination of 2 μm band antimonide semiconductor lasers coupled with seven channels of fibers. The results indicate that the beam quality is greatly improved after the beam combination, and the near-field distribution is approximately Gaussian, while the far-field exhibits a flat-top distribution. This is due to the poor quality of the output beam of the single-channel fiber, and the lateral distribution of the intensity is very uneven. When the multiplexing is performed, the lowest point of the intensity of a certain beam is likely to be superimposed with the strongest point of the other beams and tend to the average value. Moreover, more beams participating in beam combining will bring more desirable beam quality, that is, the lateral intensity distribution of the beam will be smoothed with an improved the total output power.

Data availability statement

The raw data supporting the conclusion of this article will be made available by the authors, without undue reservation.

Author contributions

SeL: Conceptualization, Drafting the manuscript, and Funding acquisition. JZ: Analysis of data, Data Curation. XC: Investigation. MS: Investigation and Editing. QL: Investigation and Validation. JA: Writing and Acquisition of data. ShL: Acquisition of data and Writing. XF: Conceptualization and Manuscript.

Conflict of interest

The authors declare that the research was conducted in the absence of any commercial or financial relationships that could be construed as a potential conflict of interest.

Publisher's note

References

1. Scholle K, Lamrini S, Koopmann P, Fuhrberg P. 2 µm laser sources and their possible applications. In: B Pal, editor. *Frontiers in guided wave Optics and optoelectronics*. Norderstedt, Germany: Books on Demand (2010). doi:10.5772/39538

2. Pal A, Sen R, Bremer K, Yao S, Lewis E, Sun T, et al. All-fiber" tunable laser in the 2 µm region, designed for CO_2 detection. *Appl Opt* (2012) 51(29):7011–5. doi:10.1364/ao.51.007011

3. Wang Q, Geng J, Jiang S. 2-µm fiber laser sources for sensing. *Opt Eng* (2014) 53(6):061609. doi:10.1117/1.oe.53.6.061609

4. Degnan JJ. Satellite laser ranging: Current status and future prospects. *IEEE Trans Geosci Remote Sens* (1985) 23(4):398–413. doi:10.1109/tgrs.1985.289430

5. Civis S, Horká V, Simecek T, Hulicius E, Pangrac J, Oswald J, et al. GaSb based lasers operating near 2.3 µm for high resolution absorption spectroscopy. *Spectrochimica Acta A: Mol Biomol Spectrosc* (2005) 61(13):3066–9. doi:10.1016/j.saa.2004.11.029

6. Gaimard Q, Nguyen-Ba T, Larrue A, Cerutti L, Rouillard Y, Teissier R, et al. Distributed - feedback GaSb - based laser diodes in the 2.3 to 3.3 µm wavelength range. In: K Panajotov, M Sciamanna, A Valle, R Michalzik, editors. *Semiconductor lasers and laser dynamics vi*. Washington, United States: SPIE (2014). p. 9134.

7. Xie S, Yang C, Huang S, Yuan Y, Zhang Y, Shang J, et al. 2.1 µm InGaSb quantum well lasers exhibiting the maximum conversion efficiency of 27.5% with digitally grown AlGaAsSb barriers and gradient layers. *Superlattices and Microstructures* (2019) 130:339–45. doi:10.1016/j.spmi.2019.05.002

8. Chiu TH, Tsang WT, Ditzenberger JA, van der Ziel JP. Room-temperature operation of InGaAsSb/AlGaSb double heterostructure lasers near 2.2 µm prepared by molecular beam epitaxy. *Appl Phys Lett* (1986) 49(17):1051–2. doi:10.1063/1.97471

9. Li ZG, Liu GJ, You MH, Li L, Li M, Wang Y, et al. 2.0 µm room temperature CW operation of InGaAsSb/AlGaAsSb laser with asymmetric waveguide structure. *Laser Phys* (2009) 19(6):1230–3. doi:10.1134/s1054660x09060085

10. Zhang Y, Tang B, Xu Y, Xu Y, Song G. Molecular beam epitaxy growth of in GaSb/AlGaAsSb strained quantum well diode lasers. *J Semicond* (2011) 32(10):103002. doi:10.1088/1674-4926/32/10/103002

11. Xing JL, Zhang Y, Liao YP, Wang J, Xiang W, Xu YQ, et al. Room-temperature operation of 2.4 µm InGaAsSb/AlGaAsSb quantum-well laser diodes with low-threshold current density. *Chin Phys Lett* (2014) 31(5):054204. doi:10.1088/0256-307x/31/5/054204

12. Xie SW, Zhang Y, Yang CA, Huang SS, Yuan Y, Zhang Y, et al. High performance GaSb based digital-grown InGaSb/AlGaAsSb mid-infrared lasers and bars. *Chin Phys B* (2019) 28(1):014208. doi:10.1088/1674-1056/28/1/014208

13. Reboul JR, Cerutti L, Rodriguez JB, Grech P, Tournie E. Continuous-wave operation above room temperature of GaSb-based laser diodes grown on Si. *Appl Phys Lett* (2011) 99:121113. doi:10.1063/1.3644983

14. Apiratikul P, He L, Richardson CJK. 2 µm laterally coupled distributed-feedback GaSb-based metamorphic laser grown on a GaAs substrate. *Appl Phys Lett* (2013) 99(12):231101. doi:10.1063/1.4808265

15. Hosoda T, Tao F, Leon S, Kipshidze G, Belenky G. High power cascade diode lasers emitting near 2 µm. *Appl Phys Lett* (2016) 108:131109. doi:10.1063/1.4944553

16. Zhang Y, Yang C-A, Shang J-M, Chen YH, Wang TF, Zhang Y, et al. GaSb-based type-I quantum well cascade diode lasers emitting at nearly 2-µm wavelength with digitally grown AlGaAsSb gradient layers*. *Chin Phys B* (2021) 30(9):094204. doi:10.1088/1674-1056/abe930

17. Yang C-A, Zhang Y, Shang J-M, Chen Y, Wang T, Tong H, et al. Research progress of 2-4µm mid-infrared antimonide semiconductor lasers(invited). *Infrared Laser Eng* (2020) 12:163–71. doi:10.3788/IRLA.13_INVITED-1075

18. Rong JM, Xing E, Zhang Y, Wang L, Shu S, Tian S, et al. Low lateral divergence 2 µm InGaSb/AlGaAsSb broad-area quantum well lasers. *Opt Express* (2016) 24(7):7246–52. doi:10.1364/oe.24.007246

19. Zhao Z, Bai Z, Jin D, Qi Y, Ding J, Yan B, et al. Narrow laser-linewidth measurement using short delay self-heterodyne interferometry. *Opt Express* (2022) 30(17):30600–10. doi:10.1364/OE.455028

frontiers | Frontiers in Physics

TYPE Brief Research Report
PUBLISHED 15 November 2022
DOI 10.3389/fphy.2022.1043435

OPEN ACCESS

EDITED BY
Liyuan Chen,
Hilase Center, Czechia

REVIEWED BY
Santosh Kumar,
Liaocheng University, China
Xiaohui Li,
Shaanxi Normal University, China

*CORRESPONDENCE
Chang Sun,
changsun@buaa.edu.cn

SPECIALTY SECTION
This article was submitted to Optics and Photonics,
a section of the journal
Frontiers in Physics

RECEIVED 13 September 2022
ACCEPTED 27 October 2022
PUBLISHED 15 November 2022

CITATION
Sun C, Ge T, Cao K and Wang Z (2022), 143.4 W high power combined white supercontinuum source using a (7 × 1) supercontinuum fiber combiner.
Front. Phys. 10:1043435.
doi: 10.3389/fphy.2022.1043435

143.4 W high power combined white supercontinuum source using a (7 × 1) supercontinuum fiber combiner

Chang Sun[1]*, Tingwu Ge[2], Kang Cao[2] and Zhiyong Wang[2]

[1]School of Instrumentation and Optoelectronic Engineering, Beihang University, Beijing, China, [2]Institute of Laser Engineering, Beijing University of Technology, Beijing, China

We demonstrate a 143.4 W high power combined white supercontinuum (SC) source using a (7 × 1) SC fiber combiner. Based on the criteria of adiabatic tapering and brightness conservation, a (7 × 1) SC fiber combiner is designed and theoretically investigated, and the simulated results of the transmission efficiencies of laser at different wavelengths of the combiner verify that the combiner has the ability of combining white SC sources efficiently. Then, the (7 × 1) SC fiber combiner is fabricated, and three white SC fiber laser sources with average power of about 50 W are set up for beam combining experiment. Finally, a 143.4 W high power combined white SC source is achieved with high combining efficiency of 97.4%. and the corresponding combined SC spectrum ranges from 450 nm to 1700 nm, which remains consistent with the overall spectral range of the three SC sources. The experiment result indicates that the (7 × 1) SC fiber combiner is greatly capable of combining high power white SC sources efficiently, thereby increasing the average power of the white SC source significantly. To the best of our knowledge, this is the first demonstration of a fiber combiner for high power white SC sources with such a high combining efficiency.

KEYWORDS

supercontinuum generation, laser beam combining, fiber lasers, high power, white supercontinuum

1 Introduction

The development of high power white supercontinuum (SC) fiber laser source which contains a large portion of visible-waveband power, is of particular interest in many areas, such as hyperspectral spectral imaging, astronomical optical frequency combs, and remote illumination, due to its broadband spectrum, high brightness, high coherence, and compact structure [1–4]. In recent years, a lot of high power white SC fiber laser sources have been demonstrated. For example, in 2016, using a 63.3 W ps pulses with a large chirp as pump source, 30.4 W white SC source was obtained with spectrum ranging from 385 nm to 2,400 nm [5]. Based on a high nonlinear photonic crystal fiber (PCF), 53.3 W white SC source with spectrum ranging from 430 nm to 2,400 nm was generated using a 120 W picosecond pulse laser in the same year [6]. In 2018, 80 W white SC source

pumped by a 114 W pulse fiber laser was obtained, and the corresponding spectral range was from 370 nm to 2,400 nm [7]. In the same year, a 215 W white SC source spanning from 480 nm to over 2,000 nm was reported with a pulses pump source of 556 W [8]. In 2020, a 104 W white SC source covering from 370 nm to 2,400 nm was generated by pumping cascaded photonic crystal fibers with 375 W ps pulse [9]. It can be seen from these reports that the commonly used method of generating high power white SC source is to couple high power pulses provided by a master oscillator power amplifier (MOPA) pulsed fiber laser into a length of PCF with high nonlinear coefficient through a mode field adapter (MFA) to stimulate high power white SC laser. This method is simple in principle and easy to implement, but there are still two technical difficulties which limit the further increase of white SC average power. The first one is the nonlinear effects during the pulses amplification process in the high power MOPA pulsed fiber laser, such as Stimulated Raman Scattering (SRS). The effects will cause the pump energy to be transferred to other wavelengths, and thus the signal pulses cannot be further linearly amplified to obtain high power output. The gain fiber with large mode field area is usually adopted to solve this problem [5], However, the excessively large mode field area will cause serious mode field mismatch between the pigtail of pulses fiber laser and the PCF, thereby reducing the coupling efficiency of the pulses. In addition, inserting a repetition frequency multiplier (RFM) before the amplifiers of the pulses fiber laser is another way to suppress nonlinear effects [6–9], yet the RFM only works in a limited frequency doubling range. Therefore, the nonlinear effects problem is difficult to completely overcome. The second one is the thermal damage of fibers under high power operation condition of fiber laser. For example, the heat accumulation on gain fibers and PCFs caused by quantum defect and on MFA caused by coupling loss will increase temperature of the fibers, which may cause the fibers to burn and even damage the entire laser. The commonly used method to solve this problem is to place the fibers prone to accumulating heat on the water-cooled heat sink [8, 10, 11], but such a complicated structure is not conducive to the practical application of white SC fiber laser.

For above two difficulties, SC beam combining technology is an ideal solution. It can not only effectively avoid nonlinear effects and fiber thermal damage because the single-channel laser source does not need to pursue high power limit, but also increase the white SC average power significantly. However, commercial fiber combiners can only work at a single wavelength, and so far, there are only a handful reports on the SC fiber combiner. In 2015, using a (3 × 1) broadband fiber combiner, a 202.2 W high power combined near-infrared SC source with spectrum ranging from 1,060 nm to 1900 nm was obtained [12]. Up to now, the fiber combiner for high power white SC sources has not been reported.

In this paper, a 143.4 W high power combined white SC source using a (7 × 1) SC fiber combiner is demonstrated. We design and theoretically investigate a (7 × 1) SC fiber combiner based on the criteria of adiabatic tapering and brightness conservation, and theoretically prove that the designed combiner has the ability to combine white SC sources efficiently by simulating the transmission efficiencies of laser at different wavelengths. Then, a (7 × 1) SC fiber combiner is fabricated, and three white SC fiber laser sources with average power of about 50 W are set up for beam combining experiment. Finally, a 143.4 W high power combined white SC source is achieved with high combining efficiency of 97.4%, and the combined spectrum ranging from 450 nm to 1700 nm remains consistent with the overall spectral range of three SC sources. The experiment result indicates that the (7 × 1) SC fiber combiner is capable of combining high power white SC sources efficiently, and has the capability of increasing the average power of the white SC source significantly. To the best of our knowledge, this is the first demonstration of a fiber combiner for high power white SC sources with such a high combining efficiency. And this research result will contribute to further increasing the white SC power, thereby broadening the application fields of white SC source.

2 Theoretical simulation

Compared with ordinary fiber combiners working at a single wavelength, the difficulty in designing a SC fiber combiner is to make it work at multiple wavelengths to achieve wide-spectrum beam combination. Therefore, two design criteria need to be followed. They are the brightness conservation [13] and the adiabatic tapering [14].

The brightness conservation formula is $\sqrt{N}D_{in}NA_{in} \le D_{out}NA_{out}$, where D_{in} and D_{out} are the diameters of output and input fibers respectively, NA_{in} and NA_{out} represent the numerical aperture of the input and output fibers respectively, and N is the number of input fibers. Based on the criteria of brightness conservation, and considering that the input fibers of the combiner and the PCF as the pigtail of a single SC source need to meet the mode field matching, and the output fiber of the combiner should support high power laser transmission, the basic structural parameters of the fiber combiner are determined as follows: The input fiber is set to 6/125 μm fiber with NA of 0.13, the output fiber is set to 100/360 μm fiber with NA of 0.2, and N is set to 7.

The general method of fabricating a fiber combiner is to insert the input fiber bundle into a silica tube at first, then tapering them, and finally splicing the tapered fiber bundle to the output fiber. The basic structure of the designed (7 × 1) SC fiber combiner is schematically shown in Figure 1A. In the process of tapering the input fiber bundle, as the fiber core diameter decreases gradually, the laser mode will no longer maintain the initial mode field distribution, and will leak into the fiber cladding to cause transmission loss. Therefore, the

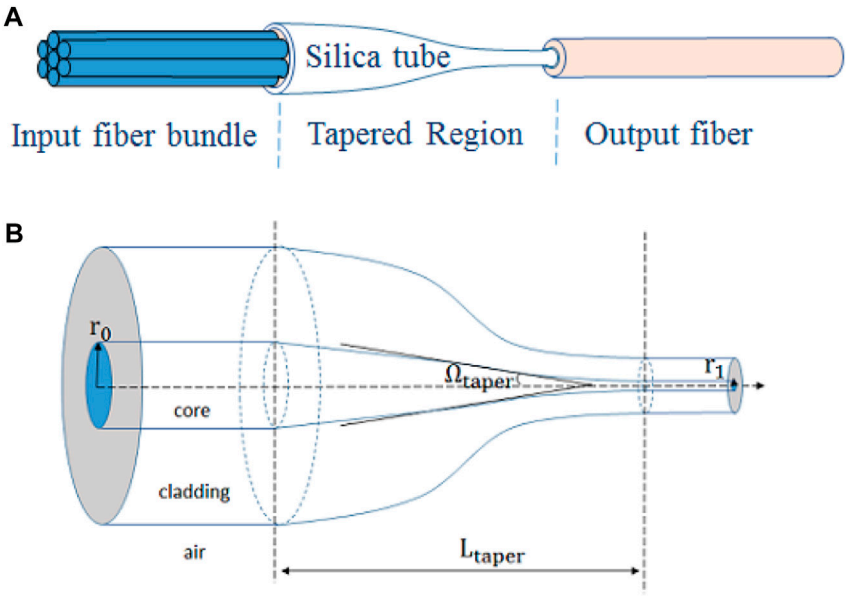

FIGURE 1
(A) The structure of the (7 × 1) SC fiber combiner. **(B)** The schematic of tapered region of a single fiber.

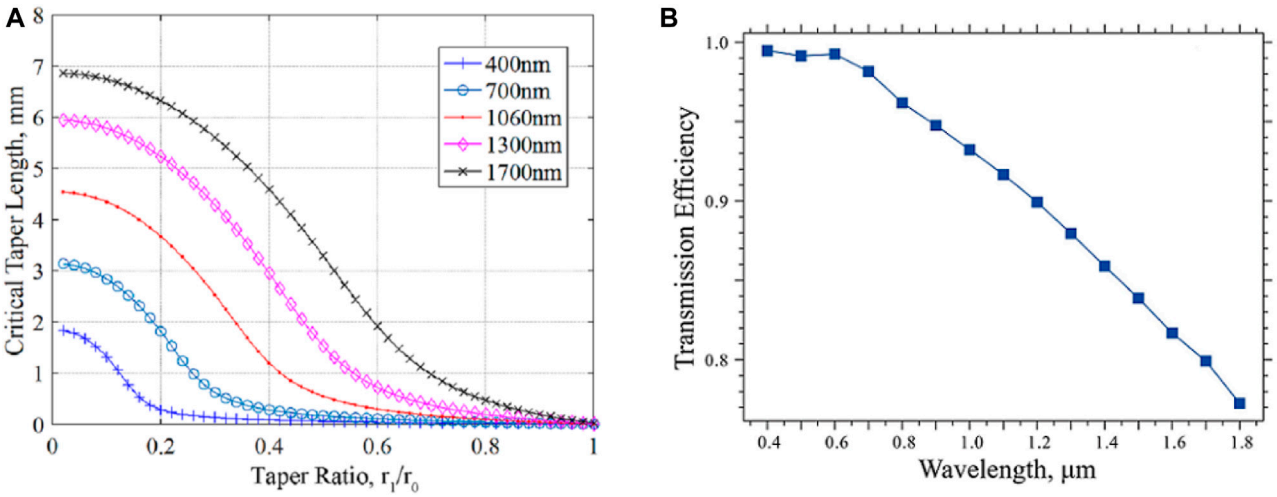

FIGURE 2
(A) The relationships between the critical taper length and TR at different wavelengths. **(B)** The transmission efficiencies of the SC combiner at different wavelengths.

transmission loss of fiber combiner mainly comes from the tapered region of input fiber bundle. The tapered region structure of a single fiber is shown in Figure 1B, where Ω_{taper} is the tapered angle, L_{taper} is the tapered region length corresponding to Ω_{taper}, r_0 is the initial core radius, and r_1 is the tapered core radius. The taper ratio is defined as TR, $TR = r_1/r_0$. In order to reduce the transmission loss of the tapered region, each input fiber should satisfy the criteria of adiabatic tapering, that is, the maximum Ω_{taper} of the tapered region should not exceed the fundamental mode diffraction diffusion angle there. This maximum Ω_{taper} is called the critical tapering angle, and the corresponding L_{taper} is the

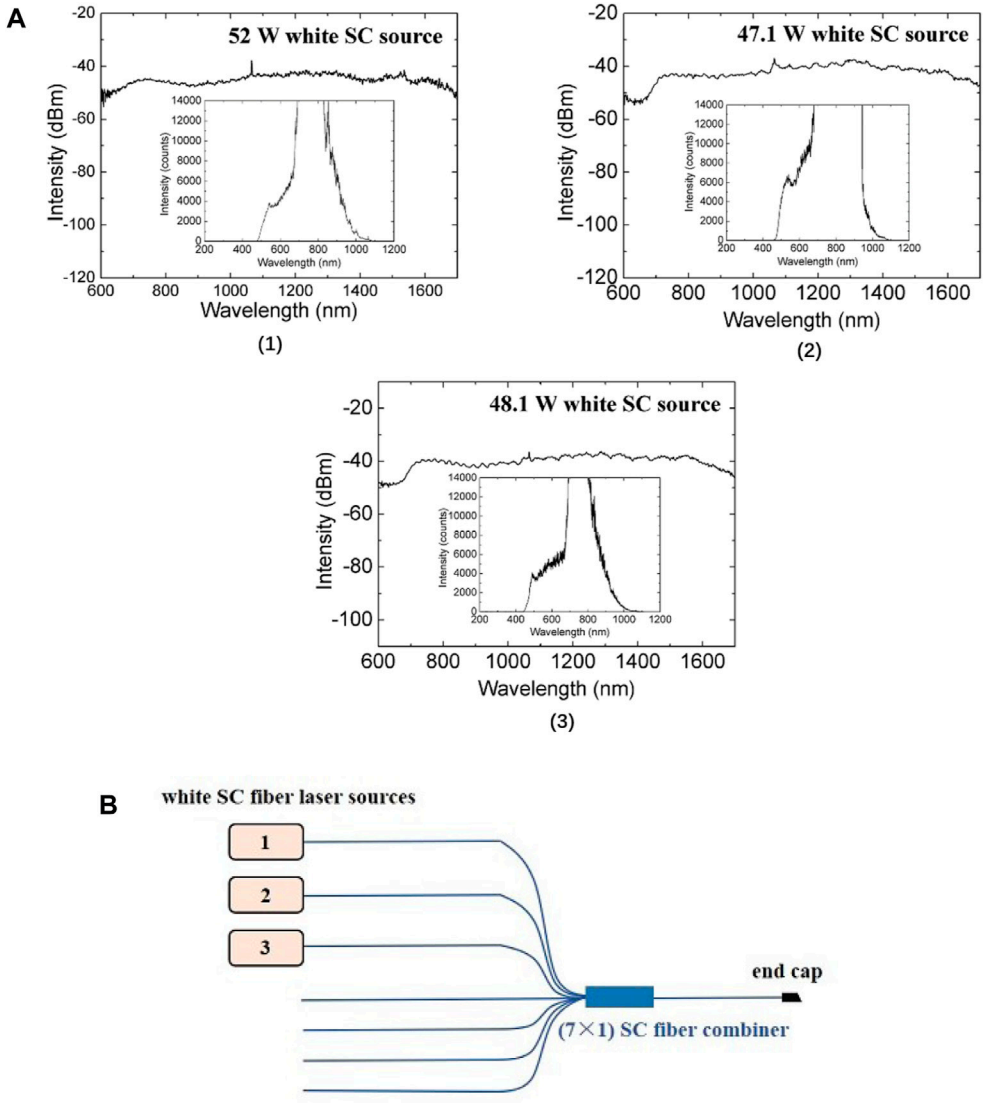

FIGURE 3
(A) The spectra of the three white SC sources. **(B)** The experimental setup of white SC beam combining.

critical tapering length. For a fixed *TR*, only when the L_{taper} is longer than the critical taper length, the tapered fiber will have relatively low transmission loss. For the SC fiber combiner operating at wide-spectrum, it is necessary to consider the adiabatic tapering conditions for different wavelengths, and determine a critical tapering length satisfying the low-loss transmission of overall SC spectrum.

Using the relevant formulas of the criteria of adiabatic tapering in the [14], the relationships between critical taper length and *TR* at the different wavelengths has been simulated, as shown in Figure 2A. It can be seen that, firstly, with the wavelength fixed, the smaller the *TR* is, the longer the critical taper length is; secondly, for a fixed *TR*, a longer wavelength corresponds to a longer critical taper length, which means that for the SC fiber combiner, only when the critical taper length corresponding to the longest wavelength is regarded as the L_{taper} of input fiber bundle of the combiner, can the low-loss transmission of the white SC source in the SC fiber combiner be guaranteed. Based on the fiber types and N value of the combiner designed above, it can be determined that the *TR* is about 0.25, and in this case, the critical taper length corresponding to the longest wavelength with 1,700 nm is 6 mm. Therefore, the L_{taper} of the input fiber bundle of the SC fiber combiner should be longer than 6 mm. In fact, the work range of the fiber tapering equipment used in this experiment is far greater than 6 mm. Meanwhile, considering that the tapered region of fiber is relatively fragile, the excessively long L_{taper} is not conducive to the working stability of the fiber combiner.

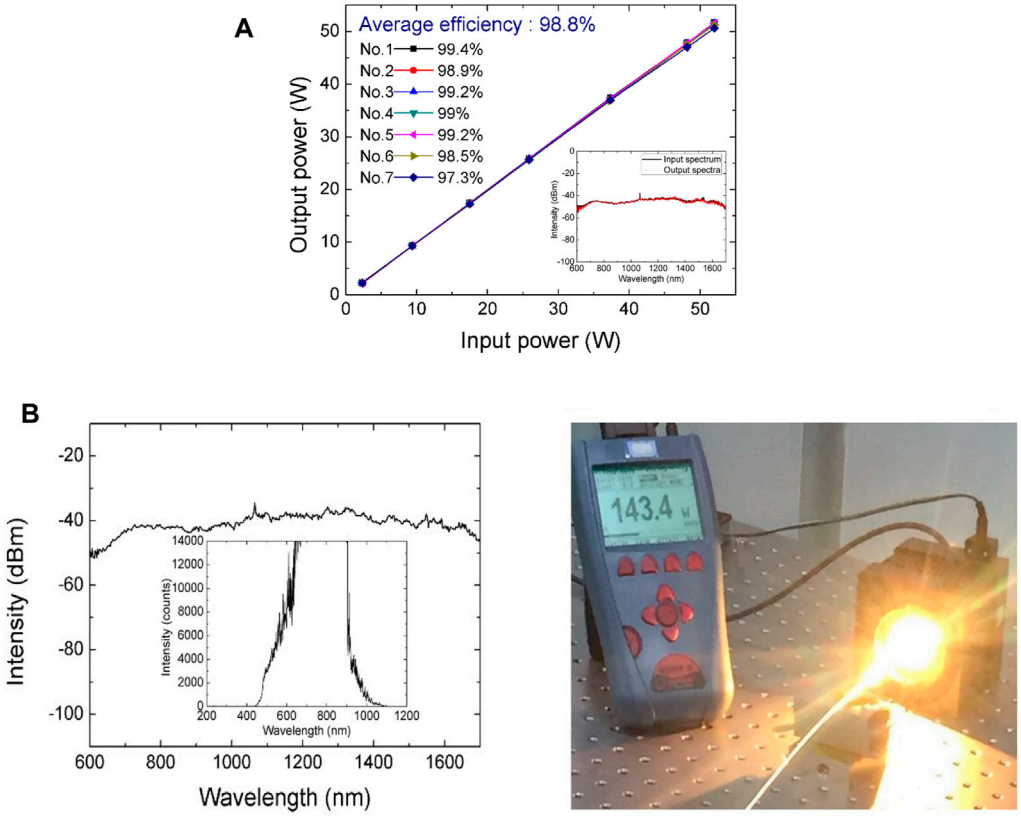

FIGURE 4
(A) The transmission efficiency of each channel of the (7 × 1) SC fiber combiner. Inset: Input spectrum and output spectra of the (7 × 1) SC fiber combiner. **(B)** The combined SC spectrum, and the photograph of white SC beam combining experimental at 143.4 W combined output power.

Therefore, for this SC fiber combiner, the L_{taper} is designed to be 15 mm.

Utilizing the specific structural parameters designed, a mathematic model of the (7 × 1) SC fiber combiner is established. Based on the Finite-Difference Beam Propagation Method, the laser transmission efficiencies at different wavelengths of a wide-spectrum source ranging from 400 nm to 1800 nm are simulated, as shown in Figure 2B. It can be seen that the shorter the wavelength is, the higher the transmission efficiency is, which is consistent with the theoretical analysis. And the average transmission efficiency of the wide-spectrum source can reach more than 90%. The simulation result proves that the designed (7 × 1) SC fiber combiner has the ability to combine white SC sources efficiently.

3 Experimental setup

Based on the structure parameters designed above, a (7 × 1) SC fiber combiner is fabricated experimentally, and three white SC fiber laser sources are set up for beam combining experiment. Their average powers are 52 W, 47.1 W and 48.1 W respectively, with the corresponding SC spectra ranging from 480 nm to 1,700 nm, from 470 nm to 1,700 nm, and from 450 nm to 1,700 nm, as shown in Figure 3A, which are measured by optical spectrum analyzers of YOKOGAWA AQ6370C (measuring range from 600 nm to 1,700 nm) and Ocean Optics HR4000 (measuring range from 200 nm to 1,100 nm). The details of the white SC fiber laser source can be found in [6]. The experimental setup is shown in Figure 3B. Three white SC fiber laser sources are connected to the three input fibers of the combiner, and a 1-cm long output end cap with an 8-deg cleaved facet is spliced to the output fiber of the combiner to eliminate back reflection and prevent end facet damage.

4 Result and discussion

Firstly, the transmission efficiencies of seven channels of the (7 × 1) SC fiber combiner are measured separately with the 52 W white SC fiber laser source. Figure 4A shows the measurement result that the transmission efficiency of each channel is above

97% and the average transmission efficiency of seven channels is up to 98.8%. Meanwhile, from the inset of Figure 4A, it can be seen that output spectrum from each channel is consistent with the input spectrum of 52 W white SC source, which indicates that the SC fiber combiner has consistent transmission efficiency for each wavelength over the overall SC range. The experiment results show that the fabricated SC fiber combiner can transmit the white SC source efficiently and uniformly.

Then, three white SC fiber laser sources and three channels selected randomly from the (7 × 1) SC fiber combiner are used to perform the white SC beam combining experiment, with No.3 channel corresponding to 48.1 W white SC source, No.4 channel corresponding to 47.1 W white SC source, and No.7 channel corresponding to 52 W white SC source. Eventually, 143.4 W high power combined white SC source is successfully achieved with high combining efficiency of 97.4%, and the corresponding combined SC spectrum ranging from 450 nm to 1700 nm is consist with the overall spectral range of three white SC sources, as shown in Figure 4B. The experiment result indicates that the fabricated (7 × 1) SC fiber combiner is greatly capable of combining high power white SC sources efficiently, and based on the high combining efficiency, the combiner has the potential to increase the average power of white SC source significantly. Meanwhile, it is worth noting that the current combined power is limited by the number of white SC fiber laser sources, thus more sources will be built in the future for beam combining experiment to obtain higher power white SC source. In addition, the combining efficiency of the SC fiber combiner is slightly lower than the average transmission efficiency of seven channels of the combiner, which may be caused by the increase of the splice point loss between the input fiber bundle and the output fiber under high power operation conditions, thus the splicing quality will be further improved in the next work.

5 Conclusion

In conclusion, the beam combining technology is an ideal method for obtaining high power white SC source, because it not only can effectively avoid some technical difficulties in the commonly used methods of generating high power white SC source, such as nonlinear effects and fiber thermal damage, but also has the ability of further increasing the white SC power. In this paper, a 143.4 W high power combined white SC source using a SC fiber combiner has been presented. Based on the criteria of adiabatic tapering and brightness conservation, a (7 × 1) SC fiber combiner has been designed and theoretically investigated, and is verified to be capable of combining white SC sources efficiently by simulating the transmission efficiencies of laser at different wavelengths. Then, the (7 × 1) SC fiber combiner is fabricated, and three white SC fiber laser sources with average power of about 50 W are set up for beam combining experiment. Finally, a 143.4 W high power combined white SC source is achieved with high combining efficiency of 97.4%, and the corresponding combined spectrum ranging from 450 nm to 1700 nm is consist with the overall spectral range of three white SC sources The experiment result indicates that the (7 × 1) SC fiber combiner is capable of combining high power white SC sources efficiently, and has the ability of increasing the average power of the white SC source significantly. At present, the combined power is limited by the number of white SC sources, thus more sources will be built in the future for beam combining to obtain higher power white SC source. To the best of our knowledge, this is the first demonstration of a fiber combiner for high power white SC sources with such a high combining efficiency, and the research result will contribute to further increasing the average power of the white SC source, thereby broadening the application fields of white SC source.

Data availability statement

The original contributions presented in the study are included in the article/Supplementary Material, further inquiries can be directed to the corresponding author.

Author contributions

CS, TG, and ZW contributed to conception and design of the study. CS performed theoretical simulations. CS and KC conducted the experiment. CS wrote the manuscript. All authors contributed to manuscript revision, read, and approved the submitted version.

Conflict of interest

The authors declare that the research was conducted in the absence of any commercial or financial relationships that could be construed as a potential conflict of interest.

Publisher's note

References

1. Dudley JM, Genty G, Coen S. Supercontinuum generation in photonic crystal fiber. *Rev Mod Phys* (2006) 78(4):1135–84. doi:10.1103/revmodphys.78.1135

2. Martinez-Ramirez D, Buller G, MoCathy A, Ren X, Morak AWS, Nichol C, Woodhouse I. Developing hyperspectral LiDAR for structure and biochemical analysis of forest data. In: *Proc. EARSEL conf. Adv. Geosci* (2012). p. 1–11.

3. Hartl I, Li XD, Chudoba C, Ghanta RK, Ko TH, Fujimoto JG, et al. Ultrahigh-resolution optical coherence tomography using continuum generation in an air-silica microstructure optical fiber. *Opt Lett* (2001) 26(9):608–10. doi:10.1364/ol.26.000608

4. Dudley JM, Taylor JR. Ten years of nonlinear optics in photonic crystal fibre. *Nat Photon* (2009) 3(2):85–90. doi:10.1038/nphoton.2008.285

5. Zou X, Wu J, Wang XD, Qiu JF, Ye Z, Sun C, Ge TW. An all-fiber supercontinuum laser source with high power of 30.4 W and ultra-wide spectrum of 385-2400 nm. In: *Proc. CLEO, OSA* (2016). Paper SW1Q.4.

6. Sun C, Ge TW, Li SY, An N, Cao K, Wang ZY. 53.3 W visible-waveband extra high power supercontinuum all-fiber laser. *IEEE Photon J* (2016) 8(6):1–7. doi:10.1109/jphot.2016.2616509

7. Qi X, Chen S, Li Z, Liu T, Ou Y, Wang N, et al. High-power visible-enhanced all-fiber supercontinuum generation in a seven-core photonic crystal fiber pumped at 1016nm. *Opt Lett* (2018) 43(5):1019–22. doi:10.1364/ol.43.001019

8. Zhao L, Li Y, Guo C, Zhang H, Liu Y, Yang X, et al. Generation of 215 W supercontinuum containing visible spectra from 480 nm. *Opt Commun* (2018) 425:118–20. doi:10.1016/j.optcom.2018.04.066

9. Zhang H, Li Y, Yan D, Dong K, Lin H, Wang J, et al. All-fiber high power supercontinuum generation by cascaded photonic crystal fibers ranging from 370 nm to 2400 nm. *IEEE Photon J* (2020) 12:1–8. doi:10.1109/jphot.2020.2983120

10. Sun C, Ge TW, Li SY, An N, Wang ZY. 67.9 W high power white supercontinuum all-fiber laser source. *Appl Opt* (2016) 55(14):3746–50. doi:10.1364/ao.55.003746

11. Chen H, Wei H, Liu T, Zhou X, Yan P, Chen Z, et al. All-fiber-integrated high-power supercontinuum sources based on multi-core photonic crystal fibers. *IEEE J Sel Top Quan Electron* (2014) 20(5):64–71. doi:10.1109/jstqe.2014.2304136

12. Zhou H, Jin A, Chen Z, Zhang B, Zhou X, Chen S, et al. Combined supercontinuum source with >200 W power using a 3×1 broadband fiber power combiner. *Opt Lett* (2015) 40(16):3810–3. doi:10.1364/ol.40.003810

13. Benoit S, Pierre P, Mathieu F. Pump combiner loss as a function of input numerical aperture power distribution. In: Proc. SPIE 7195, The International Society for Optical Engineering (2009). Paper 719523.

14. Love JD, Henry WM, Stewart WJ, Black RJ, Lacroix S, Gonthier F. Tapered single-mode fibres and devices. Part 1: Adiabaticity criteria. *IEE Proc J Optoelectron UK* (1991) 138(5):343–54. doi:10.1049/ip-j.1991.0060

frontiers | Frontiers in Physics

TYPE Mini Review
PUBLISHED 24 November 2022
DOI 10.3389/fphy.2022.1079265

OPEN ACCESS

EDITED BY
Zhi-Han Zhu,
Harbin University of Science and Technology, China

REVIEWED BY
Yue Pan,
Qufu Normal University, China

*CORRESPONDENCE
Jia-Qi Lü,
lvjiaqi@hebut.edu.cn

SPECIALTY SECTION
This article was submitted to Optics and Photonics,
a section of the journal
Frontiers in Physics

RECEIVED 25 October 2022
ACCEPTED 14 November 2022
PUBLISHED 24 November 2022

CITATION
Guo J-X, Wang W-Y, Cheng T-Y and Lü J-Q (2022), Interaction of spin-orbit angular momentum in the tight focusing of structured light.
Front. Phys. 10:1079265.
doi: 10.3389/fphy.2022.1079265

Interaction of spin-orbit angular momentum in the tight focusing of structured light

Ji-Xiang Guo[1,2], Wen-Yue Wang[1,2], Tian-Yu Cheng[1,2] and Jia-Qi Lü[1,2]*

[1]Center for Advanced Laser Technology, Hebei University of Technology, Tianjin, China, [2]Hebei Key Laboratory of Advanced Laser Technology and Equipment, Tianjin, China

As an intrinsic property of light, angular momentum has always been an important research object of light field. In the past few years, the interactions between spin angular momentum and orbital angular momentum in tightly focused structured light have attracted much attention. Different from the independent conservation in the paraxial condition, the polarization-dependent spin angular momentum and the phase-dependent orbital angular momentum are coupled under tight focusing condition based on different physical mechanisms. The research on spin-orbit interaction will be helpful to deeply understand the nature of photon as well as extend the applications of light. Here, different forms of spin-orbit interaction during the tight focusing of structured light have been briefly introduced and classified. Besides, the existing problems and development prospects in the research about spin-orbit interaction of light are discussed, including the quantitative detection of the local distribution of optical spin and orbital angular momentum in experiments and the further applications of spin-orbit interaction.

KEYWORDS

structured light, tight focus, spin-orbit interaction, spin angular momentum, orbital angular momentum

Introduction

Besides the momentum related to the local wavevector, photon with wave-particle duality can also carry angular momentum (AM), which includes the polarization-dependent spin angular momentum (SAM) [1–5] and phase-dependent orbital angular momentum (OAM) [6, 7]. In 1909, Poynting first predicted that left- and right-circularly polarized light carries the SAM of $\pm\hbar$ [5], which was experimentally proved by measuring the torque of the half-wave plate when conversing the right-hand circularly polarized light to left-hand circular polarization [8]. In 1992, Allen first proposed that the vortex beam containing a helical phase distribution exp ($il\theta$) carries OAM where l is the phase topological charge and the OAM of a single photon is $l\hbar$ [7]. In the frame of paraxial optical fields, SAM and OAM are mostly independent of each other and conserved separately during the diffraction of light in free space. While in the cases

like waveguide structures [9], subwavelength metallic structures [10, 11] and tight focusing [12–16], coupling conversion between SAM and OAM can be achieved. In the absence of light-matter interaction, the significant spin-orbital interaction (SOI) during tight focusing provides a flexible and effective approach to manipulate the AM behavior of optical field.

Previous research has established that tightly focused circularly polarized light can induce the spin-to-orbit conversion (STOC). In 2006, Bomzon et al. presented that the focusing of circularly polarized plane wave can generate vortex phase with a topological charge of 2 in the focal plane, indicating the OAM can be derived from the conversion of SAM [17]. In 2007, Zhao et al. experimentally demonstrated the STOC in focused circularly polarized (CP) Gaussian beam by observing the orbital motion of micron-sized metal particles at the focal plane [18, 19]. In 2016, Bauer et al. found that pure transversely spinning of light can be derived by tightly focusing linearly polarized Gaussian beam, where the longitudinal spin component is zero [20]. For the structured light with spatially inhomogeneous distribution of amplitude, phase and polarization where the SAM and OAM may be coexisting in single optical beam [21–32], the interaction between SAM and OAM during its tight focusing exhibits diverse forms and has attracted more and more attention in recent years [33–38]. Related investigations not only deepen the understanding of the nature of photon, but the conversion of SAM and OAM also bring additional manipulation degree of freedom for the AM of light, leading to new applications including optical micromanipulation [39–44], information storage [45, 46] microscopic imaging [47, 48] and optical communication [49–52].

Here, we first briefly introduce the classification and calculations of AM. Then, the types of spin-orbit interaction (SOI) in tightly focused structured light are classified and summarized, including STOC, catalystlike effect of OAM, coupling of SAM and OAM, and SAM induced novel OAM. In addition, the problem of the quantitative measurement of SAM and OAM local distributions and the potential application of SOI are discussed.

The classification and calculations of AM

The classification of light AM is shown in Figure 1. The AM can be divided into SAM that induces the spin motion of trapped dielectric particles and OAM that induces the orbital motion of trapped dielectric particles. SAM can be distinguished according to the direction of AM: the longitudinal-type SAM (*l*-SAM) is in the same direction of beam propagation and transverse-type SAM (*t*-SAM) is perpendicular to the direction of propagation, similar to the spinning movement of the rotor blades of an aircraft and the rolling bicycle wheel [53–56] respectively. Different from the polarization-related SAM, the phase-dependent OAM is usually associated with the orbital energy flux. OAM can be divided into intrinsic-OAM (*i*-OAM) and extrinsic-OAM (*e*-OAM). The *i*-OAM is correlated with the spiral phase wavefront, whose magnitude and direction can be defined by the topological charge. The *e*-OAM is related to the transverse coordinate of the beam centroid, similar to AM of the classical particle, which is derived from the cross-product of the

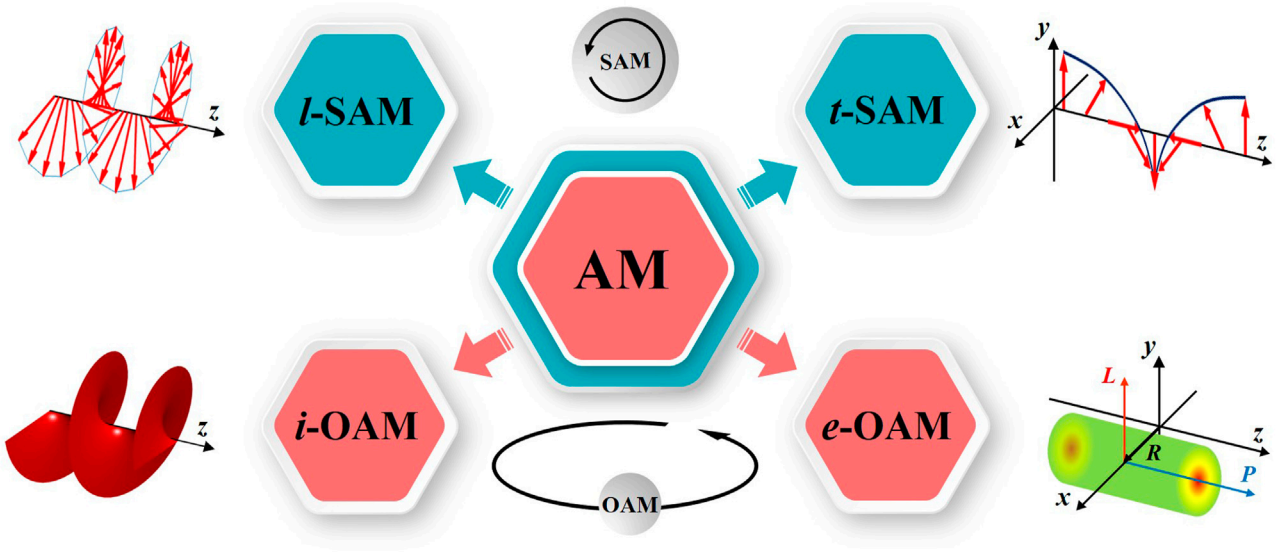

FIGURE 1
Angular momentum of light.

spatial coordinates of the beam centroid and its linear momentum [38].

For the arbitrary optical field in non-magnetic media, the temporally averaged three-dimensional SAM and OAM density distribution can be generally expressed as [57, 58].

$$\vec{S} = \frac{1}{4\omega_0}\mathrm{Im}\left[\varepsilon_0 \vec{E}^{\star} \times \vec{E}\right]$$

$$\vec{L} = \frac{1}{4\omega_0}\vec{r} \times \mathrm{Im}\left[\varepsilon_0\left(\vec{E}^{\star} \cdot (\nabla)\vec{E}\right)\right]$$

where ε_0 is the permittivity in vacuum, ω_0 is the angular frequency, and $\vec{E}^{\star}$ denotes the complex conjugate of the electric field $\vec{E}$. $\vec{S}$ denotes the SAM that contains the *l*-SAM and *t*-SAM, and $\vec{L}$ denotes the OAM including *i*-OAM and *e*-OAM associated with optical vortex and optical trajectory, respectively [34].

SOI in tightly focused structured light

The spatial manipulation of amplitude, phase and polarization in optical field leads to the generation of diverse structured light. SOI has been observed in the focusing of structured lights including linearly polarized vortex beams (LPVBs) [57], radially polarized vortex beams (RPVBs) [59], azimuthally polarized vortex beams (APVBs) [60], cylindrical vortex vector beams (CVVBs) [61], circularly polarized vortex beams (CPVBs) [62], azimuthal-variant hybridly polarized vector beams [63], radial-variant hybridly polarized vector beams [64], circularly polarized Bessel beams [65], higher-order Poincaré sphere beams (HOPBs) [66], etc. Different forms of SOI have been demonstrated including SAM to *i*-OAM conversion, OAM catalyzes the local distribution of *t*-SAM and *l*-SAM, coupling of SAM and OAM, and SAM induced novel OAM. The phenomena with complex behaviors of SOI are not only related to the numerical aperture (NA) of the focusing system, but also influenced by the spatial degrees of freedom of structured light.

Spin-to-orbit conversion

In 2011, Bliokh et al. presented a general theory of STOC in focusing optical systems based on the Debye-Wolf theory [12]. The conversion efficiency of STOC can be estimated by $1–\cos\theta$, where θ is the aperture angle of the objective, indicating that the STOC becomes more significant as the field is focused at larger NA. In 2016, Yan et al. demonstrated the STOC by tightly focusing right-hand CPVBs and RPVBs [62]. The focal fields all exhibit hollow intensity distributions with cylindrical symmetry. The radius of the ring-like field reflects the OAM of light. The larger the absolute value of OAM, the larger the radius of focusing at the focal plane is. It was found that the OAM of the focal field is not only related to the sign and quantity of topological charge of the incident light, but also its polarization distribution. The incident right-hand CPVBs with positive OAM lead to a larger radius of the ring-like focal field than that with negative OAM, and the annulus radius of the RPVBs with the same focusing parameters falls in between these two situations. This indicates that the magnitudes of OAM change during tight focusing which is attributed to the conversion of the SAM to OAM. In 2017, Chen et al. investigated the STOC of azimuthal-variant hybridly polarized vector beams under a highly nonparaxial condition [63]. It was revealed that the density distribution of the converted OAM in the focal field is influenced by the spatial polarization distribution of the incident light. Larger polarization topological charge corresponds to more irregular OAM distribution, which is caused by the superposition of the converted OAM from SAM. In 2012, Pu et al. investigated the conversion of the radial-variant SAM to OAM in tightly focused radial-variant hybridly polarized vector beams based on vectorial Debye theory [64]. The intensity distribution of the focal field changes from an elliptical spot to an annular distribution with increasing the radial index, and the phase of the *z*-polarization component associated with the local SAM of vector beam varies with azimuthal angle from $-\pi$ to π in the focus ring. Considering the SAM is radially varied, the OAM of the *z*-polarization component in the focal field also exhibits a radial distribution. This result lies in the fact that the conversion of local SAM in the radial-variant hybridly polarized vector beams to OAM under tight focusing leads to the helical phase profile.

Catalyst effect of OAM

In general, the impact of OAM on the SAM in the focal field is not reflected in conversion, but more likely performs as a catalyst for the redistribution of SAM. In 2018, Yan et al. predicted in theory that the OAM carried by the APVBs can induce local redistribution of the SAM under tight focusing conditions [60]. The focal field exhibits a sharp central focal spot unrelated to the sign of OAM carried by the incident light. It was demonstrated that the phase of the radial and azimuthal components vary periodically along the azimuthal direction, indicating the magnitude of OAM is unchanged during focusing. A π-phase jump can be found in the radial direction of the azimuthal component, which causes the inhomogeneous distribution of SAM density. The distribution of SAM and OAM with the same orientation are concentrated in the center of the focus and surrounding the annulus respectively, while the total value of SAM and OAM in the focal field is constant. These results suggest that no OAM carried by the incident APVBs is converted to SAM after tight focusing, but OAM catalyzes the local redistribution of the SAM. In the same year, Liu et al. demonstrated the catalytic effect of OAM during the focusing of

RPVBs. The OAM carried by the RPVBs can induce the conversion of transverse to three-dimensional SAM [59]. The RPBs with the total OAM of zero can induce the local *t*-SAM redistribution which is caused by the phase difference between the radial and longitudinal components. The *l*-SAM will appear when using the RPVBs with non-zero OAM as the incident light, which is attributed to the variation of spin flux caused by OAM. In 2022, Gu et al. theoretically investigated the three-dimensional distribution of SAM and OAM in tightly focused LPVBs [57]. Similarly, the incident light without carrying SAM exhibits both *t*-SAM and *l*-SAM after tight focusing. OAM is acting as a special catalyst to influence the local distribution of SAM, and the total quantity of SAM remains unchanged. In 2019, Man et al. theoretically investigated the angular momentum properties of tightly focused generalized cylindrical vortex vector beams (CVVBs) [61]. They found that existing of OAM in cylindrical vector beam leads to the appearance of longitudinal SAM in the tightly focused field. The increase of initial phase difference between the superposed beams with orthogonal polarization for generating vector beam causes the increase of the absolute value of longitudinal SAM in the focal field, and the sign of initial phase difference only affects the radial SAM density distribution.

Coupling of SAM and OAM

As the variation of total quantity and the local redistribution are both the manifestations of SOI the bidirectional influence of SAM and OAM has also been observed during the tight focusing of some structured light. In 2020, Gong et al. theoretically studied the unique SOI phenomena by tightly focused HOPBs with both the vortex phase and complex polarization distribution [66]. The OAM converted from the SAM during tight focus combined with the origin OAM jointly affects the local distribution of SAM which will in turn influence the STOC. Thus, the coupling of SAM and OAM exhibits a complex behavior in the tight focusing of HOPBs. Besides, it has been demonstrated that by controlling the superposition weights of two vortex beams with orthogonal polarization and the NA of the focusing system, specific modulation of the local SAM and OAM density distribution in the focal field can be achieved.

SAM induced novel OAM

Most of the current research considers the OAM associated with the helical phase profile, while the novel OAM induced by inhomogeneous distribution of SAM provided a new understanding of SOI in tightly focused structured light. In 2010, Wang et al. predicted the novel OAM relevant to the curl of polarization by tightly focusing the radial-variant hybridly polarized vector beams [67]. The focal field is donut-shaped distribution with a non-zero central intensity, and the maximum OAM is located at the radial of maximum intensity. They predicted that the novel OAM has a positive correlation with the gradient of radial variation of polarization. The existence of OAM is experimentally proved by observing the circular motion of the trapped isotropic particles in the focal plane. In 2021, Wang et al. presented a new strategy to produce OAM by constructing radial intensity gradient (RIG) in the focal plane of a circularly polarized light [65]. The spin-dependent local OAM obtained by focusing the CP with RIG can also trap the microparticles and realize the counterintuitive orbital motion of the microparticles in the experiment, which is attributed to the nonzero macroscopic spin flow along the azimuth. However, the changes of AM in the quantity and the local density distribution of SAM during the focusing process are still unclear.

Discussion

As summarized in Table 1, the SOI in the tight focusing of structured light can be divided into four forms as STOC, catalystlike effect of OAM, coupling of SAM and OAM, and SAM induced novel OAM. The tight focusing of different structured light can lead to different forms of SOI. For STOC, the total SAM will decrease while the OAM will also change in total quantity. The increase or decrease of OAM is determined by the directions of initial SAM and OAM. For the forms of catalystlike effect of OAM, the quantity of OAM and SAM during tight focusing remain unchanged while the local distribution of SAM will change. The coupling of SAM and OAM, where the STOC and catalystlike effect of OAM may happen simultaneously, leads to the complex variation of AM including its quantity and local distribution. For the situation of SAM induced novel OAM, the variation of SAM is still indetermined and the quantity of OAM increases from 0.

For the experimental detection of SOI, there are mainly two methods. The one mostly used method focus on the observation of the spin and orbital motion behavior of microparticles which can be trapped and driven by AM of light. This method can only act as a semiquantitative approach to evaluate the magnitude and direction of AM. The measurement of amplitude, phase and polarization based on the near field scanning optical microscopy (NMOS) system is another experimental method which has the limitations of lower accuracy, poorer stability and sensitivity [68]. It is also difficult for a single nanoprobe to achieve the measurement of multiple degrees of freedom in the focal field. Therefore, the quantitative detection of SAM and OAM distribution in the tightly focal field remains a challenge and this has actually caused arguments in the study of SOI as no rigorous and reliable experimental data can prove some of the theoretical results. Efficient and accurate experimental methods for quantitatively detecting the conversion and the localized density of SAM and OAM should be further developed.

TABLE 1 Different forms of SOI.

SOI	Structured light	SAM	OAM
STOC	CPVBs, azimuthal-variant hybridly polarized vector beams	Quantity decreases	Quantity changes
Catalystlike effect of OAM	LPVBs, CVVBs	Quantity unchanged Redistribution	Unchanged
Coupling of SAM and OAM	CPVBs, HOPBs	Quantity decreases Redistribution	Quantity changes
SAM induced novel OAM	CP with RIG, radial-variant hybridly polarized vector beams	Indetermination	Quantity increases

Benefiting from in-depth research about the SOI, the potential of structured light has been considered in many applications including optical communications, optical trapping and optical nano-probing. From another perspective, the extending of the structured light may also provide opportunities to explore new forms of SOI. It is believed that further investigation of the SOI of structured light in tightly focused systems may bring new insights into light-matter interactions and promote the development of related applications. The special distribution of SAM and OAM in the focal field region based on spin-orbit interaction has been demonstrated as an effective way to achieve particle capture and optical micromanipulation. Besides, the combination of AM and other fundamental degrees of freedom of photon may drive the development of multiplexing technology, which has the advantages of ultra-high capacity, ultra-fast speed, high security and low bit error rate, and can be used in optical communication, optical information storage, information security encryption, and high-dimensional quantum information. Furthermore, the intrinsic coupling between the polarization, phase and position of the light in the focal field makes the SOI to act as an extremely sensitive probe to the position and scattering properties of the nanoparticle. By capturing and analyzing the scattered radiation of the nanoparticle located in the tightly focused field, the variation and conversion of AM distribution can be analyzed to obtain the information about nanoparticle, which is highly attractive for optical nano-probing [69].

Conclusion

In conclusion, the interactions of spin-orbit AM in the tight focusing of structured light have been reviewed. Four different forms of SOI including STOC, catalyst like effect of OAM, coupling of SAM and OAM and SAM induced novel OAM can be summarized. With the optimization and upgrading of the detection method of local AM of light and modulation technology of structured light, the mechanism of spin-orbit interaction during tight focusing will be more clear and new forms of SOI may be demonstrated. Related research will further promote the application of structured light in optical communications, optical trapping and optical nano-probing.

Author contributions

J-XG wrote the main manuscript and prepared figure, W-YW and T-YC finished the references collection and provided valuable suggestions for the work, J-QL finished the whole manuscript modification and finalization. All authors reviewed the manuscript.

Funding

This work is supported by the National Natural Science Foundation of China (NSFC) (62005076) and the Natural Science Foundation of Hebei Province (F2020202035).

Conflict of interest

The authors declare that the research was conducted in the absence of any commercial or financial relationships that could be construed as a potential conflict of interest.

Publisher's note

References

1. Aiello A, Banzer P, Neugebauer M, Leuchs G. From transverse angular momentum to photonic wheels. *Nat Photon* (2015) 9(12):789–95. doi:10.1038/nphoton.2015.203

2. Bliokh KY, Bekshaev AY, Nori F. Extraordinary momentum and spin in evanescent waves. *Nat Commun* (2014) 5(1):3300. doi:10.1038/ncomms4300

3. Bekshaev AY, Bliokh KY, Nori F. Transverse spin and momentum in two-wave interference. *Phys Rev X* (2015) 5(1):011039. doi:10.1103/PhysRevX.5.011039

4. Neugebauer M, Bauer T, Aiello A, Banzer P. Measuring the transverse spin density of light. *Phys Rev Lett* (2015) 114(6):063901. doi:10.1103/PhysRevLett.114.063901

5. Poynting JH. The wave motion of a revolving shaft, and a suggestion as to the angular momentum in a beam of circularly polarised light. *Proc R Soc Lond A* (1909) 82(557):560–7. doi:10.1098/rspa.1909.0060

6. He C, Shen Y, Forbes A. Towards higher-dimensional structured light. *Light Sci Appl* (2022) 11(1):205. doi:10.1038/s41377-022-00897-3

7. Allen L, Beijersbergen MW, Spreeuw RJC, Woerdman JP. Orbital angular momentum of light and the transformation of Laguerre-Gaussian laser modes. *Phys Rev A* (1992) 45(11):8185–9. doi:10.1103/PhysRevA.45.8185

8. Beth RA. Mechanical detection and measurement of the angular momentum of light. *Phys Rev* (1936) 50(2):115–25. doi:10.1103/PhysRev.50.115

9. Liu W, Hu X, Jin L, Fu X, Chen Q. Generation of in-plane light beam with orbital angular momentum with an asymmetrical plasmonic waveguide. *Plasmonics* (2016) 11(5):1323–9. doi:10.1007/s11468-015-0178-x

10. Kang M, Guo Q, Chen J, Gu B, Li Y, Wang H. Near-field phase singularity in subwavelength metallic microstructures. *Phys Rev A* (2011) 84(4):045803. doi:10.1103/PhysRevA.84.045803

11. Karimi E, Schulz SA, Leon ID, Qassim H, Upham J, Boyd RW. Generating optical orbital angular momentum at visible wavelengths using a plasmonic metasurface. *Light Sci Appl* (2014) 3(5):e167. doi:10.1038/lsa.2014.48

12. Bliokh KY, Ostrovskaya EA, Alonso MA, Rodríguez-Herrera OG, Lara D, Dainty C. Spin-to-orbital angular momentum conversion in focusing, scattering, and imaging systems. *Opt Express* (2011) 19(27):26132–49. doi:10.1364/OE.19.026132

13. Bokor N, Iketaki Y, Watanabe T, Fujii M. Investigation of polarization effects for high-numerical-aperture first-order Laguerre-Gaussian beams by 2D scanning with a single fluorescent microbead. *Opt Express* (2005) 13(26):10440–7. doi:10.1364/OPEX.13.010440

14. Nieminen TA, Stilgoe AB, Heckenberg NR, Rubinsztein-Dunlop H. Angular momentum of a strongly focused Gaussian beam. *J Opt A: Pure Appl Opt* (2008) 10(11):115005. doi:10.1088/1464-4258/10/11/115005

15. Li M, Yan S, Liang Y, Zhang P, Yao B. Spinning of particles in optical double-vortex beams. *J Opt* (2018) 20(2):025401. doi:10.1088/2040-8986/aaa0e9

16. Li M, Yan S, Yao B, Liang Y, Lei M, Yang Y. Optically induced rotation of Rayleigh particles by vortex beams with different states of polarization. *Phys Lett A* (2016) 380(1-2):311–5. doi:10.1016/j.physleta.2015.08.026

17. Bomzon Z, Gu M, Shamir J. Angular momentum and geometrical phases in tight-focused circularly polarized plane waves. *Appl Phys Lett* (2006) 89(24):241104. doi:10.1063/1.2402909

18. Zhao Y, Edgar JS, Jeffries GDM, McGloin D, Chiu DT. Spin-to-orbital angular momentum conversion in a strongly focused optical beam. *Phys Rev Lett* (2007) 99(7):073901. doi:10.1103/PhysRevLett.99.073901

19. Zhao Y, Shapiro D, McGloin D, Chiu DT, Marchesini S. Direct observation of the transfer of orbital angular momentum to metal particles from a focused circularly polarized Gaussian beam. *Opt Express* (2009) 17(25):23316–22. doi:10.1364/OE.17.023316

20. Bauer T, Neugebauer M, Leuchs G, Banzer P. Optical polarization Möbius strips and points of purely transverse spin density. *Phys Rev Lett* (2016) 117(1):013601. doi:10.1103/PhysRevLett.117.013601

21. Padgett MJ, Courtial J. Poincaré-sphere equivalent for light beams containing orbital angular momentum. *Opt Lett* (1999) 24(7):430–2. doi:10.1364/OL.24.000430

22. Milione G, Sztul HI, Nolan DA, Alfano RR. Higher-order Poincaré sphere, Stokes parameters, and the angular momentum of light. *Phys Rev Lett* (2011) 107(5):053601. doi:10.1103/PhysRevLett.107.053601

23. Naidoo D, Roux FS, Dudley A, Litvin I, Piccirillo B, Marrucci L, et al. Controlled generation of higher-order Poincaré sphere beams from a laser. *Nat Photon* (2016) 10(5):327–32. doi:10.1038/nphoton.2016.37

24. Ren Z, Kong L, Li S, Qian S, Li Y, Tu C, et al. Generalized poincaré sphere. *Opt Express* (2015) 23(20):26586–95. doi:10.1364/OE.23.026586

25. Yi X, Liu Y, Ling X, Zhou X, Ke Y, Luo H, et al. Hybrid-order poincaré sphere. *Phys Rev A* (2015) 91(2):023801. doi:10.1103/PhysRevA.91.023801

26. Lerman GM, Stern L, Levy U. Generation and tight focusing of hybridly polarized vector beams. *Opt Express* (2010) 18(26):27650–7. doi:10.1364/OE.18.027650

27. Gu B, Pan Y, Rui G, Xu D, Zhan Q, Cui Y. Polarization evolution characteristics of focused hybridly polarized vector fields. *Appl Phys B* (2014) 117(3):915–26. doi:10.1007/s00340-014-5909-8

28. Holleczek A, Aiello A, Gabriel C, Marquardt C, Leuchs G. Poincaré sphere representation for classical inseparable Bell-like states of the electromagnetic field. *arXiv preprint* arXiv:1007.2528 (2010). doi:10.48550/arXiv.1007.2528

29. Ling X, Yi X, Dai Z, Wang Y, Chen L. Characterization and manipulation of full Poincaré beams on the hybrid Poincaré sphere. *J Opt Soc Am B* (2016) 33(11):2172–6. doi:10.1364/JOSAB.33.002172

30. Lü J, Wang W, Cheng T, Lu Z, Liu S. Vector optical field with the polarization varying along an arbitrary circular trajectory on the Poincaré sphere. *Opt Express* (2021) 29(24):39718–28. doi:10.1364/OE.441809

31. Chen R, Gao T, Chew K, Dai C, Zhou G, He S. Near-field characteristics of highly non-paraxial subwavelength optical fields with hybrid states of polarization. *Chin Phys B* (2017) 26(10):104202. doi:10.1088/1674-1056/26/10/104202

32. Wang X, Li Y, Chen J, Guo C, Ding J, Wang H. A new type of vector fields with hybrid states of polarization. *Opt Express* (2010) 18(10):10786–95. doi:10.1364/OE.18.010786

33. Bliokh KY, Alonso MA, Ostrovskaya EA, Aiello A. Angular momenta and spin-orbit interaction of nonparaxial light in free space. *Phys Rev A* (2010) 82(6):063825. doi:10.1103/PhysRevA.82.063825

34. Bliokh KY, Rodriguez-Fortuno FJ, Nori F, Zayats AV. Spin-orbit interactions of light. *Nat Photon* (2015) 9(12):796–808. doi:10.1038/nphoton.2015.201

35. Marrucci L, Manzo C, Paparo D. Optical spin-to-orbital angular momentum conversion in inhomogeneous anisotropic media. *Phys Rev Lett* (2006) 96(16):163905. doi:10.1103/PhysRevLett.96.163905

36. Luo H, Wen S, Shu W, Fan D. Spin-to-orbital angular momentum conversion in spin Hall effect of light. *Opt Commun* (2012) 285(6):864–71. doi:10.1016/j.optcom.2011.10.014

37. Nechayev S, Eismann JS, Leuchs G, Banzer P. Orbital-to-spin angular momentum conversion employing local helicity. *Phys Rev B* (2019) 99(7):075155. doi:10.1103/PhysRevB.99.075155

38. Shi P, Du L, Yuan X. Spin photonics: From transverse spin to photonic skyrmions. *Nanophotonics* (2021) 10(16):3927–43. doi:10.1515/nanoph-2021-0046

39. Toyoda K, Miyamoto K, Aoki N, Morita R, Omatsu T. Using optical vortex to control the chirality of twisted metal nanostructures. *Nano Lett* (2012) 12(7):3645–9. doi:10.1021/nl301347j

40. Simpson NB, Dholakia K, Allen L, Padgett MJ. Mechanical equivalence of spin and orbital angular momentum of light: An optical spanner. *Opt Lett* (1997) 22(1):52–4. doi:10.1364/OL.22.000052

41. Shvedov V, Davoyan AR, Hnatovsky C, Engheta N, Krolikowski W. A long-range polarization-controlled optical tractor beam. *Nat Photon* (2014) 8(11):846–50. doi:10.1038/nphoton.2014.242

42. Paez-Lopez R, Ruiz U, Arrizon V, Ramos-Garcia R. Optical manipulation using optimal annular vortices. *Opt Lett* (2016) 41(17):4138–41. doi:10.1364/OL.41.004138

43. Gahagan KT, Swartzlander GA. Optical vortex trapping of particles. *Opt Lett* (1996) 21(11):827–9. doi:10.1364/OL.21.000827

44. Dienerowitz M, Mazilu M, Reece PJ, Krauss TF, Dholakia K. Optical vortex trap for resonant confinement of metal nanoparticles. *Opt Express* (2008) 16(7):4991–9. doi:10.1364/OE.16.004991

45. Kim WC, Park NC, Yoon YJ, Choi H, Park YP. Investigation of near-field imaging characteristics of radial polarization for application to optical data storage. *Opt Rev* (2007) 14(4):236–42. doi:10.1007/s10043-007-0236-5

46. Ouyang X, Xu Y, Xian M, Feng Z, Zhu L, Cao Y, et al. Synthetic helical dichroism for six-dimensional optical orbital angular momentum multiplexing. *Nat Photon* (2021) 15:901–7. doi:10.1038/s41566-021-00880-1

47. Yan L, Gregg P, Karimi E, Rubano A, Marrucci L, Boyd R, et al. Q-plate enabled spectrally diverse orbital-angular-momentum conversion for stimulated emission depletion microscopy. *Optica* (2015) 2(10):900–3. doi:10.1364/OPTICA.2.000900

48. Gao J, Yan S, Zhou Y, Liang G, Zhang Z, Wen Z, et al. Polarization-conversion microscopy for imaging the vectorial polarization distribution in focused light. *Optica* (2021) 8(7):984–94. doi:10.1364/OPTICA.422836

49. Wang J, Yang J, Fazal IM, Ahmed N, Yan Y, Huang H, et al. Terabit free-space data transmission employing orbital angular momentum multiplexing. *Nat Photon* (2012) 6(7):488–96. doi:10.1038/nphoton.2012.138

50. Willner AE, Huang H, Yan Y, Ren Y, Ahmed N, Xie G, et al. Optical communications using orbital angular momentum beams. *Adv Opt Photon* (2015) 7(1):66–106. doi:10.1364/AOP.7.000066

51. Brunet C, Rusch LA. Optical fibers for the transmission of orbital angular momentum modes. *Opt Fiber Tech* (2017) 35:2–7. doi:10.1016/j.yofte.2016.09.016

52. Willner AE, Liu C. Perspective on using multiple orbital-angular-momentum beams for enhanced capacity in free-space optical communication links. *Nanophotonics* (2021) 10(1):225–33. doi:10.1515/nanoph-2020-0435

53. Banzer P, Neugebauer M, Aiello A, Marquardt C, Lindlein N, Bauer T, et al. The photonic wheel: Demonstration of a state of light with purely transverse angular momentum. *arXiv preprint* arXiv: 1210.1772 (2012). doi:10.48550/arXiv.1210.1772

54. Zhu W, She W. Transverse angular momentum and transverse barycenter shift of a focused light field due to nonuniform input angular momentum. *Opt Lett* (2014) 39(6):1337–40. doi:10.1364/OL.39.001337

55. Zhu W, Shvedov V, She W, Krolikowski W. Transverse spin angular momentum of tightly focused full Poincaré beams. *Opt Express* (2015) 23(26):34029–41. doi:10.1364/OE.23.034029

56. Li M, Yan S, Liang Y, Zhang P, Yao B. Transverse spinning of particles in highly focused vector vortex beams. *Phys Rev A* (2017) 95(5):053802. doi:10.1103/PhysRevA.95.053802

57. Zhang X, Shen B, Zhu Z, Rui G, He J, Cui Y, et al. Understanding of transverse spin angular momentum in tightly focused linearly polarized vortex beams. *Opt Express* (2022) 30(4):5121–30. doi:10.1364/OE.449583

58. Bliokh KY, Bekshaev AY, Nori F. Dual electromagnetism: Helicity, spin, momentum and angular momentum. *New J Phys* (2013) 15(3):033026. doi:10.1088/1367-2630/15/3/033026

59. Han L, Liu S, Li P, Zhang Y, Cheng H, Zhao J. Catalystlike effect of orbital angular momentum on the conversion of transverse to three-dimensional spin states within tightly focused radially polarized beams. *Phys Rev A* (2018) 97(5):053802. doi:10.1103/PhysRevA.97.053802

60. Li M, Cai Y, Yan S, Liang Y, Zhang P, Yao B. Orbit-induced localized spin angular momentum in strong focusing of optical vectorial vortex beams. *Phys Rev A* (2018) 97(5):053842. doi:10.1103/PhysRevA.97.053842

61. Meng P, Man Z, Konijnenberg AP, Urbach HP. Angular momentum properties of hybrid cylindrical vector vortex beams in tightly focused optical systems. *Opt Express* (2019) 27(24):35336–48. doi:10.1364/OE.27.035336

62. Li M, Yan S, Yao B, Liang Y, Zhang P. Spinning and orbiting motion of particles in vortex beams with circular or radial polarizations. *Opt Express* (2016) 24(18):20604–12. doi:10.1364/OE.24.020604

63. Chen R, Chew K, Dai C, Zhou G. Optical spin-to-orbital angular momentum conversion in the near field of a highly nonparaxial optical field with hybrid states of polarization. *Phys Rev A* (2017) 96(5):053862. doi:10.1103/PhysRevA.96.053862

64. Hu K, Chen Z, Pu J. Tight focusing properties of hybridly polarized vector beams. *J Opt Soc Am A* (2012) 29(6):1099–104. doi:10.1364/JOSAA.29.001099

65. Huang S, Zhang G, Wang Q, Wang M, Tu C, Li Y, et al. Spin-to-orbital angular momentum conversion via light intensity gradient. *Optica* (2021) 8(9):1231–6. doi:10.1364/OPTICA.435475

66. Yu P, Liu Y, Wang Z, Li Y, Gong L. Interplay between spin and orbital angular momenta in tightly focused higher-order Poincaré sphere beams. *Ann Phys* (2020) 532(8):2000110. doi:10.1002/andp.202000110

67. Wang X, Chen J, Li Y, Ding J, Guo C, Wang H. Optical orbital angular momentum from the curl of polarization. *Phys Rev Lett* (2010) 105(25):253602. doi:10.1103/PhysRevLett.105.253602

68. Shi P, Yang A, Meng F, Chen J, Zhang Y, Xie Z, et al. Optical near-field measurement for spin-orbit interaction of light. *Prog Quan Electron* (2021) 78:100341. doi:10.1016/j.pquantelec.2021.100341

69. Rodríguez-Herrera OG, Lara D, Bliokh KY, Ostrovskaya EA, Dainty C. Optical nanoprobing via spin-orbit interaction of light. *Phys Rev Lett* (2010) 104(25):253601. doi:10.1103/PhysRevLett.104.253601

frontiers | Frontiers in Physics

TYPE Brief Research Report
PUBLISHED 30 November 2022
DOI 10.3389/fphy.2022.1080275

OPEN ACCESS

EDITED BY
Zhenxu Bai,
Hebei University of Technology, China

REVIEWED BY
Xingtao Chen,
Nanchang University, China
Wang Pengyuan,
Dalian Institute of Chemical Physics (CAS), China
Shibo Dai,
Jinan University, China
Yuan Liu,
University of California, Santa Barbara, United States

*CORRESPONDENCE
Yu Shen,
shenyu@mail.ipc.ac.cn
Qi Bian,
bianqi@mail.ipc.ac.cn

SPECIALTY SECTION
This article was submitted to Optics and Photonics, a section of the journal Frontiers in Physics

RECEIVED 26 October 2022
ACCEPTED 14 November 2022
PUBLISHED 30 November 2022

CITATION
Chang J-Q, Shen Y, Bian Q, Zong N, Lv Z, Bo Y and Peng Q-J (2022), An exceed 60% efficiency Nd:YAG transparent ceramic laser with low attenuation loss effect.
Front. Phys. 10:1080275.
doi: 10.3389/fphy.2022.1080275

An exceed 60% efficiency Nd:YAG transparent ceramic laser with low attenuation loss effect

Jin-Quan Chang[1,2,3], Yu Shen[1,2]*, Qi Bian[1,2]*, Nan Zong[1,2], Ze Lv[1,2,3], Yong Bo[1,2] and Qin-Jun Peng[1,2]

[1]Key Lab of Solid State Laser, Technical Institute of Physics and Chemistry, Chinese Academy of Sciences, Beijing, China, [2]Key Lab of Function Crystal and Laser Technology, Technical Institute of Physics and Chemistry, Chinese Academy of Sciences, Beijing, China, [3]University of Chinese Academy of Sciences, Beijing, China

Here, the attenuation loss effect and laser performance enhancement of Nd:YAG transparent ceramics were investigated. Using a 0.6 at.% Nd:YAG ceramic rod of 3 mm diameter and 65 mm length, the scattering coefficient and absorption coefficient at 1,064 nm were measured to be 0.0001 cm^{-1} and 0.0017 cm^{-1}, respectively. For the 808-nm side-pumped laser experiment, an average output power of 44.9 W was achieved with an optical-to-optical conversion efficiency of 26.4%, which was nearly the same with that of a 1 at% single crystal. Adopting the 885-nm direct end-pumped scheme, the following laser tests demonstrated a high optical efficiency of 62.5% and maximum output power of 144.8 W obtained at an absorbed pump power of 231.5 W. This was until now the highest optical conversion efficiency acquired in an Nd:YAG ceramic laser to our knowledge. It proves that high-power and high-efficiency laser output could be generated by a high-optical quality Nd:YAG ceramic rod along with the 885-nm direct pumping technology.

KEYWORDS

attenuation loss, side-pumped, end-pumped, Nd:YAG ceramic laser, optical conversion efficiency

Introduction

Polycrystalline transparent ceramic materials have become an attractive alternative to widely used single crystals because of their favorable characteristics, such as higher doping concentration, larger scale, more function design freedom, easier manufacture, low cost, and especially superior resistance to fracture [1]. Since an effective laser output with polycrystalline Nd:YAG ceramics was first performed in 1995 [2], numerous attempts have been made in the field of high-power and high-efficiency Nd:YAG ceramic solid-state lasers. These include the output power breaking the 1 kW mark in 2002 and then the remarkable demonstration of more than 100 kW from a YAG ceramic laser system in 2009 [3]. Also, for middle- and high-power laser oscillation, increased optical conversion efficiencies from 14.5% to 52.5% have been reported one by one [4–7]. Among the important milestones, the gain medium with high optical quality is the key factor for highly efficient laser oscillation. Therefore, optical properties including optical

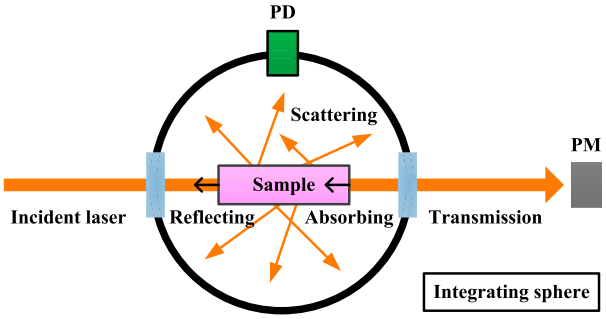

FIGURE 1
Experimental schematic diagram for the scattering coefficient measurements.

absorption, emission spectra, and fluorescence lifetime have been widely studied for Nd:YAG ceramics [8–10], and very similar results were obtained with those of Nd:YAG single crystals. However, the well-known attenuation loss that has enormous influence on the laser performance is rarely available.

Attenuation loss mainly includes the scattering and absorption effect caused by residual pores, grain boundary phases, secondary phases, and impurity ions, which will prohibit the laser output. In 1998, Ikesue et al. showed the scattering coefficients of Nd:YAG ceramics obtained from Fresnel's equation by an optical spectroscopy method [11]. Subsequently, Li et al. presented the absorption coefficients of Nd:YAG ceramics at the laser wavelength [12]. Unfortunately, they did not give a precise distinction between the scattering coefficients and the absorption coefficients. Recently, Boulesteix et al. computed the light scattering of Nd:YAG ceramics according to the Mie light scattering theory. However, the absorption effect was ignored [13]. Providing accurate measurement of the scattering and absorption coefficients could promote the material's research, such as laser experiments and fabrication technology.

This paper introduced an effective measured method of light attenuation loss by means of an integrating sphere technique, which is used to analyze the optical properties of the Nd:YAG ceramic and crystal. A 0.6 at.%-doped Nd:YAG ceramic sample has good optical quality with a scattering coefficient of 0.0001 cm^{-1} and an absorption coefficient of 0.0017 cm^{-1}. Here, an 808-nm laser diode (LD) side-pumped laser configuration was developed, delivering 26.4% of optical efficiency with 44.9 W of output power. Moreover, an end-pumped linear cavity with an 885-nm LD pump was designed to improve the optical conversion efficiency. As a result, a maximum output power of 144.8 W was obtained under the absorbed pump power of 231.5 W. The corresponding optical efficiency was calculated to be as high as 62.5%, which is a significant improvement for high-efficiency Nd:YAG ceramic lasers.

Absorption and scattering coefficient measurement

To assess the overall optical quality of the material, the measurements of light scattering and absorption were carried out at 1,064 nm, based on a homemade scattering loss analyzer with an integrating sphere. The measurement configuration is shown in Figure 1. When a laser beam is nearly at normal incidence upon the samples mounted in the center of the integrating sphere, part of the radiation is reflected, part is scattered, part is absorbed, and the rest is transmitted. The incident laser power was denoted to be P_{in}, and the scattering power and absorption power in the material were described as P_s and P_a, respectively. The transmission power passing through the samples was defined as P_T, and the Fresnel reflection coefficient of the front and back surfaces of the samples was denoted to be r. According to the law of Fresnel reflection and Lambert–Beer [14], the correlated relationship of the aforementioned power distributions can be written as

$$\begin{cases} P_T = (P_{in} - rP_{in} - P_a - P_s)(1-r) \\ P_a + P_s = P_{in}(1-r)\left[1 - \exp(-\alpha L)\right] \end{cases} \tag{1}$$

where α is the attenuation coefficient of the sample and L is the length of the sample. Considering the power loss along the beam propagation in the samples, it is evident that the scattering power P_s and absorption power P_a inside the sample are caused by the scattering and absorption mechanisms, respectively. Thus, we could obtain $\alpha = \alpha_a + \alpha_s$ and $P_a/P_s = \alpha_a/\alpha_s$, where α_a and α_s are the absorption coefficient and the scattering coefficient, respectively. After simplifying Eq. 1, we obtain

$$\begin{cases} \dfrac{P_T}{P_{in}} = (1-r)^2 - \dfrac{P_s}{P_{in}}\left(\dfrac{\alpha_a}{\alpha_s} + 1\right)(1-r) \\ \dfrac{P_s}{P_{in}}\left(\dfrac{\alpha_a}{\alpha_s} + 1\right) = (1-r)\{1 - \exp[-(\alpha_a + \alpha_s)L]\} \end{cases} \tag{2}$$

where P_{in} and P_T were measured by a power meter PM (NOVA II OPHIR). The scattered light intensity with and without the samples was collected using a calibrated photoelectric detector PD (Thorlabs Inc., DET200) mounted at the top of the integrating sphere, recorded as P_1 and P_2, respectively. Also, the output aperture of the integrating sphere was opened for measuring P_1 and closed for measuring P_2. Here, the value of P_s/P_{in} is equal to the ratio of P_1/P_2. By solving Eq. 2, the absorption coefficient α_a and the scattering coefficient α_s could be achieved.

In the measurement, two Nd:YAG ceramic samples with 0.6 at.% and 1.0 at.% doping concentrations and a Nd:YAG single crystal with 1.0 at.% doping concentration were employed, which were fabricated by the Nanyang Technological University. Each sample has a size of 3 mm diameter and 65 mm length, and both facets of samples are polished and antireflection-coated at 1,064 nm to reduce the surface reflection. Therefore, the reflectivity r at the surface of the sample is assumed to be about 0.1%.

TABLE 1 Measured values and correlative results at 1,064 nm of different samples.

Parameters	Samples		
	S1	S2	S3
Material	Ceramic	Ceramic	Crystal
Nd^{3+}-doped concentration (at%)	0.6	1.0	1.0
Ratio of transmittance (P_T/P_{in}, %)	0.986	0.981	0.987
Ratio of scattering (P_s/P_{in}, %)	0.0007	0.009	0.007
Scattering coefficient (α_s, cm^{-1})	0.0001	0.0014	0.0011
Absorption coefficient (α_a, cm^{-1})	0.0017	0.0012	0.0006
Attenuation coefficient (α, cm^{-1})	0.0018	0.0026	0.0017

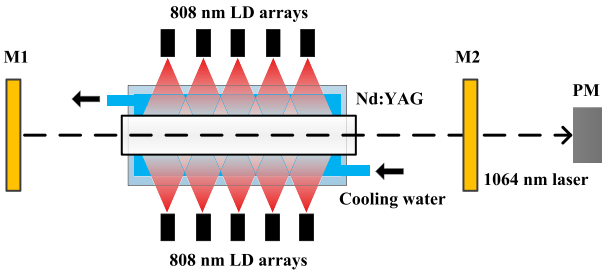

FIGURE 2
Experimental setup of the 808-nm LD side-pumped Nd:YAG laser.

Table 1 shows the corresponding scattering coefficient and absorption coefficient of each sample. Obviously, the crystal sample has the highest optical quality with the smallest attenuation coefficient of 0.0017 cm^{-1}, where the scattering coefficient and absorption coefficient were measured to be 0.0011 cm^{-1} and 0.0006 cm^{-1}, respectively. Compared with the 1 at.% Nd:YAG ceramic rod, the 0.6 at.% Nd:YAG ceramic rod with an attenuation loss of 0.0018 cm^{-1} is nearly the same as the single crystal, which could be easier to produce high-power laser output. In addition, the existence of low impurity ions during the preparation process is inevitable, which results in a large absorption coefficient with a same order of magnitude as the scattering coefficient and could not be neglected in the defects of the ceramic materials. The aforementioned data indicate that ceramic YAG is essentially identical to single-crystal YAG in optical properties measured, especially for the low scattering and absorption losses.

Laser experiment

In order to evaluate the laser performance of the ceramic samples compared with the Nd:YAG crystal, a compact flat–flat cavity was adopted, and the Nd:YAG ceramic was side-pumped with an LD at a wavelength of 808 nm for high pump absorption efficiency. The laser experimental configuration is shown in Figure 2. The samples were surrounded by arrays of diode lasers with a total pump power of 180 W. The Nd:YAG rod and LD arrays were cooled to 25°C with flowing deionized water to match the pump radiation wavelength of the LD and the 808.5 nm absorption spectrum of Nd:YAG. The mirror M1 was coated with high reflectance (HR) at 1,064 nm, and the mirror M2 was an output coupler with partial reflectivity of 80% at 1,064 nm. The 1,064 nm output power was monitored using the PM. The total cavity length is about 70 mm.

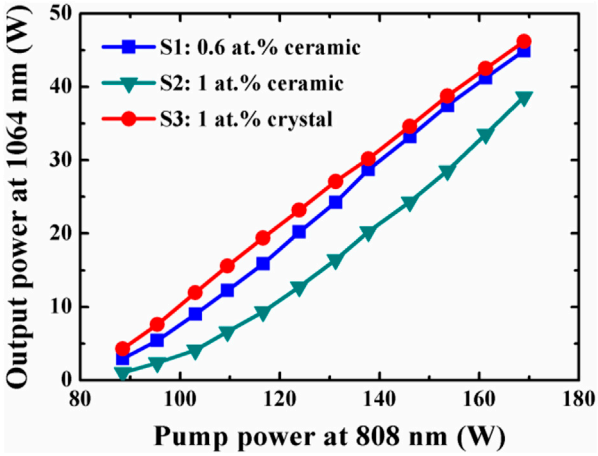

FIGURE 3
Output power of the 1,064-nm laser versus pump power at 808 nm.

The average laser output power of three Nd:YAG samples as a function of LD pump power at 808 nm is shown in Figure 3. The output power increases approximately linearly with the increase in pump power and does not show any roll-over effect, indicating that higher output can be achieved with increasing pump energy continuously. With maximum pump power of 170 W, 44.9 W and 46.2 W laser outputs were obtained at 1,064 nm for the 0.6 at.% Nd:YAG ceramic and 1 at.% Nd:YAG crystal, respectively. The corresponding optical-to-optical conversion efficiencies are 26.4% and 27.2%. The optical efficiency of the 0.6 at.% ceramic laser is only 0.8% less than that of the single-crystal laser, due to the difference in the absorbed pump power caused by different neodymium concentrations. It was proven, from the aspect of output power and laser efficiency, that the ceramic and crystal materials share almost the same laser characteristics. For the 1 at.%-doped ceramic sample, a laser output of 38.6 W was lower than that of the same doping concentration of the crystal because of the largest attenuation loss coefficient and serious thermal effect.

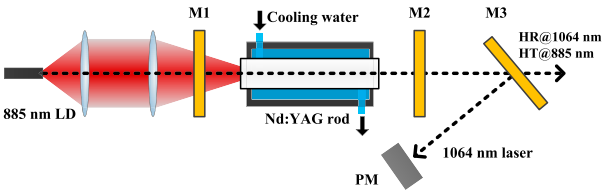

FIGURE 4
Experimental setup of 885-nm LD end-pumped Nd:YAG laser.

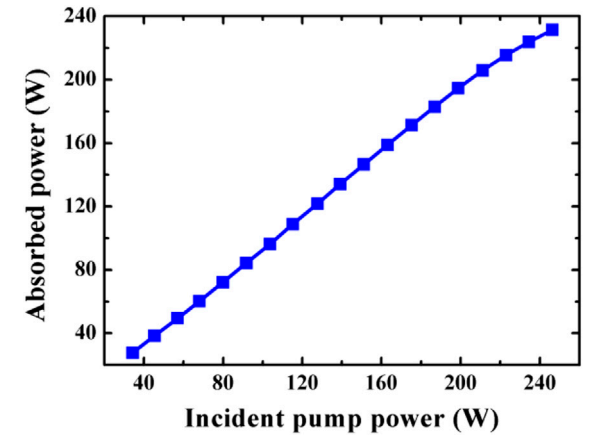

FIGURE 5
Absorbed power versus incident pump power at 885 nm.

The quantum defect between the pump and laser emission wavelength is one of the major factors that limit the LD-pumped solid-state lasers from generating high power and high efficiency [15]. Compared to traditional 808 nm pumping, adopting 885-nm diodes will have a reduction in the thermal load by nearly 30% and will thus lead to an improvement in the overall laser efficiency. The 0.6 at.% Nd:YAG ceramic rod was employed as the measured sample, and an end-pumped plane–plane linear cavity was designed. Figure 4 shows the schematic diagram of the laser oscillation measurement. An 885-nm fiber-coupled diode laser (DILAS, 400 μm diameter and 0.22 NA) was used as the pump source, delivering the maximum power of 250 W. It is focused into the ceramic sample using a coupling lens of 1:1. The laser sample was cooled by the re-circulating filtered water at 16°C, in order to effectively alleviate the thermal effect of the gain medium. The input mirror M1 was coated with a high-transmission film at a pump wavelength of 885 nm and an HR film at 1,064 nm. Also, the output coupler M2 has a transmission of 20% at 1,064 nm. The cavity length of the resonator is about 73 mm to keep the cavity mode in the sample matching the pump mode. The mirror M3 is adopted to separate the pump light and output laser.

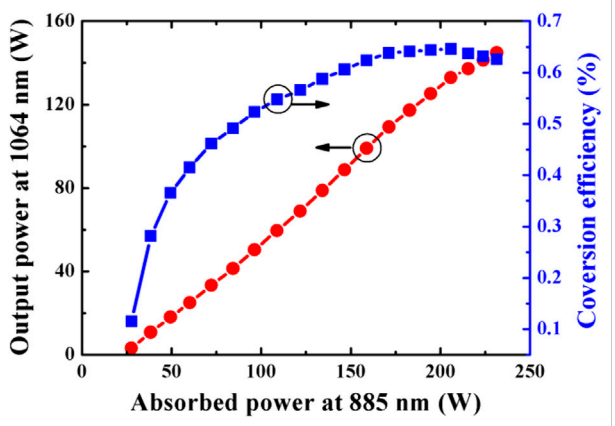

FIGURE 6
Output power of the 1,064-nm laser versus absorbed power at 885 nm.

The optical efficiency for a reasonable comparison could be calculated based on the absorbed pump power. First, the absorbed pump power was estimated by monitoring the pump power passing through the sample at different incident levels, as shown in Figure 5. The absorption power increased and the absorption coefficient decreased with increasing the input pump power. For instance, the absorption coefficient varied from 0.6 cm^{-1} to 0.43 cm^{-1} and corresponds to a pump absorption of 97.9% and 94%, which is attributed to the absorption saturation behavior of a lower doping concentration.

As shown in Figure 6, the output power at 1,064 nm increased linearly in accordance with the absorbed pump power. At the absorbed pump power of 231.5 W, the maximum output power was as high as 144.8 W, with a corresponding optical-to-optical conversion efficiency of 62.5%. The optical conversion efficiency versus absorbed pump power is also given in Figure 6. Actually, the maximum conversion efficiency of about 64.6% was obtained at 205 W of absorbed pumping. To the best of our knowledge, this is the highest optical conversion efficiency of all 1,064-nm laser systems with end-pumped laser modules. The main reason for achieving such high efficiency is the lower quantum defect for 885 nm pumping in combination with the effect of good mode matching and high pump absorption for an end-pumped scheme. The decrease in efficiency after 205 W was caused by the serious thermal effect on the laser ceramic rod for high-power operation.

Discussion and conclusion

In conclusion, the comparison of the laser performance of the Nd:YAG ceramics and crystal as well as attenuation loss are introduced and analyzed, based on an integrating sphere and

808-nm LD side-pumped laser experiment. As a result, the Nd:YAG ceramic could be processed to access almost identical optical properties with the single crystal. Moreover, a 0.6 at.% Nd:YAG ceramic rod was further investigated for producing high optical conversion efficiency, by means of 885-nm LD direct end-pumped technology. Under an absorbed power of 231.5 W, the maximum output power of 144.8 W was obtained with an optical efficiency of 62.5%, which is the highest efficiency the 1,064-nm Nd:YAG ceramic laser ever reported.

Data availability statement

The original contributions presented in the study are included in the article/supplementary material; further inquiries can be directed to the corresponding authors.

Author contributions

YS conceived the project. J-QC conducted the experiment. QB wrote the manuscript and all authors contributed to discussions during its preparation. YB and Q-JP supervised the project.

Funding

This work was Supported by the National Key Research and Development Program of China(key special projects, Young Scientist Program, No. 2022YFB3607900), Key Laboratory Foundation of Chinese Academy of Sciences, Key Lab of Solid State Laser(No. CXJJ-22S020), the National Science Foundation for Young Scientists of China (Grant No. 11504389, 51890864 and 62005295).

Conflict of interest

The authors declare that the research was conducted in the absence of any commercial or financial relationships that could be construed as a potential conflict of interest.

Publisher's note

All claims expressed in this article are solely those of the authors and do not necessarily represent those of their affiliated organizations, or those of the publisher, the editors, and the reviewers. Any product that may be evaluated in this article, or claim that may be made by its manufacturer, is not guaranteed or endorsed by the publisher.

References

1. Lupei V, Lupei A, Ikesue A. Transparent polycrystalline ceramic laser materials. *Opt Mater* (2008) 30(11):1781–6. doi:10.1016/j.optmat.2008.03.003

2. Ikesue A, Kinoshita T, Kamata K, Yoshida K. Fabrication and optical properties of high-performance polycrystalline Nd: YAG ceramics for solid-state lasers. *J Am Ceram Soc* (1995) 78(4):1033–40. doi:10.1111/j.1151-2916.1995.tb08433.x

3. Li J, Pan Y, Zeng Y, Liu W, Jiang B, Guo J. The history, development, and future prospects for laser ceramics: A review. *Int J Refractory Met Hard Mater* (2013) 39:44–52. doi:10.1016/j.ijrmhm.2012.10.010

4. Lu JLJ, Song JS, Prabhu M, Xu J, Ueda K, Yagi H, et al. High-power Nd: $Y_3Al_5O_{12}$ ceramic laser. *Jpn J Appl Phys* (2000) 39(10B):L1048–50. doi:10.1143/jjap.39.l1048

5. Qi Y, Zhu X, Lou Q, Ji J, Dong J, Wei Y. Nd: YAG ceramic laser obtained high slope-efficiency of 62% in high power applications. *Opt Express* (2005) 13(22):8725–9. doi:10.1364/opex.13.008725

6. Guo W, Cao Y, Huang Q, Li J, Huang J, Huang Z, et al. Fabrication and laser behaviors of Nd: YAG ceramic microchips. *J Eur Ceram Soc* (2011) 31(13):2241–6. doi:10.1016/j.jeurceramsoc.2011.05.020

7. Lapucci A, Ciofini M, Pucci M, D'Uva M. High efficiency, diode pumped 170 W Nd: YAG ceramic slab laser. *J Eur Opt Society-Rapid Publications* (2011) 6:11047. doi:10.2971/jeos.2011.11047

8. Lu J, Prabhu M, Xu J, Ueda K-I, Yagi H, Yanagitani T, et al. Highly efficient 2% Nd: Yttrium aluminum garnet ceramic laser. *Appl Phys Lett* (2000) 77(23):3707–9. doi:10.1063/1.1331091

9. Yagi YT, Takaichi K, Ueda K, Kaminskii AA. Characterizations and laser performances of highly transparent Nd^{3+}: $Y_3Al_5O_{12}$ laser ceramics. *Opt Mater* (2007) 29(10):1258–62. doi:10.1016/j.optmat.2006.01.033

10. Li J, Wu Y, Pan Y, Liu W, An L, Wang S, et al. Solid-state-reaction fabrication and properties of a high-doping Nd: YAG transparent laser ceramic. *Front Chem Eng China* (2008) 2(3):248–52. doi:10.1007/s11705-008-0048-6

11. Ikesue A, Yoshida K. Scattering in polycrystalline Nd: YAG lasers. *J Am Ceram Soc* (1998) 81(8):2194–6. doi:10.1111/j.1151-2916.1998.tb02607.x

12. Li J, Wu Y, Pan Y, Liu W, Huang L, Guo J. Fabrication, microstructure and properties of highly transparent Nd: YAG laser ceramics. *Opt Mater* (2008) 31(1):6–17. doi:10.1016/j.optmat.2007.12.014

13. Boulesteix R, Maitre A, Baumard JF, Rabinovitch Y, Reynaud F. Light scattering by pores in transparent Nd: YAG ceramics for lasers: Correlations between microstructure and optical properties. *Opt Express* (2010) 18(14):14992–5002. doi:10.1364/oe.18.014992

14. Deng W, Yang T, Cao J, Zang E, Li L, Chen L, et al. High-efficiency 1064 nm nonplanar ring oscillator Nd: YAG laser with diode pumping at 885 nm. *Opt Lett* (2018) 43(7):1562–5. doi:10.1364/ol.43.001562

15. Koechner W. *Solid-state laser engineering*, 1. Springer (2013).

frontiers | Frontiers in Physics

TYPE Brief Research Report
PUBLISHED 01 December 2022
DOI 10.3389/fphy.2022.1084594

OPEN ACCESS

EDITED BY
Zhi-Han Zhu,
Harbin University of Science and Technology, China

REVIEWED BY
Song Yang,
Technical University of Denmark, Denmark
Fei Wang,
Changchun University of Science and Technology, China

*CORRESPONDENCE
Zhenao Bai,
baizhenao@hotmail.com
Weiguo Wang,
wangwei5878@sina.com

SPECIALTY SECTION
This article was submitted to Optics and Photonics, a section of the journal Frontiers in Physics

RECEIVED 30 October 2022
ACCEPTED 22 November 2022
PUBLISHED 01 December 2022

CITATION
Zhang Z, Bai Z, Song X, Zhang Y, Liang B, Liu T and Wang W (2022), 178-W picosecond green laser with active beam-pointing stabilization. *Front. Phys.* 10:1084594. doi: 10.3389/fphy.2022.1084594

178-W picosecond green laser with active beam-pointing stabilization

Zhendong Zhang[1], Zhenao Bai[2]*, Xiaoquan Song[3], Yakai Zhang[4], Bo Liang[5], Tingxia Liu[1] and Weiguo Wang[1]*

[1]Changchun Institute of Optics, Fine Mechanics and Physics, Chinese Academy of Sciences, Changchun, China, [2]Aerospace Information Research Institute, Chinese Academy of Sciences, Beijing, China, [3]China Aerospace Academy of Systems Science and Engineering, Beijing, China, [4]Center for Advanced Laser Technology, Hebei University of Technology, Tianjin, China, [5]The Military Representative Office in Changchun of Military Representative Bureau of Space System Equipment Department, Changchun, China

Picosecond lasers with high average power and high beam quality have been widely used for precision processing and space exploration. In this study, we report a high-power picosecond green laser using a multistage Yb-doped rod-shaped photonic crystal fiber as an amplifier combined with a beam combination. The single amplification module achieves a 1,030 nm laser output of 146.8 W, and the maximum second harmonic generation (SHG) power is 92 W with a frequency conversion efficiency of 63.5%. The combined beam of the two SHGs resulted in a final output of 178 W with a repetition frequency of 24.07 MHz, pulse width of 50.1 ps, and beam quality factor of M^2 = 1.16. Furthermore, an adaptive filter control method of a two-axis fast-steering mirror was applied to suppress the beam jitter to up to 45 Hz.

KEYWORDS

photonic crystal fiber, picosecond amplifiers, second harmonic generation, beam jitter suppression, beam-pointing stabilization

Introduction

High-power laser sources with high beam quality and spectral diversity are of broad interest for various applications [1–5]. Among them, ultrashort pulse (picosecond and femtosecond) lasers are widely used in industrial processing, precision manufacturing, and waveguide etching because of their negligible heat-affected zones [6–10]. Compared to nanosecond pulses, picosecond lasers have a higher peak power that can control the processing depth and precision more effectively and greatly improve the processing quality [11–13]. Meanwhile, compared to femtosecond pulses, picosecond lasers achieve high-power output with higher stability easier [14–17]. In addition to achieving a high-power output, short-pulse lasers at specific wavelengths are also necessary for various applications. For example, the need for green picosecond pulsed lasers is also more widespread, as many materials in industrial processes absorb visible light more significantly than infrared light and in marine and space exploration, where the transmission medium absorbs less of the green wavelength [18–21]. Currently,

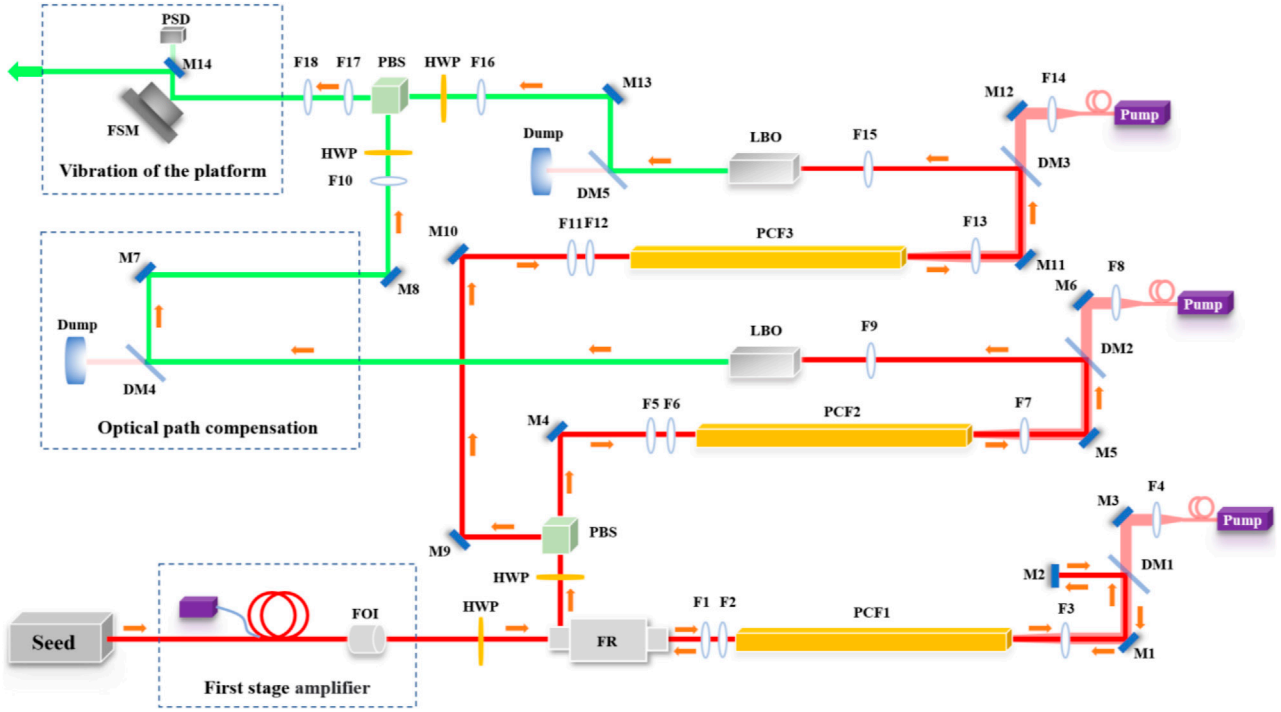

FIGURE 1
Schematic showing the layout of the laser system. FOI, fiber optic isolator; HWP, half-wave plate; FR, Faraday rotator; M, mirrors; F, focus lens; PBS, polarizing beam splitter. FSM, fast steering mirror; PSD, position sensitive detector.

picosecond pulses can be amplified by rod-tape photonic crystal fibers (PCF), which can achieve extremely high amplification efficiency, polarization preservation, and excellent beam quality output [22–24]. Its difference from traditional optical fiber, with its characteristics of cut-off-free single-mode transmission, adjustable dispersion, high birefringence, large mode area, and high nonlinearity coefficient, realizes single-mode transmission in the large mode field of optical fiber, which makes a breakthrough in high peak power transmission and amplification of optical fiber [24–26]. In addition, beam jitter is an issue that must be addressed to extend the application of lasers to moving platforms such as aircraft, ships, vehicles, and satellites [27, 28]. Beam jitter caused by engine vibration, atmospheric turbulence, and attitude changes severely limits the pointing performance of laser beams on moving platforms [29].

In this study, we report a picosecond amplification structure using a multi-stage Yb-doped rod-shaped PCF, divided into a two-stage pre-amplification and a one-stage main amplification structure. The single main amplification module finally achieves a 1,030 nm laser output of 146.8 W. The frequency doubling crystal is an LiB_3O_5(LBO) crystal, and the output second harmonic generation (SHG) wavelength was 514.2 nm with a maximum output power of 92 W. The conversion efficiency from 1,030 nm to 514.2 nm was 63.5%. The two SHGs were combined to obtain a final output of 178 W at 514.2 nm. The repetition frequency of the laser is 24.07 MHz, pulse duration is 50.1 ps, and beam quality factor M^2 is measured to be 1.16. An adaptive filtering control method is applied to suppress the beam jitter of a two-axis fast-steering mirror (FSM) to increase the output stability. The FSM, driven by a voice coil driver, is placed in the optical path in front of the laser exit to isolate the laser beam from the disturbance. Using a position-sensitive detector (PSD) as a beam deviation sensor, the system effectively suppresses laser beam jitter up to 45 Hz, resulting in a high pointing stability of 178 W green light output.

Experiment and results

The laser amplification and frequency doubling experimental setup are shown in Figure 1, which consists of a pre-amplification module, main amplification module, frequency doubling module, and optical range compensation module. The mode-locked fiber laser (EOAS-MLFL-P-50-22-1,030-50) outputs seeds with a repetition frequency of 22 ± 2 MHz, pulse duration of 50 ± 2.5 ps, and central wavelength of 1,030 ± 1 nm. The output seed light is amplified by a primary fiber prevention module, which aims to increase the efficiency of the photonic crystal fiber amplifier (PCFA) afterward. The amplified seed light then

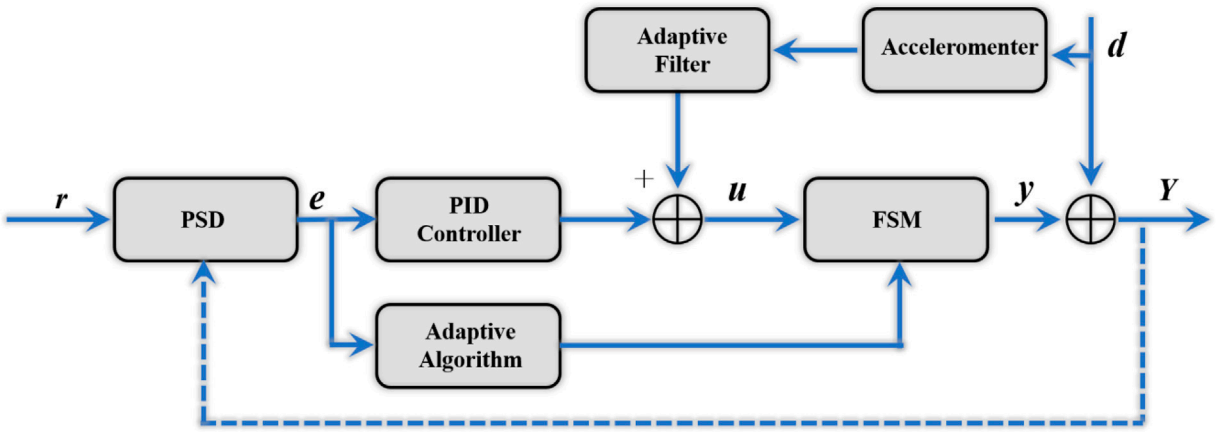

FIGURE 2
Controller schematic of adaptive in parallel with PID.

passes through the optical isolator as signal light into the secondary PCF preamplifier. In secondary pre-amplification, the signal light is collimated and focused by a coupling lens set and then injected into a rod-taped PCF, where the PCF is pumped by a fiber-coupled diode with a central wavelength of 976 nm, and the pumped light is collimated and focused into the PCF.

In the PCF (aeroGAIN-ROD-2.1, mode field diameter 65 ± 5 μm), the signal light receiving core diameter is approximately 85 μm, and after passing through the coupling lens set, the signal light matches the receiving core diameter by more than 90%. The pump light receiving diameter is 260 μm, and after passing through the coupling lens set, the pump light spot with a diameter of 200 μm and NA = 0.22 was injected into the PCF with a 1:1 coupling ratio to achieve 95% energy within 250 μm. After secondary pre-amplification, the 1,030 nm laser was split into two beams using a half-wave plate and a polarization splitting prism for respective amplification and frequency doubling. The split beam was first coupled through a coupling lens set to the PCF for single-pass amplification. The signal light and pump light coupling system of the rod-tape PCF was identical to that of the secondary preamplification module.

The signal light is amplified again and then passed through the focusing lens as the fundamental frequency light for frequency doubling. The frequency-doubling crystal was an LBO crystal (type I, 3 mm × 3 mm × 15 mm) with a combination of angle and temperature matching, a cut angle of $\theta = 90^{\circ}$, $\varphi = 12.6^{\circ}$, and a corresponding temperature of 55°C. The advantage of this is that the best matching efficiency can be obtained while avoiding strong convection owing to large temperature gradients, which can affect the output light stability. A dichroic mirror was then used to separate 1,030 nm from the SHG, which was collected by a collector, and the SHG was then combined. Before the beam combining process, one of the beams needs to be compensated for the optical range to match the temporal overlap of the two beams. After passing through a collimating lens and half-wave, the two SHGs are combined in a polarizing beam-splitting prism and then collimated and expanded into the beam jitter suppression module.

Beam jitter suppression experiments were performed after the green laser was output. The experimental optical path is shown in Figure 1, where a two-axis FSM driven by a voice coil driver is placed in the optical path behind the laser exit, with the laser placed on a jitter platform. A small portion of the laser beam was split into the PSD by adding a semi-transparent and semi-reflective mirror to the beam path. By using the PSD as a beam deviation sensor, the FSM effectively suppresses laser beam dithering. The controller program design is shown in Figure 2. The principle is that when the system is switched on, the reference signal contains a large direct-current component, which can destabilize the adaptive filter. Therefore, a proportional-integral-derivative (PID) controller was adopted in parallel with the adaptive filter to stabilize the entire controller. As shown in Figure 2, once the PID controller is connected in parallel with the adaptive filter, the initial bias error is eliminated, and the adaptive filter works properly. In the experiment, the vibration platform generated a broadband disturbance signal with a frequency of 0–50 Hz to test the stabilization effect of the controller.

In our experiment, the signal power after the second-stage pre-amplification was 80 W, and the pump power was 162 W. In one of the main amplification stages, the output power increased linearly as the pump power increased, and the conversion efficiency first increased and then plateaued, as shown in Figure 3A. At the maximum pump power of 360 W,

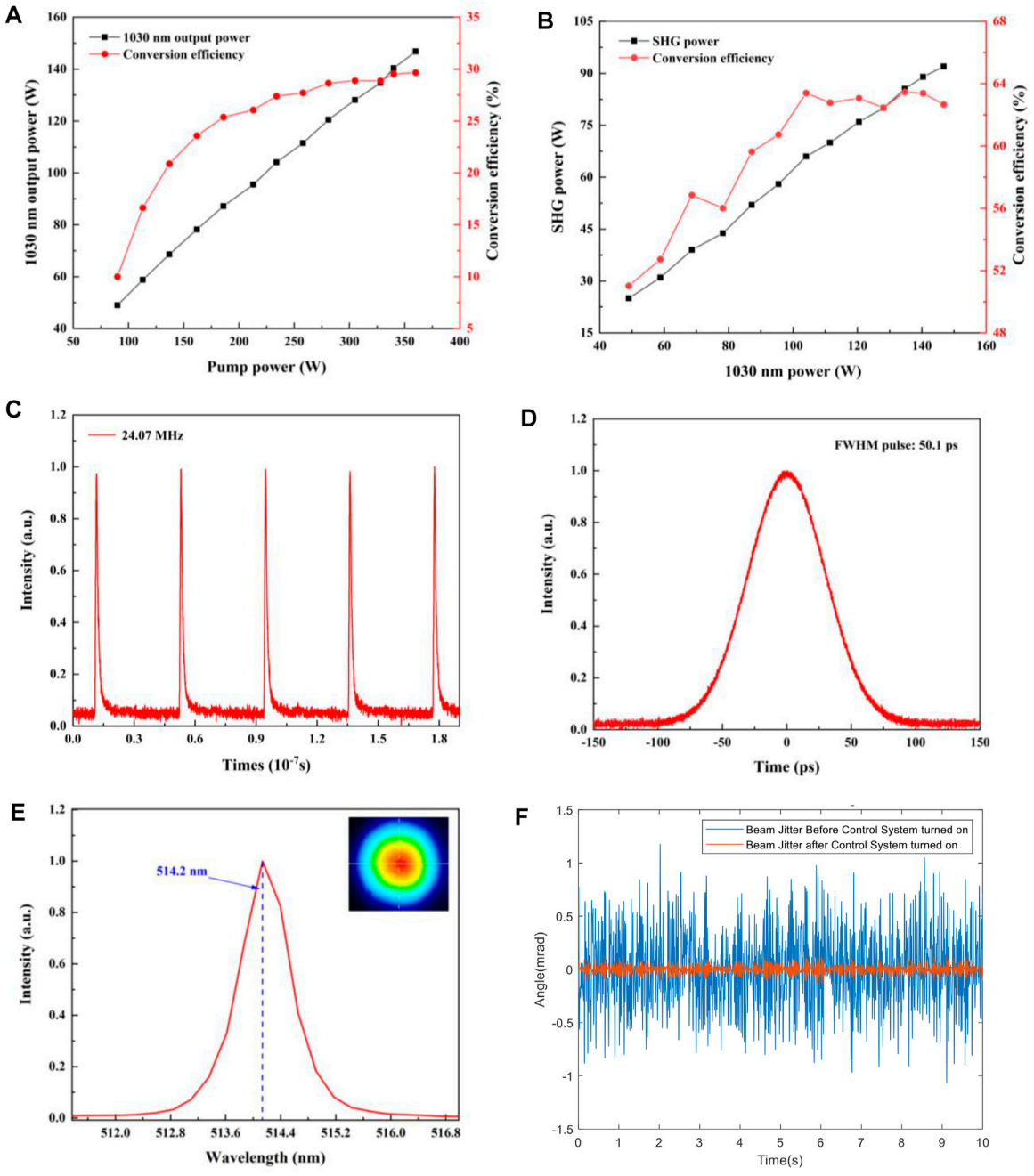

FIGURE 3
Compilation of output characteristics of the green laser. **(A)** 1,030 nm output power plotted against the pump power; **(B)** output SHG power at 512 nm plotted against the 1,030 nm input power; **(C)** Normalized pulse characteristics of the output with a close-up shown inset; **(D)** temporal characteristic of a single output pulse with an autocorrelation trace; **(E)** normalized wavelength spectrum of the amplified laser output; **(F)** Beam jitter before and after control system turned on.

maximum power of 146.8 W was obtained for the 1,030 nm output with an optical-to-optical conversion efficiency of 29.7%. By designing the coupling lens set for the signal and pump lights, more signal light can enter the fiber bar core, which can effectively suppress amplified spontaneous emission (ASE) and enable the fiber bar to obtain a higher gain, while a good coupling spot can also effectively improve the quality of the amplified beam. The output power of the amplification device has not yet reached saturation, and there is room for further improvement owing to the pumping power of the diode. Figure 3B shows the

output power curve of the SHG with the pump power. From the figure, it can be observed that the output power of the second harmonic increases as the pump power increases, and the maximum power of 92 W is obtained at the 1,030 nm power of 146.8 W for SHG output. The frequency conversion efficiency increases first, saturating at a 1,030 nm power of 104.1 W. The highest conversion efficiency occurs at the pumping power of 134.7 W, with a conversion efficiency of 63.5%. Subsequently, as the power increased, the efficiency decreased slightly, although the output power increased. This is partly due to the broadening of the 1,030 nm spectrum caused by the increase in laser power, partly due to the change in the divergence angle of the amplified beam, and partly due to the increased thermal effect of the doubled crystal caused by the increase in power. However, the results of the experiments were approximately the same as those mentioned above. At the maximum pump power of 360 W, 131 W of 1,030 nm laser output was output, and after the frequency-doubling crystal, 86 W of SHG was output, with a frequency doubling efficiency of 65.6%. The two frequency-doubled beams were combined to obtain a laser output of 178 W at 514 nm. The final output frequency of the SHG was 24.07 MHz with a pulse width of 50.1 ps, as shown in Figures 3C,D. The spectra measured using the spectrometer are shown in Figure 3E. The central wavelength was 514.2 nm. In the case of amplification, the fundamental mode signal light in the core is fully amplified owing to the cut-off-free single-mode characteristics of the fiber rod, whereas the light escaping into the cladding is not amplified. A larger core-cladding power ratio results in a higher beam quality of the output light, $M^2 = 1.16$. The vibration platform generated a broadband disturbance signal with frequencies ranging from 0 Hz to 50 Hz. With the use of the jitter suppression system, the jitter was effectively suppressed by approximately 18.4 dB, as shown in Figure 3F.

Conclusion

In this study, the seed light was amplified using a multi-stage rod-tape photonic crystal fiber, and a two-way amplification structure was incorporated to reduce the effect of thermal effects on the output light. The coupling system in the amplification module was designed independently to achieve mode-matching. The single amplification module achieves a 1,030 nm laser output of 146.8 W, and the maximum second harmonic generation (SHG) power is 92 W with a frequency conversion efficiency of 63.5%. After combining the beams, a green laser of 514.2 nm with a repetition frequency of 24.07 MHz, pulse width of 50.1 ps, and power of 178 W was output, with $M^2 = 1.16$. An adaptive filter control method for beam jitter suppression with a two-axis FSM was also applied to suppress laser beam jitter up to 45 Hz. The results can be used as a reference for the future realization of highly stable and miniaturized green picosecond pulsed lasers in the 100 W or even kW class for stable operation on mobile platforms.

Data availability statement

The raw data supporting the conclusion of this article will be made available by the authors, without undue reservation.

Author contributions

ZZ, Investigation, data analysis, and Writing-original draft preparation. ZB, Conceptualization, data analysis, Writing-review and editing, and funding acquisition. XS, Writing-review and editing. YZ, data analysis, Writing-original draft preparation, and Writing-review and editing. BL, Writing-review and editing. TL, Writing-review and editing. WW, Conceptualization and Supervision. All authors have read and agreed to the published version of the manuscript.

Funding

This work was supported by the Guangdong Key Research and Development Program (2018B090904003).

Conflict of interest

The authors declare that the research was conducted in the absence of any commercial or financial relationships that could be construed as a potential conflict of interest.

Publisher's note

All claims expressed in this article are solely those of the authors and do not necessarily represent those of their affiliated organizations, or those of the publisher, the editors and the reviewers. Any product that may be evaluated in this article, or claim that may be made by its manufacturer, is not guaranteed or endorsed by the publisher.

References

1. Jackson SD. Towards high-power mid-infrared emission from a fibre laser. *Nat Photon* (2012) 6(7):423–31. doi:10.1038/nphoton.2012.149

2. Fan ZW, Qiu JS, Kang ZJ, Chen YZ, Ge WQ, Tang XX. High beam quality 5 J, 200 Hz Nd: YAG laser system. *Light Sci Appl* (2017) 6(3):e17004. doi:10.1038/lsa.2017.4

3. Chen H, Bai Z, Yang X, Ding J, Qi Y, Yan B, et al. Enhanced stimulated Brillouin scattering utilizing Raman conversion in diamond. *Appl Phys Lett* (2022) 120(18):181103. doi:10.1063/5.0087092

4. Bai Z, Zhao Z, Tian M, Jin D, Pang Y, Li S, et al. A comprehensive review on the development and applications of narrow-linewidth lasers. *Microw Opt Technol Lett* (2022) 64(12):2244–55. doi:10.1002/mop.33046

5. Jin D, Bai Z, Lu Z, Fan R, Zhao Z, Yang X, et al. 22.5-W narrow-linewidth diamond Brillouin laser at 1064 nm. *Opt Lett* (2022) 47(20):5360–3. doi:10.1364/ol.471447

6. Wang X, Li C, Hong W, Ma C, Xing Y, Feng J. Fabrication of ordered hierarchical structures on stainless steel by picosecond laser for modified wettability applications. *Opt Express* (2018) 26(15):18998–9008. doi:10.1364/oe.26.018998

7. Esmail I, Yazdan Sarvestani H, Gholipour J, Ashrafi B. Engineered net shaping of alumina ceramics using picosecond laser. *Opt Laser Tech* (2021) 135:106669. doi:10.1016/j.optlastec.2020.106669

8. Qin Z, Ai J, Du Q, Liu J, Zeng X. Superhydrophobic polytetrafluoroethylene surfaces with accurately and continuously tunable water adhesion fabricated by picosecond laser direct ablation. *Mater Des* (2019) 173:107782. doi:10.1016/j.matdes.2019.107782

9. Guo B, Sun J, Lu Y, Jiang L. Ultrafast dynamics observation during femtosecond laser-material interaction. *Int J Extrem Manuf* (2019) 1(3):032004. doi:10.1088/2631-7990/ab3a24

10. Bai Z, Chen H, Gao X, Li S, Qi Y. Highly compact nanosecond laser for space debris tracking. *Opt Mater* (2019) 98:109470. doi:10.1016/j.optmat.2019.109470

11. Chichkov BN, Momma C, Nolte S, Alvensleben F, Tunnermann A. Femtosecond, picosecond, and nanosecond laser ablation of solids. *Appl Phys A Mater Sci Process* (1996) 63(2):109–15. doi:10.1007/bf01567637

12. Bai Z, Bai Z, Kang Z, Lian F, Lin W, Fan Z. Non-pulse-leakage 100-kHz level, high beam quality industrial grade Nd: YVO_4 picosecond amplifier. *Appl Sci* (2017) 7(6):615. doi:10.3390/app7060615

13. Qi Y, Yang S, Wang J, Li L, Bai Z, Wang Y, et al. Recent advance of emerging low-dimensional materials for vector soliton generation in fiber lasers. *Mater Today Phys* (2022) 23:100622. doi:10.1016/j.mtphys.2022.100622

14. Zhang Q, Zhao Y, Wei Z. Sub-10 fs laser pulses with repetition rate of 1.1 GHz by a Ti: Sapphire oscillator. *Chin Sci Bull* (2009) 54(20):3649–52. doi:10.1007/s11434-009-0191-6

15. Eckerle M, Dietrich T, Schaal F, Pruss C, Osten W, Ahmed MA, et al. Novel thin-disk oscillator concept for the generation of radially polarized femtosecond laser pulses. *Opt Lett* (2016) 41(7):1680–3. doi:10.1364/ol.41.001680

16. Li K, Wang Y, Yu Y, Yue J, Song C, Cao C, et al. Amplification of high repetition-rate, picosecond laser pulses using a zig-zag slab configuration. *Opt Laser Tech* (2023) 157:108717. doi:10.1016/j.optlastec.2022.108717

17. Hubka Z, Antipenkov R, Boge R, Erdman E, Greco M, Green JT, et al. 120 mJ, 1 kHz, picosecond laser at 515 nm. *Opt Lett* (2021) 46(22):5655–8. doi:10.1364/ol.440448

18. Peng R, Guo L, Zhang X, Li F, Cui Q, Bo Y, et al. 43W picosecond laser and second-harmonic generation experiment. *Opt Commun* (2009) 282(4):611–3. doi:10.1016/j.optcom.2008.10.049

19. Wang W, Liu J, Chen F, Li L, Wang Y. 532-nm picosecond pulse generated in a passively mode-locked Nd:YVO_4 laser. *Chin Opt Lett* (2009) 7(8):706–8. doi:10.3788/col20090708.0706

20. Cai Y, Gao F, Chen H, Yang X, Bai Z, Qi Y, et al. Continuous-wave diamond laser with a tunable wavelength in orange-red wavelength band. *Opt Commun* (2023) 528:128985. doi:10.1016/j.optcom.2022.128985

21. Bai Z, Williams RJ, Kitzler O, Sarang S, Spence DJ, Wang Y, et al. Diamond Brillouin laser in the visible. *APL Photon* (2020) 5(3):031301. doi:10.1063/1.5134907

22. Zheltikov A. High-peak-power nonlinear-optical processes in photonic crystal fibers. In: *Proceedings of the conference on lasers and electro-optics/quantum electronics and laser science conference and photonic applications systems technologies*. California: Long BeachOptica Publishing Group (2006). F 2006/05/21[C].

23. Boullet J, Zaouter Y, Desmarchelier R, Cazaux M, Salin F, Saby J, et al. High power ytterbium-doped rod-type three-level photonic crystal fiber laser. *Opt Express* (2008) 16(22):17891–902. doi:10.1364/oe.16.017891

24. Chen H, Bai Z, Wang J, Zhang B, Bai Z. Hundred-watt green picosecond laser based on LBO frequency-doubled photonic crystal fiber amplifier. *Infrared Laser Eng* (2021) 50(11):20200522. doi:10.3788/irla20200522

25. Reena D, Saini TS, Kumar A, Kalra Y, Sinha RK. Rectangular-core large-mode-area photonic crystal fiber for high power applications: Design and analysis. *Appl Opt* (2016) 55(15):4095–100. doi:10.1364/ao.55.004095

26. Limpert J, Schmidt O, Rothhardt J, Roser F, Schreiber T, Tunnermann A, et al. Extended single-mode photonic crystal fiber lasers. *Opt Express* (2006) 14(7):2715–20. doi:10.1364/oe.14.002715

27. Shi H, Song Y, Liang F, Xu L, Hu M, Wang C. Effect of timing jitter on time-of-flight distance measurements using dual femtosecond lasers. *Opt Express* (2015) 23(11):14057–69. doi:10.1364/oe.23.014057

28. Serafino G, Ghelfi P, Pérez-millán P, Villanueva GE, Palaci J, Cruz JL, et al. Phase and amplitude stability of EHF-band radar carriers generated from an active mode-locked laser. *J Lightwave Technol* (2011) 29(23):3551–9. doi:10.1109/jlt.2011.2170811

29. Hu S, Yu H, Duan Z, Zhu Y, Cao C, Zhou M, et al. Multi-parameter influenced acquisition model with an in-orbit jitter for inter-satellite laser communication of the LCES system. *Opt Express* (2022) 30(19):34362–77. doi:10.1364/oe.465592

frontiers | Frontiers in Physics

TYPE Brief Research Report
PUBLISHED 01 December 2022
DOI 10.3389/fphy.2022.1093179

OPEN ACCESS

EDITED BY
Zhenxu Bai,
Hebei University of Technology, China

REVIEWED BY
Xiaobo Hu,
Zhejiang Sci-Tech University, China
Xiaotao Mi,
Changchun Institute of Optics (CAS), China

*CORRESPONDENCE
Liwen Sheng,
shengliwen2008@163.com
Lin Huang,
huanglin@ceyear.com

SPECIALTY SECTION
This article was submitted to Optics and Photonics, a section of the journal Frontiers in Physics

RECEIVED 08 November 2022
ACCEPTED 21 November 2022
PUBLISHED 01 December 2022

CITATION
Zhang A, Qiao S, Sheng L, Huang L, Liu Z, Ju J, Zhang Z, Yin B, Li P, Liu J and Wei Y (2022), Study on external cavity diode laser with a wide mode-hopping free tuning range.
Front. Phys. 10:1093179.
doi: 10.3389/fphy.2022.1093179

Study on external cavity diode laser with a wide mode-hopping free tuning range

Aiguo Zhang[1], Shan Qiao[1], Liwen Sheng[1,2,3]*, Lin Huang[1,2,4]*, Zhiming Liu[1], Junwei Ju[1], Zhihui Zhang[1], Bingqi Yin[1], Peng Li[1], Jiaqing Liu[1,2] and Yu Wei[1]

[1]Ceyear Technologies Co., Ltd, Qingdao, China, [2]Science and Technology on Electronic Test and Measurement Laboratory, Qingdao, China, [3]School of Electronic Engineering, Xidian University, Xi'an, China, [4]School of Information Science and Engineering, Shandong University, Qingdao, China

A wide mode-hopping free and narrow linewidth tunable laser diode source with a Littman-Metcalf arrangement based on a diffraction grating is presented. Several experiments are carried out to demonstrate the tuning characteristics and spectral linewidth of the proposed external-cavity diode laser source. A wide no mode-hopping continuous wavelength tuning range about 59.13 nm in ultra-C-band with a narrow spectral linewidth of less than 100 kHz is obtained. An optical signal to noise ratio of more than 65 dB and an output power more than 14.8 dBm over the whole tuning range can also be realized in a long-term free running condition. The proposed tunable laser allows simultaneously mode-hopping free and narrow linewidth tunable radiation, thus opening a door for practical application such as coherent detection.

KEYWORDS

tunable laser, mode-hopping free, littman-metcalf arrangement, narrow linewidth, coherent detection

Introduction

Compared to most other types of tunable laser (e.g., distributed Bragg reflector laser, vertical cavity surface emitting laser, and distributed feedback laser), external cavity diode laser (ECDL) has been broadly studied and acted as a prior selected laser source for its prestigious characteristics such as narrow linewidth, broad wavelength tuning range, single mode, and compactness. It therefore makes the ECDL a versatile measuring tool for many applications in fields including optical frequency-domain reflectometry (OFDR), coherent optical communication, precision spectroscopy, and atomic physics [1–7]. Particularly, most applications require that the output wavelength of the ECDL can be scanned continuously over time. Consequently, it is critical to build and maintain an ECDL system with a wide mode-hopping free (MHF) tuning range.

Shortly after the first tunable ECDL configuration was developed in the early 1980s [8], many novel external-cavity designs have been presented. Probably the most classical designs of the tunable ECDL can be divided into two types, the Littrow-type external-cavity configuration [9, 10] and the Littman-Metcalf-type external-cavity

configuration [11, 12]. In the former configuration, the ECDL system basically consists of a laser diode (or called gain chip) and a wavelength selected element (or called dispersion element). The latter configuration is mainly composed of a gain chip, a dispersion element, and a cavity mirror added. These two classical structures use diffraction gratings for wavelength selection. K. Fedorova et al reported a 1494–1667 nm widely tunable coherent radiation based on an InGaAs-InP strained multiple quantum well (MQW) laser chip generated from Littrow-type external-cavity configuration [13]. The maximum side mode suppression ratio (SMSR) was about 50 dB at around 1550 nm with the linewidth of less than 0.4 nm. Yuan et al demonstrated an InAs/InP quantum-dot (QD) laser system with a classical Littrow-type external-cavity design operating at pulsed injection current, the tunable range of which reached 190 nm [14]. Wang et al proved that a proper high diffraction grating groove number (1200 lines/mm) and first-order diffraction efficiency (91%) can improve laser performance and achieve wider tuning range (209.9 nm) [15]. However, these works have barely focused on the MHF tuning characteristics. It also should be noted that the wavelength tuning through the dispersion element in Littrow-type external-cavity structure results in the displacement of the 0^{th}-order output beam. Laterly, Guo et al successfully demonstrated a new and enhanced structure for mirror-grating Littrow-type ECDL to obtain a large MHF tuning range (4.34 nm) and remain the lateral displacement of the output beam (0.033 mm) almost unchanged when the diffraction grating was tuned [16]. Obviously, the presented mirror-grating method require rather complicated monitoring system in order to guarantee that the mirror and the diffraction grating rotate synchronously, and keep parallel to each other. These are not the cases in the Littman-Metcalf-type external-cavity design. The synchronization of the external-cavity mode and the diffraction grating-feedback wavelength is guaranteed by the special external-cavity configuration. K. Repasky et al studied the effect of the electronic feedback loop on the cavity resonance condition as the laser was tuned [17]. With electronic feedback, it can be found that the continuous tuning range can be extended to over 65 GHz based on the Littman-Metcalf external-cavity arrangement. Gong et al proposed a unique method to extend the MHF tuning range of a Littman-Metcalf-type ECDL by synchronous tuning with mode matching [18]. The maximum no mode-hop tuning range of 78 GHz was obtained operating at 774.5 nm with an unoptimized reflector pivot position. Meanwhile, some groups focus on studying the tuning performance of Littman-based ECDL with different hybrid methods. A high-power ECDL centered at 1329 nm with a tunable range of 111 nm was reported by K. Leung, and the total average output power was 131 mW, which was performed by incorporating two serial semiconductor optical amplifiers (SOA) in the laser cavity [19]. The wavelength tuning was realized by a compact 72-facet polygon scanner. Zhang et al presented a modified Littman-Metcalf structure based on a simple single-axis-MEMS mirror and a fused silica etalon [20]. The measured wavelength tuning range of the proposed ECDL was about 40 nm in C-band. Although there have been some reports on the widely tunable diffraction grating-coupled ECDL, the continuous wavelength tuning with a wide MHF tuning range seems less reported.

In this work, experimental results of a wide tunable external-cavity diode laser with classical Littman-Metcalf set-up are reported. The output power is about 16.5 dBm at the emitting wavelength of 1550 nm, and the maximum SMSR exceeds 60 dB is obtained in almost the full tuning spectral range of the presented Littman-Metcalf arrangement. Furthermore, the output wavelength can be changed continuously in a range of 59.13 nm without mode-hopping with an optical signal to noise ratio of more than 65 dB and an output power more than 14.8 dBm over the entire tuning range, which is about 95 times enhancement compared with the mode matching method [18]. The lasing wavelength is tunable and operating in single frequency with a narrow linewidth of no more than 100 kHz. Its output beam has good directional stability when tuned.

Experimental setup

The experimental setup of the proposed tunable ECDL is built in a Littman-Metcalf configuration, as shown schematically in Figure 1. The tunable ECDL consists of a commercially available single angled facet gain chip (Thorlabs, SAF1550S2) and an external cavity, which is generally formed by a molded aspherical lens (Edmund, 87155), a blazed diffraction grating (Newport Richardson, 33025FL01-155R, the S and P plane average diffraction efficiency of the m = 1 spectral order around 1500 nm is about 70%), a homemade gold mirror and a linear motor. The single angled facet gain chip with typical beam divergence of 31° in y-direction (transverse) and 17° in x-direction (lateral) fixed on a thermoelectric cooler (TEC) is coated a 10% reflectivity film on its normal facet (or called left/rear facet) and a 0.005% antireflection (AR) film on its angled facet (or called right/front facet). A continuous wave (CW) light from the gain chip is collimated by a molded aspherical lens (MAL) with a numerical aperture (NA) of 0.55 and a focal length of 4.51 mm, and then is incident on a 900 lines/mm blazed diffraction grating. The first-order diffraction of the blazed grating is diffracted on the surface of the cavity mirror, and then reflected back to the same blazed grating mounted in Littman-Metcalf configuration. Finally, the diffractive beam is

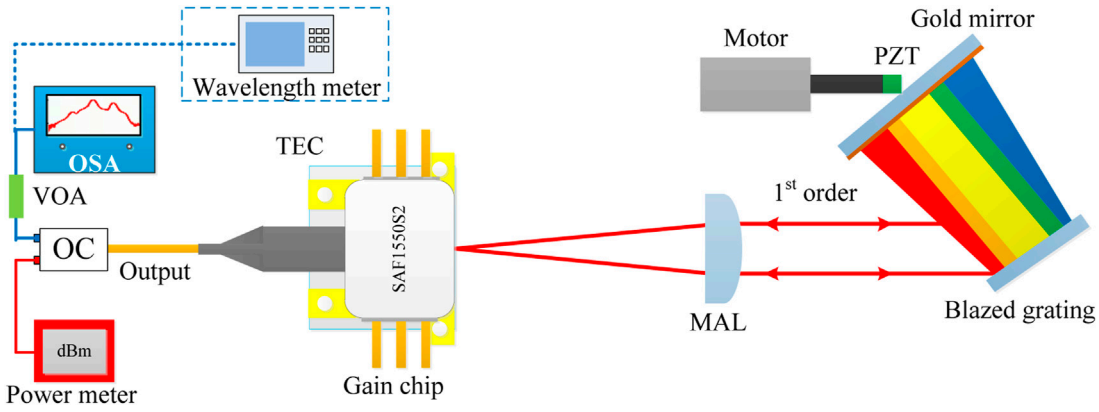

FIGURE 1
Schematic diagram of the ECDL built in the Littman-Metcalf configuration. TEC, thermoelectric cooler; MAL, molded aspherical lens; PZT, piezoelectric transducer; OC, optical coupler; VOA: variable optical attenuator.

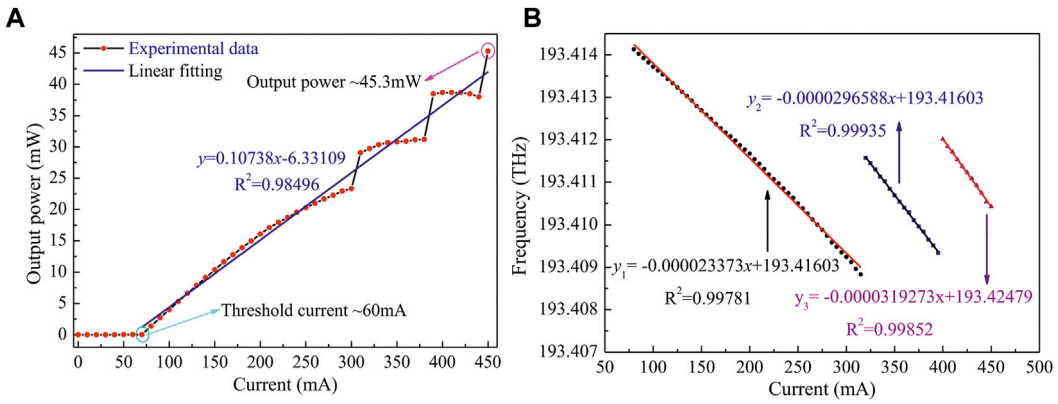

FIGURE 2
(A) Measurement of the output power characteristics of the ECDL as a function of the injection current at 1550 nm. **(B)** Measurement output frequency shift as a function of the injection current in the Littman-Metcalf-type external-cavity configuration.

coupled back into the single angled facet gain chip to form the resonator. The operation from one wavelength (mode) to another wavelength is achieved by rotating the gold mirror driven by a piezoelectric transducer (PZT) motor. The output of the selected wavelength is taken from the fiber output and is divided into two equal parts by a 50/50 commercial optical coupler (OC). After passing through the 3 dB OC, the power of light coupled from the external cavity could be measured using an optical power meter (Thorlabs, PM100D). Meanwhile, an optical spectrum analyzer (OSA: Yokogawa, AQ6370D) with a resolution of 20 pm. is applied to monitor the spectral changes of the ECDL scheme. In order to verify the ability to achieve a wide MHF tuning range at the same time, a wavelength meter (Yokogawa, AQ6151B) is used to obtain the MHF traces. It is worth noting that a variable optical attenuator (VOA) with an attenuation of 9 dBm is applied to prevent the OSA or the wavelength meter from being damaged due to the excessive output power.

Experimental results and discussion

After adding the external cavity to the commercially available single angled facet gain chip, MAL focal adjustment and wavelength selected element alignment are carried out to optimize the optical feedback. Optimum alignment is accomplished when the gain chip threshold current is reduced to a minimum value [21]. Figure 2A shows the output power

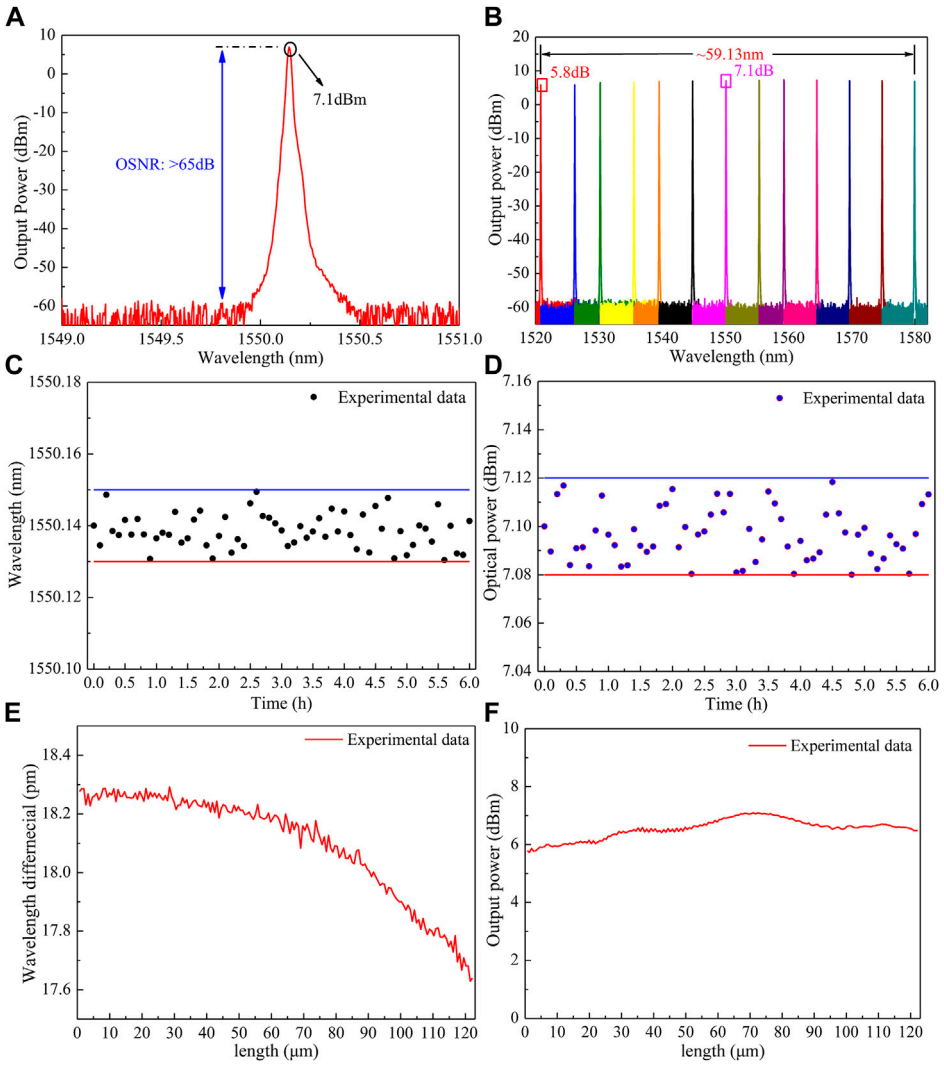

FIGURE 3
(A) The optical spectrum of the present ECDL operating 1,550.14 nm. **(B)** The superimposed optical spectra for different resonance wavelengths. **(C)** The wavelength long-term stability of the present ECDL. **(D)** The output power stability of the laser. **(E)** The mode-hopping free performance of the proposed ECDL. **(F)** The relationship between the optical output power and the physical length of the ECDL cavity.

characteristics of the ECDL *versus* the injection current (the step is 10 mA) at the absence of the commercial optical coupler, the output power increases linearly with the increasing of injection current. The output power at the maximum injection current of the home made laser diode driver (450 mA) is 45.3 mW. The slope efficiency and the gain chip threshold current are approximately 0.11 mW/mA and 60 mA, respectively. However, it should be noted that the output power will suddenly jump when the injection current tuned up from 300 mA to 310, 380–390, and 440–450 mA, respectively. It may result from current-induced mode jumps.

To fully demonstrate the effect of injection current on the tuning characteristics of the ECDL output frequency (wavelength), the injection current is increased from 80 to 450 mA with 5 mA/step. Then the relation between injection current and output frequency in the Littman-Metcalf external cavity configuration is plotted in Figure 2B, where linear regression is performed to obtain the frequency tuning rate of the injection current, respectively. As displayed in Figure 2B, the frequency tuning rate of the injection current are determined to be approximately 0.0234 GHz/mA, 0.0297 GHz/mA and 0.0319 GHz/mA, respectively. Furthermore, it can be observed that the proposed ECDL has a mode hopping interval, which can reasonably explain the phenomenon in Figure 2A. The MHF interval with respect to the injection current adjustment range is changed when

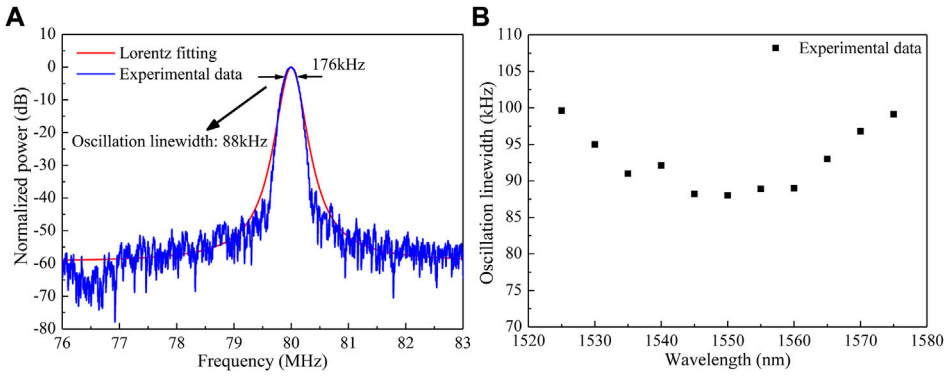

FIGURE 4
(A) Delayed self-heterodyne spectra of the proposed ECDL operating at wavelength of 1550 nm. **(B)** The linewidth vs oscillation wavelength. The linewidth performance is measured using the traditional DSH arrangement with a total length of 20 km single-mode fiber and an 80 MHz fibre-coupled AOM.

injection current changes and moves to the shorter MHF range as the injection current increases. Therefore, it is necessary to avoid this mode hopping interval when the ECDL is working.

Subsequently, the basic characteristics of the proposed ECDL are measured. Figure 3A displays the optical spectrum of the present ECDL operating 1,550.14 nm, single-mode operation with high optical signal to noise ratio (OSNR) of more than 65 dB can be observed. The designed total physical lengths of the laser cavity are changed to obtain superimposed optical spectra for different resonance wavelengths. The tunable wavelength range is about 59.13 nm from 1,520.82 nm to 1,579.95 nm, as shown in Figure 3B. What's more, it can be seen in Figure 3B that the ECDL exhibits output power more than 14.8 dBm (taking the fixed attenuation value into account) over the whole tuning range when the injection current is about 410 mA while maintaining a high OSNR over 65 dB. Later, an experiment is carried out to demonstrate the wavelength long-term stability of the present ECDL. A wavelength meter is adopted to measure the wavelength fluctuations of the present ECDL during free running. The monitoring ambient temperature fluctuates by roughly 1 ˚C about an average roughly 22 ˚C, and the results of the wavelength long-term stability are obtained over period of 6 h with 0.1 h step. As depicted in Figure 3C, the maximum deviation in the ECDL wavelength is only 10 pm indicating an excellent passive wavelength long-term stability. Under the similar experimental conditions, the output power stability of the laser is measured. Then the relation between the output power and free running time in the proposed ECDL arrangement is plotted in Figure 3D. It can be observed that from Figure 3D that the maximum deviation in the output power is only 0.02 dB indicated good power stability.

To fully demonstrate the mode-hopping free performance of the proposed ECDL system, a corresponding experiment is implemented to valid the basis characteristic. In the current implementation, the overall physical length of the ECDL cavity is designed to be about 50 mm, namely from the gain chip rear (left) output facet to the gold mirror front facet, and corresponds to an axial mode spacing of 23.1 pm operating at 1520 nm [21]. The mode spacing is changed when laser wavelength (in vacuum) changes, and moves to the bigger axial mode spacing as the wavelength increases. The maximum axial mode spacing is about 24.9 pm operating at 1580 nm. For a given laser resonator mode, an about 0.76 μm variation in the physical length of the ECDL cavity causes a relative wavelength detuning of 23.1 pm. Therefore, as displayed in Figure 3E, when the variations of the total physical length are changed with 0.664 μm step, the variations of the adjacent wavelength subtract are less than one mode spacing, which indicates a mode-hopping free tunable output is ability to be realized. Figure 3F illustrates the relationship between the optical output power and the physical length of the ECDL cavity. It can be seen that the measured trace is smooth (no suddenly power jump) which also demonstrates a mode-hopping free tunable output can be achieved.

At last, the spectral linewidth performance of the proposed ECDL system is illustrated using traditional delayed self-heterodyne (DSH) arrangement with a total length of 20 km single-mode fiber (Corning, SMF28e) and an 80 MHz fibre-coupled acousto-optic modulator (AOM) which is fabricated by the Gooch & Housego [22, 23]. The spectral linewidth of the beat signal is depicted in Figure 4A. Thanks to the relative long laser cavity and low noise direct current (DC) source, the full width at half maximum (FWHM) of the Lorentzian fit is roughly 176 kHz operating at 1550 nm. In addition, as plotted in Figure 4B, the spectral linewidth of the proposed ECDL is less

than 100 kHz over the entire tuning range. Notice that the obtained spectral linewidth of the designed lasing system in the central part of the whole tuning range is narrower than that in the two edges of the whole tuning range. This is because the resonator wavelengths in the two edges of the whole tuning range have larger diffraction angles which will result in an extra wavelength-dependent coupling loss.

Conclusion

In conclusion, a wide mode-hopping free and narrow linewidth tunable laser source is designed, which is based on a classical Littman-Metcalf configuration. Meanwhile, the tuning characteristics and spectral linewidth of the proposed external-cavity diode laser are investigated experimentally. A wide no mode-hopping continuous wavelength tuning range about 59.13 nm in ultra-C-band (namely, 1,520.82–1,579.95 nm) with an optical signal to noise ratio of more than 65 dB and an output power more than 14.8 dBm over the whole tuning range can be achieved in a long-term free running. The spectral linewidth performance of the designed tunable laser source measured using delayed self-heterodyne method is less than 100 kHz. With the help of this designed tunable laser source, it has the potential in the application of higher rate (800 Gbit/s and 1 Tbit/s) coherent systems with higher-order modulation formats (coherent optical orthogonal frequency division multiplexing). Future work shall focus on the optimization of the length of the laser cavity design to further reduce the spectral linewidth.

Data availability statement

The raw data supporting the conclusion of this article will be made available by the authors, without undue reservation.

Author contributions

Conceptualization, LS, AZ, SQ, and LH; Methodology, LS, AZ, and LH; Software, PL, JJ, and ZZ; Validation, AZ, ZL, and BY; Formal analysis, SQ and JL; Investigation, YW and LS; Resources, LH and LS; Data curation, SQ; Writing—original draft preparation, LS and SQ; Writing—review and editing, LH and LS; Visualization, LS; Supervision, LH; Project administration, LS and LH; Funding acquisition, LS, SQ, and LH. All authors have read and agreed to the published version of the manuscript.

Funding

This research was funded in part by National Key Research and Development Plan (2022YFF0705900); In part by National Natural Science Foundation of China (61605034); In part by Qingdao Postdoctoral Applied Research Project (20266153, 21290111); In part by Special Support for Postdoctoral Creative Funding in Shandong Province (202103076); And in part by Science and Technology on Electronic Test and Measurement Laboratory Foundation (ZF332).

Acknowledgments

Thanks to Shuai Zhou and Jilei Han for their support during the experiments.

Conflict of interest

Authors AZ, SQ, LS, LH, ZL, JJ, ZZ, BY, PL, JL, and YW are employed by Ceyear Technologies Co., Ltd.

Publisher's note

References

1. Xu P, Yu X, Chen Z, Sheng L, Liu J, Zhou S, et al. Distributed refractive index sensing based on bending-induced multimodal interference and Rayleigh backscattering spectrum. *Opt Express* (2021) 29(14):21530–8. doi:10.1364/OE.430637

2. Yang X, Yin Y, Li X, Sheng L, Liu J, Zhou S, et al. External cavity diode laser as a stable-frequency light source for application in laser cooling of molecules. *Chin Opt Lett* (2016) 14(7):071403. doi:10.3788/COL201614.071403

3. Robins N, Lance A, Close J, Sheng L, Liu J, Zhou S, et al. Piezo-locking a diode laser with saturated absorption spectroscopy. *Appl Opt* (2008) 47(28):5163–6. doi:10.1364/AO.47.005163

4. Schioppo M, Brown R, McGrew W, Hinkley N, Fasano R, Beloy K, et al. Ultrastable optical clock with two cold-atom ensembles. *Nat Photon* (2017) 11(48):48–52. doi:10.1038/NPHOTON.2016.231

5. Ma Y, Yang Q, Tang Y, Chen S, Shieh W. 1-Tb/s single-channel coherent optical OFDM transmission over 600-km SSMF fiber with subwavelength bandwidth access. *Opt Express* (2009) 17(28):9421–7. doi:10.1364/OE.17.009421

6. Duan L, Lukin M, Cirac J, Zoller P. Long-distance quantum communication with atomic ensembles and linear optics. *Nature* (2011) 414(413):413–8. doi:10.1038/35106500

7. Doringsho K, Ernsting I, Rinkle R, Schiller S, Wicht A. Low-noise, tunable diode laser for ultra-high-resolution spectroscopy. *Opt Lett* (2007) 32(413):2876–8. doi:10.1364/OL.32.002876

8. Lang R, Kobayashi K. External optical feedback effects on semiconductor injection laser properties. *IEEE J Quan Electron* (1980) 16(413):347–55. doi:10.1109/jqe.1980.1070479

9. Arnold A, Wilson J, Boshier M. A simple extended-cavity diode laser. *Rev Scientific Instr* (1998) 69(413):1236–9. doi:10.1063/1.1148756

10. Hawthorn C, Weber K, Scholten R. Littrow configuration tunable external cavity diode laser with fixed direction output beam. *Rev Scientific Instr* (2001) 72(413):4477–9. doi:10.1063/1.1419217

11. Harvey K, Myatt C. External-cavity diode laser using a grazing-incidence diffraction grating. *Opt Lett* (1991) 16(413):910–2. doi:10.1364/OL.16.000910

12. Sheng L, Zhang A, Qiao S, Huang L, Zhang Z, Liu Z, et al. Study of longitudinal allowance error for mode-hopping free external cavity tunable semiconductor lasers. *Eletro-optic Technol Appl* (2021) 36(5):66–72.

13. Fedorova K, Cataluna M, Kudryashov I, Khalfin V, Rafailov E. Broadly tunable InGaAsP-InP strained multi-quantum-well external cavity diode laser. *IEEE Photon Technol Lett* (2010) 22(413):1205–7. doi:10.1109/LPT.2010.2051661

14. Yuan H, Gao F, Yang T. Ultra-broadband tunable single- and double-mode InAs/InP quantum dot external-cavity laser emitting around 1.65μm. *Opt Lett* (2018) 43(413):3025–8. doi:10.1364/OL.43.003025

15. Wang Y, Wu H, Chen C, Zhou Y, Wang Y, Liang L, et al. An ultra-high-SMSR external-cavity diode laser with a wide tunable range around 1550 nm. *Appl Sci* (2019) 9:4390. doi:10.3390/app9204390

16. Guo H, Olamax G. Analysis of no mode-hop tuning of mirror-grating external-cavity diode laser. *Opt Commun* (2018) 421:90–3. doi:10.1016/j.optcom.2018.03.074

17. Repasky K, Nehrir A, Hawthorne J, Switzer G, Carlsten J. Extending the continuous tuning range of an external-cavity diode laser. *Appl Opt* (2006) 45(35):9013–20. doi:10.1364/AO.45.009013

18. Gong H, Liu Z, Zhou Y, Zhang W. Extending the mode-hop-free tuning range of an external-cavity diode laser by synchronous tuning with mode matching. *Appl Opt* (2014) 53(33):7878–84. doi:10.1364/AO.53.007878

19. Leung M, Mariampillai A, Standish B, Lee K, Munce N, Vitkin I, et al. High-power wavelength-swept laser in Littman telescope-less polygon filter and dual-amplifier configuration for multichannel optical coherence tomography. *Opt Lett* (2009) 34(18):2814–6. doi:10.1364/OL.34.002814

20. Zhang D, Zhao J, Yang Q, Liu W, Fu Y, Li C, et al. Compact MEMS external cavity tunable laser with ultra-narrow linewidth for coherent detection. *Opt Express* (2012) 20(18):19670–82. doi:10.1364/OE.20.019670

21. Zhang L, Liu T, Chen L, Xu G, Jiang C, Liu J, et al. Development of an interference filter-stabilized external-cavity diode laser for space applications. *Photonics* (2020) 7(12):7010012. doi:10.3390/photonics7010012

22. Zhao Z, Bai Z, Jin D, Qi Y, Ding J, Yan B, et al. Narrow laser-linewidth measurement using short delay self-heterodyne interferometry. *Opt Express* (2022) 30(17):30600–10. doi:10.1364/OE.455028

23. Zhao Z, Bai Z, Jin D, Chen X, Qi Y, Ding J, et al. The influence of noise floor on the measurement of laser linewidth using short-delay-length self-heterodyne/homodyne techniques. *Micromachines* (2022) 13(8):1311. doi:10.3390/mi13081311

frontiers | Frontiers in Physics

TYPE Brief Research Report
PUBLISHED 08 December 2022
DOI 10.3389/fphy.2022.1102323

OPEN ACCESS

EDITED BY
Liyuan Chen,
Hilase Center, Czechia

REVIEWED BY
Yajun Pang,
Hebei University of Technology, China
Pibin Bing,
North China University of Water Conservancy and Electric Power, China
Li Xing,
Shanghai Jiao Tong University, China

*CORRESPONDENCE
Jianxin Zhang,
zhjx_aa@126.com
Chunyan Wang,
wangcy@bnu.edu.cn

SPECIALTY SECTION
This article was submitted to Optics and Photonics,
a section of the journal
Frontiers in Physics

RECEIVED 18 November 2022
ACCEPTED 25 November 2022
PUBLISHED 08 December 2022

CITATION
Fan X, Zhang J, Li S, Li S, Wang Y, Du F, Huang X, Li Y, Zhang L and Wang C (2022), A method to achieve spectral beam combining based on a novel symmetric grating.
Front. Phys. 10:1102323.
doi: 10.3389/fphy.2022.1102323

A method to achieve spectral beam combining based on a novel symmetric grating

Xinmin Fan[1,2], Jianxin Zhang[1,2,3]*, Sensen Li[4], Shun Li[1,2], Yan Wang[1,2], Fei Du[1,2], Xiaodong Huang[1,2], Yingde Li[1], Lujun Zhang[1,2] and Chunyan Wang[1,2]*

[1]School of Physics and Electronic Information, Weifang University, Weifang, China, [2]Weifang Key Laboratory of Laser Technology and Application, Weifang University, Weifang, China, [3]Weifang Academy of Advanced Opto-Electronic Circuits, Weifang, China, [4]Science and Technology on Electro-Optical Information Security Control Laboratory, Tianjin, China

A symmetric grating is proposed to obtain higher output power in spectral beam combination by increasing the number of lasers and spectral utilization. The grating allows laser beams to be incident from both sides of the grating normal to achieve coaxial beam combining, so the number of beams and the combined output power are doubled compared with the traditional grating under the same spectral line-width. The grating is designed with the central wavelength of 4.65 μm, and the calculation results show that this grating is very advantageous for spectral beam combining, especially for the light waves in the range 4.55–4.71 μm, where their diffraction efficiencies are high (over 80%) and correspond to a wide and linear range of incidence angles. Meanwhile, based on the symmetric gratings we further propose a circular grating to achieve the same frequency spectral beam combining. This beam combining design will not increase the laser spectral line width while enhancing the laser power, reducing the requirements for the unit laser spectral line width, which is very meaningful in some application fields and will further enrich the research of spectral beam combining.

KEYWORDS

spectral beam combination, symmetrical grating, circular grating, same frequency spectral beam combination, coaxial beam combining

1 Introduction

The output power of a single laser beam is often difficult to meet scientific and industrial needs due to the gain saturation, non-linear effects and device damage. Combining multiple laser beams is an effective way to obtain higher output power to solve this problem [1]. In 1986, Wilfrid B. Veldkamp of Lincoln Laboratory first proposed a method for coherent beam combining of multi-channel lasers using binary phase gratings and achieved 6 GaAlAs laser beams combination [2, 3]. In 2011, Thales Research and Technology in France reported the coherent beam combining of 5 quantum-cascade lasers by a binary phase or Dammann grating [4]. All of the above solutions are coherent beam combining, which requires a high degree of coherence between different channel

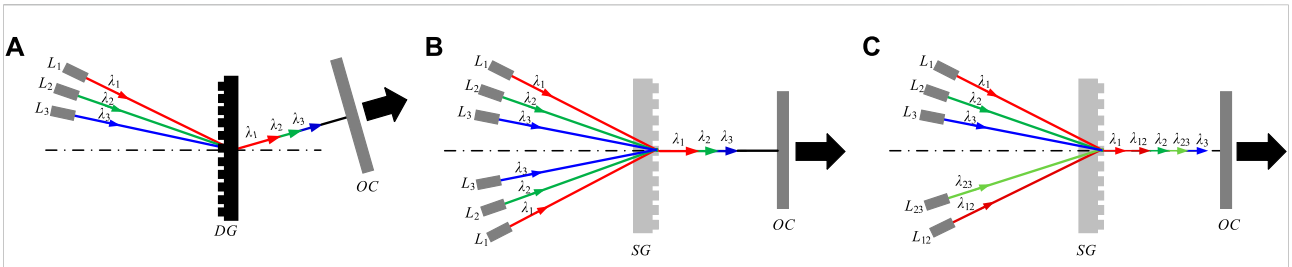

FIGURE 1
Comparison of the two spectral beam combining schemes of **(A)** the traditional grating and **(B)** the symmetrical grating. **(C)** The second spectral beam combination scheme of the symmetric grating.

lasers and is hard to accomplished experimentally, especially when the number of lasers is large [5–9]. The feasibility of a spectral beam combining (incoherent beam combining) scheme was proposed by Christopher C. Cook et al. at Lincoln Laboratory in 1999 [10] and was experimentally achieved for a semiconductor laser array in 2000, where the combined beam quality was almost identical to that of the single emitter [11], and in the same year, they have also successfully achieved spectral beam combining of 11-channel lasers [12]. Since then, the study of spectral beam combination has attracted extensive attention [13, 14].

Theoretically, the more lasers, the higher the combined beam output power, but increasing the number of lasers will bring many problems, mainly in: 1) difficulty in optical path arrangement, because the existing spectral beam combination schemes require that all emitters (or laser arrays) can only be on the same side of the grating normal; 2) the spectral of each emitter must be broadband, and the more the emitters are, the wider their spectral must be, otherwise the efficiency of the spectral beam combination will be reduced.[15]

To overcome these above problems, we propose a symmetric grating for the spectral beam combining, and also develop a circular grating (two-dimensional grating) to achieve the same frequency spectral beam combining, which greatly enriches the study of spectral beam combining.

2 Novel spectral beam combining scheme

2.1 Symmetric grating and its spectral beam combining scheme

Compared with traditional grating, our symmetric grating has the following features: The diffracted light can be emitted perpendicular to the grating plane if the laser beam is incident on the grating at a suitable angle, so it can also be emitted perpendicular to the grating plane when the laser beam incident at the symmetrical position (or angle) on the other side of the grating normal. This allows multiple laser beams to be incident from both sides of the grating normal to achieve spectral beam combining. Meanwhile, the incident light can only be on one side of the normal of the traditional grating for spectral beam combining. Take the example of the three-channel lasers L_1, L_2, and L_3, the differences between the two spectral combining schemes of the traditional grating and the symmetrical grating are given in Figures 1A,B respectively. DG and SG are the traditional diffraction grating and the symmetric grating respectively, and OC is the coupling output mirror that partially reflects and partially transmits the spectral lines of the unit lasers L_1, L_2, and L_3 so that the three channels lasers are locked to the central wavelengths λ_1, λ_2 and λ_3 respectively and are coaxially combined.

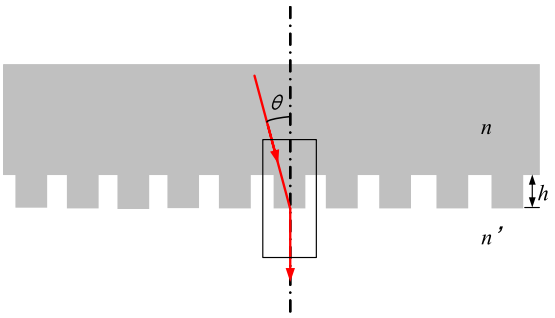

FIGURE 2
Schematic diagram of the ray trace in the grating (the simulation unit is in the black box).

Compared with traditional gratings, it can be seen that the symmetrical grating has the advantages of a larger number of lasers, higher spectral utilisation, smaller space requirement and the ability to combine beam at the same frequency. As shown in Figure 1C, there is also another spectral beam combining scheme where the positions of the lasers on either side of the grating normal can be asymmetrical compared with Figure 1B, L_{12} and L_{23} are located between L_1 and L_2, L_2, and L_3 respectively, which their corresponding wavelengths λ_{12} and λ_{23} are between λ_1 and λ_2, λ_2, and λ_3 respectively.

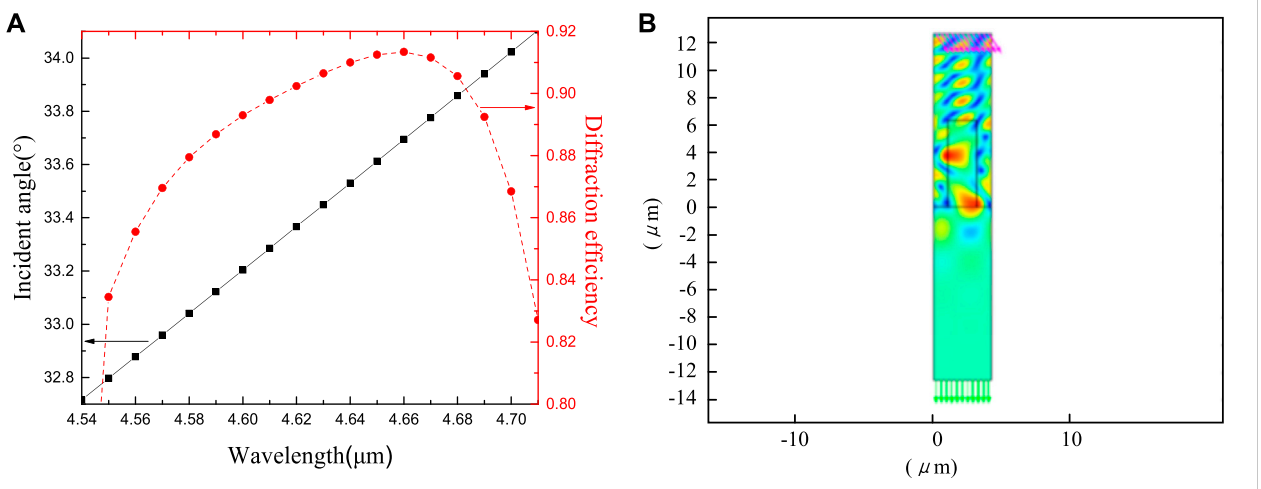

FIGURE 3
(A) Variations of the optimal incidence angle and diffraction efficiency with laser wavelength; **(B)** The electric field distribution for the laser beam of 4.6 μm at the optimal incidence angle of 33.2°, the purple and the green arrows represent the directions of incident light and diffracted light respectively.

2.2 Parameter design and the spectral beam combining effect

A theoretical study and parametric design have been carried out for the new grating proposed above. In order to obtain high first-order diffraction efficiency, we have designed a sub-wavelength dielectric grating assuming the central wavelength of 4.56 μm [16]. As shown in Figure 2, the simulation unit is in the black box, and the refractive index of grating material n, air refractive index n', grating period d, duty cycle η and ridge height h are respectively set at 2.0, 1.0, 4.2, 0.5 and 6.3 μm.

As shown in Figure 3A, calculations show that this grating is ideally suited for spectral beam combining, as it has a high diffraction efficiency (>80%) for the incident light in the range 4.55–4.71 μm, with a maximum diffraction efficiency of 91.4% at 4.66 μm, and a relatively significant difference in the incidence angle of these lights while their diffracted lights are emitted perpendicular to the grating plane. Figure 3B shows the electric field distribution of incident and diffracted light in the grating for the laser beam of 4.6 μm, the purple arrows represent the direction of incident light (33.2°) and the green arrows represent the direction of diffracted light, which is consistent with the initial assumptions and calculations made earlier. Due to the left-right symmetry of the grating structure (see Figure 2), the beam incident from the right side of the grating normal has the same direction of emission.

From the previous simulation and analysis, it is clear that the symmetrical grating is perfectly feasible for spectral beam combining, and has the advantages of high spectral utilisation and small space occupation compared with traditional grating combining scheme. But as shown in Figure 1B, this grating can only combine two beams of the same frequency (or same wavelength). If a grating could combine multiple beams of light at the same frequency, the spectrum of each laser does not need to be broadband, and the combined laser beam is not broadband anymore which is very meaningful in some application fields [17]. To this end, we further develop a circular grating.

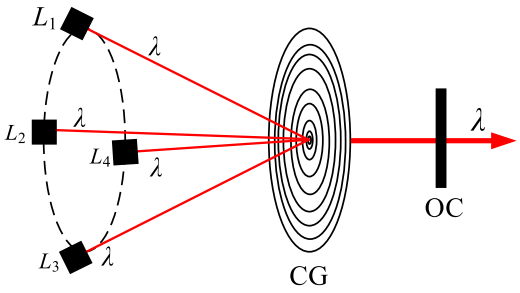

FIGURE 4
The same frequency spectral beam combining scheme based on the circular grating.

2.3 Circular grating and its spectral beam combining scheme

The so-called circular grating means that the grating grooves are not straight but circular, so that the same frequency beam is incident on the same solid angle to the center of the circular grating to achieve coaxial same frequency spectral beam combining. A schematic diagram of a 4-channel lasers spectral beam combining using the circular grating is given in Figure 4, CG is the circular

grating and OC is the coupling output mirror respectively. Obviously, the overall output power of the combined beam can be increased by increasing the number of the same frequency lasers at this solid angle, and further increased by increasing the number of different wavelength lasers at other solid angles.

3 Conclusion

To increase the number of lasers and spectral utilisation for greater output power of the combined beam, we propose a symmetric (one-dimensional) grating and a circular grating (two-dimensional). Compared with traditional spectral combining scheme, the symmetrical grating spectral beam combining scheme can double the total output power of the combined beam by doubling the number of lasers for the same spectral line-width. The grating was designed with a central wavelength of 4.65 μm, and the calculations show that this grating is ideally suited for spectral beam combining with a high diffraction efficiency (>80%) and a relatively significant difference in the incidence angle for the incident light in the range 4.55–4.71 μm. In addition, a circular grating is further proposed for the same frequency spectral beam combining. The ideas of symmetrical grating, circular grating and same frequency spectral beam combining proposed in this study will further enrich the study of spectral beam combination.

Data availability statement

The raw data supporting the conclusion of this article will be made available by the authors, without undue reservation.

Author contributions

XF: Conceptualization, Original draft, Review and Editing JZ: Numerical simulation, Software SEL: Conceptualization SHL: Numerical simulation YW: Investigation FD: Review and Editing XH: Numerical simulation, Review and Editing YL: Review LZ: Writing, Review and Editing CW: Original draft, Review, Funding acquisition.

Funding

This work is supported by the Shandong Provincial Natural Science Foundation, China (No. ZR2020QA072).

Conflict of interest

The authors declare that the research was conducted in the absence of any commercial or financial relationships that could be construed as a potential conflict of interest.

Publisher's note

All claims expressed in this article are solely those of the authors and do not necessarily represent those of their affiliated organizations, or those of the publisher, the editors and the reviewers. Any product that may be evaluated in this article, or claim that may be made by its manufacturer, is not guaranteed or endorsed by the publisher.

References

1. Yan A, Liu L, Dai E, Sun J, Zhou Y. Simultaneous beam combination and aperture filling of coherent laser arrays by conjugate Dammann gratings. *Opt Lett* (2010) 35:1251. doi:10.1364/OL.35.001251

2. Veldkamp WB, Leger JR, Swanson GJ. Coherent summation of laser beams using binary phase gratings. *Opt Lett* (1986) 11:303. doi:10.1364/OL.11.000303

3. Leger JR, Swanson GJ, Veldkamp WB. Coherent beam addition of GaAlAs lasers by binary phase gratings. *Appl Phys Lett* (1986) 48:888–90. doi:10.1063/1.96648

4. Bloom G, Larat C, Lallier E, Lehoucq G, Bansropun S, Lee-Bouhours MSL, et al. Passive coherent beam combining of quantum-cascade lasers with a Dammann grating. *Opt Lett* (2011) 36:3810. doi:10.1364/OL.36.003810

5. Nabors CD. Effects of phase errors on coherent emitter arrays. *Appl Opt* (1994) 33:2284. doi:10.1364/AO.33.002284

6. Lucas-Leclin G, Schimmel G, Albrodt P, Hanna M, Georges P. Coherent combining architectures for high-brightness laser diodes. In: 2017 IEEE High Power Diode Lasers and Systems Conference (HPD) (2017). p. 49. doi:10.1109/HPD.2017.8261095

7. Chang H, Chang Q, Xi J, Hou T, Su R, Ma P, et al. First experimental demonstration of coherent beam combining of more than 100 beams. *Photon Res* (2020) 8:1943. doi:10.1364/PRJ.409788

8. Sakakibara R, Mio N. Simplified system for relative phase control between two input beams for coherent polarization beam combination. *Appl Opt* (2020) 59:10289. doi:10.1364/AO.405132

9. Albrodt P, Niemeyer M, Crump P, Hamperl J, Moron F, Georges P, et al. Coherent beam combining of high power quasi continuous wave tapered amplifiers. *Opt Express* (2019) 27:27891. doi:10.1364/OE.27.027891

10. Cook CC, Fan TY. Spectral beam combining of Yb-doped fiber lasers in an external cavity[C]. *Adv Solid State Lasers* (1999) 26:PD5. doi:10.1364/ASSL.1999.PD5

11. Daneu V, Sanchez A, Fan TY, Choi HK, Cook CC. Spectral beam combining of a broad-stripe diode laser array in an external cavity. *Opt Lett* (2000) 25:405. doi:10.1364/OL.25.000405

12. Tso Yee F, Sanchez A, Daneu V, Aggarwal RL, Buchter SC, Goyal A, et al. Laser beam combining for power and brightness scaling[C]. In: 2000 IEEE Aerospace Conference Proceedings (Cat No00TH8484) (2000). p. 49. doi:10.1109/AERO.2000.879830

13. Huang RK, Chann B, Missaggia LJ, Donnelly JP, Harris CT, Turner GW, et al. High-Brightness wavelength beam combined semiconductor laser diode arrays. *IEEE Photon Technol Lett* (2007) 19:209–11. doi:10.1109/LPT.2006.890717

14. Cao Y, Shu S, Sun F, Zhao Y, Tong C, Wang L. Development of beam combining technology in mid-infrared semiconductor lasers(invited). 红外与激光工程 (2018) 47:1003002. doi:10.3788/irla201847.1003002

15. Sun S, Tan H, Meng H, Guo L, Gao S, Wu D, et al. High brightness diode laser by coupler free grating external cavity spectral beam combining. *Infrared Laser Eng* (2019) 48:306006. doi:10.3788/irla201948.0306006

16. Pan T, Ye J, Zhang Z, Xu Y. Inverse design of coupled subwavelength dielectric resonators with targeted eigenfrequency and Q factor utilizing deep learning. *Opt Lett* (2022) 47:3359. doi:10.1364/OL.463040

17. Zhao Z, Bai Z, Jin D, Qi Y, Ding J, Yan B, et al. Narrow laser-linewidth measurement using short delay self-heterodyne interferometry. *Opt Express* (2022) 30:30600–10. doi:10.1364/OE.455028

frontiers | Frontiers in Physics

TYPE Brief Research Report
PUBLISHED 20 December 2022
DOI 10.3389/fphy.2022.1072023

OPEN ACCESS

EDITED BY
Liyuan Chen,
Hilase Center, Czechia

REVIEWED BY
Hongli Wang,
Korea Advanced Institute of Science and Technology, South Korea
Zhang Jing,
Chinese Academy of Sciences (CAS), China

*CORRESPONDENCE
Yi Chen,
chenyi@cjlu.edu.cn

SPECIALTY SECTION
This article was submitted to Optics and Photonics, a section of the journal Frontiers in Physics

RECEIVED 17 October 2022
ACCEPTED 25 November 2022
PUBLISHED 20 December 2022

CITATION
Zhou L, Chen Y, Guo X, Shi Y, Zhao T, Zhan C and Jin S (2022), Influence of the focusing characteristics of near-infrared lasers on the maintenance of plasma luminescence.
Front. Phys. 10:1072023.
doi: 10.3389/fphy.2022.1072023

Influence of the focusing characteristics of near-infrared lasers on the maintenance of plasma luminescence

Lian Zhou, Yi Chen*, Xin Guo, Yan Shi, Tianqi Zhao, Chunlian Zhan and Shangzhong Jin

College of Optical and Electronic Technology, China Jiliang University, Hangzhou, Zhejiang, China

The interaction of 980-nm continuous laser radiation with the plasma of a continuous optical discharge in xenon lamps at a pressure of p = 12 atm has been studied. The threshold power and characteristics of the laser required to sustain the xenon plasma became our focus. According to the theory of Gaussian beam propagation, the laser parameters after collimation and focusing are obtained by combining ZEMAX simulation and the actual measurement. The influence of the beam waist ω_0, which determines the power density distribution at focus, and the Rayleigh range Z_0, which determines the energy concentration range, on the threshold maintenance power is expounded. The results show that there is a threshold power density for the generation of plasma, whose value is about 1,500–2,000 W/mm^2, and that the threshold maintenance power of the plasma shows an overall decreasing trend with decreasing ω_0. When ω_0 is reduced to a higher power density that can easily maintain the thermodynamic equilibrium process of the plasma, the mismatch between Z_0 and the plasma size caused by the decrease in Z_0 makes the threshold power tend to be stable and increasing.

KEYWORDS

laser-maintained plasma, threshold power density, waist radius, Rayleigh length, ZEMAX

1 Introduction

When high-power CW laser energy is radiated to the gas, the molecules or atoms in it will be ionized, forming a high-temperature and high-particle density plasma environment composed of electrons, ions, and neutral particles [1]. Under the conditions of Stark broadening, the electrons in the xenon lamp and mercury lamp with higher pressure undergo active free–free transition in the process of reverse bremsstrahlung radiation [2], producing highly bright and stable light with a stronger UV distribution [3, 4], which is widely used in many fields such as semiconductor measurement, material characterization, and hyperspectral imaging [5–7].

Since the photon energy is comparable to the excitation and ionization potentials of most gases, multiphoton absorption and cascade ionization are considered to be

important mechanisms for plasma generation by laser–gas interactions [8], but even with xenon, which has the lowest thermal conductivity and ionization energy among all non-radioactive rare gases [9], the laser energy required to produce plasma is enormous. On the other hand, once the plasma is generated, the center of higher temperature and high-electron density is formed. At this time, the local thermodynamic equilibrium of the plasma [10] can be maintained by injecting lower energy to achieve long-term stable luminescence. The plasma in this state absorbs the energy of laser light through inverse bremsstrahlung [11, 12] to balance the energy loss generated by radiation and other processes, and this energy is far less than the breakdown threshold of gas.

In this work, a xenon lamp was selected as the object to generate plasma, and xenon in the lamp was pre-ionized by DC high-voltage ignition to form an initial plasma discharge channel, in which some atoms in the gas were transferred from the ground state to the excited state, obtaining more energy. Before pre-ionization, we focused the laser between the two electrodes of the lamp to maintain the continuous emission of the plasma generated by pre-ionization. Through preliminary maintenance experiments with the existing pressurized xenon lamps in the laboratory, a xenon lamp bulb with a charge pressure of 12 atm, which was the easiest to maintain, was selected. The threshold power of the laser required to maintain the plasma at this charging pressure was studied with the help of different lens combinations, and the regularity of the plasma maintenance process was analyzed in combination with the characteristics of the focused beam.

2 Research contents

In the literature [13], a spherical heat transfer model was developed for a focused laser beam, and the effect of plasma temperature on the laser power required for the equilibrium process was investigated from the perspective of laser absorption by the plasma. At a constant pressure P, the absorption coefficient $\mu_\omega(T_k)$ exists in a rising process due to the increase in plasma temperature T caused by laser injection; subsequently, the electron and ion density n decreases with the increase in temperature T and the absorption coefficient also decreases, as shown in Eqs 1, 2, where $\Theta(T_k)$ was the heat flux potential, which varied monotonically with temperature. Corresponding to the absorption of the laser by the plasma, there exists a threshold power P_0 enabling the plasma to enter a steady state, that is, a local thermodynamic equilibrium state, and when the plasma is unable to maintain this state, that is, the injected laser energy does not allow the plasma to reach the desired temperature, the ionization becomes so weak that the absorption of the laser can even be neglected.

$$P_0 \approx \frac{2\pi\Theta(T_k)}{\mu_\omega(T_k)}, \tag{1}$$

$$P \sim nT = constant. \tag{2}$$

2.1 Experimental setup

The laser-maintained plasma setup is shown in Figure 1. A semiconductor laser with a central output wavelength of 980 nm is selected as the laser source, and the output is fiber-coupled, with the pigtail being a multimode fiber of 106.5 μm core diameter produced by Everbright Photonics Co., Ltd.

Highly ionized plasma was formed by using a DC high voltage to break down the xenon gas between the electrodes, and then, continuous laser energy was focused on the location of the plasma to maintain its continuous and stable luminescence [14]. We measured the numerical aperture (NA) value of the outgoing laser using the knife-edge method [15], that is, 0.14, and it corresponded to the far-field divergence angle of the outgoing laser. In order to obtain a more concentrated laser distribution, the laser output from the fiber had gone through the collimation and focusing process of the lens group [16] before being focused between the two electrodes of the xenon lamp.

2.2 Experimental method

Lenses ①, ②, and ③ with numerical apertures of 0.79, 0.76, and 0.625 were selected as the collimating lenses, respectively, and lenses ④, ⑤, and ⑥ with focal lengths slightly greater than the bulb radius were selected as the focusing lenses, which were combined for the experimental study of the laser-maintained plasma. The aforementioned lenses were aspherical.

We selected the xenon lamp charging pressure of 12 atm, and the minimum laser power that can maintain the continuous and stable emission of plasma for more than 10 min was taken as the threshold power under this combination. The characteristic parameters of the focused beam under different combinations were obtained using ZEMAX simulation and actual measurements. The focused laser beam still propagates according to the characteristics of a Gaussian beam, and the radius of the beam waist, which affects the laser power density, and the Rayleigh length, which affects the degree of energy concentration, became the objects of our focus.

2.2.1 ZEMAX simulation

We took the lens combination ②+⑥ as an example and set the object height, wavelength, and object NA to 0.05 mm, 0.98 μm, and 0.14, respectively, in the lens data editor according to the parameters of the incident laser. We input the lens parameters into the lens data editor and set the corresponding initial distance, respectively, and then optimize the thickness of the distance between the exit surface of the optical fiber and the front surface of the collimating lens and the

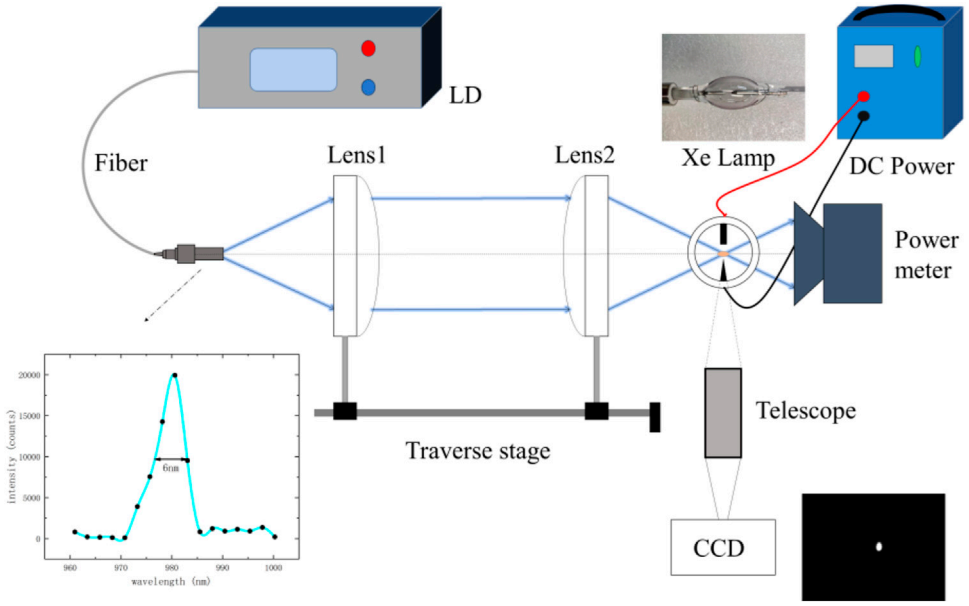

FIGURE 1
Experimental schematic diagram. The near-infrared semiconductor laser (illustrated as the spectrum of the central wavelength, FWHM is about 6 nm, and the laser can reach a maximum power of up to 70 W), after being collimated and focused by a position adjustable lens group, enters the middle of the electrode of the xenon lamp with a diameter of 18 mm and a pressure of 12 atm. The bulb is externally connected with a high-voltage arc excitation device to form the initial plasma (this voltage will be removed after laser injection) and uses a power meter (F150A-BB-26, Ophir) and a CCD camera (MV-CA016-10UM, Hikrobotics) to record the laser spot and plasma information.

distance between the rear surface of the focusing lens and the image plane to obtain the best collimation and focusing effect. The optical path in the shadow mode is shown in Figure 2A.

Observing the distribution of the light beam on the image plane, the converged light beam obtained a good focusing effect. On the premise of ensuring that the aberration was as small as possible, the small spot output was realized and the spot size radius at the focal point was only 31 μm. This result was better reflected in the scattered spot distribution of the light beam, as shown in Figure 2B.

The simulation of the initial lens combination using ZEMAX was an aid for us to exclude the effect of optical path aberration and determine the radius of the focused beam to facilitate the selection of a lens set that met the plasma maintenance conditions.

2.2.2 Beam parameter measurement

According to the propagation characteristics of the Gaussian beam, as shown in Figure 2C, the focused beam can be fit well into the hyperbolic equation [17]. The CCD was used to record the spot image including the focus within a range of about 4 mm before and after the focus. A total of 11 photographs were collected, of which at least five points were within the Rayleigh length of the focused beam [18].

The attenuated laser was directly incident on the image surface of the CCD after focusing to obtain a clear spot image near the focal point. Again, using the combination ②+⑥ as an example, the spot image taken near the focal point is shown in Figure 2D.

Combined with the spot position, the focused laser transmission can be represented by fitting the hyperbolic equation:

$$\omega(z)^2 = Az^2 + Bz + C, \tag{3}$$

Where $\omega(z)$ corresponds to the radius of the spot at position z. A, B, and C are the three coefficients obtained from the least squares fit; each parameter of the laser can be expressed by A, B, and C, respectively, as

$$\begin{cases} \omega_0 = \sqrt{C - B^2/4A} \\ \theta = \sqrt{A} \\ Z_0 = \dfrac{\sqrt{AC - B^2/4}}{A} \end{cases}, \tag{4}$$

Where ω_0, θ, and Z_0 denote the beam waist radius, beam divergence angle, and Rayleigh length at the focal plane, respectively. We took the combination ②+⑥ as an example, and its spot size and fitted data are shown in Figure 2D. The NA, beam waist radius, and Rayleigh length obtained according to Eq. 4 were 0.238, 63.903 μm, and 0.268 mm, respectively.

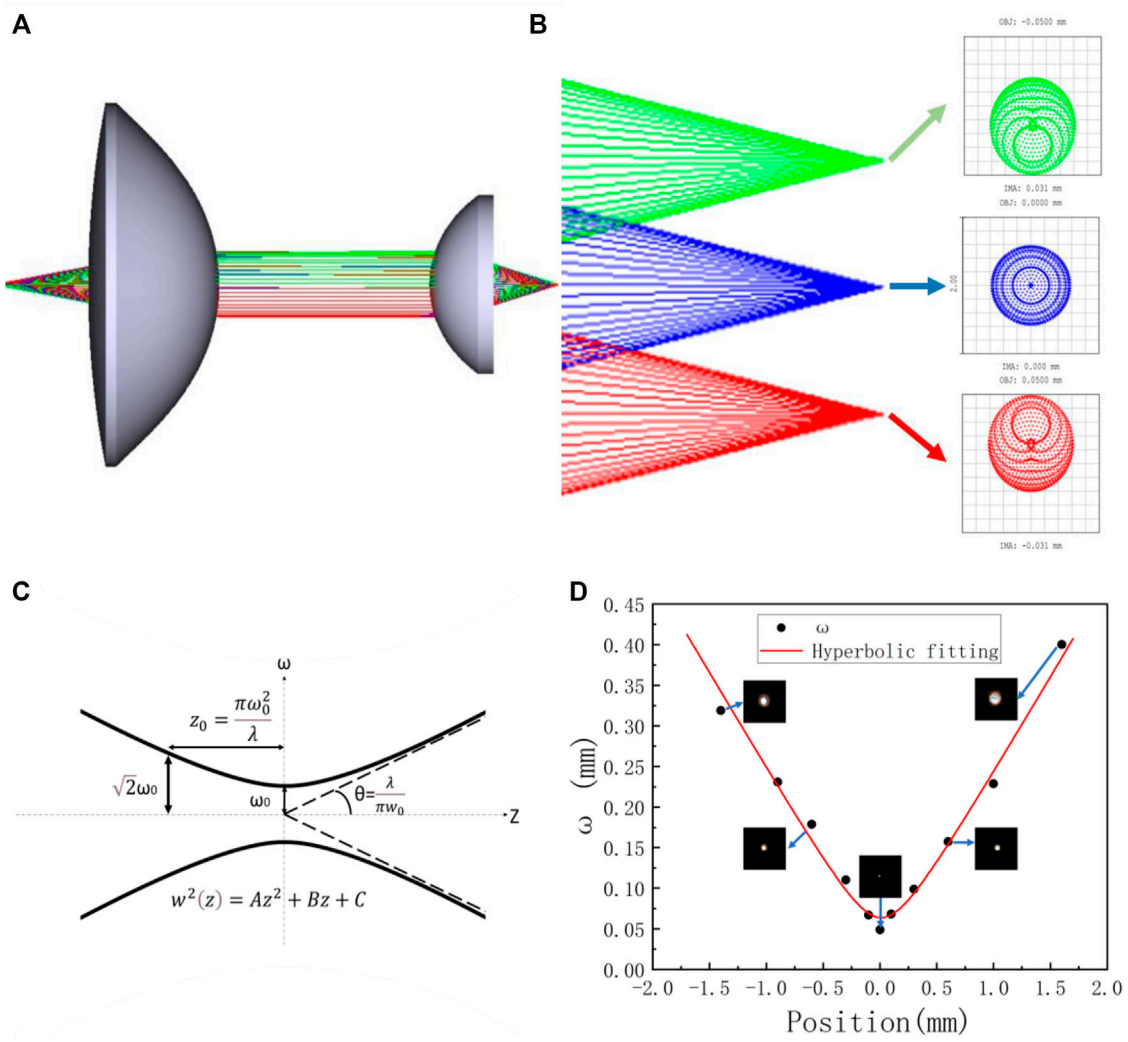

FIGURE 2
Simulation result graph and actual measurement graph of the combination ②+⑥. **(A)** 3D layout of the beam in ZEMAX; **(B)** focal plane light map and diffuse spot images corresponding to object heights of 0 and ±0.05 mm; **(C)** schematic diagram of Gaussian beam propagation and its parametric relationships, is the waist radius, Z_0 is the Rayleigh length, θ is the far-field divergence angle, and λ is the wavelength; **(D)** spot radius at different positions and their hyperbolic fits (inset shows the spot images acquired by the CCD (VEN-161-61U3M-M05, China Daheng Group, Inc.) corresponding to each position).

3 Result analysis

The aforementioned combination was simulated and compared with the focused beam characteristic parameters fitted after CCD measurement, and the results are shown in Table 1. It can be observed that the NA obtained by simulation and actual measurement data fitting was not much different, and the difference in the beam waist radius was also basically maintained at the same level. The difference was caused by the aberration of the optical path and the diffraction of the beam during the actual beam propagation [19]. With the increase in NA, the threshold power tended to decrease gradually. In order to analyze this reason, we first carried out simulation analysis on the selected combinations. The simulated data and the photographs recorded by the camera verified that some combinations showed obvious deviation from the simulation curve of ω_0 in Figure 3A due to the existence of aberration. Other combinations met the characteristics of Gaussian beam propagation, that is, with the increase of NA, the beam waist radius gradually decreased. It was worth noting that in the actual beam transmission, the beam waist radius cannot be ideally reduced with the increase in NA; as obtained in the simulation, as shown in Figure 3A, after NA was greater than 0.15, the change slope of the measurement curve was smaller

TABLE 1 Simulation and fitting parameters of the focused beam with different lens combinations.

Lens combination	Measure Z_0/mm	Measure NA	Simulation NA	Measure ω_0/mm	Simulation ω_0/mm	Threshold power/W
1 (①+③)	1.046	0.104	0.093	0.108	0.077	56.7
2 (①+⑥)	0.782	0.125	0.112	0.098	0.064	49.9
3 (①+⑤)	0.518	0.148	0.124	0.077	0.058	45.9
4 (①+④)	0.405	0.170	0.149	0.069	0.053	42.9
5 (③+⑥)	0.407	0.176	0.169	0.072	0.042	45.6
6 (③+⑤)	0.370	0.188	0.185	0.070	0.038	46.9
7 (②+⑥)	0.268	0.238	0.220	0.064	0.031	46.6
8 (②+⑤)	0.253	0.243	0.243	0.062	0.029	47.1

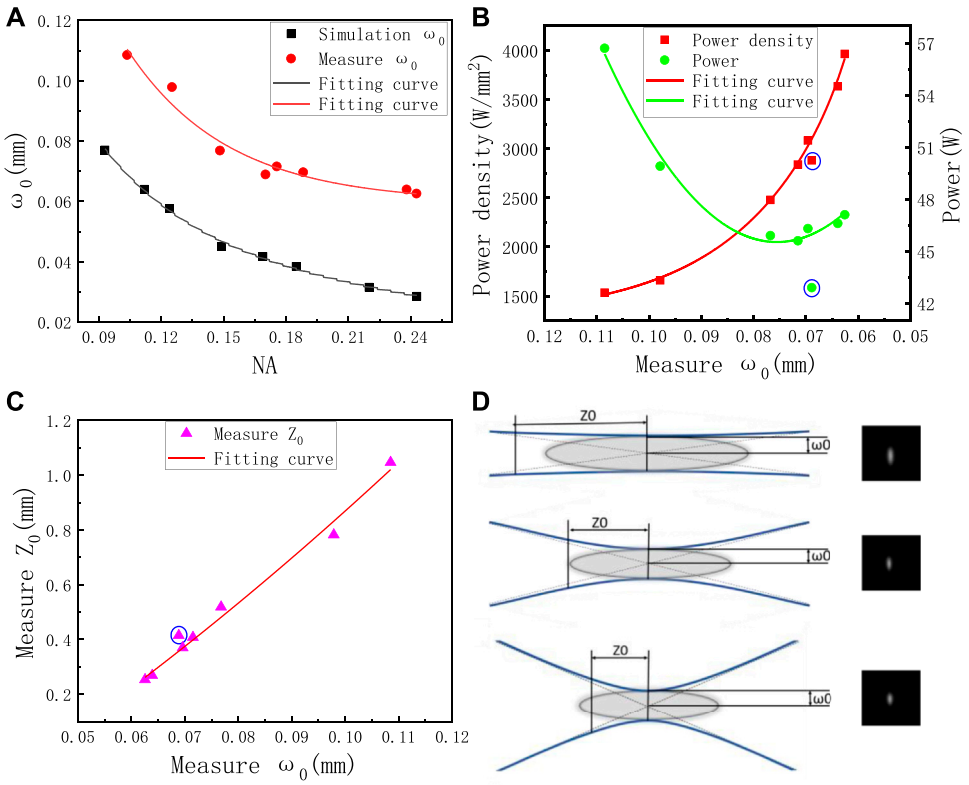

FIGURE 3
(A) Plot of the beam waist radius versus NA under simulation and the actual measurement; **(B)** effect of on the threshold power and its density; **(C)** relationship between and Rayleigh length at the focal point; **(D)** schematic diagram of laser focusing and the formed plasma morphology under different NA values, with insets showing the plasma images collected under different NA values.

than that of the simulation curve, which will directly affect the threshold power density of the laser at the focal point.

We studied the threshold power affected by the beam waist radius and Rayleigh length for eight combinations with small aberrations and no excessive energy loss (this energy loss is mainly reflected in the shading of the laser energy by the experimental device) and established its relationship with the threshold power, as shown in Figure 3B, with the beam waist radius as the independent variable. The threshold power density represents the average distribution of laser energy at the focal

plane and was numerically equal to the ratio of the threshold power to the focal plane area, which showed an opposite trend to the threshold power with ω_0, and this relationship can be better explained by the variation of the plasma luminescence size with the laser focusing NA in Figure 3D. If the NA was small, that is, ω_0 and Z_0 is large, although the plasma size was larger at this time, but its longitudinal dimension was still less than the Rayleigh length of the focused laser, and the threshold power density at this time reflects the power conditions that should be met when the plasma was lit; as NA increases, Z_0 decreases to the same scale as the plasma length, the power density at the luminous edge still met the value required in the first case, and the power density at the focal plane was in a rising stage due to the decrease of ω_0; this process continued until the Rayleigh length was smaller than the plasma length, that is, the case of large NA, and the power density beyond the Rayleigh length still met the threshold power density for maintaining the plasma under this condition, which also meant that the plasma needed more energy to maintain, and the maintenance power that should be continuously decreasing becomes stable and appears to increase. In addition, this trend was further increased by the fact that the decrease in ω_0 tends to level off with increasing NA during the actual transmission. In summary, we believed that a certain threshold power density was necessary for the formation of a stable plasma; this value was in the approximate range of 1,500–2,000 W/mm^2, but the required laser power was also influenced by the Rayleigh range and the relative length of the plasma size when analyzed from the point of view of plasma maintenance. This was also better verified by combination 4 (circled in Figures 3B,C), that is, ①+④, which had a lower threshold power due to its larger Rayleigh length than the combination in the same ω_0 conditions.

4 Discussion and conclusion

We adopted the method of combining simulation and experimental measurement to study the continuous and stable luminescence process of the laser-maintained xenon plasma at a fixed pressure. The following main conclusions were drawn for this process.

In the selection of optical path, the lens should be chosen from a lens group with small aberration and large energy transmission to obtain a focused beam, the poor focusing effect mainly occurred in the case of large NA, and ZEMAX in this process can play a preliminary screening role. In addition, the beam waist radius decreased with increasing NA, and the elevated power density was to some extent conducive to the reduction of the threshold power, but as the Rayleigh length also decreased along with it, the reduced energy concentration region reduced the plasma size, while the mismatch between the two sizes can make the plasma maintenance require higher power, and the threshold power no longer decreased or even appeared to increase slowly, and the two factors, ω_0 and Z_0, each played a major role in maintaining the laser threshold of the plasma in different NA ranges.

Data availability statement

The original contributions presented in the study are included in the article/Supplementary Material; further inquiries can be directed to the corresponding author.

Author contributions

YC conceived the project, LZ and XG conducted the experiment, LZ and YC wrote the manuscript, YS provided ZEMAX scheme guidance, TZ helped with the measurement, CZ and SJ provided theoretical guidance and supervised the project. And all authors contributed to discussions during its preparation.

Funding

This work was funded by the Fundamental Research Funds for the Provincial Universities of Zhejiang (No: 2021YW03).

Conflict of interest

The authors declare that the research was conducted in the absence of any commercial or financial relationships that could be construed as a potential conflict of interest.

Publisher's note

Supplementary material

The Supplementary Material for this article can be found online at: https://www.frontiersin.org/articles/10.3389/fphy.2022.1072023/full#supplementary-material

References

1. Huddlestone RH, Leonard SL. *Plasma diagnostic techniques*. Massachusetts: Plasma Diagnostic Techniques (1965).

2. Kozlov G, Kuznetsov V, Masyukov V. Radiative losses by argon plasma and the emissive model of a continuous optical discharge. *Zh Eksp Teor Fiz* (1974) 66: 954–64.

3. Silfvast W, Wood O. Comparison of radiation from laser-produced and dc-heated plasmas in xenon. *Appl Phys Lett* (1974) 25(5):274–7. doi:10.1063/1.1655470

4. Biberman LM, Norman GÉ. Continuous spectra of atomic gases and plasma. *Sov Phys Usp* (1967) 10(1):52–90. doi:10.1070/pu1967v010n01abeh003199

5. Taudt C, Baselt T, Nelsen B, Assmann H, Greiner A, Koch E, et al. Characterization of edge effects in precision low-coherence interferometry using broadband light sources. *Opt Meas Syst Ind Inspection X* (2017) 10329:748–53. doi:10.1117/12.2270318

6. Ojaghi A, Fay ME, Lam WA, Robles FE. Ultraviolet hyperspectral interferometric microscopy. *Sci Rep* (2018) 8(1):9913–6. doi:10.1038/s41598-018-28208-0

7. Taudt C, Baselt T, Nelsen B, Assmann H, Greiner A, Koch E, et al. Evaluation of the thermal stability of a low-coherence interferometer for precision surface profilometry. *Photonic Instrumentation Eng IV* (2017) 10110:302–8. doi:10.1117/12.2252375

8. Bekefi G. *Principles of laser plasmas*. New York (1976).

9. Wang Y. *The reaseach based on the simulation of microwave plasma light source*. University of Electronic Science and Technology of China (2015). (in chinese).

10. Van Der Mullen J. On the atomic state distribution function in inductively coupled plasmas—II: The stage of local thermal equilibrium and its validity region. *Spectrochimica Acta B: At Spectrosc* (1990) 45(1-2):1–13. doi:10.1016/0584-8547(90)80078-W

11. Seely JF, Harris EG. Heating of a plasma by multiphoton inverse bremsstrahlung. *Phys Rev A (Coll Park)* (1973) 7(3):1064–7. doi:10.1103/PhysRevA.7.1064

12. Mora P. Theoretical model of absorption of laser light by a plasma. *Phys Fluids* (1982) 25(6):1051–6. doi:10.1063/1.863837

13. Raĭzer YP. Optical discharges. *Sov Phys Usp* (1980) 23(11):789–806. doi:10.1070/pu1980v023n11abeh005064

14. Zimakov V, Kuznetsov V, Solovyov N, Shemyakin A, Shilov A, Yakimov M, et al. Interaction of near-IR laser radiation with plasma of a continuous optical discharge. *Plasma Phys Rep* (2016) 42(1):68–73. doi:10.1134/s1063780x15110100

15. Khosrofian JM, Garetz BA. Measurement of a Gaussian laser beam diameter through the direct inversion of knife-edge data. *Appl Opt* (1983) 22(21):3406–10. doi:10.1364/AO.22.003406

16. Dickson LD. Characteristics of a propagating Gaussian beam. *Appl Opt* (1970) 9(8):1854–61. doi:10.1364/AO.9.001854

17. Yan H. *Evaluation of beam characteristics of high power semiconductor laser*. Changchun University of Science and Technology (2019). (in chinese).

18. Xiong X. *The measuring system of laser beam parameter and quality*. JiLin university (2007). (in chinese).

19. Mouroulis P, Macdonald J, Macdonald J. *Geometrical optics and optical design*. New York: Oxford University Press (1997). p. 351p.

frontiers | Frontiers in Physics

TYPE Brief Research Report
PUBLISHED 05 January 2023
DOI 10.3389/fphy.2022.1110683

OPEN ACCESS

EDITED BY
Zhenxu Bai,
Hebei University of Technology, China

REVIEWED BY
Hang Yuan,
Harbin Institute of Technology, China
Hongli Wang,
Korea Advanced Institute of Science and Technology, South Korea

*CORRESPONDENCE
Qilin Gao,
gaoqilinking@163.com

SPECIALTY SECTION
This article was submitted to Optics and Photonics, a section of the journal Frontiers in Physics

RECEIVED 29 November 2022
ACCEPTED 19 December 2022
PUBLISHED 05 January 2023

CITATION
Zhu X, Liu C, Gao Q, Su H and Sun S (2023), Spatiotemporal shaping of high power laser pulses based on stimulated brillouin scattering.
Front. Phys. 10:1110683.
doi: 10.3389/fphy.2022.1110683

Spatiotemporal shaping of high power laser pulses based on stimulated brillouin scattering

Xuehua Zhu[1,2,3], Chuangchuang Liu[1,2], Qilin Gao[4]*, Hao Su[1,2] and Sizhou Sun[1,2]

[1]School of Electrical Engineering Anhui Polytechnic University, Wuhu, China, [2]Key Laboratory of Advanced Perception and Intelligent Control of High-End Equipment, Ministry of Education, Anhui Polytechnic University, Wuhu, China, [3]Anhui Province Key Laboratory of Optoelectronic Materials Science and Technology, Wuhu, China, [4]College of Aerospace Engineering Guizhou Institute of Technology, Guiyang, China

We proposed and numerically demonstrated the combination of temporal and spatial shaping of high power nanosecond laser pulses based on stimulated Brillouin scattering (SBS) in this paper. With the intensity-dependence characteristic of SBS, the higher intensity parts of the laser beam obtain higher reflectivity, and the incident non-uniform high power laser beam would be well smoothed. A parameter adjustable feedback control loop was used to tailor the output temporal profile by pre-compensating the temporal profile of the input pump. In our numerical simulation, a 3 ns super-Gaussian shaped single-frequency laser pulse with a 527 nm wavelength was used as the pump. And the heavy fluorocarbon FC-70 was chosen as the Brillouin medium. Simulation results show that the laser spatial modulation can be significantly pulled down when the energy efficiency is maintained above 90% in our beam smoothing system with suitable laser intensity. The flat-toped laser pulses both in temporal and spatial domain were demonstrated to be achievable simultaneously. The method proposed here paves a simple and effective way to optimizing the near field pattern and temporal shape of high power laser systems.

KEYWORDS

spatial beam smoothing, pulse shape control, high power lasers, stimulated brillouin scattering, pre-compensation

1 Introduction

High-power lasers have broad applications in various fields [1–4], especially in the research of inertial confinement fusion for clean energy exploring. Controlling the uniformity of laser spatial and temporal profile acts a significant role in mitigating laser-induced damage and laser transmission in high-power laser systems. The spatial non-uniformity in a laser beam is mainly comes from the uneven gain in the active laser medium and the diffraction modulation caused by the intensity and phase perturbation of laser components. Because the optics damage in high power laser systems is closely related to the local intensity, the over-high local intensity should be suppressed by spatial beam shaping.

In the past decades, laser system engineering has accumulated several techniques to avoid excessive spatial modulation by using liquid crystal spatial light modulators (SLMs) [5–7], random phase plates [8], far-field spatial filter [9], and so on. Randomized phase plates is randomly arranged by hundreds of small units with 0 or π phase delay, and the far-field smoothing is realized through the superposition of diffraction of each unit. It is insensitive to wave-front distortion, but it has some problems such as low diffraction efficiency and easy to be

affected by incident wavelength. In general, SLM combined with spatial filtering can realize arbitrary spatial shaping in high-power laser systems. SLM is an active programmable beam shaping device, which can pre-compensate the non-uniformity of laser beam profile by adjusting the transmissivity of each pixel, with good results. However, the total transmissivity of SLM devices is relatively low [7], and the beam quality is improved at the cost of the output energy. In our previous research, we proposed a more effective method based on SBS to enhance laser near-field uniformity with high energy transmittance [10, 11]. SBS attracts extensive attention owing to its wide applications both in high quality laser generation [12–15], optical amplification [16, 17] and distributed optical fiber sensing [18]. In addition to the above applications, a special application called SBS optical limiting has attracted extensive attention [19–21]. When high power lasers with uneven beam profiles are injected into Brillouin medium and SBS is excited, the transmitted light energy and power will be limited to a certain level. A flat-topped profile in temporal or spatial domain can be obtained as a result of the non-linear properties of SBS [19]. This kind of optical limiting is easier to be realized in non-focusing scheme than multiphoton absorption and intensity dependent polarization rotators based optical limiting for its simpler structure and lower threshold [22, 23].

The SBS beam smoothing benefits from the higher reflectivity of higher intensity parts of laser beam, then a non-linear distortion occurs between profiles of output and input pulses. To obtain a flat-topped profile both in temporal and spatial domain, the input laser pulse shape should be pre-compensated strictly before introducing into the medium cell. In this paper, we demonstrate the temporal shaping of the output laser pulse from a Brillouin beam smoothing system by controlling the temporal profile of the pump laser with a feedback control loop. A top hat profile both in the temporal and spatial domain are obtained simultaneously in our numerical simulation with an energy efficiency of about 90%, which paves the way for the application of SBS in optical field shaping of high power laser systems.

2 Theory

The purpose of our work is to obtain top hat laser pulses both in temporal and spatial domain with SBS. The temporal pulse shape controlling and spatial beam smoothing process can be described by the following equations:

$$\nabla_T^2 \boldsymbol{A_P} + \frac{\partial \boldsymbol{A_P}}{\partial \boldsymbol{z}} + \frac{\boldsymbol{n}}{\boldsymbol{c}} \frac{\partial \boldsymbol{A_P}}{\partial \boldsymbol{t}} = \boldsymbol{ig\rho A_S} \tag{1}$$

$$\nabla_T^2 \boldsymbol{A_S} + \frac{\partial \boldsymbol{A_S}}{\partial \boldsymbol{z}} - \frac{\boldsymbol{n}}{\boldsymbol{c}} \frac{\partial \boldsymbol{A_S}}{\partial \boldsymbol{t}} = \boldsymbol{-ig\rho^* A_P} \tag{2}$$

$$\frac{\partial \boldsymbol{\rho}}{\partial \boldsymbol{t}} + \frac{\boldsymbol{1}}{\boldsymbol{2}} \boldsymbol{\Gamma \rho} = \frac{\boldsymbol{i\gamma q^2}}{\boldsymbol{16\pi \Omega_B}} \boldsymbol{A_P A_S^*} + \boldsymbol{f} \tag{3}$$

where the amplitude of the pump and Stokes are represented as A_p and A_s, and ρ is the amplitude of acoustic wave; n is the refractive index of the medium, c is the speed of light, g is the Brillouin gain coefficient, γ is the electrostrictive constant, q is wave vector of the acoustic wave, Ω_B and Γ denote the acoustic frequency and Brillouin linewidth, f is the thermal noise which initiates the spontaneous Brillouin scattering and it can be described as a Gaussian random function in our model. The first terms of the two optical field equations illustrate the diffraction of the pump and Stokes light, which can be used to study 3D property of SBS.

By numerically solving the equations, the SBS process with a large aperture pump can be simulated. In our simulation, the split-step Fourier method is used by assuming that in propagating the optical field over an iteration step, the diffraction and non-linear effects can be treated independently. In general, diffraction and non-linear effects act together along the length of the medium cell, but the above assumption acts well when the iteration step size is small enough. Fast Fourier transformation method is utilized to deal with the laser diffraction, while an implicit finite differencing in time and a backward differencing scheme in space are used for the algorithm of non-linear effects calculation.

The main parameters of non-linear medium and laser source used in our simulation are set as follows: the wavelength of pump light is 0.527 μm, the pump pulse duration is 3 ns, the refraction index of the non-linear material is 1.303, the Brillouin gain coefficient is 0.2 cm/GW, the acoustic frequency is 2.14 GHz and the phonon time is 5 ps (parameters above are corresponds to heavy fluorocarbon liquid materials FC-70 [11]). The beam diameter used in our simulation is 40 mm. The length of the medium cell is 350 mm.

3 Numerical results and discussions

3.1 Beam smoothing effect by SBS

With the proposed numerical model, spatial beam smoothing effect of a large aperture high power laser was studied. When the mean intensity of the pump is set to 1.68 GW/cm^2, the calculated 3D intensity distribution of the input and output laser in the near field are shown in Figures 1A, B. It can be seen clearly from the pictures that after propagating through the medium and exciting SBS, hot spots have been cleaned up, and the near field pattern was smoothed obviously. The energy conversion efficiency of the beam shaping system is calculated to be above 95%. The spatial modulation caused by the high spatial frequency components (see Figure 1A) can easily be removed in the far-field by conventional spatial filtering of the high-order spatial frequencies. But the pinhole spatial filtering system needs a high vacuum environment to prevent air breakdown at the focal point from polluting the optical element and requires complicated design to avoid ghost damage. The simple structure and high energy efficiency are the main advantages of our beam smoothing method compared with the traditional scheme.

The above simulation results verified that the near field of high power laser could be well cleaned up by SBS. However, when we focus on the time domain, the waveform of output pulse becomes distorted compared with the input laser pulse. Simulation results are shown in Figure 1C, the black dash line denotes the waveform of the pump pulse, the solid red line represents the temporal profile of the output laser pulse (the residual pump), and the solid blue line stands for that of the backward SBS. The parameters used here are the same as those above. It can be seen clearly from this figure that the transmitted laser is distorted noticeably in the trailing edge of the pump pulse. The main reason for this phenomenon is that part of the pump energy is taken off by the reflected Stokes light due to the non-linear development of

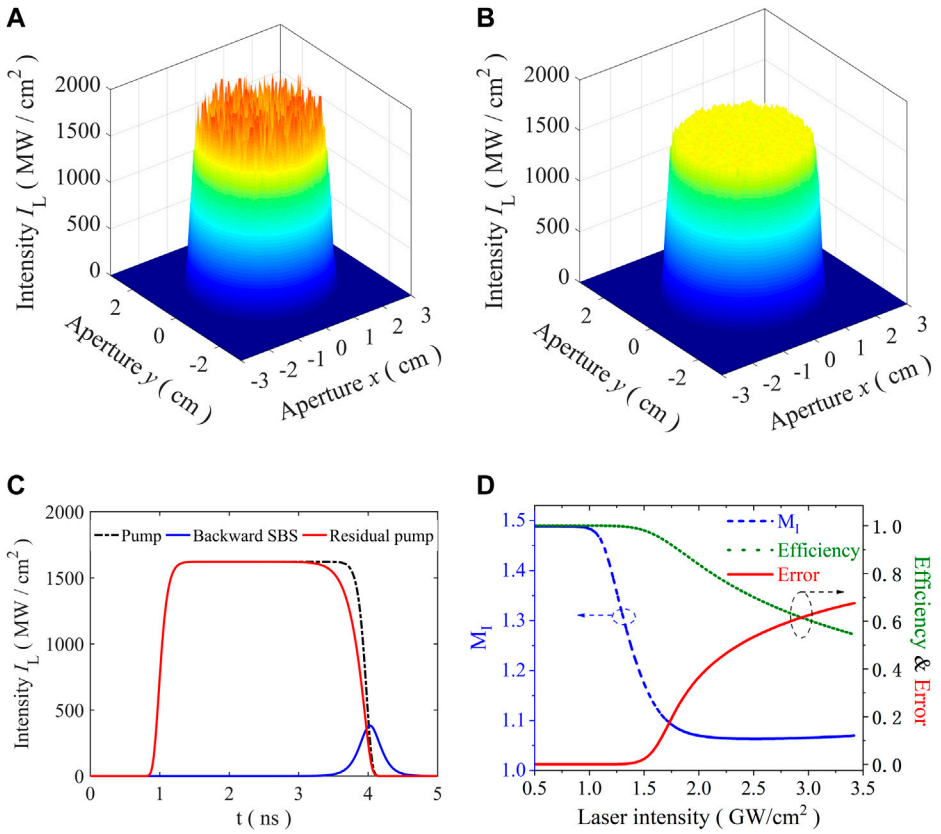

FIGURE 1
Numerical results of SBS beam smoothing. **(A)** Near field pattern of the pump **(B)** Near field pattern of the output light **(C)** Typical waveforms of the pump, Stokes and output pulse (residual pump) **(D)** Evolution of MI, η and PDR with the increasing of laser intensity.

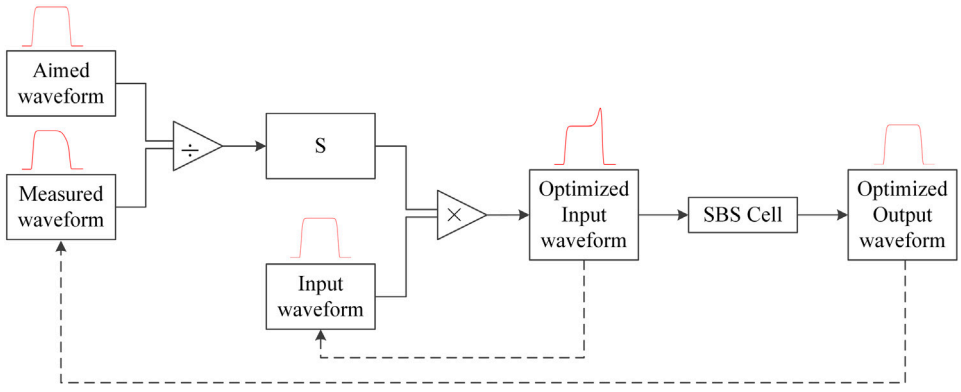

FIGURE 2
The process of the waveform pre-compensation.

SBS process. This distortion is harmful for applying the proposed beam smoothing scheme in high-power laser systems.

To quantitatively evaluate the SBS beam shaping effect, three parameters named the near field intensity modulation index (MI), energy efficiency (η) and pulse distortion ratio (PDR) were utilized. MI is defined as the ratio of the peak intensity to the average intensity in the flat top area of the laser field. Energy efficiency is related to the percentage of the output laser energy out of the total input laser energy. PDR denotes the distortion degree of the output pulses, and it is calculated with the following equation (24):

$$PDR = \sqrt{\frac{\sum\left(T(t) - \frac{\sum T(t)R(t)}{\sum R^2(t)}R(t)\right)^2}{\sum T^2(t)}} \quad (4)$$

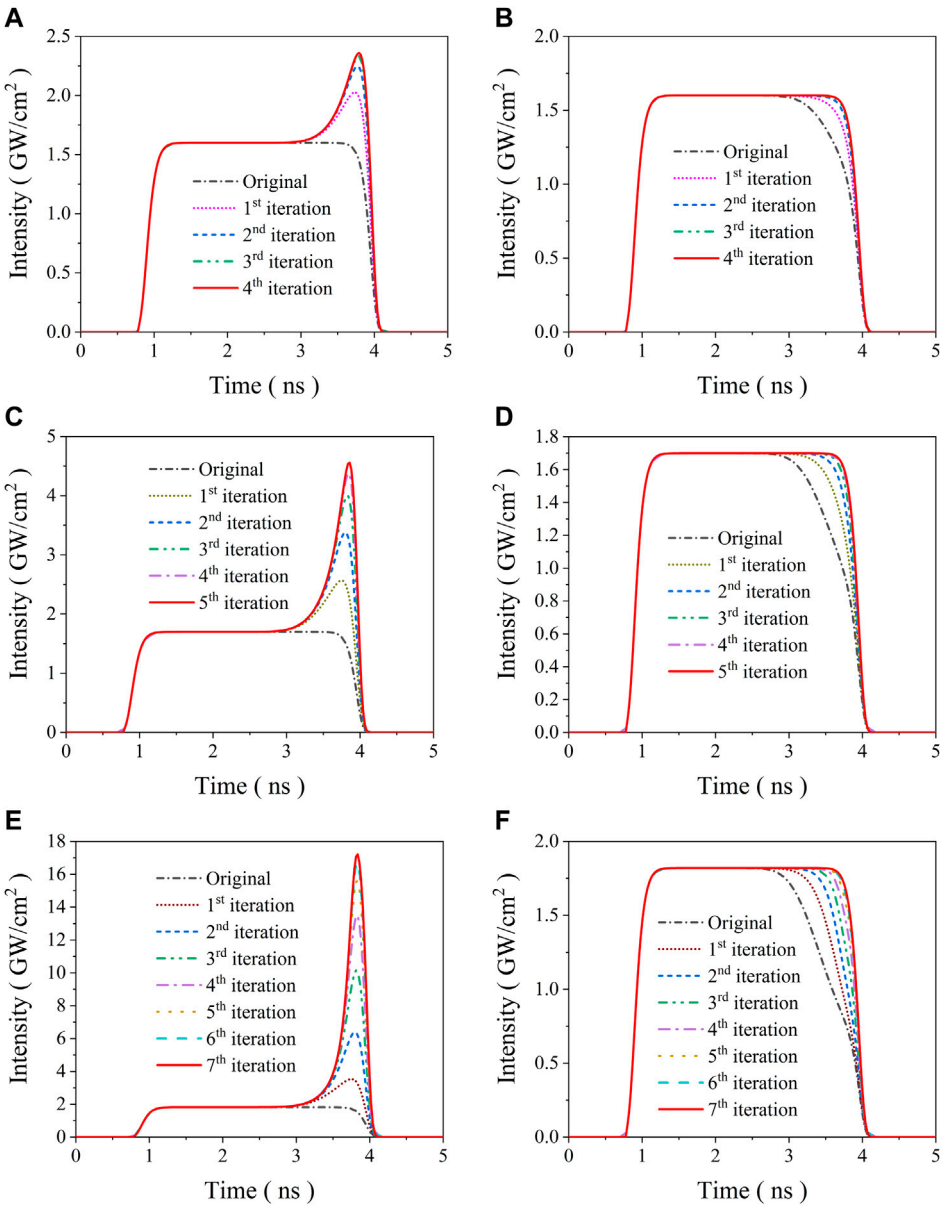

FIGURE 3
Simulation results of the pulse compensation with different pump intensities. **(A,B)** represent the pre-compensated pump waveforms and related output laser waveforms with the top-hat intensity of 1.6 GW/cm^2, **(C,D)** draw the correspond results with the top-hat intensity of 1.7 GW/cm^2, while **(E,F)** shows that of 1.82 GW/cm^2.

where T(t) and R(t) represent the temporal profile of the input (target) and the output (result) pulse shape, respectively. The above three parameters were calculated with the changing of pump laser intensity, and the results are shown in Figure 1D. The calculated results indicate that the MI factor decreases sharply with the raise of the pump intensity. The MI factor can be mitigated largely from 1.49 to 1.08 with an energy efficiency of 89.7% when the pump intensity is 1.82 GW/cm^2. The calculated energy efficiency of our scheme is much higher than that of the widely used method with SLM. However, time-domain distortion of the output pulse increases rapidly with the laser intensity, and the PDR was calculated to 0.25 when the pump laser intensity is 1.82 GW/cm^2. Thus, it is necessary to take some steps to balance the MI reduction and the PDR increase.

3.2 Pre-compensation of the laser pulses

According to the above explanation, the output laser pulse distortion in the time domain occurs in the falling edge of the pulse because of the avalanche increase of the Stokes light by extracting pump energy. Thus, it is easily comes to mind that the output pulse profile distortion would be weakened if the rear pulse edge has much higher intensity. Then, we utilize the following feedback compensation algorithm for pump pre-compensation, which is based on the ratio between the targeted and the obtained waveform. The pre-compensated pump profile can be described as:

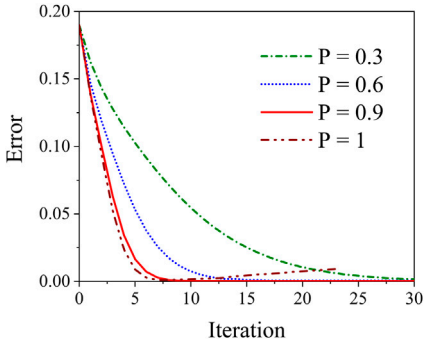

FIGURE 4
The relationship between output pulse distortion ratio and the calculation iteration with different parameter P.

$$\boldsymbol{I_n(t) = I_{n-1}(t) \cdot [P(S-1)+1]} \quad (5)$$

Where $I_{n-1}(t)$ represents the pump profile of the previous iteration, $S = \frac{T(t)}{R_{n-1}(t)}$ denotes the difference between the target waveform and the output laser pulse of the previous iteration, and P stands for the additional parameter which ranges from 0 to 1. The process of the waveform compensation with Equation 5 is shown in Figure 2. During each iteration, we calculate the parameter S with the aimed waveform and the measured waveform, firstly. Then the optimized pump profile of this iteration can be obtained after multiplying the previous pump waveform by the calculated parameter S. When the optimized pump is injected into the Brillouin cell, the output pulse will turn out to be much closer to the aimed profile. We repeat the above procedure until the output pulse is identical to the aimed pulse waveform.

To study the proposed feedback algorithms under test, we numerically simulated the compensation process with different laser intensities. The laser peak intensity used here were 1.6 GW/cm^2, 1.7 GW/cm^2 and 1.82 GW/cm^2 with a 3 ns pulse duration, and the parameter P of Equation 5 was set to 0.9. The calculated results are shown in Figure 3. Figures 3A, B draw the optimized pump and the related output pulses of each iteration with 1.6 GW/cm^2 pump. It can be seen from these two pictures that, when the proposed pre-compensation method is used, the back of the pump pulse rises and the output pulse distortion disappears gradually with the increase of the iteration times. A perfect flat-top output pulse can be obtained within four iterations. Figures 3C, D show the calculated results with a laser intensity of 1.7 GW/cm^2, the same phenomenon appears and the optimized flat-top output pulse was realized when five iterations were carried out. When the laser intensity was set to 1.82 GW/cm^2, seven iterations in our algorithm were needed to compensate the output pulse distortion (see Figures 3E, F). The energy conversion efficiencies of the SBS system for the optimized pump waveform with the above three peak intensities are calculated to be 92.3%, 81.1% and 52.3%, respectively. Then, we can conclude from the above simulation results that the output pulse profile can be pre-compensated with our algorithms perfectly, and the iteration times increase with the rise of pump intensity. The main reason is that much higher SBS reflectivity and more serious output pulse distortion occur with higher pump intensity. Meanwhile, it should be taken into consideration that the optimum temporal profiling necessitates a pronounced trailing edge of the pump pulse, whose required intensity is nearly one order of magnitude higher than that of the flat-top range when the laser intensity is 1.82 GW/cm^2. It is a challenge to produce such a laser pulse in practice, although pulse stacking technique has been widely used in high power laser systems. And it may even threatens the safe operation of the laser system when the trailing peak is too high. In view of these reasons, our temporal-spatial beam smoothing system should be operated slightly above the SBS threshold according to Figure 1D. This condition can be achieved by choosing suitable medium with low gain coefficient for powerful laser operation.

The proposed compensation algorithms shown in Equation 5 consist of an important parameter P, which controls the feedback depth of our method. Then, it is necessary to evaluate the influence of this parameter on output pulse pre-compensation. The above mentioned parameter PDR was calculated during each iteration with different P when the pump intensity was fixed as 1.82 GW/cm^2, the numerical results are shown in Figure 4. It can be seen clearly from this picture that the value of PDR drops sharply with the increase of iteration numbers, which indicates that the output pulse is compensated gradually with the proposed algorithms of this work. The compensate process develops more quickly with an increasing value of P. The output pulse can be optimized properly and the value of PDR remains nearly zero when the parameter P is below 0.9. But there exists an interesting phenomenon that the PDR index rebounds from bottom with the further increase of iteration number when the parameter P is set to 1, which indicates an instable compensation. From the above results we can draw a conclusion that the index P should be chosen slightly smaller than 1, and 0.9 is a proper value used in our calculation.

4 Conclusion

In this paper, we have presented a method to correct the temporal pulse profile at the output of a Brillouin cell used for laser beam smoothing by changing the pump pulse utilizing a feedback loop. This method is applied simply using the knowledge of the input and of the output of the system. We numerically studied the dependence of the pulse compensation performance on the number of iterations and the proportionality factor P. In our numerical simulation, a 3 ns 20th order super-Gaussian shaped laser pulse with a 527 nm wavelength was used as the pump and FC-70 was chosen as the Brillouin medium. The calculated results indicate that the near field modulation index droops obviously with a proper laser intensity and the output pulse distortion decrease exponentially as a function of iterations. Our method minimizes the error between the output pulse profile and the target flat-top laser pulse, only about seven iterations are needed to complete the compensate process for 1.82 GW/cm^2 pump intensity (which is the proper laser intensity for beam smoothing in our simulation) with a parameter value of 0.9. This simple spatiotemporal shaping scheme has good application potential in the output optimization high power and energy nanosecond lasers.

Data availability statement

The original contributions presented in the study are included in the article/supplementary material, further inquiries can be directed to the corresponding author.

Author contributions

XZ: Conceptualization, Programming, Acquisition of data, Drafting the manuscript, Funding acquisition CL: Analysis of data, Data Curation QG: Investigation, Visualization HS: Writing–Review and Editing SS: Investigation, Validation.

Funding

This work was funded by the National Science Foundation of China (No: 11704083), the Key Program of Natural Science Foundation of Anhui Provincial Education Department (No: KJ2020A0347) and the Open Research Fund of Anhui Province Key Laboratory of Optoelectronic Materials Science and Technology (No: OMST201903).

Conflict of interest

The authors declare that the research was conducted in the absence of any commercial or financial relationships that could be construed as a potential conflict of interest.

Publisher's note

References

1. Betti R, Zhou CD, Anderson KS, Perkins LJ, Theobald W, Solodov AA. Shock ignition of thermonuclear fuel with high areal density. *Phys Rev Lett* (2007) 98:155001. doi:10.1103/physrevlett.98.155001

2. Ping Y, Amendt P, Baker K, Smalyuk VA, Chen H, Khan S, et al. Reaching 30% energy coupling efficiency for a high-density-carbon capsule in a gold rugby hohlraum on NIF. *Nucl Fusion* (2021) 61:086028. doi:10.1088/1741-4326/ac108d

3. Rauscher P, Hauptmann J, Wetzig A, Beyer E. Domain refinement of grain oriented electrical steel with high power laser beam sources. *Int J Mod Phys B* (2014) 28:1442003. doi:10.1142/s021797921442003x

4. Hambling D. Laser weapon shouts, then burns people. *New Sci* (2018) 240:14. doi:10.1016/s0262-4079(18)31924-9

5. Ma H, Zhou P, Wang X, Ma Y, Xi F, Xu X, et al. Near-diffraction-limited annular flattop beam shaping with dual phase only liquid crystal spatial light modulators. *Opt Express* (2010) 18:8251–60. doi:10.1364/oe.18.008251

6. Li JN, Tang Y, Kuang Z, Schille J, Loeschner U, Perrie W, et al. Multi imaging-based beam shaping for ultrafast laser-material processing using spatial light modulators. *Opt Lasers Eng* (2019) 112:59–67. doi:10.1016/j.optlaseng.2018.09.002

7. Wu Y, Nie J, Shao L. Method to measure the phase modulation characteristics of a liquid crystal spatial light modulator. *Appl Opt* (2016) 55:8676–82. doi:10.1364/ao.55.008676

8. Dixit SN, Thomas IM, Woods BW, Morgan AJ, Henesian MA, Wegner PJ, et al. Random phase plates for beam smoothing on the Nova laser. *Appl Opt* (1993) 33:2543–54. doi:10.1364/ao.32.002543

9. Xiong H. Filtering differences and explanation of far-field spatial filters. *J Russ Laser Res* (2021) 42:181–9. doi:10.1007/s10946-021-09948-3

10. Zhu X, Wu D, Wang G, Wang Z. High efficiency laser spatial beam smoothing based on stimulated Brillouin scattering. *Laser Phys* (2019) 29:065402. doi:10.1088/1555-6611/ab16e0

11. Zhu X, Yang H, Wang G, Wu D, Qiu Y. Optimising of the material and laser parameters for high-power laser spatial beam smoothing based on stimulated Brillouin scattering. *Laser Phys* (2019) 29:075402. doi:10.1088/1555-6611/ab232a

12. Wang H, Cha S, Kong HJ, Wang Y, Lu Z. Rotating off-centered lens in SBS phase conjugation mirror for high- repetition-rate operation. *Opt Express* (2019) 27:9895–905. doi:10.1364/oe.27.009895

13. Wang Y, Zhu X, Lu Z, Zhang H. Generation of 360 ps laser pulse with 3 J energy by stimulated Brillouin scattering with a nonfocusing scheme. *Opt Express* (2015) 23:23318–28. doi:10.1364/oe.23.023318

14. Yang F, Gyger F, Thevenaz L. Intense Brillouin amplification in gas using hollow-core waveguides. *Nat Photon* (2020) 14:700–8. doi:10.1038/s41566-020-0676-z

15. Cui C, Wang Y, Lu Z, Yuan H, Wang Y, Chen Y, et al. Demonstration of 2.5 J, 10 Hz, nanosecond laser beam combination system based on non-collinear Brillouin amplification. *Opt Express* (2018) 26:32717–27. doi:10.1364/oe.26.032717

16. Zhu ZH, Chen P, Li HW, Zhao B, Zhou ZY, Hu W, et al. Fragmentation of twisted light in photon-phonon nonlinear propagation. *Appl Phys Lett* (2018) 112:161103. doi:10.1063/1.5020082

17. Zhu ZH, Gao W, Mu CY, Li HW. Reversible orbital angular momentum photon-phonon conversion. *Optica* (2016) 3(2):212–7. doi:10.1364/optica.3.000212

18. Bashan G, London Y, Diamandi HH, Zadok A. Distributed cladding mode fiber-optic sensor. *Optica* (2020) 7:85–92. doi:10.1364/optica.377610

19. Lu ZW, Hasi WLJ, Gong HP, Li Q, He WM. Generation of flat-top waveform by double optical limiting based on stimulated Brillouin scattering. *Opt Express* (2006) 14:5497–501. doi:10.1364/oe.14.005497

20. Hasi WLJ, Lu ZW, Fu ML, Lu HH, Gong S, Lin DY, et al. Improved output energy characteristic of optical limiting based on double stimulated Brillouin scattering. *Appl Phys B* (2009) 95:711–4. doi:10.1007/s00340-009-3485-0

21. Xu Y, Huang J, Wu Z, Lu Y. Non-linear optical limiting technology based on backward stimulated Brillouin scattering in grade-index optical fibres. *Electron Lett* (2021) 57:589–90. doi:10.1049/ell2.12204

22. Gu B, Rui GH, Xue YX, He J, Cui YP. Large enhancement of optical limiting effects in anisotropic two-photon absorbers by radially polarized beams. *J Opt Soc Am B* (2016) 33:2512–7. doi:10.1364/josab.33.002512

23. Lefort L, Barthelemy A. Intensity-dependent polarization rotation associated with type II phase-matched second-harmonic generation: Application to self-induced transparency. *Opt Lett* (1995) 20:1749–51. doi:10.1364/ol.20.001749

24. Oliveira P, Addis S, Gay J, Ertel K, Galimberti M, Musgrave I. Control of temporal shape of nanosecond long lasers using feedback loops. *Opt Express* (2019) 27:6607–17. doi:10.1364/oe.27.006607

frontiers | Frontiers in Physics

TYPE Brief Research Report
PUBLISHED 10 January 2023
DOI 10.3389/fphy.2022.1115544

OPEN ACCESS

EDITED BY
Zhenxu Bai,
Hebei University of Technology, China

REVIEWED BY
Qizhi Xu,
Beijing Institute of Technology, China
Jun Wang,
Nanjing University of Science and Technology, China

*CORRESPONDENCE
Wei Jin,
jw15536305816@163.com

SPECIALTY SECTION
This article was submitted to Optics and Photonics, a section of the journal Frontiers in Physics

RECEIVED 04 December 2022
ACCEPTED 19 December 2022
PUBLISHED 10 January 2023

CITATION
Zhang P, Jin W, Ren D and Lyu Y (2023), Measurement and reconstruction of geometric parameters of the barrel bore based on the laser scanning strategy. *Front. Phys.* 10:1115544.
doi: 10.3389/fphy.2022.1115544

Measurement and reconstruction of geometric parameters of the barrel bore based on the laser scanning strategy

Pengjun Zhang, Wei Jin*, Dongdong Ren and Yunfei Lyu

School of Mechatronics Engineering, North University of China, Taiyuan, China

The inner surface defects can be displayed intuitively by measuring the geometric parameters of rifling of the artillery barrel. In this paper, the parameters of the barrel bore were scanned based on the high-precision laser, and the three-dimensional reconstruction of the bore shape was conducted based on the test data. The wavelet transform was used for multiple de-noising of the test data, and the Delaunay triangulation interpolation algorithm was used to reconstruct the three-dimensional contour structure of the barrel bore, forming a high-fidelity measurement strategy for the parameters of the barrel bore. The results show that this measurement strategy can achieve the high-precision measurement of the geometric parameters of barrel rifling, and the accuracy can reach .001 mm. By comparing the measured value of rifling with the standard value, the flaw points in the rifling of the birth tube can be accurately specified. The three-dimensional model reconstruction based on the massive sample data realizes the high-fidelity measurement of rifling geometric parameters. This measurement strategy can provide support for the visualization of barrel rifling and effectively improve the detection accuracy of the barrel bore.

KEYWORDS

laser detection, inner bore, geometric reconstruction, rifling, laser scanning

1 Introduction

As the key component of artillery, the surface quality of the artillery barrel has an important influence on the firing accuracy, service life, projectile velocity, and other tactical and technical indicators [1]. The traditional barrel bore detection method mainly depends on the detection machinery to identify the relevant technical personnel use endoscope for defect detection. This detection method is not only time-consuming and labor-intensive, with detection accuracy, reliability, and low degree of automaton, but also the operator has certain technical requirements, and the subjective error is very large [2, 3]. With the development of photoelectric technology, sensor technology, image processing, computer technology, precision machinery technology, and electrical control technology, the detection technology of the barrel is also constantly improving. The current detection methods are mainly attributed to two categories. One is the contact measurement, such as the air plug gauge method. This kind of method is relatively mature, and the measurement time is short. It is mainly used in factory production detection, but it also has the disadvantage of low accuracy so that it cannot be widely applied [4, 5]. The other is the non-contact measurement, which uses optical scanning and reflection methods. Non-contact measurement methods include the CCD camera detection method, laser projection detection method, and laser triangulation method [6].

1) CCD camera detection method: This method uses the projection head in the barrel bore surface-projected aperture orthogonal to its axis, and then, the CCD camera is used to image the aperture; then, the image was used after relevant calculation to detect the barrel bore size [7, 8]. The advantages of the CCD camera detection method are high detection accuracy and fast image processing speed. The disadvantage is that the aperture must be imaged in the imaging area, and there are strict requirements on the focal length; otherwise, the detection accuracy will be greatly reduced.
2) Laser projection method: The annular laser emitted by the laser emitter in the laser projection detection system is reflected and projected onto the barrel bore to form an annular light spot. The light spot is then reflected by another mirror, and the receiving lens forms an optical image ring on the CCD. The image size of a section of the barrel can be obtained by processing the ring [9, 10]. When the detection system moves along with the barrel diameter, the size of the whole barrel can be measured. Although this detection method has high detection accuracy, the disadvantage is low detection efficiency [11].
3) Laser triangulation detection method: When the light source emitted by the semiconductor laser is illuminated to the surface of the inner wall of the barrel, the distance between the light source and the surface of the inner wall of the barrel is different, the angle of light reflection will be changed, and its imaging position on the linear CCD array of the laser displacement sensor will be changed synchronously [12, 13]. The advantages of the laser triangulation method are simple structure, a small measurement point, small shape, strong anti-interference ability, high measurement accuracy, and continuous measurement. However, the disadvantage is that the installation and debugging are relatively complicated [14].

The research purpose of this paper is to establish the artillery barrel bore detection system based on multi-laser sensor fusion. The system adopts the design method of combining the laser displacement sensor and laser range finder with an automatic feed device. According to the principle of the laser triangulation test, the experiment was carried out for an artillery barrel.

2 Barrel detection system

2.1 Laser triangulation test

The laser triangulation method is a measurement method designed by using the stability of the laser source and the propagation characteristics of the laser. The laser beam emitted by the laser is reflected on the surface of the measuring object, and the reflected light falls on the receiving surface through the mirror. The position of the falling spot will change with the distance between the laser and the measuring object, and the measuring distance can be calculated according to the falling point [15].

A laser is placed above the surface of the measured object, and the laser emits a beam to the measured surface through the condenser lens. Some of the laser will diffuse because the surface cannot be absolutely smooth. A lens is placed in front of the photodetector for imaging convergence, and the diffusely reflected laser will converge to a spot on the optical sensor. When the measured object is reversed, the spot will shift [16]. According to the displacement value, the angle θ between the incident laser and the divergent laser, the image distance L_1 and the object distance L_2, and the displacement value of the measured surface can be obtained. The relevant microprocessor is used to calculate and obtain the numerical results. The laser triangulation test diagram is shown in Figure 1.

2.2 Geometric characteristic parameter processing of the bore

The bore detection system uses the laser displacement sensor and laser range finder to collect the axial and radial data. Due to the measurement accuracy of the sensor and the vibration of the test equipment in the process of movement and other factors, the acquisition signal will be interfered, affecting the measurement accuracy of the data. Therefore, it is necessary to denoise the collected signal to reduce or eliminate the influence of the noise signal on the original signal and, thus, improve the measurement accuracy of the system.

2.2.1 Denoise method based on wavelet transformation

For the noise signal caused by the measurement accuracy of the sensor and the vibration in the acquisition process, the signal is usually denoised by filtering. In this paper, the wavelet transform of the ordered point filtering is used as the noise reduction method of system error. Wavelet transform is a new numerical analysis method based on the short-time Fourier transform (STFT) [17]:

$$F(w) = \int_{\infty}^{\infty} f(t)^{\star} e^{-iwt} dt, \tag{1}$$

$$WT(a,\tau) = \frac{1}{\sqrt{a}} \int_{-\infty}^{\infty} f(t)^{\star} \psi\left(\frac{t-\tau}{a}\right) dt, \tag{2}$$

where ω is the frequency of the Fourier transform, a is the scale of the wavelet transform for controlling the scaling of the wavelet transform and corresponds to the frequency, and τ is the shift of the wavelet transform which controls the shift of the wavelet function and corresponds to the time.

The approximate expansion of the wavelet transform is shown as follows:

$$f(t) = \sum_{k} \sum_{j} a_{j,k} \psi_{j,k}(t), \tag{3}$$

where $a_{j,k}\psi_{j,k}$ is the wavelet pole number, and the combination transformation of $a_{j,k}\psi_{j,k}$ forms the small basis of the wavelet transform.

The mother wavelet and father wavelet jointly determine the function of the wavelet transform, and the complete expansion is shown as follows:

$$f(t) = \sum_{k=-\infty}^{\infty} c_k \varphi(t-k) + \sum_{k=-\infty}^{\infty} \sum_{j=0}^{\infty} d_{j,k} \psi\left(2^j t - k\right), \tag{4}$$

where $\psi(t)$ is the mother wavelet and $\varphi(t)$ is the father wavelet (scale function). When $\psi(t)$ and $\varphi(t)$ have been initialized, the function $f(x)$ can be expanded into a linear combination of scaling functions and wavelet functions at different scales and positions [18], as shown in Eq. 4. In this equation, j is the scale order; the larger the j, the smaller the scale is, and the smaller the j, the larger the scale is; k is the position coefficient.

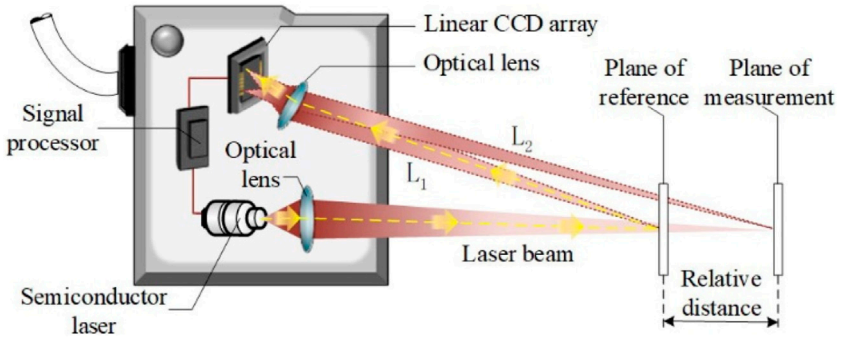

FIGURE 1
Laser triangulation test principle diagram.

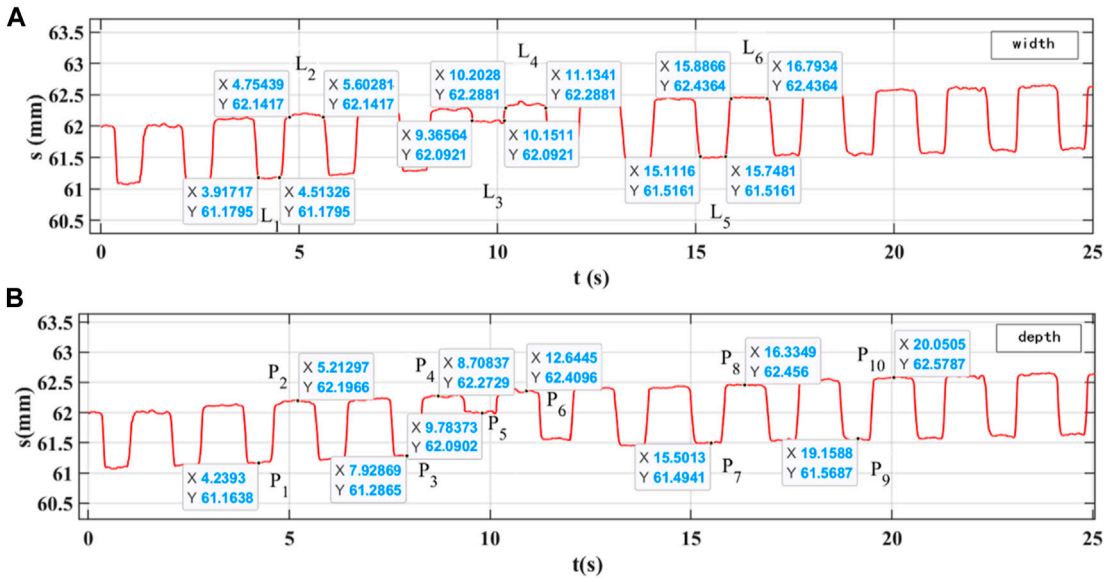

FIGURE 2
Barrel bore contour curve diagram. **(A)** Width of rifling. **(B)** Depth of rifling.

$$f(x) = \sum_{k} c_{j_0,k}\varphi_{j_0,k}(x) + \sum_{j>j_0}\sum_{k} d_{j,k}\psi_{j,k}(x), \tag{5}$$

where $c_{j_0,k}$ is the approximate coefficient and $d_{j,k}$ is the detail coefficient.

Their relationship is described by the following equation:

$$c_{j_0,k} = \int f(x)\varphi_{j_0,k}(x)dx, \tag{6}$$

$$d_{j,k} = \int f(x)\psi_{j,k}(x)dx. \tag{7}$$

In this paper, the wavelet base used in the wavelet transform is a function, and the approximate wavelet coefficients and detail wavelet coefficients under scale 3 are extracted. Then, the threshold of each layer is selected by using the unbiased likelihood estimation principle of the stein, and the threshold size is set to obtain the filtered data.

2.2.2 Calculation of rifling parameters after noise reduction

The width and depth of the filtered barrel rifling are collected and drawn into a curve. The standard barrel is tested, and the data on a certain section of the barrel are collected, as shown in Figure 2.

1) Width calculation

Assuming that two points $M_1(x_1,y_1)$ and $N_1(x_2,y_1)$ are taken on the continuous negative line and the positive line, the width calculation formula of the hatching and the width rifling rib is

$$l = \frac{2\pi(x_2 - x_1)y}{60}. \tag{8}$$

The width value of the rifling rib L_1 is 3.818 mm, L_3 is 5.104 mm, and L_5 is 5.104 mm; the width value of hatching L_2 is 6.045 mm, L_4 is 6.072 mm, and L_6 is 5.924 mm.

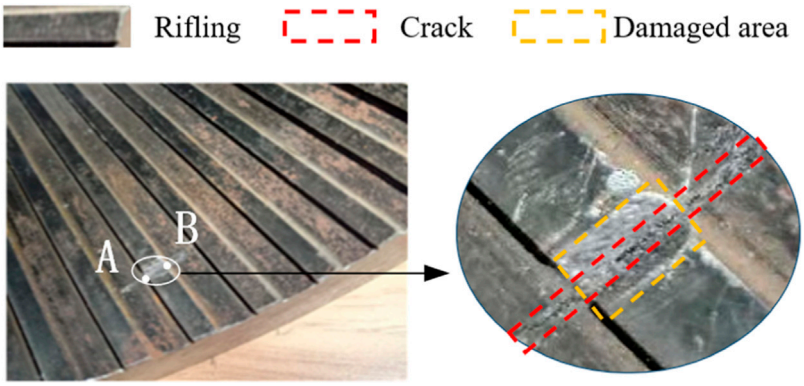

FIGURE 3
Bore flaw diagram.

2) Depth calculation

Collect the cross-sectional view of the barrel and measure several points at different positions on the continuous hatching and rifling rib and then calculate the depth value. The depth value of L_1 and L_2 is 1.033 mm, the depth value of L_3 and L_4 is .975 mm, and the depth value of L_4 and L_5 is .319 mm.

The width and depth of the processed and calculated rifling are compared with the standard parameters. The standard width of hatching is $6.06^{+0.3}_{-0.3}$ mm, the standard width of the rifling rib is $4.04^{+0.3}_{-0.3}$ mm, and the standard depth of the rifle is .98 mm.

Comparing the width test value with the standard parameters, the rifling rib L_3 shows the abnormal data. The width test value and depth test value of the other hatching and rifling rib are within the standard value error range. Finally, the test value can be accurate to .001 mm .

3) Defect calculation

It is a rifling diagram of the barrel, and the rifling rib in this position is abrasion. The section where the position is measured and the rifling diagram is obtained is shown in Figure 3.

In Figure 3, the coordinates of points A and B are A (9.366, 62.092) and B (10.151, 62.092) respectively; according to Eq. 8, the distance between the width of the defect is 5.104 mm. The depth value measured is .319 mm, and the standard rifling depth is .98 mm. We can calculate the wear depth of the defect is .661 mm.

3 3D reconstruction based on the Delaunay triangulation algorithm

The flexibility of the mesh surface reconstruction method is sufficient. For simple or complex surfaces, triangles or their variant forms can be used to fit and express. This method has strong versatility, which can be used across platforms for different fitting requirements, and it has become a common method in the 3D surface reconstruction [19]. The triangle is the smallest unit that represents a surface. Any surface can be decomposed into numerous small triangle surfaces. Therefore, this technique, as the triangulation method, is used commonly in mesh generation. There are many algorithms in the triangulation method, and Delaunay triangulation is one of them [20].

In this paper, the laser is used to scan the bore of the barrel in the radial direction to obtain the data on the profile of the bore at a certain cross-section position. Scanning multiple cross-sections of the barrel repeatedly along the axial direction to obtain the data from multiple profiles, then the data on multiple profiles are processed by three-dimensional data conversion. A function is used for three-dimensional drawing, and the specific steps are as follows:

1) Reading the data to be reconstructed and correcting by using the cosine theorem.
2) De-noising of the corrected data by the wavelet transform.
3) Coordinate conversion of the denoised data, converting polar coordinates into rectangular coordinates, $x_i = R_i \cos\theta_i$, $y_i = R_i \sin\theta_i$, and forming the x vector and y vector, respectively. Because the motor is in uniform motion during the operation, the angle of each turn of the motor keeps consistent, $\theta_i = i \times \frac{2\times\pi}{m}$, particularly $i \in \{1, m\}$, m is the total number of sampling points per lap. Draw a two-dimensional curve in the x–y plane with the converted two-dimensional data.
4) Taking the data collected by the laser range finder as the value of the z axis, the z vector of the z axis is formed, and it can obtain the coordinate value of the three-dimensional space (x, y, and z).
5) Drawing the three-dimensional curved figure of the tube bore after noise reduction.
6) Delaunay triangulation of x, y, and z vectors to form a new point set DT.
7) Drawing a 3D surface graph through a surface construction function.
8) A three-dimensional curved surface of the artillery barrel can be obtained by color filling with the shading function.

It can be seen from Figure 4 that the surface model of the barrel bore can be obtained after the three-dimensional reconstruction of the barrel bore based on Delaunay triangulation. After the local amplification, the flaws and defects of the barrel bore can be discovered and judged intuitively, which is mutually supported by the defects calculated by the two-dimensional curve, and provides visual support for the inner bore detection data.

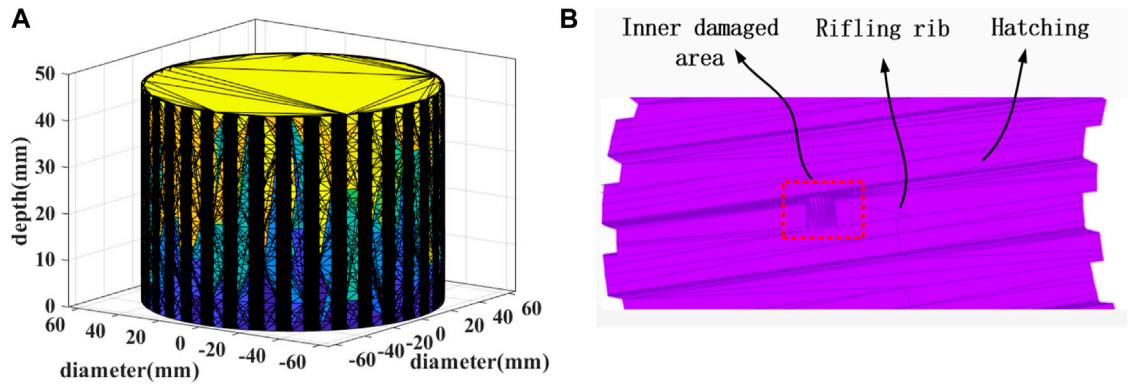

FIGURE 4
Three-dimensional reconstruction based on Delaunay triangulation. **(A)** Section of the barrel reconstruction model. **(B)** Damaged area reconstruction.

4 Conclusion

Based on the principle of the laser triangulation method, this paper studies the test technique of geometric parameters of the barrel bore. We performed laser scanning measurements on the actual barrel damage characteristics and reconstructed the three-dimensional model. The conclusion is as follows:

1) According to the principle of the laser triangulation test, the geometric parameters of rifling width, depth, and inner radius are extracted by the high-precision laser test method. The data measured can achieve a .001 mm level of accuracy. We obtained the data after noise reduction and the reconstructed artillery barrel contour curve.
2) The geometric parameters of the barrel bore are extracted and analyzed. By comparing the test values with the standard values, the defects of the barrel are accurately restored, and the quantitative non-destructive testing of defects is effectively solved.
3) The Delaunay triangulation algorithm is used to transform multiple contour data and changes the three-dimensional reconstruction of the barrel surface, which can realize the intuitive expression of the structure and defects of the barrel.

Data availability statement

The original contributions presented in the study are included in the article/Supplementary Material; further inquiries can be directed to the corresponding author.

Author contributions

PZ suggested a detection technology route based on the laser measurement of the barrel parameters and studied multiple noise reduction of the experimental data by the wavelet transform. In addition, the 3D contour structure of the barrel was reconstructed by the Delaunay triangulation interpolation algorithm. WJ analyzed the references in detail, constructed the main content of the manuscript, and was responsible for submission and improvement of the manuscript. He carried out numerical analysis of the collected geometric parameter characteristic curves and reconstructed the barrel 3D model, according to the technical route of this paper. DR established and successfully debugged the experimental system for detecting the internal parameters of the barrel. YL completed all the test items and experimental data collection job, according to the research needs.

Funding

This study was funded by the Pre-Researching Key Project of National Defense: 208052020305.

Conflict of interest

The authors declare that the research was conducted in the absence of any commercial or financial relationships that could be construed as a potential conflict of interest.

Publisher's note

All claims expressed in this article are solely those of the authors and do not necessarily represent those of their affiliated organizations, or those of the publisher, the editors, and the reviewers. Any product that may be evaluated in this article, or claim that may be made by its manufacturer, is not guaranteed or endorsed by the publisher.

References

1. Shen C, Zhou K, Lu Y, Li J. Modeling and simulation of bullet-barrel interaction process for the damaged gun barrel. *Defence Tech* (2019) 15(6):972–86. doi:10.1016/j.dt.2019.07.009

2. Wu B, Liu B, Zheng J, Wang T, Chen R, Chen X, et al. Strain-based health monitoring and remaining life prediction of large caliber gun barrel. *Measurement* (2018) 122:297–311. doi:10.1016/j.measurement.2018.02.040

3. Shanmugamani R, Sadique M, Ramamoorthy B. Detection and classification of surface defects of gun barrels using computer vision and machine learning. *J Meas* (2015) 60:222–30. doi:10.1016/j.measurement.2014.10.009

4. Huang FS, Chen L. CCD camera calibration technology based on the translation of coordinate measuring machine[C]//Applied Mechanics and Materials. *Trans Tech Publications Ltd* (2014) 568:320–5.

5. Fu X, Zhang Y, Zhang W, Li Q, Kong T. Research on the size of ring forgings based on image detection and point cloud data matching method. *Int J Adv Manufacturing Tech* (2022) 119(3):1725–35. doi:10.1007/s00170-021-08268-9

6. Choi YK, Pak JH, Seo K, Jeong SM, Lim T, Ju S. Realization of infrared display images using infrared laser projection method. *Opt Lasers Eng* (2021) 145:106677. doi:10.1016/j.optlaseng.2021.106677

7. Mueller T, Reithmeier E. Image segmentation for laser triangulation based on Chan–Vese model. *[J] Meas* (2015) 63:100–9. doi:10.1016/j.measurement.2014.12.007

8. Wu C, Chen B, Ye C. Detecting defects on corrugated plate surfaces using a differential laser triangulation method. *Opt Lasers Eng* (2020) 129:106064. doi:10.1016/j.optlaseng.2020.106064

9. Han Y, Sun H, Lu Y, Zhong R, Ji C, Xie S. 3D point cloud generation based on multi-sensor fusion. *Appl Sci* (2022) 12(19):9433. doi:10.3390/app12199433

10. Zhang X, Fan F, Gheisari M, Srivastava G (2019). A novel auto-focus method for image processing using laser triangulation[J]. *IEEE Access* 7.

11. Fu G, Menciassi A, Dario P. Development of a low-cost active 3D triangulation laser scanner for indoor navigation of miniature mobile robots. *Robotics Autonomous Syst* (2012) 60(10):1317–26. doi:10.1016/j.robot.2012.06.002

12. Wang B, Lan J, Gao J. LiDAR filtering in 3D object detection based on improved RANSAC. *Remote Sensing* (2022) 14(9):2110. doi:10.3390/rs14092110

13. Yang Y, Zhang Y, Wang Y, Liu D. Design of 3D laser radar based on laser triangulation. *KSII Trans Internet Inf Syst* (2019) 13(5):2414–33.

14. Son H, Kim C. Automatic segmentation and 3D modeling of pipelines into constituent parts from laser-scan data of the built environment. *Automation in Construction* (2016) 68:203–11. doi:10.1016/j.autcon.2016.05.010

15. Jung S, Lee YS, Lee Y, Lee K. 3D reconstruction using 3D registration-based ToF-stereo fusion. *Sensors* (2022) 22(21):8369. doi:10.3390/s22218369

16. Lu X, Schaefer S, Luo J, Low rank matrix approximation for 3D geometry filtering[J]. *IEEE Trans Visualization Comp Graphics* (2020) 1835–47. doi:10.1109/TVCG.2020.3026785

17. Xie Z, Yu D, Zhan C, Zhao Q, Wang J, Liu J, et al. Ball screw fault diagnosis based on continuous wavelet transform and two-dimensional convolution neural network. *Meas Control* (2022) 002029402211076. doi:10.1177/00202940221107620

18. Kedzierski M, Fryskowska A. Methods of laser scanning point clouds integration in precise 3D building modelling. *[J] Meas* (2015) 74:221–32. doi:10.1016/j.measurement.2015.07.015

19. Bhattarai S, Dahal K, Vichare P, Chen W. Adapted Delaunay triangulation method for free-form surface generation from random point clouds for stochastic optimization applications. *Struct Multidisciplinary Optimization* (2020) 61(2):649–60. doi:10.1007/s00158-019-02385-6

20. Sun H, Wang S, Bai J, Zhang J, Huang J, Zhou X, et al. Confocal laser scanning and 3D reconstruction methods for the subsurface damage of polished optics. *Opt Lasers Eng* (2021) 136:106315–5. doi:10.1016/j.optlaseng.2020.106315

frontiers | Frontiers in Physics

TYPE Mini Review
PUBLISHED 11 January 2023
DOI 10.3389/fphy.2022.1099101

OPEN ACCESS

EDITED BY
Baitao Zhang,
Shandong University, China

REVIEWED BY
Tao Zhang,
Guangdong University of Technology, China
Maojin Yun,
Qingdao University, China

*CORRESPONDENCE
Huarong Deng,
dhr@shao.ac.cn

SPECIALTY SECTION
This article was submitted to Optics and Photonics, a section of the journal Frontiers in Physics

RECEIVED 15 November 2022
ACCEPTED 30 November 2022
PUBLISHED 11 January 2023

CITATION
Long M, Deng H, Zhang H, Tan K, Lin Hs, Wu Z and Zhang Z (2023), An aperture of 21 cm telescope with polarized coaxial for satellite laser ranging.
Front. Phys. 10:1099101.
doi: 10.3389/fphy.2022.1099101

An aperture of 21 cm telescope with polarized coaxial for satellite laser ranging

Mingliang Long[1], Huarong Deng[1]*, Haifeng Zhang[1,2], Kai Tan[1], Hai sheng Lin[3], Zhibo Wu[1,2] and Zhongping Zhang[1,2,4]

[1]Shanghai Astronomical Observatory, Chinese Academy of Sciences, Shanghai, China, [2]Key Laboratory of Space Object and Debris Observation, Chinese Academy of Sciences, Nanjing, China, [3]School of Mechatronic Engineering and Automation, Shanghai University, Shanghai, China, [4]East China Normal University State Key Laboratory of Precision Spectroscopy, Shanghai, China

With the development of aerospace and space scientific research, satellite laser ranging (SLR) has put forward higher requirements for response speed, data density, and measurement accuracy. In coaxial common optical path laser ranging, the emitted laser and the received laser echoes pass through the same optical system. Due to the reversibility of the optical path, the laser emission, monitoring, and laser echoes' optical path all pass through the same optical system structure, and the response speed and ranging ability of the laser ranging system have been greatly improved. Based on the SLR system of the Shanghai Astronomical Observatory (SHAO), the laser transmitting telescope with an aperture of 21 cm was used to build a polarized coaxial SLR system. It uses a picosecond pulsed laser with a pulse repetition frequency of 2 kHz and a single-pulse energy of 2 mJ. Also, a 4f system was applied to shrink the laser echo beam and filter out noise, the measurements of low-Earth orbit and long-distance high-orbit satellites were realized, and the ranging accuracy was ~2 cm. As far as we know, this is currently the smallest aperture telescope for SLR globally, which is conducive to the miniaturization and integrated development of SLR systems.

KEYWORDS

satellite laser ranging, polarized coaxial, high pulse repetition frequency, 4f system, picosecond laser

1 Introduction

Laser ranging accuracy can reach sub-centimeters by satellite laser ranging (SLR), and it is widely used in determining the satellite attitude, high-precision time comparison, precision orbit setting, relativity verification, and other fields [1–5]. The emission optical path of the laser in the coaxial telescope laser ranging system would be the same as the monitoring optical path for the satellites, and also, the optical system of the return laser echoes through the same as the structure. The field of view for laser beam emission is the field of view monitored by the coaxial telescope. When the satellites fall in the field of view covered by the laser beam emission, the aiming of the satellites can be quickly achieved. At the same time, since the laser beam is emitting, the monitoring optical path and laser echoes' optical path all pass through the same optical structure, the changes in the surrounding ambient temperature have the same impact on the monitoring, emission, and laser echoes' optical path, and it can enhance the long-term stability of the laser ranging system, which is conducive to solving the problem of automated target aiming of the laser ranging system. Compared with the separate sending and receiving SLR, it can reduce the influence of aiming off-target caused by the influence of environmental factors on the transmitting optical path and the receiving optical path caused by the circling of

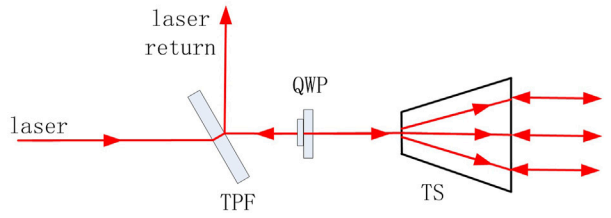

FIGURE 1
Schematic representation of a polarized coaxial generator for SLR.

TABLE 1 Measurement results of the polarized coaxial for SLR at the PRF of 2 kHz.

Number	Date	Satellite	Point	RMS/cm
1	2022/2/25	Glass132	547	1.89
2	2022/2/23	Ajisai	18,420	2.26
3	2022/2/24	Ajisai	412	2.33
4	2022/2/24	Cryosat2	190	1.9

the transmitting laser. At the end of the 20th century, the National Aeronautics and Space Administration (NASA) used a coaxial telescope to develop a highly automated SLR system named SLR2000 [6]. A high-precision sub-millimeter-level ranging Space Geodesy Satellite Laser Ranging (SGSLR) system also uses a coaxial telescope in recent years [7].

The coaxial telescope laser ranging in lunar laser ranging (LLR) can make full use of the advantages of large-aperture telescopes to compress the divergence of the laser beam angle [8]. At present, there are only a few LLR observatories in the world, such as Apollo (an aperture of 3.5 m telescope) in America, MLRS (McDonald Laser Ranging Station, an aperture of 2.7 m telescope), Grasse (an aperture of 1.5 m telescope) in France, and MLRO (Matra Laser Observation Observatory, an aperture of 1.5 m telescope) in Italy [8, 9]. In China, the Yunnan Observatory of the Chinese Academy of Sciences has developed the LLR system based on an aperture of 1.2 m coaxial telescope, which used a mechanical rotating mirror with a pulse repetition frequency (PRF) of 10 Hz [10]. Immediately afterward, the LLR of the 'Tian Qin Project' of Sun Yat-sen University was up to 100 Hz [11]. At present, the rotating mirror method is generally used in the process of coaxial ranging. However, it is affected by the speed of turning the mirror, and the PRF is low and hard to increase; this makes the amount of measurement data small, and also a large-energy laser pulse output is required, which puts forward much higher requirements for the laser.

In this paper, a polarization coaxial telescope laser ranging method was applied to build a small SLR with an aperture of 21 cm telescope based on the SLR system of the Shanghai Astronomical Observatory (SHAO). With the polarization coaxial telescope, the PRF of SLR can be raised higher than that of a rotating mirror.

2 Analysis of polarized coaxial laser ranging

As the equation laser ranging [12], the average number of laser echo points D per unit time is:

$$D = fe^{-(n_1+n_2)}\left(1 - e^{-\frac{16}{\pi^2}\bullet\frac{\lambda\eta_q}{hc}\bullet\frac{E_t A_r A_s}{R^4\theta_t^2\theta_s^2}\bullet T^2\bullet K_t\bullet K_r\bullet\alpha}\right), \quad (1)$$

where λ is the wavelength of the laser, h is the Planck constant, c is the light velocity, η_q is the quantum efficiency of a single-photon detector (SPAD), E_t is the single-pulse laser energy, A_r is the effective receiving area of the telescope, A_S is the reflection area of the reflector, T is atmosphere one-way transparency, K_t is the efficiency of transmitting optics, K_r is the efficiency of receiving optics, α is the attenuation factor, θt is the divergence of the laser beam, and θ_s is the reflector divergence angle. R is the distance from the ground station to satellite, n_1 is generated by background noise, and n_2 is generated by the dark noise of the SPAD itself. From the aforementioned formula, in order to increase the average number of laser echo points D, the PRF

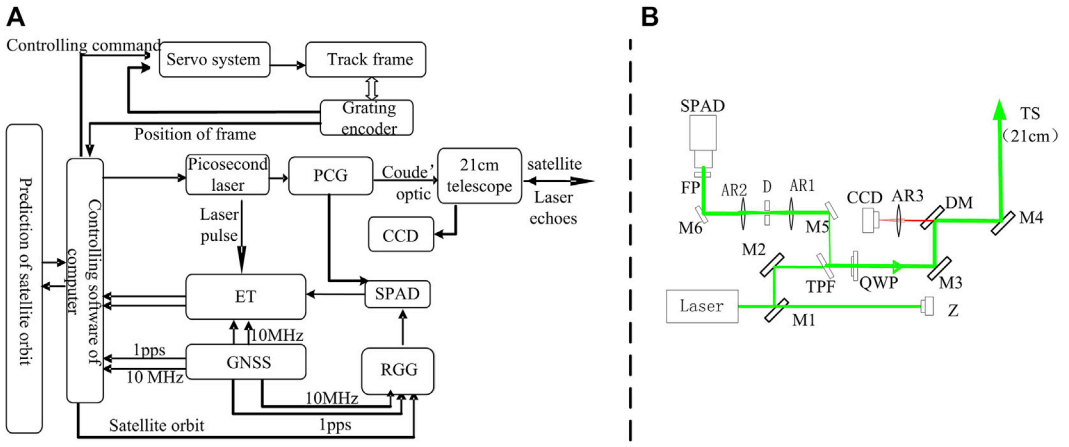

FIGURE 2
Structure **(A)** and optical path diagram **(B)** of the polarized coaxial SLR system.

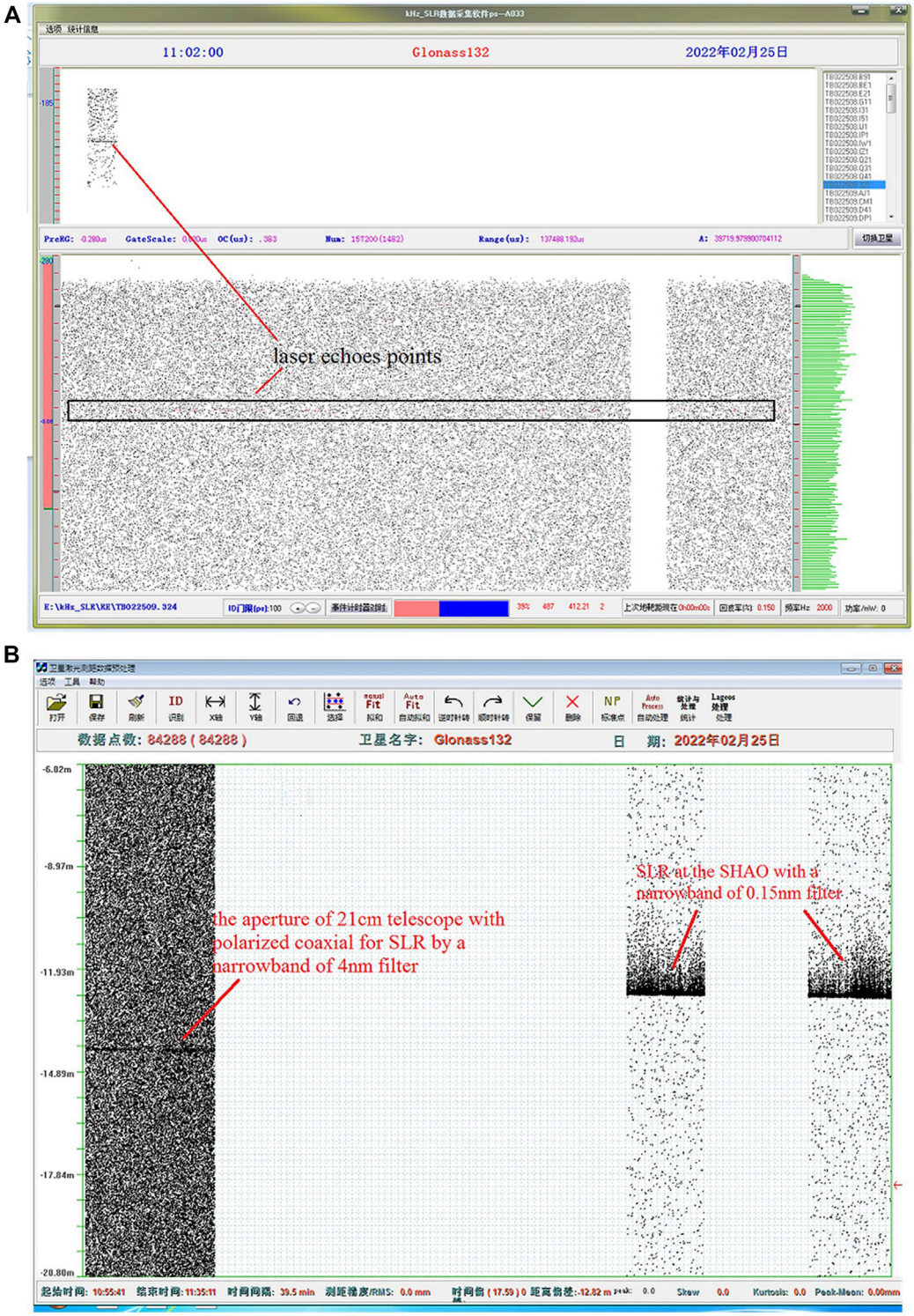

FIGURE 3
Real-time measurement **(A)** and data processing of the Glonass 132.

of the laser should be increased; therefore, when D is constant, increasing the PRF can reduce the single-pulse energy of the pulse laser or the effective receiving area of the system, that is, a receiving telescope with a small-aperture telescope and a low-pulse energy laser with a high PRF can be used. It is much easier to be achieved than that of a large-aperture telescope with large pulse laser energy in a low PRF.

Polarized coaxial laser ranging only requires the polarization state of the output laser, and there is no requirement for the PRF. It is possible to achieve laser ranging with a high PRF. The polarization coaxial method is shown in Figure 1, and the TFP is the thin film plate polarizer, the QWP is the quarter wave plate, and the TS is the telescope, which make a polarized coaxial

generator (PCG). The linearly polarized laser passes through the TFP, and its polarization rotates 90° through the QWP to become a circularly polarized laser, and is emitted from the TS. The returned laser echo passes through the TS, QWP, at this time the circularly polarized laser changes to the vertically polarized laser, it would be reflected by the TPF, and the laser echoes would be obtained by the SPAD, therefore, laser emission and laser echoes received would be by the same telescope, and also this has nothing to do with the PRF of the laser, the high frequency coaxial laser ranging systems can be applied, which can reduce the single-pulse energy of the laser, and the small receiving area to improve the measurement accuracy and enhance the stability of the system.

3 High PRF of the polarized coaxial satellite laser ranging system

The system is designed based on the SLR of the SHAO [13–15], as shown in Figure 2. Compared with the traditional high PRF of the SLR system of the SHAO [15], its laser transmitting telescope with an aperture of 21 cm was applied, the laser emission, laser reception, and satellite monitoring were all used by the aperture of 21 cm telescope system. The average power of 4 W at the wavelength of 532 nm ps laser with a divergence angle of 0.6 mrad was used, and its pulse width is about 30 ps, the PRF was 2 kHz, and beam quality was $M^2 = 1.2$.

The structure of polarized coaxial SLR was as shown in Figure 2A. The satellite orbit prediction parameters are downloaded to the controlling software of the computer, and the computer processes convert the satellite orbit prediction parameters, then it sends out controlling command to the servo system, which controlled the telescope mount to track the satellite with accurate feedback track from the grating encoder. The satellite would be monitored by the aperture of 21 cm polarized coaxial telescope's monitoring charge coupled device (CCD). At this time, the laser is ignited by a ranging gate generator (RGG) through the coupé optics and the aperture of 21 cm telescope to the satellite, and also the laser pulse is processed by a discriminator, and it is sent to the event timer (ET). The ET (USB, A033 origin Latvia) would be started, and it sent the start time of laser pulses t_1 to the computer, and gated pulses from RGG would be sent to SPAD (by East China Normal University, China). The laser echoes passed through the receiving system to the SPAD, and the return time t_2 is obtained by the ET. In all, the RGG, computer, and ET were provided high-precision time from the GNSS′ clock. Delaying of $\triangle t_0$ from the polarized coaxial SLR system is considered, with the speed of light C, and the range of satellite R was as shown:

$$R = \frac{(t_2 - t_1 - \Delta t_0)\bullet C}{2}. \quad (2)$$

The optical path diagram of polarized coaxial SLR is shown in Figure 2B, M1, M2, M3, M5, and M6 are 45° reflective mirrors with high reflectivity mirrors at the wavelength of 532 nm green laser, DM is a 45° dichroic mirror, which is highly reflectivity at the wavelength of 532 nm and highly transmission efficiency at the other wavelengths (more than 550 nm). M4 is a 45° reflective mirror that is highly reflective in the entire visible band. The lenses AR1 and AR2 comprise a 4f system, which can reduce the laser beam to one-third. D is a small aperture, and it is located in the focal position of AR, FP is a narrow band of 4 nm filter, the SPAD is a single-photon detector, Z is the laser pulse photoelectric probe, and TS is the aperture of 21 cm telescope. The laser beam from the laser was transmitted by the M1, M2, TPF, QWP, M3, DM, M4, and TS to the satellite, and the return laser echoes were transmitted by the M4, DM, QWP, TPF, M5, AR1, D, AR2, M6, and FP to the SPAD.

The beam size of the laser echoes from the TS is larger than the receiving aperture of the SPAD. The laser echo beam needs to be compressed to reach the allowable receiving caliber of the SPAD, therefore, the lenses AR1 and AR2 are used to form a 4f system, which can reduce the laser echo beam to one-third. The laser will have part of the laser diffused and diffuse reflected on the mirrors. A small hole aperture D is inserted at the focus position of the 4f system, which can filter out most of the diffuse light into the SPAD. At the same time, the entire echo receiving part is placed in a dark box to avoid diffuse light entering the SPAD from other spaces, and also the diffuse laser from diffuse and diffuse reflection can easily enter the field of view, which would saturate interference of CDD. In this, the satellite was monitored by the CCD when the laser was output.

4 Measurement results and discussion

With the aforementioned configuration of the SLR system, an aperture of 21 cm telescope with polarized coaxial for SLR was built, the data measurement results are shown in Table 1.

As shown in Figure 3, it is the real-time measurement (Figure 3A) and measurement data processing (Figure 3B) of the laser echo detection of the far-Earth Satellite of Glonass 32, it is about 20,000 km far away, the ranging precision of root mean square is 1.89 cm. As in Figure 3B, owing to the narrow band of the 4 nm filter, the aperture of the 21 cm telescope with polarized coaxial for SLR has more noise points than that of conventional SLR at the SHAO with a narrow band of 0.15 nm filter. Also, if a narrow band of 0.15 nm filter is used in polarized coaxial for SLR, the noise points would be reduced, and the number of laser echo points would be increased.

5 Conclusion

From the laser ranging equation, the requirements of pulse energy and receiving telescope size in the SLR system can be reduced by increasing the PRF of laser ranging. Through the transformation of the original ranging system of the SHAO, a PRF of 2 kHz polarized coaxial laser ranging system with an aperture of 21 cm telescope has been established. A satellite that is 20,000 km away satellite was measured with an RMS of 1.89 cm: as far as we know, this is currently the smallest aperture telescope for

SLR globally for a satellite at this distance. It is demonstrated that the system could achieve small-size receiving telescopes for SLR, and it would provide high-precision laser ranging with high repetition frequency for the LLR, which can provide the basis for the miniaturization, integration, and automation development of the SLR ranging system in the future.

Author contributions

ML conceived the project, and ML, HD, HZ, ZW, and HL conducted the experiment. ML wrote the manuscript, and all authors contributed to discussions during its preparation. ZZ and ML supervised the project.

Funding

This work was supported by the Shanghai Science and Technology innovation action (21142201900) and the Natural Science Foundation of Shanghai (20ZR1467500).

Conflict of interest

The authors declare that the research was conducted in the absence of any commercial or financial relationships that could be construed as a potential conflict of interest.

Publisher's note

All claims expressed in this article are solely those of the authors and do not necessarily represent those of their affiliated organizations, or those of the publisher, the editors, and the reviewers. Any product that may be evaluated in this article, or claim that may be made by its manufacturer, is not guaranteed or endorsed by the publisher.

Supplementary material

The Supplementary Material for this article can be found online at: https://www.frontiersin.org/articles/10.3389/fphy.2022.1099101/full#supplementary-material

References

1. Schreiber K, Kodet J. The application of coherent local time for optical time transfer and the quantification of systematic errors in satellite laser ranging. *Space Sci Rev* (2018) 214:22. doi:10.1007/s11214-017-0457-2

2. Bonin J, Chambers D, Cheng M. Using satellite laser ranging to measure ice mass change in Greenland and Antarctica. *The Cryosphere* (2018) 12:71–9. doi:10.5194/tc-12-71-2018

3. Zhao S, Steindorfer M, Kirchner G, Zheng Y, Koid F, Wang P, et al. Attitude analysis of space debris using SLR and light curve data measured with single-photon detector. *Adv Space Res* (2020) 65(5):1518–27. doi:10.1016/j.asr.2019.12.005

4. Lucchesi DM, Anselmo L, Bassan M, Pardini C, Peron R, Pucacco G, et al. Testing the gravitational interaction in the field of the Earth via satellite laser ranging and the Laser Ranged Satellites Experiment (LARASE). *Class Quan Gravity* (2015) 32(50):155012. doi:10.1088/0264-9381/32/15/155012

5. Bai Z, Chen H, Gao X, Li S, Qi Y, Bai Z. Highly compact nanosecond laser for space debris tracking. *Opt Mater* (2019) 98:109470. doi:10.1016/j.optmat.2019.109470

6. Degnan JJ, Mcgarry J, Zagwodzki T, Donovan H, Patterson D, Steggerda C, et al. *NASA's photon-counting SLR2000 satellite laser ranging system: Progress and applications*. Maui, HI (2002).

7. Mcgarry JF, Hoffman ED, Degnan JJ, Cheek J W, Clarke C, Diegel I, et al. NASA's satellite laser ranging systems for the twenty-first century. *J Geod* (2019) 93(11):2249–62. Springer Berlin Heidelberg. doi:10.1007/s00190-018-1191-6

8. Battat J, Murphy TW, Adelberger EG, Gillespie B, Hoyle CD, Mcmillan RJ, et al. Corrigendum: The Apache point observatory lunar laser-ranging operation (Apollo): Two years of millimeter-precision measurements of the earth-moon range (2009, PASP, 121, 29). *Publ Astron Soc Pac* (2009) 121:049201. doi:10.1088/1538-3873/129/974/049201

9. Courde C, Torre JM, Samain E, Martinot-Lagarde G, Aimar M, Albanese D, et al. Lunar laser ranging in infrared at the Grasse laser station. *Astron Astrophysics* (2017) 602. doi:10.1051/0004-6361/201628590

10. Li Y, Fu H, Wan L, Tang R, Li Z, Zhai D, et al. Research and experiment of lunar laser ranging in Yunnan Observatories. *Chin J lasers* (2019) 46(1). doi:10.3788/cjl201946.0104004

11. Gao T, Zhou L, Zhang C, Zhao H, Wu X, Li M. Lunar laser ranging based on a 100 Hz repetition frequency. *Appl Opt* (2021) 60(36):11058. doi:10.1364/ao.442263

12. Long M, Zhang H, Yu RZ, Wu Z, Qin S, Zhang Z. Satellite laser ranging at ultra-high PRF of hundreds of kilohertz all day. *Front Phys* (2022) 10:1036346. doi:10.3389/fphy.2022.1036346

13. Long M, Zhang H, Meng L, Wu Z, Deng H, Qin S, et al. Satellite laser ranging at high-repetition 10 kHz in all day. *J.Infrared Millim Waves* (2020) 39:778~785.

14. Long M, Zhang Z, Chen Z, Zhang H, Deng H, Wu Z, et al. A picosecond laser at 1 kHz with dual-length of regenerative amplifier for the SLR in the daytime. *Optik (Stuttg)* (2018) 171:833–8. doi:10.1016/j.ijleo.2018.06.143

15. Deng H, Zhang H, Long M, Wu Z, Tang K, Zhang Z. 4 kHz repetition rate satellite laser ranging system and its application. *Acta optica sinica* (2019) 39:0314002. doi:10.3788/aos201939.0314002

frontiers | Frontiers in Physics

TYPE Brief Research Report
PUBLISHED 12 January 2023
DOI 10.3389/fphy.2022.1115447

OPEN ACCESS

EDITED BY
Zhenxu Bai,
Hebei University of Technology, China

REVIEWED BY
Jianglin Zou,
Beijing University of Technology, China
Xiaorong Guan,
Nanjing University of Science and Technology, China

*CORRESPONDENCE
Pengjun Zhang,
zhangpj@nuc.edu.cn

SPECIALTY SECTION
This article was submitted to Optics and Photonics, a section of the journal Frontiers in Physics

RECEIVED 04 December 2022
ACCEPTED 28 December 2022
PUBLISHED 12 January 2023

CITATION
Ren D, Zhang P, Yu J, Yao Y and Li X (2023), Study on the quenching depth and surface hardness of metal materials by laser quenching variable parameters.
Front. Phys. 10:1115447.
doi: 10.3389/fphy.2022.1115447

Study on the quenching depth and surface hardness of metal materials by laser quenching variable parameters

Dongdong Ren[1], Pengjun Zhang[1]*, Jiahui Yu[1], Yangwu Yao[1] and Xiaoyang Li[2]

[1]School of Mechatronics Engineering, North University of China, Taiyuan, China, [2]Military and Political Training Department, Shijiazhuang Division of PLAA Infantry Academy, Shijiazhuang, China

Laser quenching is one of the most outstanding gear tooth surface quenching methods due to its high efficiency, environmental friendliness, and performance consistency. Since gear tooth surface laser quenching requires repeated scanning, changing the laser scanning velocity and power by program control can meet the needs of variable depth quenching. The effects of laser scanning velocity and output power on the quenching depth and surface Rockwell hardness after quenching were studied and experimentally analyzed. The result shows that by adjusting the parameters, the surface hardness of the specimen changes slightly with the actual received laser energy. However, the quenching depth can be consistent with the laser scanning velocity. The maximum surface Rockwell hardness that a laser quenched material can achieve depends on the material itself, not on the laser power or scanning velocity. Compared with accelerated laser quenching, decelerated laser quenching is more suitable for tooth surface machining due to the cumulative effect of energy within the quenching depth range of metal materials.

KEYWORDS

laser quenching, quenching depth, Rockwell hardness, scanning velocity, dimensionless power

1 Application introduction

High-frequency laser quenching is a technology widely used in the heat treatment process of metal materials, which is an effective method to improve the mechanical properties of steel with high carbon content [1, 2]. Feng [3] studied the microstructure and mechanical properties of composite strengthened high chromium cast iron by laser quenching and laser shock processing. The microstructure observation, microhardness, residual stress and full width at half maximum (FWHM) measurement, impact toughness, and wear experiment were carried out on untreated, laser quenched, and laser quenched-laser shock peening high chromium cast iron samples. Tang [4] adopted a new laser induction hybrid quenching process, combined with laser and electromagnetic induction heat source, to improve the depth and uniformity of the laser hardening layer of 42CrMo steel. Li [5] established a combination of temperature and microstructure prediction models for laser quenching of GCr15 bearing steel. Based on the experimental results, the temperature and microstructure evolution of GCr15 bearing steel during laser quenching were simulated. YasudaT [6] characterized the nanomechanics and sub-microstructure of laser quenching-induced heat-affected zone (HAZ) of carbon steel.

The mechanical properties of the samples were characterized by nanoindentation, and the microstructure was observed by using a scanning electron microscope (SEM).

The gear transmission system relies on the meshing contact of the gear tooth surface to transmit power. One of the biggest influencing factors of the non-linear dynamic characteristics of the system is the dynamic meshing stiffness. One of the factors affecting the dynamic meshing stiffness of the gear system is the local material stiffness of the meshing area of the tooth surface, which is determined by the surface hardness of the material and the characteristics of the shallow structure. At present, laser quenching is one of the most environment friendly and easy-to-control process quality among several gear tooth surface quenching technologies, which has the highest consistency of mechanical properties after quenching. Related physical and chemical mechanisms and processing equipment and technology are constantly being widely studied and applied. Surface hardening heat treatment is widely used to improve tooth surface properties such as wear and rolling contact fatigue [7, 8]. After the experiment, Cai [9] found that the cracks mainly appeared in the top fillet, pitch circle, and tooth root of the gear. The size and distribution of slag inclusions in 16MnCr5 steel also had a certain influence on the origin of gear surface cracks. Barglik, J [10] measured the microstructure of gears by continuous dual-frequency induction hardening of small gears made of special quality steel AISI 4340. Li [11] studied the quenching microstructure and hardness distribution of 40Cr gear steel by means of a Axioskop 2 scanning electron microscope, KEYENCE VH-Z100R ultra-depth 3D microscope, and Q10M microhardness experimenter and revealed the mechanical behavior and phase hardening law of the material during quenching.

In general, in the application of the processing industry, the high consistency of the mechanical performance of the products is guaranteed by the initial settings of the laser, such as source power, wavelength, and other parameters. Therefore, many studies have been carried out based on invariant laser source characteristic parameters [12]. In this paper, several laser light source parameters that can be automatically adjusted by the laser control system are selected, and their changes in the mechanical properties of the gear tooth surface after quenching are experimented and studied. Considering that the laser quenching technology is applied to gear tooth surface quenching with a modulus more than 5, the results will be excellent. Therefore, we focus on the laser light source power, scanning velocity, and scanning frequency to analyze the tooth surface quenching depth and Rockwell hardness. At the same time, in order to obtain more accurate numerical results in the experiment, the laser quenching experiment was carried out by using the method of plane specimen and laser vertical scanning in the process of controlling the experiment variables.

2 Theoretical analysis of laser quenching

Laser scanning quenching used in this paper is a directional transmission of heat by transforming a cylindrical laser beam passing through a set of zoom field lens into a fan-shaped beam illuminating the target surface, and then, a local heating layer is formed on the surface of the material. The heat conduction from the high-temperature surface of the material to the substrate is the main heat transfer mode of laser quenching, and it is also the key to phase transformation hardening during laser quenching. Laser quenching phase transformation hardening can obtain higher residual compressive stress on the surface, which is determined by the characteristics of laser quenching local treatment.

As the material cools, the structure changes and its unit volume also changes, resulting in an increase in the volume of the material and an increase in compressive stress, and the direction of this structural transformation is opposite to the direction of heat conduction, that is, the inner layer points to the surface of the material. Therefore, the volume of the material's structural transformation increases, causing the compressive stress to expand from the inner layer to the surface, resulting in a hardened layer with a high residual compressive stress in the hardened layer. The local rapid heating and cooling make the ultra-fine grain austenite of the steel grow very late, and the martensite structure after laser phase transformation strengthening becomes very fine lath martensite and contracture martensite to obtain an ultra-fine grain size and phase transformation structure. The line scanning laser and its gear quenching principle and basic working mode are shown in Figure 1.

As shown in Figure 1, the scanning laser is protected by the CO_2 shielding gas flow, which is emitted from the laser equipment output after passing through the zoom field lens and directly irradiated on the surface of the gear teeth. After irradiation, an elliptical spot is formed on the surface of the gear. The power of the laser energy emitted by the laser during operation and transmitted to the surface of the target material is derived as follows:

$$P_L = P/\eta = Q\frac{\pi ab}{2\eta\eta_0}\cdot \exp\left[-2\cdot\frac{x^2+(y-v\cdot t)^2}{ab}\right]^{-1}, \tag{1}$$

where P_L is the laser source power, η is the laser source emission efficiency, Q is the laser energy density, η_0 is the laser quenching energy efficiency, a and b are the spot half-axis length on the x and y axes, respectively, and v is the laser scanning velocity.

According to the change mechanism of the laser absorption rate, the laser absorption rate of the steel alloys will gradually increase with the increase of its own resistivity [13]. The relationship is as follows:

$$A = 0.1457\sqrt{\frac{\rho}{\lambda}} + 0.09e^{-0.5\sqrt{\frac{\lambda\cdot c}{\rho N}}} + \frac{\rho}{N\lambda - 10^{-6}}, \tag{2}$$

where A is the laser absorption rate, ρ is the resistivity of the material, N is the number of electrons outside the material, λ is the laser wavelength, and c is a fixed constant.

For a more accurate analysis of the relationship between the laser source and the quenching properties, the output power of the source and the actual laser energy received by the surface of the quenched object need to be accurately quantified. The change of energy in the interaction between the laser and the metal material follows the energy conservation equation:

$$E_0 = E_r + E_a + E_t, \tag{3}$$

where E_0 is the laser energy incident on the surface of the material, E_r is the energy reflected by the material, E_a is the energy absorbed by the material, and E_t is the energy retained after the laser passes through the material.

Eq. 3 can be transformed into the following equation:

$$1 = \frac{E_r}{E_0} + \frac{E_a}{E_0} + \frac{E_t}{E_0} = R + \alpha + T, \tag{4}$$

where R is the reflection coefficient, α is the absorption coefficient, and T is the transmission coefficient.

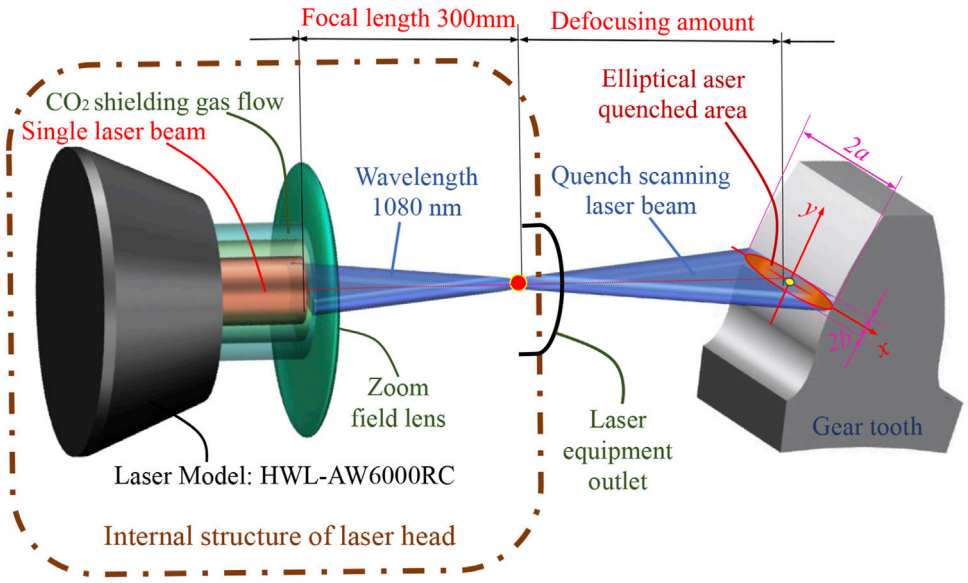

FIGURE 1
Variable depth quenching principle of gears by laser quenching.

During high-power laser quenching, the heat transfers to the surface of the steel instantaneously, so this causes the surface temperature to accumulate rapidly and rises to the critical point of phase transformation of the steel and continues to rise. As soon as laser scanning is completed, the heat in this region is rapidly transferred to the metal matrix, and the rapid decrease of temperature leads to the rapid conversion of some austenite structures into martensite. The carbon element in the retained austenite cannot diffuse, resulting in an increase in the carbon content of the martensite, thus resulting in an increase in the hardness of the region after laser scanning. Using the energy balance of the solid–liquid interface as the detection criterion of interface motion, the mathematical model for predicting and controlling the tissue under rapid solidification conditions is as follows [14]:

$$\mu = (2B - B - a) + \left[(2B - B - a)^2 - b\right]^{1/2}. \tag{5}$$

In the equation,

$$\begin{cases} a = (1-k)\varepsilon/(k+V), \\ 2B = \dfrac{aV}{1+V} + \dfrac{1-k}{1+k}, \\ b = \dfrac{a(a+V+k)}{1+V}, \\ V = \delta_i/D_i, \end{cases} \tag{6}$$

where k is the equilibrium distribution coefficient, δ_i is the jump distance between atoms, D_i is the interface diffusion coefficient, V is the velocity constant obtained by the solid–liquid interface when the molten pool reaches the quasi-steady state, and ε is the dimensionless concentration coefficient of the interface temperature. In the three cases of steady state ($\mu < 0$), the corresponding structures formed by rapid solidification are the planar crystal structure, cellular crystal structure, ($\mu = 0$) and dendritic structure ($\mu > 0$).

For the isothermal kinetic model of diffusive phase transition [15], the basic form is as follows:

$$f_{(T,t)} = 1 - \exp[-bt^n], \tag{7}$$

where $f_{(T,t)}$ is the amount of the new phase, t is the time, and b and n are the material constants under certain conditions.

For non-diffusion martensitic transformation, the amount of transformation is only determined by temperature and has nothing to do with time. The martensitic transformation formula can be expressed as follows [16]:

$$f_m = f^*\left(1 - \left(\frac{T - M_f}{M_s - M_f}\right)^{2.5}\right), \tag{8}$$

where T is the current temperature, M_s is the starting temperature of martensitic transformation, M_f is the termination temperature of martensitic transformation, and f_m is the martensite content.

According to the aforementioned analysis, when we use high-power laser quenching equipment to quench the surface layer of the gear tooth surface, we can analyze the actual quenching effect of laser quenching on steel by the quenching experiment of different laser light source power and frequencies, scanning spot sizes, and scanning velocities (quenching depth and surface Rockwell hardness). In addition, the effect of laser scanning velocity on the mechanical properties of steel was studied. In order to eliminate the influence of the gear tooth profile radian on the laser scanning velocity and angle and, at the same time, to ensure the single variable principle of the experiment and control the variable accuracy in the experiment process, we used cuboid specimens for experimenting. As a widely used material, the experimental results of 45 steel would be highly representative. Its high carbon content could also show the mechanical performance change suitability during laser quenching, so it is used as the target material of our experiment specimens.

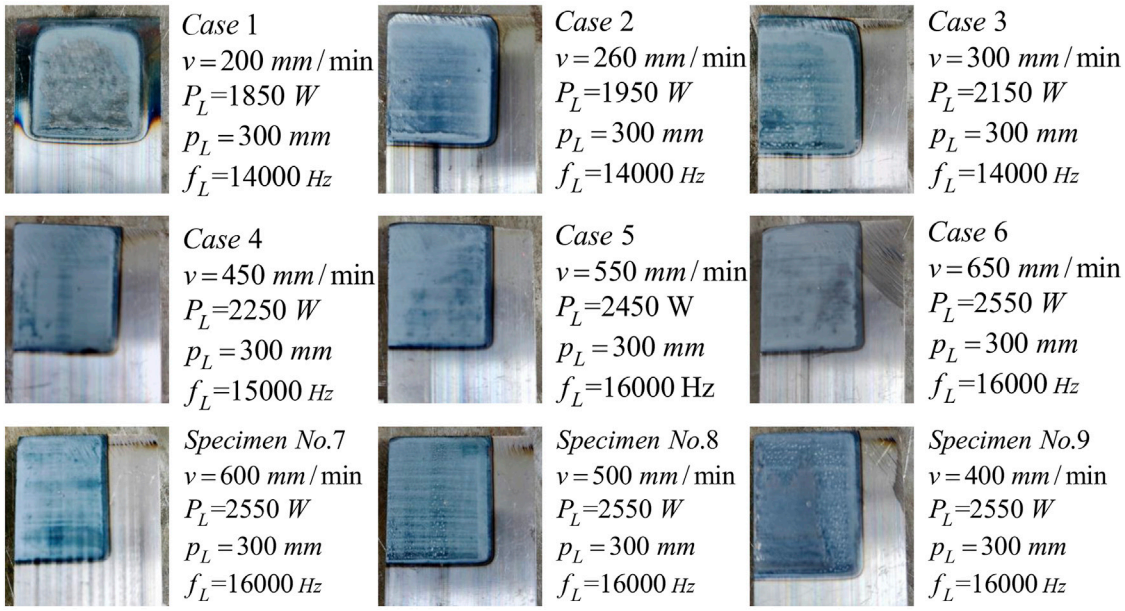

FIGURE 2
Actual morphology of 9 specimens after laser quenching.

TABLE 1 Results of the laser quenching depth and surface hardness.

Parameter	Case 1	Case 2	Case 3	Case 4	Case 5	Case 6	Case 7	Case 8	Case 9
Scanning velocity (mm/min)	200	250	300	450	550	650	600	500	400
Laser power(W)	1850	1950	2100	2250	2400	2550	2550	2550	2550
Laser focus (mm)	300	300	300	300	300	300	300	300	300
Depth of quenching (mm)	0.90	0.80	0.60	0.50	0.40	0.40	0.55	0.80	0.90
Rockwell hardness (HRC)	60	58	61	54	58	55	61	61	61

3 Experimental process

In order to obtain reasonable experiment results, this paper uses HWL-AW6000RC laser quenching equipment which can stably control the high-power output parameters of the laser to experiment the laser quenching treatment of the surface of 45 steel specimens. The maximum power of this type of laser equipment is 6000 W, and the actual output power of the laser source can reach 3000 W. The laser beam is a single beam, and the scanning range is 0–30 mm. During the experiment, laser focal length is fixed (300 mm) and the laser scanning width is 20 mm, which is slightly less than the width of the specimen.

The material of the experiment specimen is 45 steel, and the size of each specimen is 30 × 20 × 5 mm. Before the experiment, the surface roughness of each sample was uniformly treated and cleaned with alcohol. The experiment was divided into three groups. The first group was quenched with stable velocity, including 27 cases. The second group was subjected to an accelerated quenching experiment, including 12 cases. The third group conducted a deceleration experiment, including 12 cases. In the first group, nine well-behaved specimens were taken as reference and the average surface Rockwell hardness was experimented. Finally, the actual quenching depth is measured after the experiment, and the average Rockwell hardness and quenching depth are determined at three positions for the other two specimens. After the preliminary selection and trial analysis of the laser light source and quenching parameters, we selected the following parameters for formal experiment analysis.

In this laser quenching experiment group, nine qualified samples in the first group were selected for display. Figure 2 shows the actual morphology and their different parameters after laser quenching.

It can be known from the laser quenching experiment results that the surface consistency of the quenching experiment at a fixed laser scanning velocity is consistent, and the results under the same experiment conditions are basically consistent identically.

Based on this result, we determine that the laser quenching power and frequency used in variable velocity laser quenching as follows are consistent with cases 7, 8, and 9.

After experimenting with the surface Rockwell hardness of the cases, we cut the specimens longitudinally without damage and

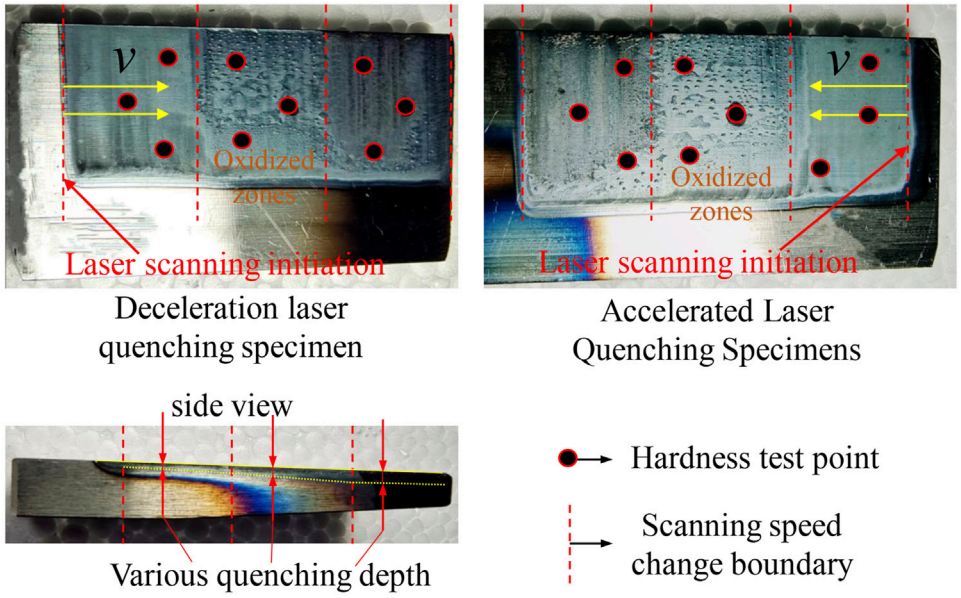

FIGURE 3
Schematic diagram of specimen morphology after accelerated and decelerated laser quenching.

TABLE 2 Dimensionless results of variable quenching parameters.

	Case 1	Case 2	Case 3	Case 4	Case 5	Case 6	Case 7	Case 8	Case 9	Case 10	Case 11
Dimensionless energy	3.92	4.08	4.25	4.43	4.63	4.85	5.10	5.37	5.67	6.00	6.38
Dimensionless depth (velocity increase)	4.0	5.0	5.8	6.5	7.0	7.5	8.1	8.45	8.6	8.85	9.0
Dimensionless depth (velocity decrease)	4.0	5.0	5.7	6.7	7.2	7.5	8.1	8.6	8.8	8.9	9.0

measured the actual quenching depth. The laser quenching depth and surface Rockwell hardness of every case as a reference for the further experiment are shown in Table 1.

The Rockwell hardness experiment of steel specimen material before laser quenching is 30HRC. Comparing the results in the aforementioned table, it can be found that high-power and high-frequency laser scanning quenching can quickly increase the surface hardness of the material with a thickness of 1 mm. But for 45 steel, on the surface layer within 1 mm after laser quenching, its Rockwell hardness can only reach 61HRC, which is related to its material composition. In addition, according to the aforementioned experiment results and empirical analysis, the laser light source power and quenching scanning velocity are the most important parameters affecting the material properties after quenching.

The laser scanning velocity changes in both accelerated and decelerated laser quenching experiments (scanning velocity varies from 400 to 650 mm/min). The scanning velocity is smoothly changed by the automatic control system of the laser itself. The experiment process was carried out at standard room temperature. At the same time, the laser quenching process was only protected by the CO_2 protective gas of the laser itself, and different degrees of spotted oxidation zones appeared in the intermediate variable velocity stage of the laser quenching specimen. However, after the hardness experiment, we find that spotted oxidation zones had little effect on the surface hardness of the specimen. The morphology of comparative specimens after accelerated and decelerated laser quenching is shown in Figure 3.

It can be seen from the aforementioned figure that the variable velocity laser quenching process shows little difference in morphology, and the quenching area and boundary area of the material surface after laser quenching still maintain a high surface quality.

On the side view of the uncut section, it can be seen that the quenching layer at the edge of the specimen is also consistent with the variation of the scanning velocity. It can be seen that the quenching scheme of automatic control of scanning velocity by the laser quenching system can meet the process requirements of variable depth and surface hardness. In addition, because the surface of the specimen is not protected by inert gas during the quenching process, the morphology of the intermediate variable velocity region of the laser quenching of the specimen shows a certain amount of spotted oxidation zones, which may be due to the unstable quenching velocity.

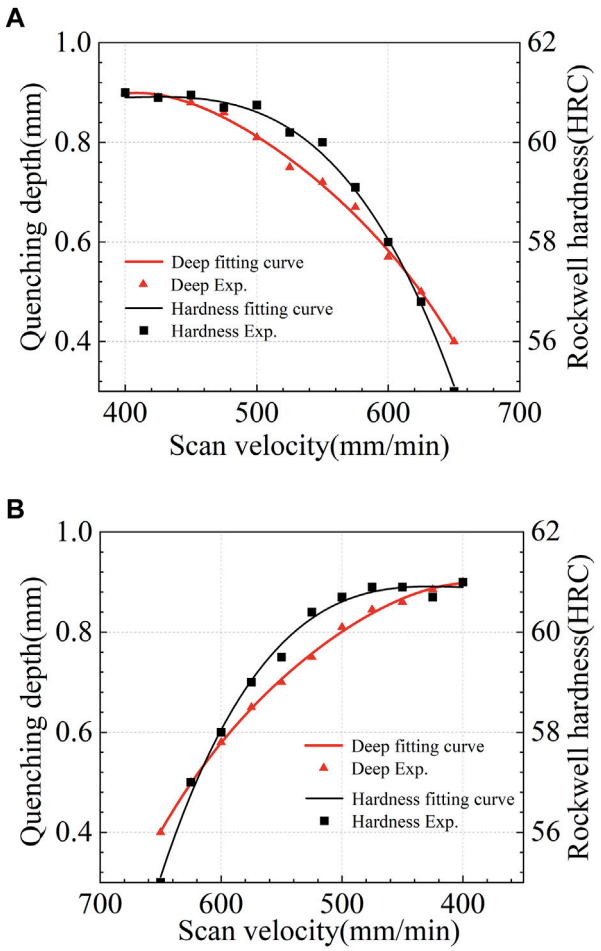

FIGURE 4
(A) Deceleration quenching results. **(B)** Accelerated quenching results. Results of variable quenching scanning velocity.

4 Results and discussion

After completing all the experiment cases, we performed Rockwell hardness experiments on the surface of specimens quenched by a variable velocity laser. The specimen was then subjected to a non-destructive longitudinal cutting to measure its actual quenching depth. The measurement results of the second group of specimens are averaged, and the distribution results are interpolated by multiple term functions to obtain the fitting results, as shown in Figure 4.

As it is shown in Figure 4A, during the scanning process of deceleration laser quenching, the actual quenching depth of the specimen is basically consistent with the reference specimen, and the average hardness is basically consistent with the reference specimen in the initial stage, but it tends to the maximum value and remains stable in the final stage of deceleration.

It can be seen from Figure 4B that during the scanning process of decelerated laser quenching, the actual quenching depth of the specimen is basically consistent with that of the reference specimen, while the hardness is basically consistent with the result of the reference specimen in the initial stage of acceleration. However, in the final stage of acceleration, there is a slight change and its value decreases slightly faster.

From the previous numerical analysis, it can be seen that whether it is accelerated or decelerated scanning; the effect of laser quenching on the surface Rockwell hardness of 45 steel is consistent with that of constant velocity scanning. The reason is that despite the high frequency and high-power laser quenching used in the experiment, the energy transfer efficiency is sufficient to meet the energy demand of the phase change of the material surface structure in a short time, but the increase of hardness depends on the specific composition of the structure, especially the carbon content level. However, during variable speed quenching in a short time, the accumulative effect of laser energy on the surface of the material and the temperature rise of the shallow layer of the material are different, resulting in a slight difference in the final quenching performance.

Then, we numerically analyzed the actual output power of the dimensionless laser and the average quenching depth of the variable velocity scanning quenching specimen, ignoring the effect of laser scanning time. The results are shown in Table 2.

According to Table 2, when the influence of the heat accumulation effect caused by scanning time on the quenching depth is not considered (that is, when the influence of the scanning velocity is not considered), the laser source power in the laser quenching process is almost proportional to the actual quenching depth because the higher the laser output power in unit time, the more heat the material receives, resulting in a rapid temperature rise and faster radiation to the deep material.

Although the output power and scanning velocity of the laser source have a major impact on the actual effect of quenching, the program control adjustment of the scanning velocity can change the quenching performance within a certain range when the laser power is inconvenient to change in production applications. Coincidentally, for a commonly used small gear with the modulus about 5–10, the laser scanning velocity adjustment range can be applied to their tooth surface quenching depth changes. However, according to [17] and Equations 4, 8, the maximum hardness of metal materials achieved by laser quenching is related to the material itself. Therefore, in practical applications, when the same material is quenched to a specified depth using variable parameter laser parameters, its final performance can be determined by dimensionless laser scanning speed and power.

5 Conclusion

Variable velocity laser quenching is one of the most effective methods to precisely control the variable depth quenching process of the gear tooth surface, compared with other quenching techniques and control methods. Although laser quenching has excellent consistency and controllability compared to other quenching techniques, we do not recommend changing the scanning velocity too fast to avoid other uncontrollable damage on the surface of the specimen during laser quenching without inert gas protection. For further summary, we have the following conclusions.

1) The quenching experiment of 45 steel with fixed focus was carried out by changing the laser scanning velocity. It was found that the change of the laser quenching depth with the laser scanning velocity can be controlled within a reasonable range, and the surface hardness of the quenched sample also meets the expectation with an increase in percentage from 80% to 100%.
2) By adjusting the parameters of the laser source power and the scanning velocity for quenching experiments, we found that the

surface hardness of the specimen does not change with the excessive laser energy received in fact. The reason is that the microstructure characteristics of the alloy at a given quenching depth, especially the carbon content, determine its maximum hardness level.

3) Taking constant velocity laser quenching as a reference, the Rockwell hardness of the specimens after accelerated and decelerated laser quenching is taken into consideration and analyzed. Compared to the results of material properties under two experiment conditions, it is found that the rate characteristics of heat accumulation effect deceleration quenching may be more suitable for laser quenching of the gear surface with increased laser quenching depth.

Data availability statement

The original contributions presented in the study are included in the article/supplementary material; further inquiries can be directed to the corresponding author.

Author contributions

DR proposed the idea of this paper, finished the formulation and implementation of the research content and experiment program, and then completed the main writing of the manuscript. PZ investigated and sorted out the application of laser equipment and the related literature studied in this paper, and undertook the manuscript collation and submission process. JY carried out the experimental implementation process and operated the experiment data collection, screening, and statistical analysis in this paper. YY analyzed the mechanism and application background of laser quenching for strengthening the mechanical properties of alloy materials. In addition, YY provided a correction for the research direction and technical route of this paper. XL provided the materials' parameter data for the experiment process and the mechanical performance analysis device.

Funding

This study was funded by the Pre-Researching Key Project of National Defense: 208052020305.

Acknowledgments

The authors thank Dongguan Huawei Laser Equipment Co., Ltd., for their full support of laser quenching equipment and experimenting provided for this paper. The authors declare that this study received contribution from Huawei Laser Equipment Co., Ltd. The company was not involved in the study design, collection, analysis, interpretation of data, the writing of this article or the decision to submit it for publication.

Conflict of interest

The authors declare that the research was conducted in the absence of any commercial or financial relationships that could be construed as a potential conflict of interest.

Publisher's note

References

1. Zhang W, Yang S, Lin Z, Tao W. Weld morphology and mechanical properties in laser spot welding of quenching and partitioning 980 steel. *J Manufacturing Process* (2020) 56: 1136–45. doi:10.1016/j.jmapro.2020.05.057

2. Biungxu W, Yuming P, Yu L, Lyu N, Barber GC, Wang R, et al. Effects of quench-tempering and laser hardening treatment on wear resistance of gray cast iron. *J Mater Res Tech* (2020) 9(4):8163–71. doi:10.1016/j.jmrt.2020.05.006

3. Feng A, Wei Y, Liu B, Chen C, Pan X, Xue J. Microstructure and mechanical properties of composite strengthened high-chromium cast iron by laser quenching and laser shock peening. *J Mater Res Tech* (2022) 20:4342–55. doi:10.1016/j.jmrt.2022.08.148

4. Zehao T, Qunli Z, Hua H, Zhijun C, Junsheng C, Jianhua Y. Geometric characteristics and microstructure of laser-induction hybrid quenching hardened layer on 42CrMo steel. *Rare Metal Mater Eng* (2022) 51(7):2519–28.

5. Li Z, Wen Z, Su F. Modeling research on laser quenching process of GCr15 bearing steel basing on material properties obtained with experimental methods. *Mater Res Express* (2021) 8(9):096516. doi:10.1088/2053-1591/ac2341

6. Yasuda T, Shozui R, Nishimoto K, okumoto Y, Ohmura T. Nano-mechanical and sub-micro-structural characterization of spot-laser-quenched carbon steel[J]. *Tetsu Hagane-Journal Iron Steel Inst Jpn* (2022) 108(7):405–23. doi:10.2355/tetsutohagane.TETSU-2021-090

7. Sugimoto T, Ju DY. Influence of thermal boundary conditions on the results of heat treatment simulation. *Mater Trans* (2018) 59:950–6. H-M2018816. doi:10.2320/matertrans.H-M2018816

8. Su Y, Oikawa K, Shinohara T, Kai T, Horino T, Idohara O, et al. Neutron Bragg-edge transmission imaging for microstructure and residual strain in induction hardened gears. *Scientific Rep* (2021) 11(1):4155–14. doi:10.1038/s41598-021-83555-9

9. Cai S, Sun J, He Q, Shi T, Wang D, Si J, et al. 16MnCr5 gear shaft fracture caused by inclusions and heat treatment process. *Eng Fail Anal* (2021) 126:105458. doi:10.1016/j.engfailanal.2021.105458

10. Barglik J, Ducki K, Kuc D, Smagor A, Smalcerz A. Hardness and microstructure distributions in gear wheels made of steel AISI 4340 after consecutive dual frequency induction hardening. *Int J Appl Electromagnetics Mech* (2020) 63(S1):S131–40. doi:10.3233/jae-209111

11. Li C, Gao H, Chen X, Liu Z, Han X. Study on multi-field coupled evolution mechanism of laser irradiated 40Cr steel quenching process based on phase change induced plasticity. *Met Mater Int* (2022) 28(8):1919–37. doi:10.1007/s12540-021-01093-5

12. Muthukumaran G, Dinesh Babu P. Laser transformation hardening of various steel grades using different laser types. *J Braz Soc Mech Sci Eng* (2021) 43(2):103–29. doi:10.1007/s40430-021-02854-4

13. Jun C, Qunli Z, Jianhua Y, Jibin F. Laser absorptivity of metallic materials [J]. *Appl Opt* (2008)(05) 793–8.

14. Guo W, Kar A. Interfacial instability and microstructural growth due to rapid solidification in laser processing. *Acta Materialia* (1998) 46(10):3485–90. doi:10.1016/s1359-6454(98)00050-0

15. Avrami M. Kinetics of phase change. I general theory. *J Chem Phys* (1939) 7(12): 1103–12. doi:10.1063/1.1750380

16. Koistinen DP, Marburger R. A general equation prescribing the extent of the austenite-martensite transformation in pure iron-carbon alloys and plain carbon steels. *Acta metallurgica* (1959) 7:59–60. doi:10.1016/0001-6160(59)90170-1

17. Ibrahim MZ, Sarhan AAD, Kuo TY, Yusof F, Hamdi M. Characterization and hardness enhancement of amorphous Fe-based metallic glass laser cladded on nickel-free stainless steel for biomedical implant application. *Mater Chem Phys* (2019) 235:121745. doi:10.1016/j.matchemphys.2019.121745

Frontiers in Physics

Investigates complex questions in physics to understand the nature of the physical world

Addresses the biggest questions in physics, from macro to micro, and from theoretical to experimental and applied physics.

Discover the latest Research Topics

See more →

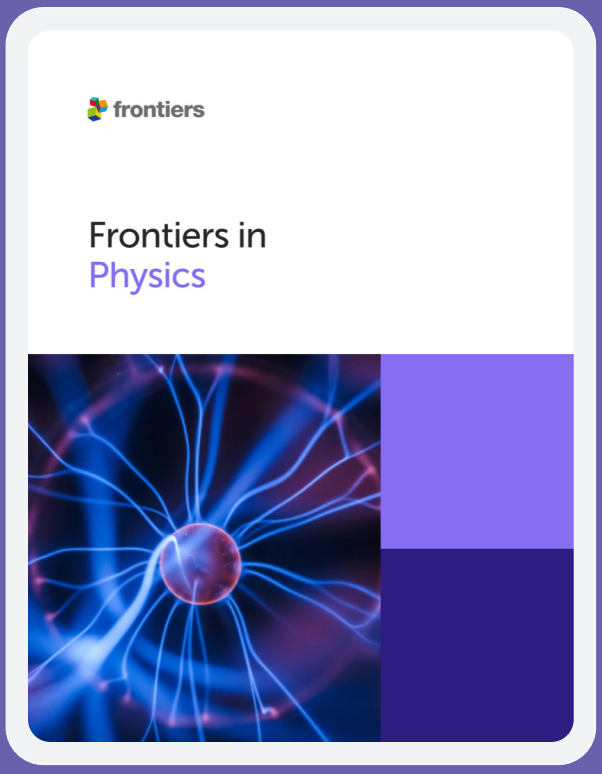

Frontiers

Avenue du Tribunal-Fédéral 34
1005 Lausanne, Switzerland
frontiersin.org

Contact us

+41 (0)21 510 17 00
frontiersin.org/about/contact